PRE-ERUPTIVE TIMESCALES AND PROCESSES OF LARGE SHALLOW MAGMA SYSTEMS REVEALED BY COMPOSITIONAL VARIABILITY IN SILICIC IGNIMBRITES

by

Amanda C. Laib

A thesis

submitted in partial fulfillment

of the requirements for the degree of

Master of Science in Geology

Boise State University

August 2016

BOISE STATE UNIVERSITY GRADUATE COLLEGE

DEFENSE COMMITTEE AND FINAL READING APPROVALS

of the thesis submitted by

Amanda C. Laib

Thesis Title: Pre-eruptive Timescales and Processes of Large Shallow Magma Systems Revealed by Compositional Variability in Silicic Ignimbrites

Date of Final Oral Examination: 20 April 2016

The following individuals read and discussed the thesis submitted by student Amanda C. Laib, and they evaluated her presentation and response to questions during the final oral examination. They found that the student passed the final oral examination.

Mark Schmitz, Ph.D.	Chair, Supervisory Committee
Brittany D. Brand, Ph.D.	Member, Supervisory Committee
V. Dorsey Wanless, Ph.D.	Member, Supervisory Committee
James Crowley, Ph.D.	Member, Supervisory Committee

The final reading approval of the thesis was granted by Mark Schmitz, Ph.D., Chair of the Supervisory Committee. The thesis was approved for the Graduate College by Jodi Chilson, M.F.A., Coordinator of Theses and Dissertations.

DEDICATION

To my dad, who inspired my love of science and sense of curiosity, but who left this world before I could teach him about rhyolite; to my mom, from whom I learned strength and integrity, and who will be forced to read every last word of this document; and also to my big brother who has always been my hero.

ACKNOWLEDGEMENTS

I would like to extend immense appreciation to my advisor, Dr. Mark Schmitz, for his utmost patience, guidance, support, inspiration, and thought-provoking discussions, in addition to countless donuts. Thanks to my advisory committee who provided me with invaluable feedback, challenging me to be a better researcher, writer, and speaker. Dr. Brittany Brand encouraged me to broaden my perspective by zooming out from the zircon scale, Dr. Dorsey Wanless drove me to be thorough in validating my results and interpretations, and Dr. James Crowley was my geochronology and lab methods guru throughout.

Paul Olin and Liz Lovelock provided help in the field, as did Martin Streck at Portland State University, whose input greatly improved the outcomes of this research. Thanks to Debbie Pierce and Marion Lytle for help in the mineral separation and LA-ICP-MS labs, respectively. Tiffany Rivera is greatly appreciated for her mentorship during all stages of this project. Warmest gratitude to the cohort of graduate students in the Isotope Geology Lab—Claire Ostwald, Josh Ekhoff, Vince Isakson, and Mike Mohr—who promoted a sense of community and motivated me to work as hard as they do. Finally, the biggest thanks of all to my family, and my partner, Troy Smith, and his family for their love and support during my time in graduate school.

This work was funded by the National Park Service at John Day Fossil Beds National Monument, National Science Foundation, Geological Society of America, and Boise State University Department of Geosciences.

ABSTRACT

Intracontinental magmas are stored at shallow crustal depths and commonly produce compositionally variable deposits when erupted. A core objective of igneous petrology is to understand the processes and pathways by which these magmas are generated and differentiated. Despite decades of research, debate persists regarding the comparative effects of processes like assimilation, fractional crystallization, and magma mixing in the production of compositional zonation. There are two end member hypotheses of how compositional variability develops in pre-eruptive magma bodies; one proposes long-term storage and crystal fractionation of a mafic or intermediate parent magma, while the other proposes a more transient system resulting from crustal melting, high magma flux rates, and magma mixing. This study examines the relative influences of fractional crystallization and magma mixing in the development of compositional heterogeneities in crustal intracontinental magmas and the timescales over which these processes occur.

The Picture Gorge Ignimbrite (PGI) and Rattlesnake Tuff (RST) in east central Oregon are contrasting examples of compositional variability in rhyolitic ashflow tuffs that provide case studies for both gradational and abrupt styles of compositional variability, respectively. Disequilibrium textures in zircon crystals from both tuffs offer evidence of open system recharge and magma mixing in the pre-eruptive magma chambers. Trace element chemistry and Ti-in-zircon crystallization temperatures of zircon crystals from the PGI record a reheating event coupled with a change in magma

chemistry that coincides with an episode of zircon resorption followed by recrystallization. The zircon crystal record of the RST magma system is markedly more complicated as illustrated by complex crystallization textures and intracrystal thermochemical zoning profiles. Complexity of the RST system is further revealed by bimodal feldspar compositions and widely variable glass compositions that form fractional crystallization and mixing arrays between and within compositional groups.

Tandem LA-ICPMS and CA-TIMS U-Pb geochronology on crystals demonstrate multigenerational antecrystic growth in both the PGI and RST systems occurring over 10^4 year timescales. Petrochronologic analysis of these two rhyolites preclude protracted closed system differentiation as a mechanism for compositional evolution and development of a compositionally zoned pre-eruptive magma body. Rather, thermochemical gradients in both systems were likely imparted primarily by magma rejuvenation and hybridization. Results suggest that, in the PGI magma body, a single recharge episode allowed for homogenization of the hybrid magma prior to eruption, while greater magma flux rates in the RST magma resulted in incomplete pre-eruptive mixing and preservation of distinct magma compositions that were mingled upon eruption.

TABLE OF CONTENTS

LIST OF TABLES

LIST OF FIGURES

LIST OF ABBREVIATIONS

HSR	High Silica Rhyolite
ITE	Incompatible Trace Elements
ME	Major Elements
TE	Trace Elements
REE	Rare Earth Elements
LREE	Light Rare Earth Elements
MREE	Middle Rare Earth Elements
HREE	Heavy Rare Earth Elements
PGI	Picture Gorge Ignimbrite
RST	Rattlesnake Tuff
JDF	John Day Formation
CL	Cathodoluminescence
LA-ICPMS	Laser Ablation-Inductively Coupled Plasma Mass Spectrometry
IGL	Isotope Geology Lab
BSU	Boise State University
CA-ID-TIMS	Chemical Abrasion-Isotope Dilution-Thermal Ionization Mass Spectrometry
HF	Hydrofluoric Acid
HCl	Hydrochloric Acid
HNO_3	Nitric Acid

XRF	X-ray fluorescence
HLP	High Lava Plains
HAOT	High Aluminum Olivine Tholeiites
PCT	Prater Creek Tuff
HFSE	High Field Strength Element

CHAPTER ONE: INTRODUCTION

Crustal Magmatic Systems

The study of rhyolite petrogenesis is foundational to the field of igneous petrology and the effort to understand the origins and continuing evolution of continental crust (Bowen 1928; Smith 1960; Lipman and Bachmann 2015). Rhyolitic ignimbrites are produced by the most voluminous and violent volcanic eruptions on earth. The geochemical, depositional, and stratigraphic nature of these deposits provides important information concerning pre-eruptive processes that combine to produce cataclysmic eruptions. Despite ongoing research, debate surrounds the generation, emplacement, and storage of highly evolved silicic liquids in the shallow crust, and the timescales over which the contributive processes occur (Bachmann and Bergantz 2004; Glazner et al. 2008; Streck 2014). This debate is complicated by the diversity of tectonic environments that host rhyolitic volcanism (Bachmann and Bergantz 2008).

Early magmatic evolution studies proposed that rhyolite could be generated by extensive crystal fractionation of basalt (Bowen 1928; Tuttle and Bowen 1958). Modern studies commonly use geochemical variation to establish a liquid line of descent connecting rhyolite domes to mafic and intermediate parental magma (Nekvasil et al. 2000; McCurry et al. 2008; Whitaker et al. 2008). The ‘crystal mush’ model—the dominant model to explain crystal-poor rhyolites—also invokes fractional crystallization (Bachmann and Bergantz 2004). Protracted differentiation of an intermediate parent magma produces a body of crystal cumulates containing highly evolved interstitial melt.

The evolved melt is extracted from the crystalline mush framework and forms a lens of crystal-poor eruptible rhyolitic magma capping a cogenetic batholithic crystalline residue. In this model, the cumulate mush is preserved as a pluton, while the crystal-poor rhyolite is erupted.

When broadly applied to the generation of crystal-poor rhyolitic ignimbrites, closed system crystal fractionation models are problematic for the following reasons: 1) an immense volume of parent magma, regardless of initial composition, is needed to produce the voluminous bodies of silicic magma typical of caldera-forming rhyolite eruptions (Bachmann and Bergantz 2003; Lipman 2007; Hildreth and Wilson 2007; Streck and Grunder 2008); 2) minimum magma flux estimates for large ignimbrite eruptions are inconsistent with those of pluton assembly (Glazner et al. 2004; Crowley et al. 2007; Annen 2009; Tappa et al. 2011; Rivera et al. 2014); 3) trace element patterns of aplite dikes, remnants of late-stage plutonic magma extraction, record markedly different crystallization histories than those of high silica rhyolites (SiO_2 >74 wt %, hereafter HSR) (Hildreth 2004; Glazner et al. 2008); 4) 'hot and dry', crystal-poor rhyolites, for example, from the bimodal High Lava Plains volcanic province in central Oregon, record isotopic compositions and crystallization temperatures that are inconsistent with predicted interstitial melt compositions of crystal mushes (Streck and Grunder 2008; Streck 2014); and 5) there is a lack of physical evidence for the presence of unerupted parental mush in most cases (Streck and Grunder 2008; Streck 2014; Wolff et al. 2015).

Recycling of pre-existing evolved crust via melting is an appealing alternative to the crystallization driven mush model because it eliminates problems of the heat, space and time needed to generate, accommodate and fractionate a large intermediate parental

magma body (Dufek and Bergantz 2005; Streck and Grunder 2008; Bindeman and Simakin 2014). Partial melting of silicic or intermediate crust would produce a silicic liquid enriched in incompatible trace elements (ITE), which would resemble an extensively fractionated magma. However, some partial melting models do not accurately reproduce the compositions of enriched rhyolitic magmas (Halliday et al. 1991), without invoking small degrees of fractional crystallization to rationalize discrepancies in major elements (Streck 2002). Thus, the notion of partial melting to produce an apparently evolved silicic magma in the shallow crust does not preclude the contribution of fractional crystallization to the petrogenetic process.

Compositional Zoning

The crystal mush model and partial melting of heterogeneous crust are both called upon to explain compositional variability commonly observed in ignimbrites. Numerous types of compositional variability are displayed by large volume silicic eruptive sequences (Hildreth 1981). Generally, these are of two main types: gradational variability, where a change in composition occurs gradually in eruptive stratigraphy or in compositional space, and abrupt variability, where compositional change occurs sharply and may be accompanied by a compositional gap (Williams et al. 1942; Smith 1979).

Gaps in major element composition are often associated with abrupt changes in crystal content (Smith 1979; Hildreth 1981), which is compatible with a model of melt extraction where mush-derived crystals are entrained in the later erupted magma (Hildreth 2004; Bachmann and Bergantz 2008). However, this process alone cannot explain the development of subtler thermal and trace element gradients. Bachman and

Bergantz (2008) suggest that gradients develop following separation of the melt and as a result of different processes, including inhibited convection and wall rock assimilation.

Recent modifications to the mush model require open system rejuvenation of either a near solidus magma or an underlying cumulate pile to explain both abrupt and gradational styles of zoning (Streck and Grunder 2008; Huber et al. 2012; Streck 2014; Wolff et al. 2015). Thermal fluctuation caused by influx of hot magma supports formation of an eruptible magma despite residence times on the order of 10^4-10^5 years (Bachmann and Bergantz 2008; Tappa et al. 2011; Rivera et al. 2013; Bindeman and Simakin 2014). Incremental assembly of a magma body can cause compositional heterogeneity, either inherited from the rejuvenating magma (Streck and Grunder 2008; Huber et al. 2012) or resulting from punctuated episodes of partial melting of the underlying cumulate mush, producing progressively less evolved liquid from each subsequent extraction (Wolff et al. 2015).

Evidence for open system behavior in compositionally zoned ignimbrites is documented at a range of spatial scales. A deposit typically displays an overall decrease in melt evolution from early to late eruptive products preserved in composition of bulk material (Smith 1960; Fisher 1966; Hildreth 1979; Smith 1979; Hildreth 1981). There may also be compositionally distinct populations of individual pumices, hosting distinct mineral assemblages and representing separate magma compositions within an eruptive sequence (Streck and Grunder 1997; Wright et al. 2011). Individual mineral grains often display compositional diversity accompanied by complex crystallization and resorption textures that correspond to changes in crystallization temperatures (Wark et al. 2007; Claiborne et al. 2010; Rivera et al. 2014).

Compositional variability in eruptive products of large silicic systems is a record of the state of a compositionally zoned magmatic system immediately prior to ascent. Volcanic glass compositions characterize the final liquid phase of a magma, thus providing a fleeting view of a transient system. Modal mineral compositions contribute a more archival view of the whole system evolution. Crystallization of modal minerals is the primary control of the major element (ME) budget in a cooling magma. However, because ME are proportionally dominant components of magma chemistry, only large compositional shifts can be recorded by modal phases. If pre-eruptive processes like fractional crystallization, rejuvenation, and magma mixing create only small shifts in ME composition, these processes will be undetectable in the modal record. Consequently, a more sensitive record is required to interpret a detailed historical perspective of the magma.

Trace element (TE) abundances are substantially lower than ME in magmatic systems, and so modest degrees of magma evolution can result in pronounced changes in the TE composition of a system (Allègre and Minster 1978). For this reason, they offer a more suitable tool than ME in the study of pre-eruptive processes in silicic magmas, which may result in only minor ME compositional changes. Rare earth elements (REE), La through Lu (atomic numbers 57-71), are a particularly useful group of TE. They are all trivalent (+3 charge) and have similar physical and chemical properties. However, as their atomic numbers increase, their ionic radii decrease in what is known as the "lanthanide contraction," causing a systematic variance among compatibilities of light, middle, and heavy REE (LREE, MREE and HREE, respectively).

Slight changes in compatibility result in fractionation among the REE, which is more pronounced in some minerals than others. For example, residual magma in a zircon ($ZrSiO_4$) saturated system will become depleted in HREE and Zr as crystallization progresses because zircon preferentially consumes those elements. Similarly, chevkinite incorporates LREE and so depletes the surrounding liquid as it crystallizes. Zircon and chevkinite are examples of accessory phases that comprise a volumetrically insignificant proportion of most magmatic systems, but strongly favor REE and therefore cause prominent fractionation signatures. An REE concentration plot of a zircon-bearing magma would have a negative slope, from La to Lu, while a chevkinite-bearing melt would have a positive slope.

Among REE, Eu concentration is particularly responsive to crystallization because it can be reduced to a divalent oxidation state (Eu^{+2}) and substitute for Ca^{2+}, primarily in plagioclase feldspar. Eu depletion relative to other REE is recorded by other phases within the system as a negative Eu anomaly. Increasing Eu depletion, or a larger negative Eu anomaly, indicates more extensive plagioclase fractionation. Since plagioclase is a dominant phase in the mineral assemblage of silicic magmas, Eu anomalies in eruptive products are employed as a proxy for magma crystallinity. Eu depletion may be more pronounced in rhyolites produced in the hot-dry-reduced extensional tectonomagmatic environments (Glazner et al. 2008; Bachmann and Bergantz 2008).

Divalent Eu substitution in plagioclase is an exception to the general incompatibility of TE in the modal phases of magmatic systems. Due to their incompatibilities, TE are excluded from crystallizing phases and increasingly enriched in

the liquid phase of a progressively fractionating magma. As enrichment occurs, TE rich trace minerals reach saturation and begin to crystallize. These non-modal accessory phases that tend to concentrate TE provide a comprehensive and high fidelity record of the magmatic environment. Zircon is a Zr-silicate accessory mineral found in most felsic rocks, which incorporates TE, especially HREE, Hf, Y, U, Th and to a lesser degree LREE and MREE, through a variety of mechanisms. The simplest of these involves substitution of a tetravalent cation (i.e., Hf^{4+}, U^{4+}, Th^{4+}) for Zr^{4+}. However, coupled substitution of of $REE^{3+} + P^{5+}$ for $Zr^{4+} + Si^{4+}$ is the dominant mechanism (Hoskin and Schaltegger 2003).

Uranium (U), similar to HREE, is relatively compatible in the zircon crystal structure during crystallization, while lead (Pb) is essentially excluded. Coincidentally, two radioactive isotopes of U decay to two different isotopes of Pb, ^{235}U to ^{207}Pb, and ^{238}U to ^{206}Pb, with half-lives of $7.0381 \pm 0.0048 \times 10^8$ and $4.4683 \pm 0.0024 \times 10^9$ years, respectively (Jaffey et al. 1971). The inverse relationship of the compatibilities of these isotopes in the zircon crystal lattice and allow for the determination of a zircon crystallization age by determination of the daughter to parent isotopic ratio in zircon crystals.

Ti is another valuable trace element, as its substitution in zircon, primarily for Si, is temperature dependent. The Ti-in-zircon geothermometer provides a tool for interpreting the thermal history of a crystallizing magma (Ferry and Watson 2007). Zircon typically reaches saturation early in felsic magmas (Watson 1979; Corfu et al. 2003) and grows throughout the crystallization history of a magma, recording the evolutionary path as it forms. Zircon crystals retain their composition through a wide

range of magmatic temperatures and conditions due to low diffusivity of trace element impurities (Cherniak and Watson 2003).

The TE and isotopic characteristics of the zircon crystals in a system combine to produce a robust and thorough thermochemical and temporal record of the system. ME and TE compositions of whole rock, glass, and modal phases supplement the zircon record in magmatic systems to delineate timing and relationships between open and closed system magmatic processes. The work presented here employs a multi-system approach of zircon chemistry in combination with modal phase feldspar, whole rock, and glass chemistry in resolving the timing, temperature, and degree of magma mixing and fractional crystallization in the development of a compositionally zoned magma chamber. In situ microanalysis of volcanic glass shards reveals the fine scale of chemical heterogeneity that is unresolvable using whole rock and bulk glass analytical methods, which perhaps unintentionally homogenize mingled magma compositions (Eichelberger et al. 2000; Shane et al. 2004).

The Picture Gorge Ignimbrite (PGI) and the Rattlesnake Tuff (RST) are contrasting examples of compositional zoning with which to test this approach. They generally exhibit a decrease in melt evolution throughout the eruptive sequence, suggesting roof downward tapping of a chemically stratified magma body (Smith 1979; Hildreth 1981). However, the nature of the progression from most to least evolved eruptive products differs. The PGI has a thermochemical gradient preserved in the modal mineral assemblage, accompanied by only a slight change in bulk rock chemistry (Fisher 1966). In contrast, compositional variability in the RST is characterized by abrupt changes and gaps in modal mineral, bulk rock, and glass chemistry (Streck and Grunder

1997). This study examines the influence and timing of open and closed system processes in the PGI and RST magma chambers to explain divergent styles of compositional zoning.

CHAPTER TWO: PICTURE GORGE IGNIMBRITE

Compositional Diversity in Silicic Magmas

The nature of compositional variability commonly found in large volume silicic tuffs may display one of numerous styles (Hildreth 1981). Often, there is a strong stratigraphic correlation in which early erupted products comprise a cool, chemically evolved magma, defined primarily by major element concentration and phenocryst assemblage, and later erupted products represent a hotter more primitive magma composition. In this style of compositional zoning, the nature of the progression can be either gradational or abrupt, with either subtle or significant ranges in composition (Smith 1979). Deposits that are subtly gradational in major elements (ME) will likely exhibit thermal gradients coupled with significant trace element (TE) variability (e.g., Hildreth 1979; Wolff et al. 2015).

Igneous petrologists seek to determine the nature of the processes contributing to the development of thermochemical variability and stratification in pre-eruptive silicic magma chambers. Early studies explained the occurrence of subtle gradients revealed by geothermometry of modal mineral assemblages using a closed system fractional crystallization model for magma differentiation (Fisher 1966). Later work illustrated the importance of accessory phases and their control of the TE budget in a crystallizing magma body (Allègre and Minster 1978; Smith 1979; Hildreth 1981). Accessory phases record the history of magmas as expressed by trace elements; however, they do not necessarily influence the evolutionary course of the magma imprinted by the modal

mineral assemblage. Because of this behavior, accessory phases are particularly valuable to the study of compositional zoning characterized by subtle, gradational variability. Igneous zircon is an especially robust accessory phase and geochronometer, allowing for inspection of timescales and temporal relationships of magmatic processes and how they influence the nature of magma differentiation.

We explored the zircon petrochronology of the Oligocene age Picture Gorge Ignimbrite (PGI) in central Oregon, a large volume rhyolitic to rhyodacitic ashflow tuff that possesses a thermochemical gradient with minor variability in ME composition. We show that the zircon record preserves no simple stratigraphically controlled changes in composition, but rather that individual crystals display two crystal growth stages that grew in magmas with two distinct TE compositions. Using these results, we present a refined model that requires influx and mixing of hotter, more primitive magma into the PGI magma body.

Background and Regional Stratigraphy

Widespread fallout tuffs and pyroclastic rocks of the John Day Formation (JDF) are a chronicle of voluminous and explosive Eocene to Miocene silicic magmatism in eastern and central Oregon. The JDF comprises four members: Big Basin, Turtle Cove, Kimberly, and Haystack Valley (Figure 1). K-Ar ages range from 39.7 Ma at the basal contact with the underlying Clarno Formation, to 22.6 Ma near the upper contact with the Picture Gorge Basalt that overlies the JDF (Fiebelkorn et al. 1982). The Turtle Cove Member is known for the abundant and diverse fossil assemblage preserved in its striking aquamarine colored beds of tuffaceous sediments, which are capped by a cliff forming ashflow tuff, the PGI.

The PGI covers an estimated 3000 km^2 of eastern and central Oregon and forms a conspicuous marker bed in the stratigraphy of the JDF. It reaches a maximum thickness of approximately 50 m near the town of Mitchell, Oregon, and thins to the north and east. Based on isopach data, Fisher (1966) proposed a source southwest of Mitchell (Figure 2). Later work suggested that the John Day Formation tuffs were derived from volcanism associated with the ancestral Cascade Range. Recently, more thorough geologic mapping has discovered three proximal Paleogene caldera structures—Wildcat Mountain, Tower Mountain, and Crooked River—to which John Day volcanism has been attributed (Figure 2). Geochemical data links the PGI specifically with the intracaldera Tuff of Barnes located in the Crooked River Caldera complex (McClaughry et al. 2009).

Compositional Zoning in the Picture Gorge Ignimbrite

Fisher (1966) was the first to examine the PGI, detailing two cooling units that comprise an eruptive sequence, resting upon a discontinuous basal fallout unit. The fallout unit reaches a maximum thickness of 3 m and shows neat planar bedding that grades upward. Minor lithics (<5%) are present in a white to buff colored fine to coarse-grained ash matrix.

The two cooling units of the PGI comprise six zones defined by degree of welding. Zone 1 is an unwelded ash flow similar to the fallout unit in thickness and color but lacks the bedded structure and is somewhat coarser grained with minor amounts of unflattened pumice fragments. Color and degree of welding in zone 1 transition upward to zone 2, a darker and more densely welded tuff. Zone 2 reaches thicknesses up to 15 m, up to 2 m of which is black perlitic vitrophyre. Dense welding diminishes upward to the lighter colored vapor phase zone 3, which contains lithics and whole flattened pumices,

up to ~5 cm, in a fine vitreous buff to green colored tuff matrix. The uppermost zone of the lower cooling unit, zone 4, is the thickest, least welded, and most altered zone of the PGI; it is also more lithic rich than any other zone. The contact between the lower and upper cooling units (zone 4 to 5 contact) is marked by a sharp transition from the unwelded tuff of zone 4 to the partially welded tuff of zone 5. Zone 5 transitions to the uppermost zone 6, which is poorly welded and not laterally continuous.

Although rocks of the JDF are pervasively altered, Fisher (1966) identified a petrologic gradient in the modal mineral assemblage of the PGI. This gradient exhibits a progressive decrease in magma evolution and increase in magma temperature with increase in stratigraphic height. More specifically, this gradient includes an up-section increase in the modes of anorthite, Mg-rich augite, Fe-Ti oxides, and oxyhornblende, indicating that minerals in stratigraphically higher positions crystallized at hotter temperatures than minerals found in lower positions (Fisher 1966).

The stratochemical profile in the PGI promoted the model of a chemically stratified pre-eruptive magma chamber (Figure 3). In this model, the pre-eruptive magma stratigraphy is progressively tapped from the roof downward so that the up-section eruptive sequence represents the pre-eruptive down-section stratigraphy. This model requires a vertically elongated magma body, which would inhibit convective mixing and preserve the thermochemical profile that developed through fractional crystallization of the source magma (Fisher 1966).

Progressive fractionation and formation of a thermochemical gradient in a narrow, vertical magma body might also promote systematic and stratigraphically controlled changes in zircon trace element chemistry and crystallization temperature. The small size

and equal distribution of zircon crystals from the PGI, coupled with the high viscosity of silicic magmas, suggest that zircon settling is unlikely. Therefore, zircon extracted from an upper portion of PGI stratigraphy would provide information about magmatic conditions in a lower portion of the magma, and vice versa for zircon extracted from lower in PGI stratigraphy (Figure 3).

Methods

Samples from zones 1, 2, 4, and 5 were collected from exposure at the Foree Trail area near Kimberly, OR (Figure 2). Zircon and feldspar crystals were extracted from all four samples using conventional density and magnetic methods and then handpicked in a microscope. Selected crystals were placed in a muffle furnace at 900°C for 60 hours in a quartz beaker to anneal minor radiation damage. Annealing intensifies cathodoluminescence (CL) emission, promotes more reproducible interelement fractionation during laser ablation inductively coupled plasma mass spectrometry (LA-ICPMS), and prepares the crystals for chemical abrasion (Mattinson 2005).

Annealed zircons were again handpicked. Individual grains were mounted in epoxy, ground down to expose a cross section of the crystal interior, then polished, carbon coated and imaged by CL using a JEOL JSM-T300 scanning electron microscope equipped with a Gatan MiniCL detector. Compiled CL images were examined to identify consistent and dominant CL patterns among grain populations and used to guide selection of LA-ICPMS spot analyses.

CL images of individual grains were measured using the digital image program ImageJ to determine the proportion of CL dark cores versus CL bright rims. The total cross sectional area for polished surfaces of individual crystals were calculated following

Bindeman (2003). The same method was then used to determine area of dark cores. The difference between total surface area and core surface area was calculated as the area of the rim.

LA-ICPMS analysis utilized an X-Series II quadrupole ICPMS and New Wave Research UP-213 Nd:YAG UV (213 nm) laser ablation system in the Isotope Geology Lab (IGL) at Boise State University (BSU). Using a 25 μm wide spot to ablate a total of 274 spots on 195 grains, trace element concentrations and preliminary $^{238}U/^{206}Pb$ dates were determined. Crystallization temperatures were calculated using the Ferry and Watson (2007) Ti-in-zircon thermometer.

Candidates for high-precision chemical abrasion-isotope dilution-thermal ionization mass spectrometry (CA-ID-TIMS) U-Pb analysis were chosen based on CL zoning patterns, LA-ICPMS $^{238}U/^{206}Pb$ dates, and quality of LA-ICPMS data, suggesting that the individual zircon grains were representative of a typical crystal from an identified population. Zircon grains were removed from epoxy mounts, triple rinsed in HNO_3, loaded individually into fifteen 300 μL Savillex microcapsules, and 4 drops of 29 M hydrofluoric acid (HF) were added to each. Microcapsules were then placed into a large Teflon Parr liner with 7 ml of 29 M HF. The Parr vessel was then inserted into a steel jacket and placed in a 180 °C oven for 12 hours to chemically abrade the zircon crystals (Mattinson 2005). This chemical abrasion step reduces the effects of Pb loss by removing the high-U, typically outer zircon domains, that have experienced open system radiation damage.

After chemical abrasion, the contents of the microcapsules were transferred into 3 mL Savillex beakers, from which the HF was removed and abraded grains were rinsed in

ultrapure H_2O before being immersed in HNO_3 for one hour of ultrasonic cleaning. Beakers were removed from ultrasonic bath and fluxed on a hot plate for an additional hour. In the meantime, microcapsules were rinsed and fluxed in 6M HCl to ensure removal of all residual products of chemical abrasion. Next, the HNO_3 was removed, and washed zircons were then returned to their respective microcapsules and spiked with EARTHTIME isotope dilution tracer solution (ET535; Condon et al. 2007). Four drops of HF were added to the microcapsules containing spiked zircons. Microcapsules were again loaded with 7 ml 29 M HF into the larger Parr liner and steel jacket and the entire assembly went into a 220 °C oven for 48 hours. The dissolved zircon + spike solutions were then dried down to salts in microcapsules and re-dissolved overnight in 6M HCL in a 180°C oven. The HCl-based ion exchange chromatographic procedure detailed by Krogh (1973) was used to separate U and Pb from the zircon matrix. Uranium and Pb were eluted into the same Teflon beaker and dried down with 2 μL of 0.05M H_3PO_4.

The extracted U and Pb were then loaded onto individual Re filaments using 2 μL of a slurry composed of H_3PO_4 and silca gel. Isotopic measurements were performed on an IsotopX Isoprobe-T mass spectrometer in the IGL. $^{238}U/^{206}Pb$ TIMS dates and uncertainties for each analysis were calculated using the algorithms of Schmitz and Schoene (2007) and the U decay constants of Jaffey et al. (1971). Uncertainties are based upon non-systematic analytical errors, including counting statistics, instrumental fractionation, tracer subtraction, and blank subtraction.

Approximately 100-200 mg of feldspar separates from each sample were sequentially dissolved for initial common Pb analysis following Housh and Bowring (1991). Feldspar grains loaded into 15 mL Teflon beakers with 2 mL 3.5M HNO_3 and

fluxed on a hot plate for 30 minutes. The acid was then removed and discarded before the grains were triple rinsed in ultra pure water. The rinsed feldspars were then fluxed for 30 minutes in 6M HCl. The acid was again removed, discarded, and the grains were again triple rinsed. These two leaching steps were repeated once. Next, 1 mL of HF was added to the feldspar grains, which were then fluxed on the hot plate for another 30 minutes. An aliquot of the dissolved feldspar solution was separated from the remaining solid fraction (L4 in Table 1) of the samples and placed into a clean 5 mL Teflon beaker. The solid residue was again triple rinsed. This HF leaching step was repeated three more times (L5-L7). An aliquot of the resulting HF-feldspar solution was reserved each time, then all were dried down in the 5 mL beakers on a hot plate. Dried samples were then redissolved in 1 mL 0.5M HBr. Anion exchange in a dilute HBr medium was used to separate Pb, which was then eluted into a clean 5 mL Teflon beaker. A microdrop of H_3PO_4 was added to the Pb separate and then dried. One drop of 16M HNO_3 along with one drop of H_2O_2 was placed on the spot of redried sample in the beaker. The resulting slurry was dried for the final time before being prepped for mass spectrometry as detailed above in the U-Pb zircon methods. Pb isotope composition of feldspars was the used as an estimate of initial common Pb in zircon age determination (Schmitz and Schoene 2007).

Approximately 20 g of powdered whole rock samples from zones 2, 3, 4, and 5 were sent to Washington State University GeoAnalytical Laboratory to determine major element oxide compositions and concentrations of 19 trace elements using X-ray fluorescence (XRF) analysis as described by Johnson et al. (1999) (Tables 2 and 3). Fractions of the same whole rock samples were dissolved using a method of low-dilution di-Lithium tetraborate fusion followed by mixed acid digestion. The resulting solutions

were then analyzed on an Agilent model 4500 ICPMS to determine REE + Ba, Th, Nb, Y, Hf, Ta, U, Pb, Rb, Cs, Sr, Sc, and Zr concentrations (Table 4).

Due to significant alteration of the other samples, glass analysis was performed only on preserved glass from zone 2 vitrophyre. Glass composition of vitrophyre was determined using LA-ICPMS in situ on a polished billet mounted in epoxy. A 40 μm beam was used at 10 Hz frequency and 5.5 J/cm^2 to ablate 20 spots. Raw count rates were reduced using PlasmaLab software and internally normalized to XRF determined SiO_2 concentration and LA-ICP-MS determined ^{29}Si count rates. Two point calibrations were created off line using USGS BIR-1 and BCR-2 standard reference materials. In situ glass shard data is shown in Table 4. Standard reference material data is shown in Table 5.

Results

CL Textures and Zoning

PGI zircons are nearly unimodal in morphology. Most grains are elongate with aspect ratios no greater than 1:4. All four samples also had a small number of skeletal grains (22 in total out of 454 that were picked and mounted). We identified two zircon populations based on CL response; the dominant set is characterized by sector-zoned CL dark crystal cores, truncated and overgrown by CL bright rims (Figures 4 and 6). Boundaries between core and rim domains are smooth and undulating, unlike the faceted boundaries between oscillatory zones typical of igneous zircon crystals. A less common group of whole bright grains was also present.

Chemically zoned microstratigraphy is present in zircon crystals from throughout PGI stratigraphy. However, variation in the volume of growth that occurred during rim crystallization is apparent in CL images of polished crystal cross sections. Crystal rim

surface areas comprise a greater proportion of the total cross-sectional surface areas in zircons from zone 5, the uppermost zone sampled for this study, than do crystal rims of zircons from stratigraphically lower vitrophyre of zone 2. On average, surface areas of zone 5 zircons are composed of 48% rim. Zone 2 zircons, with an average value of 38%, have consistently lower proportions of rim growth (Figure 4).

LA-ICPMS Zircon Trace Element Analysis

LA-ICPMS results for PGI zircons are shown in Tables 6, 7, 8, and 9. Results for trace element standard reference materials are shown in Table 10. Spots placed on dark core and bright rim crystal surfaces revealed significant compositional variability in the microstratigraphy of the zircon crystals. Chemical domains characterized by differences in HREE abundance correlate to differences in CL response.

PGI Upper Cooling Unit-Zone 4 and Zone 5

Zircon crystals cores from the sample AL051209 (zone 5) range in crystallization temperature from 676 to 811 °C, Eu anomaly ranges from 0.09 to 0.36, U concentration varies from 134 to 1203 ppm, and Y (a proxy for HREE) concentration spans 1422 to 11074 ppm. Rims from this sample range in crystallization temperature from 673 to 815 °C, Eu anomaly varies from 0.09 to 0.27, U content rages from 120 to 893 ppm, and Y concentration from 1269 to 3503 ppm.

Sample AL071202 (zone 4) cores range in crystallization temperature from 695 to 802 °C, with Eu anomalies ranging from 0.25 to 0.11, U concentration varies from 141 to 369 ppm, and Y from 1938 to 4865 ppm. Zone 4 zircon crystal rims have crystallization temperatures ranging from 731 to 916 °C, Eu anomalies from 0.14 to 0.28, U content ranges from 127 to 230 ppm, and Y concentrations from 1151 to 1921 ppm.

PGI Lower Cooling Unit – Zone 1 and 2

Crystal cores from sample ECL091117 (vitrophyre of zone 2) vary in crystallization temperature from 715 to 800 °C, Eu anomalies range from 0.11 to 0.29, U concentration varies from 96 to 469 ppm, and Y from 1114 to 2901 ppm. Crystal rims span crystallization temperatures from 723 to 763 °C, Eu anomalies vary from 0.12 to 0.4, U concentration ranges from 140 to 258 ppm, and Y from 1867 to 6714 ppm.

Zircon crystal cores from sample ECL091116 (zone 1) have crystallization temperatures ranging from 694 to 842 °C, Eu anomalies ranging 0.14 to 0.19, U concentrations that vary from 164 to 494 ppm, and Y from 1685 to 4251 ppm. Zircon crystal rims from zone 1 vary in crystallization temperature from 715 to 851 °C, with Eu anomalies ranging from 0.08 to 0.19, U content that ranges from 138 to 231 ppm, and Y concentrations from 1473 to 2322 ppm.

Regardless of stratigraphic position, crystal rim compositions show that cores and rims crystallized over similar temperature ranges. Europium anomaly for both chemical domains also has overlapping ranges (Figure 5 a, b, and c). Eu/Eu* and Ti-in-zircon crystallization temperatures are positively correlated for crystal cores and rims, with lower Eu anomaly values corresponding to higher crystallization temperatures (Figure 5a). Eu/Eu* REE ratio, Th/Y, are negatively correlated, with increasingly negative Eu anomaly corresponding to an increase in Th/Y, indicating enrichment in Th, depletion in Y, or both as feldspar is fractionated (Figure 5b). Despite the similarities in Ti-in-zircon temperature and Eu/Eu* among cores and rims, a distinct HREE pattern did emerge in which bright rims are depleted in HREE when compared to cores, illustrated by Y concentrations superimposed on CL images of PGI zircon grains in Figure 6. Eu/Eu*

versus Y, demonstrates differing HREE compositions for the two chemical domains, with rims having depleted concentrations relative to cores (Figure 5c). This differing Y content between crystal cores and rims is further illustrated using two REE ratios (Figure 5d).

CA-IDTIMS Zircon U-Pb Geochronology

Thirty single zircon crystals from throughout PGI stratigraphy were selected for CA-IDTIMS analysis to determine $^{206}Pb/^{238}U$ dates (Table 11). Of those analyses, 4 from the lower cooling unit (1 from sample ECL091116, and 3 from sample ECL091117) were immediately discarded due to either lack of sufficient radiogenic Pb, contamination by common Pb, or a combination of the two. Ten of the remaining analyses were from the lower cooling unit and 16 were from the upper cooling unit. Outliers from both data sets were identified and rejected using a 95% confidence interval with paired Thompson's Tau and Chauvenet's rejection criteria.

Upper cooling unit zircon crystals range in $^{206}Pb/^{238}U$ dates from 29.022 ± 0.042 to 29.097 ± 0.026 Ma, yielding a weighted mean date of 29.070 ± 0.011 (MSWD= 2.06; n=10). Six other analyses have to older dates ranging from 37.652 ± 0.039 to 29.159 ± 0.041 Ma. Zircon crystals from the lower cooling unit yielded a weighted mean date of 29.067 ± 0.011 Ma (n=9; MSWD 1.63), spanning from 29.038 ± 0.060 to 29.085 ± 0.026 Ma. Other dates were older at 29.419 ± 0.073 Ma, and younger at 28. 945 ± 0.067 Ma (Table 11). The two data sets from the upper and lower cooling units are statistically irresolvable and, when combined, yield a mean date of 29.069 ± 0.008 Ma (n=19; MSWD=1.76) (Figure 7).

Discussion

Zircon ‘Microstratigraphy’ and Magmatic Processes

In the model of a vertically elongated magma body that is compositionally stratified due to a steep thermal gradient (Fisher 1966), zircon crystals extracted from the stratigraphically lower cooling unit of the ignimbrite might reflect cool, shallow, and evolved magmatic conditions of the top of the magma chamber. Likewise, zircon grains from stratigraphically higher positions might have a composition reflecting the hotter and generally more mafic magma at greater depth, including hotter crystallization temperatures, smaller Eu/Eu* values, and lower concentrations of incompatible HREE+Y than zircon crystals from the lower cooling unit. However, we found very little stratigraphic variability in zircon composition or crystallization temperature; the abundance, morphology, and geochemistry of zircon crystals is consistent among all zones of PGI stratigraphy. This lack of variability suggests that zircon crystals began to crystallize early from the PGI magma, continued to grow through the evolutionary progression of the PGI magma, and were uniformly distributed within a convectively homogenizing magma chamber prior to eruption.

PGI zircon is compositionally zoned on an intracrystal scale rather than on a stratigraphic scale. CL dark cores represent an early zircon growth stage and are relatively enriched in HREE, preserving an evolved magma composition. CL bright rim overgrowths are depleted in HREE relative to cores and preserve a later stage of growth from a more TE depleted magma composition. Anhedral to subhedral reaction boundaries juxtapose dark core and bright rim growth domains. The embayed texture of the sharp dark core to bright rim transition, coupled with a compositional transition, indicates

zircon crystal dissolution at some point in the lifetime of the magma, followed by a second stage of saturation and crystallization.

The Eu anomaly (Eu/Eu*) in zircon is a useful index of the degree of crystallization in the host magma. Eu/Eu* values decrease during magma crystallization as Eu is consumed by plagioclase and depleted in the residual liquid. Eu/Eu* values for crystal cores and rims have similar ranges, suggesting that both stages of crystallization initiated in melts with similar Eu concentrations, relative to HREE concentrations, and then continued to crystallize as magma became more Eu depleted. Likewise, cores and rims have overlapping Ti-in-zircon crystallization temperatures, implying down temperature crystallization progression for both chemical domains. The relationship between these two indices of evolution is illustrated in Figure 5a, in which decreasing Ti-in-zircon temperatures are coupled with decreasing Eu/Eu* values (greater negative Eu anomalies) for both rim and core analyses.

Figure 5b shows Eu/Eu* declining rapidly relative to HREE until values of about 0.15, where the rate of decline decreases. These Eu/Eu* values correspond to Ti-in-zircon crystallization temperatures ranging from about 675 to 800 °C, which fall within an acceptable range for eutectic crystallization of a relatively dry, rhyolitic magma (Gualda et al. 2012; Bindeman and Simakin 2014). The rapid consumption of Eu slows relative to other HREE as the system cools; this change in the rate of Eu/Eu* may be related to the entry of quartz onto the solidus, which effectively decreases the bulk distribution coefficient of Eu for the system.

Two progressions of magma evolution are thus recorded by distinct zircon crystal core and rim growth phases. The difference in HREE chemistry between cores and rims

reveals a compositional distinction between the two separate batches of magma. Figure 6 illustrates this difference with Y concentration of relatively enriched dark cores and relatively depleted bright rims. The difference in composition of the core versus rim magma source is accentuated by examining trace element ratios for those growth domains. Figure 5c displays the overlapping evolutionary path of both magmas, as demonstrated in Eu/Eu* values, but also the fundamental disparity in the composition of the two magmas, as shown in Y concentration. This compositional disparity is further illustrated in Figure 5d, using Y in two REE ratios.

Zircon Equilibrium in the Erupted PGI Magma

Our understanding of rhyolite system dynamics in part relies on our interpretation of the systematics of trace element (TE) incorporation in zircon. We sought to examine the degree of equilibrium partitioning of TE between PGI melt and zircon. To do so, we used four previously published sets of partition coefficients (*D* values) and glass compositions from the PGI zone 2 vitrophyre to model TE compositions of zircons in equilibrium with the melt composition at the time of eruption (Figure 9). The four sets of *D* values used for this study were determined either via analysis of zircon/matrix pairs, from natural felsic systems (Colombini et al. 2011; Nardi et al. 2013) or from experimental zircon crystals grown in felsic melts under controlled laboratory conditions (Rubatto and Hermann 2007; Luo and Ayers 2009). $D^{zircon/whole\ rock}$ values from Nardi et al. (2013) illustrate partitioning between zircon and granitoid whole rock matrix. The three other studies report partitioning between zircon and rhyolitic glass, $D^{zircon/melt}$, by measuring TE contents of zircon crystals and the glass matrix from which they were separated.

Glass and whole rock compositions measured via LA- and solution-ICPMS show only minor differences (Table 4). Partitioning between zircon and whole rock, and zircon and glass, were both tested. Modeled compositions lie within or near the range of the most TE enriched compositions of PGI zircon crystal cores. Zircon crystallizing in equilibrium with the PGI melt immediately prior to eruption would have been enriched in Y, Th, U, and likely all HREE. In contrast to the modeled equilibrium zircon composition, PGI zircon crystal rims have relatively depleted compositions.

Due to prevalent devitrification throughout PGI stratigraphy, we only captured the glass composition of zone 2, a densely welded zone in the lower cooling unit. This lower stratigraphic zone of the ignimbrite may have occupied a cool and shallow horizon in the pre-eruptive magma chamber (Smith 1979). Perhaps the upper cooling unit, derived from a hotter horizon at greater depth and presumably closer to the source of the invading magma, contains the glass that was in equilibrium with PGI zircon crystal rims. Unfortunately, primary glass compositions in the upper cooling are pervasively altered to zeolite and clays (Fisher 1963).

Factors other than composition influence the degree to which zircon is able to incorporate TE impurities. PGI zircon compositions most closely match modeled values determined using the temperature dependent experimental partition coefficients of Rubatto and Hermann (2007) at 900 and 950 °C, temperatures at or exceeding the highest PGI Ti-in-zircon crystallization temperatures. This discrepancy may be attributed to the experimental composition, which was formulated to examine zircon/melt and zircon/garnet partitioning in metamorphic systems.

Luo and Ayers (2009) also assessed the temperature dependence as well as effects of pressure and oxygen fugacity of TE partitioning in zircon. The degree to which modeled zircon compositions match actual zircon compositions using the *D values* of Luo and Ayers (2009) is variable among Y, Th and U. For Y and Th, there is greatest agreement with *D values* determined at 900°C and 1200°C and at 1.5 GPa with an Ni-NiO buffer. *D values* for U most closely match at lower temperature and pressure, 800°C at 0.1 and 0.2 GPa, also with an Ni-NiO buffer. Again, disparities arise between the modeled compositions and what we observe in the natural system. In this case, the experimental composition used by Luo and Ayers (2009) was designed to reproduce zircon/melt TE partitioning in homogenous peralkaline melts where zircon solubility and growth rates are high (Watson 1979).

Peraluminous systems, like the PGI magma, have zircon solubility orders of magnitude lower than in peralkaline systems (Linnen and Keppler 2002). It is worth noting that due to the artificially rapid zircon crystal growth rates, and resulting disequilibrium TE partitioning, Luo and Ayers (2009) recommend using natural zircon/matrix pairs when applying *D values* to petrogenetic models. More experimental partition coefficient research is required to further establish comprehensive and quantitative understanding of TE partitioning in zircon that can be applied to a specific problem within a set of dynamic geologic systems.

A Refined PGI Magma Chamber Model

Relationships among Eu/Eu*, crystallization temperatures, and HREE proxies for magma evolution are found in both zircon core and rim growth domains, which represent early and late periods of zircon crystallization, respectively. The model of a single

differentiation progression in a monogenetic batch of magma cannot explain the internal microstructures, the apparent cooling and differentiation indices, and unique HREE concentrations for the two stages of crystallization recorded in the PGI zircons. Evidence for thermal input following the initial crystallization stage coupled with later stage crystallization from a less evolved magma composition requires open system evolution of the PGI magma system.

As the first generation of PGI magma cooled, crystallinity increased as is recorded in the Ti-in-zircon temperatures and progressive ingrowth of Eu-anomaly in the PGI zircon cores. This stage was interrupted by a reheating event coupled with a change in magma chemistry, caused by the addition of hotter, zircon undersaturated magma to the system. The resulting magmatic conditions caused existing zircon grains to partially dissolve. Next, the hybrid magma rehomogenized, and again began to cool and crystallize. The rim stage of crystallization records this second period of evolution from the mixed magma batch.

Zircon grains sampled from higher positions in the ignimbrite stratigraphy are presumed to be from deeper within the magma chamber while those recovered from lower positions should have resided in the shallow portion of the chamber immediately prior to eruption. Shallow crustal magmatic systems are rejuvenated with hotter, less evolved magma generated in deeper crustal environments. Addition of hot magma to the pre-eruptive PGI system is likely to have occurred at the base of the chamber and would have begun to change the thermodynamic conditions of the deep chamber sooner than the shallow chamber. This suggests that zircon grains that occupied positions closer to the base of the magma chamber would experience a greater degree of reaction due to greater

temperatures and more time spent in contact with the new magma. Although zircon grain size is consistent and crystals are evenly distributed throughout PGI stratigraphy, crystal rim domains of zircons from the stratigraphically higher upper zone of the PGI are thicker than rim domains of zircon found in the vitrophyre.

Previously, the modal mineral record of the PGI was interpreted to be the result of prolonged differentiation of a homogeneous batch of magma (Fisher 1966). The zircon record of the PGI investigated in this study provides evidence of crystallization from two separated magma batches. Magma mixing as an alternative to the long lived closed system evolution of the previous model might explain the stratigraphic changes in the PGI modal mineral assemblage. This could be tested further with imaging techniques that elucidate crystallization textures and in situ analysis to examine intracrystal chemical variability (Stelten et al. 2013).

Implications

This study of the thermochemical gradient in the PGI resolves uncertainties concerning the development of compositional variability in shallow voluminous silicic magmas. The case study provided by the gradational style of variability in the PGI is one in which time between rejuvenation of the magma system and eruption was sufficient to allow for at least hybridization, if not homogenization of the two magmas. Because of the lack of preserved volcanic glass, the degree of homogenization in the melt is not resolvable. However, the PGI zircon chronicles a maximum of ca. 35 Kya of magma chamber dynamics responsible for the compositional variability found in the silicate and oxide mineral phases (Fisher 1966), and indicates significant post-recharge crystallization. The trace element record of PGI zircon reveals that the invading magma

that imparted this variability was hotter and less evolved than the existing PGI magma, but that the hybrid magma was progressing toward a more evolved composition prior to eruption. This study suggests that, while mixing and fractional crystallization are both fundamental controls on the compositional evolution of magmas, open system mixing is the primary process contributing to compositional zoning in the PGI magma.

CHAPTER THREE: RATTLESNAKE TUFF

Compositional Zoning

Large volume silicic ash-flow tuffs frequently exhibit one of numerous styles of compositional variability (Williams et al. 1942; Fisher 1966; Smith 1979; Hildreth 1981; Streck and Grunder 1997; Shane et al. 2008; Bachmann et al. 2014; Wolff et al. 2015). Some styles follow a general eruptive progression from rhyolite or rhyodacite compositions that grade into less evolved, more crystal-rich intermediate compositions later in the eruption (Bacon and Druitt 1988). Crystal-poor HSR often display moderate variation in ME composition over a narrow (<3 wt %) range in SiO_2, but vary strongly in TE composition (Hildreth 1979). Zoning in compositionally variable deposits can occur gradationally or abruptly, and may be accompanied by gaps in composition.

The nature of compositional variation is determined by the timing and relationships among pre-eruptive processes like cooling, fractional crystallization, assimilation, magma recharge, and magma mixing. Pre-eruptive processes, in turn, are influenced by local and regional tectonic setting. The work presented here examines compositional variability in the RST, a voluminous and compositionally zoned HSR ash-flow tuff located in the High Lava Plains (HLP) of east and central Oregon.

There are two dominant models for the generation of large, compositionally zoned rhyolitic magma bodies in the shallow crust. One model invokes protracted storage and extensive crystal fractionation of a mafic or intermediate parent magma, ultimately forming a crystal mush from which a differentiated melt is extracted (Hildreth 2004;

Bachmann and Bergantz 2004). The mush model predicts coeval plutonic roots abandoned upon eruption of the melt. The second model invokes an ephemeral system generated by anatexis of existing crust with frequent magma influx, mixing and amalgamation. We examined both accessory mineral and glass compositions in the RST and determined that the compositional gaps and gradients in the RST magma developed due to partial melting of existing crust, recurring recharge of segregated magma bodies, breaching and mixing of those bodies, and incomplete pre-eruptive homogenization. The temporal context provided by zircon petrochronology indicates that these magma dynamics occurred $<10^5$ years prior to eruption, ruling out a model of long-lived magma evolution.

Regional Setting

The HLP spans an area approximately 275 km long and 90 km wide and formed during multiple pulses of volcanism beginning in the Oligocene and continuing until nearly present day (Ford et al. 2013). The province is bounded to the north by the accretionary complexes of the Blue Mountains Province, to the south by the northwestern most Basin and Range Province, and to the west by the Cascade volcanic arc. To the east, the HLP is separated from the Owyhee Plateau by a sharp gradient in the $^{87}Sr/^{86}Sr$ isotopic ratio, the '0.704-0.706 line', a feature that distinguishes Precambrian North American crust from younger allochthonous terranes added to the continent during Phanerozoic subduction along the western margin of the continent (Leeman et al. 1992).

Structures in the southern HLP transition northward from large NNE striking Basin and Range normal faults, to small, NW striking normal faults of the Brothers Fault Zone (Lawrence 1976). The physical expression of the volcanic province is an arcuate

trough extending from the Owyhee Plateau to the Cascade Arc. Eagar et al. (2011) report an average crustal thickness for the HLP of about 31 km. The zone of thinnest crust (<25 km) is located in the center of the province, thickening abruptly toward the Owyhee Plateau in the east and the Cascade arc in the west. Thin crust extends north into the Blue Mountains and south in to the Basin and Range, perpendicular to the time progressive trend of rhyolite volcanism and crustal extension in the HLP (Eagar et al. 2011).

Bimodal volcanism of the HLP initiated roughly 12 Ma (Jordan et al. 2004; Ford et al. 2013) west of the Steens Mountain escarpment (Eagar et al. 2011), which exposes dykes associated with the 16.6 Ma Steens Flood Basalts (Swisher et al. 1990; Hooper et al. 2002). Volcanic rocks of the HLP include sparse intermediate compositions, and nearly equal amounts of mafic and felsic lavas (Draper 1991). Basalts are widespread flows of high aluminum olivine tholeiites (HAOT), unique to the HLP, and show no spatial-temporal trend (Hart et al. 1984). Rhyolites have a distinct northwestward age progression (Walker et al. 1974), loosely mirroring the northeastward younging trend of silicic volcanism associated with the Yellowstone Hotspot (Pierce and Morgan 1992).

There are several Oligocene and younger widespread rhyolite ashflows in the region, but rhyolitic volcanism in the HLP peaked in the Late Miocene (Jordan et al. 2004). The 7.266±0.010 Ma RST (this study) is perhaps the largest of these Late Miocene eruptions, comprising an estimated 280 km^3 of > 99% HSR and originally blanketing 30,000-40,000 km^2 of the region (Streck and Grunder 1995). Two other large volume ashflow tuffs, the 9.74±0.02 Ma Devine Canyon Tuff (Jordan et al. 2004) and the 8.648±0.006 Ma Prater Creek Tuff (this study; PCT), are thought to have erupted from

the Harney Basin, near the inferred source of the RST (Macleod et al. 1976; Streck and Grunder 1995) (Figure 10).

Overview of Zoning, Gaps and Groups

In addition to being voluminous, the RST is extraordinary for its physical characteristics, including strikingly banded pumices that illustrate dramatic compositional diversity, and extreme facies variations that suggest a complex eruptive setting. The RST has been extensively studied by Streck and Grunder (1995; 1997; 1999; 2008), who identified clustered chemical compositions in glass shards and whole pumices. These clustered compositions comprise five discrete chemical groups, which were named A, B, C, D, and E in order of most to least evolved; compositional groups are defined primarily by LREE, Rb, Ba, Eu, Ta, Zr, Hf, Th, Ti, and Fe concentrations (Streck and Grunder 1997). Whole pumices in these groups are crystal poor and are visually homogenous, varying from white to grey with increase in Fe content, and degree of magma evolution decreases. Pumices range little in weight % SiO_2, but with these slight variations, other elements vary significantly and consistently. Changes in both crystal content and mineralogy also occur from group to group, although not always systematically. For example, the quartz to feldspar ratio increases from E to A, but group A contains feldspar compositions that differ considerably from the other four groups.

Streck and Grunder (1997) proposed a progressive differentiation model in which the least evolved HSR is a parent magma that produces a more evolved magma via roof downward nonmodal fractionation in a lens shaped magma chamber. From the newly differentiated magma, another even more evolved liquid is produced and so on, with each increasingly evolved composition giving rise to another. This produces a compositionally

stratified magma body, layered with the denser parent HSR at the base and the least dense most highly evolved HSR at the top (Figure 11).

In addition to the variety of HSR compositions, the RST also includes enclaves of more mafic compositions ranging from basalt to dacite (Streck and Grunder 1999). These mafic inclusions differ from the typical mid ocean ridge basalt-like HAOT basalts of the HLP (Hart et al. 1984) in that they have more evolved ITE contents. Streck and Grunder elaborated on their earlier model of the RST magma system (1997) to include interaction between a basaltic magma pooled at the base of the chamber and the lowermost group E rhyolite (1999). The overlying rhyolite acts as a density trap that restricts the basalt to greater depths, while the hotter basaltic magma provides the rhyolitic magma with thermal influx. This feedback between compositionally disparate but adjoined magmas allows for prolonged differentiation of the whole system to produce ITE enrichment in the mafic compositions and fostering compositional stratification of the rhyolitic compositions.

Physical Volcanology and Sampling

The type section locality of the RST, as specified by Streck et al. (1999), overlies a ~5 m thick sequence of pyroclastic surge and fallout deposits interbedded with reworked tuffaceous sediments that are thought to be associated with the waning of the PCT system (Figure 12b; Figure 13). The base of the RST is ~1 m of neatly laminated lapilli fallout tuff comprising two sequences of <1 to 3 cm thick beds that are fining upward and internally grade upward. The basal fallout sequence is precursory to the main ignimbrite. The contact between fallout and the base of the ignimbrite is marked by a sharp transition in color, from buff to grey, and in depositional nature, from laminar,

well-sorted fallout to cross-stratified pyroclastic surge deposits. This pyroclastic horizon is ~1.5 m thick and contains approximately 10% light colored lapilli pumice in a fine-grained matrix of mixed light and dark glass shards. The onset of welding is gradual and degree of welding increases upward into 1 m densely welded black vitrophyre capped by ~20 m of the lithophysal zone that grades from perlitic black vitrophyre with lithophysae to devitrified tuff with lithophysae.

At localities more proximal to the source, the RST is more pumice rich. At these localities, thick sections are partially or unwelded mixed glass shard matrix with whole pumices that are up to >50 cm in size (Figure 12a). Pumices are either uniform in color, ranging from white to black, or banded with various mixtures of white, grey, and black (Figure 12c). The mixed shard matrix, like the banded pumices, are a color mixture of white, gray, and black.

Figure 10 shows sample collection sites and Figure 13 shows relative position of samples in RST stratigraphy. Sample WNFM061223 was collected for a different study and is from a distal fallout deposit near the east side of the Cascades, west of the study area shown here. Field work was completed over two days in August 2013 and two days in September 2014. RST-2-1 and RST-6-1 were collected from a road cut on US Highway 20 west of Burns, Oregon. The RST is partially welded at this location, with both vitric and devitrified facies occurring within one meter of each other. Pumices in both facies are faintly flattened. RST-1-1, RST-1-3, RST-2-2, and RST-2-3, in addition to seven other samples, were collected from the Silver Creek Ranch location north of Riley, Oregon, where the RST is pumice-rich and poorly welded (Figure 12a). RST-5-1 is densely welded black vitric tuff with large fiamme collected from exposure near the

confluence of Silver and Wickiup creeks. Samples PCT-7-1, PCT-7-2, RST-7-3, and RST-7-4 are all ash-rich and were collected from the type locality at a road cut on Oregon State Highway 395 north of Burns north of Burns (Figure 12a). PCT-7-1 and PCT-7-2 were collected from two separate fallout deposits interbedded with tuffaceous sediments that underlie the RST at this location. PCT-7-1 is from the base of the exposure about 6 m beneath the contact with the RST, and PCT-7-2 is from approximately 2 m beneath this contact. RST-7-3 is from the bedded fallout approximately 0.5 m below the contact with the overlying pyroclastic horizon. RST-7-4 is from the incipiently welded tuff in the transitional zone between unwelded tuff and densely welded vitrophyre.

Methods

Whole rock samples were analyzed by X-ray fluorescence (XRF) at Washington State University GeoAnalytical Laboratory. All other sample processing and analysis was completed in the IGL facilities at BSU. RST zircon and feldspar extraction, processing, and analysis followed the methods detailed above in PGI chapter, except for samples RST-2-1, RST-2-2, and RST-2-3, which were analyzed by LA-ICPMS using 12 x 40 μ traverses.

Following standard density separation, an aliquot of the light fraction of each sample, consisting dominantly of glass shards with minor amounts of low density mineral phases, was then mounted in 1” round epoxy molds. Glass shard mounts were then polished to expose clean surfaces of individual shards and then loaded into a ThermoElectron X-Series II quadrupole ICPMS equipped with New Wave Research UP-213 Nd:YAG UV (213 nm) laser ablation system. Using a 40 μm beam at 10 Hz frequency and 5 J/cm^2 fluence, 15 to 40 spots were placed on individual glass shards for

each tuff or whole pumice sample. Raw count rates were reduced using PlasmaLab software and internally normalized to XRF determined SiO_2 concentration and LA-ICPMS determined ^{29}Si count rates. Two point calibrations were created off line using United States Geological Survey (USGS) Basalt-Iceland, Reykjavik-1 (BIR-1), and Basalt-Columbia River-2 (BCR-2) standard reference materials. In situ glass shard data is shown in Table 7.1. Standard reference material data is shown in Table 7.2.

Feldspar grains were handpicked under a microscope from the remaining aliquots of light fractions. Five to eleven grains from each sample were mounted in epoxy rounds and then ground and polished to expose fresh surfaces. Using the same laser ablation system as above with an 80 μm beam, 10 Hz frequency and 5 J/cm^2 fluence, a total of 60 spots were placed on feldspar grains. Raw data was reduced offline and internally normalized to previously published RST feldspar SiO_2 concentrations (Streck and Grunder 1997) and LA-ICPMS determined ^{29}Si. The data was calibrated using USGS BCR-2 standard reference material. All LA-ICPMS experiments completed for this study used NIST 610 (National Institute of Standards and Technology) and NIST 612 for instrumental tuning and quality control.

Results

Whole Rock, Bulk Glass and In Situ Glass Shard Chemistry

Five pumice samples analyzed by XRF fall wholly within the HSR compositional range spanned by RST pumices identified by Streck and Grunder (1997) (Tables 12 and 13). Three of these five pumices were physically similar in character, white to light grey in color and crystal poor. One falls in the group B range and two fall in the group C range (Figure 14). Two were grey in color, and, fell in the group D pumice range. A sixth

pumice is macroscopically banded white and dark grey. The banded pumice and three tuff samples collected for this study were not analyzed by XRF.

The range of incompatible trace element (ITE) concentrations in RST compositional groups captured by LA-ICPMS *in situ* glass shard analysis is greater than previously determined from bulk glass separates using solution ICPMS and INAA methods (Streck and Grunder 1997; Olin and Wolff 2010) (Figure 15). Despite the crystal-poor character of the RST, glass separates are slightly offset from whole rock pumice compositions consistent with mineral exclusion. LA-ICPMS analyses of individual glass shards from the three tuff horizons and from four pumices are detailed below and listed in Table 14. Standard reference materials analyses are shown in Table 15.

Basal Fallout Tuff

Glass shards from the basal fallout tuff are peraluminous (molar Al > Na+K+Ca), but approaching peralkaline, and show the least variability of all RST glasses examined for this study (Figure 15). FeO values vary by less than 1 wt % and Ba values vary by only 5 ppm. The basal fallout glass composition generally corresponds well with the whole rock group A pumice composition (Streck and Grunder 1997), with depletion in Eu, Hf, and Zr, and low Eu/Eu* values (Figure 16). However, basal fallout glass is subtly enriched in U relative to the essentially aphyric group A pumice composition.

Unwelded Tuff

The unwelded tuff at the base of the main ignimbrite is compositionally similar to the basal fallout tuff, with little range in FeO and Ba (Figure 15), enrichment in U, depletion in Eu, Hf, and Zr, as well as low Eu/Eu* values (Figure 16). A subset of glass

from this sample is peralkaline and slightly more depleted in Ba relative to the rest of the unwelded tuff data. Basal fallout and unwelded tuff correlate and form linear trends in Hf vs. Y and Y vs. Th that are notably separate from the other RST glasses.

Welded Tuff

Welded tuff is peraluminous and displays the most scatter and greatest compositional diversity of all samples, spanning compositions from whole rock group A pumice to whole rock group D pumice (Streck and Grunder 1997). This sample is also significantly enriched in Ba and forms a trend that diverges from the rest of the field of RST glasses in Ba compositional space (Figure 15). Welded tuff glass analyses overlap with the enriched U compositional trend that is defined by the two underlying tuff samples, but also overlaps with the other dominant compositional trend characterized by depletion in U, and enrichment in Eu, Hf, and Zr (Figure 16).

Group B Pumice

Glass shards from the group B pumice comprise two compositional subsets. One generally corresponds the basal fallout and unwelded tuff samples, with low Ba (Figure 15) and high U (Figure 16) concentrations. This low Ba subset is peralkaline and even more depleted in Eu, Hf, Y, and Zr, with lower Eu/Eu* values. The second subset is peraluminous, with more scatter and more closely matches whole rock group B pumice composition (Streck and Grunder 1997). This peraluminous subset is enriched in Eu, Hf, and Zr, depleted in U, and has subtly elevated Eu/Eu* values when compared to the peralkaline group B glass subset.

Group C Pumices

Glass shard analyses from two separate group C pumices are peraluminous, but have differing compositional spreads shown in FeO, Ba, Eu, La, and Hf (Figure 15). One is skewed toward group B compositions (group C pumice #2), while the other (group C pumice #1) is more tightly bunched closer to whole rock group C pumice compositions (Streck and Grunder 1997). Group C pumice #1 forms well-defined linear trends defined by relatively wide ranging La and Hf concentrations coupled with little change in Ba. Group C pumice #2 broadly follows these linear trends, but with more scatter. The two group C pumices are enriched in Eu, Hf, and Zr, depleted in U and have high Eu/Eu* values.

Group D Pumices

Glass shards from two individual group D pumices are the most peraluminous of all RST glasses analyzed for this study. Both group D pumices display considerable range and are skewed toward group C pumices with lower wt% FeO (Streck and Grunder 1997). However, one of these pumices (group D pumice #1) includes a minor subset that matches basal tuff glass shard and group A pumice whole rock compositions (Figure 15). With respect to incompatible elements La, Hf, and Ba, the main set of group D glass shard data (pumices #1 and #2) generally agree with group D pumice whole rock data, although they are more enriched in Zr than the whole rock compositions for all RST HSR pumices. Group D glass overlaps with group C glass, peraluminous group B glass and welded tuff glass in Hf vs. Y and Y vs. Th to form linear trends that are subparallel to, though less well defined as the trend formed by peralkaline group B, unwelded tuff, and basal fallout glasses.

Banded Pumice

Glass shards from the banded pumice show significant scatter and variability in composition (Figure 15). Similar to the welded tuff, this banded pumice spans the entire range of RST glass compositions. The scatter in banded pumice glass compositions diverges from other RST glass compositions in La, Ba, Hf, U, and Eu/Eu*. This sample includes both peraluminous and peralkaline compositions, similar to the unwelded tuff and group B pumice, but less lightly grouped. The remarkable compositional diversity of the banded pumice will be discussed in more detail in a following section.

REE Compositions

High and low Ba analyses for the unwelded and welded tuffs, group B pumice, and group C pumice #2 are plotted individually to illustrate their mixed nature (Figure 17). Averaged values for basal fallout and group C pumice #1 are plotted because they have little range in Ba and comprise a low Ba and high Ba endmember composition, respectively. The high Ba analyses all share a common LREE enrichment, with shallower Eu anomalies compared to the low Ba analyses with depletion in LREE and deeper Eu anomalies. Relationships between Ba and HREE compositions are not as clear as those between Ba and LREE. For example, high and low Ba group B pumice analyses have the lowest HREE concentrations. HREE patterns are generally flat with some analyses showing modest Gd to Lu depletion, others showing modest enrichment and still others varying mildly throughout LREE.

Banded pumice REE concentrations vary by two orders of magnitude compared to other RST pumice and tuff compositions, including both depletion and enrichment in REE, although skewed toward more depleted concentrations (Figure 18). Analyses

depleted in REE have either positive or weakly negative Eu anomalies, or U shaped patterns, rather than the ‘seagull’ shaped patterns typical of high silica rhyolites. The most enriched shard also has the deepest Eu anomaly. Magnetic and nonmagnetic separates have overlapping ranges, however, the most enriched shard is from the magnetic fraction and the less enriched shards are from the nonmagnetic fraction. The nonmagnetic fraction also has consistently lower Ba concentrations.

Feldspar Chemistry

Bulk feldspar Pb isotope results are shown in Table 16 and in situ LA-ICPMS results are shown in Table 17. With the exception of one crystal from the welded tuff, polished grains did not exhibit any zoning, however, laser spots targeted crystal cores and rims to examine intracrystal compositional variation. In no crystals was core to rim compositional variation found. All of the pumice and tuff samples include at least a minor sanidine feldspar component (Figure 19). Feldspars from group B pumice, both group C pumices and the unwelded tuff are exclusively sanidine, with tightly grouped compositions. Feldspars from the welded tuff are both sanidine and anorthoclase. Feldspars from the basal fallout tuff are sanidine and plagioclase, including oligoclase and andesine. The widest compositional range was found in feldspars from the banded tuff, which are mainly plagioclase (oligoclase, andesine, labradorite, and bytownite) with more anorthitic compositions than basal fallout tuff plagioclase. The banded pumice also included one sanidine composition that overlaps with the dominant RST feldspar compositional group. Feldspar crystals from all other samples are euhedral, while banded pumice feldspar crystals are corroded with no developed crystal faces.

Zircon CL Textures and Zoning

Zircon crystals extracted from the PCT are easily distinguished from RST zircon crystals because of contrasting morphologies. Although we report PCT zircon crystallization ages in a later section, these will not be discussed further. Zircon grains extracted from all RST pumice and tuff samples are similar in physical character to each other, but unusual when compared to most other igneous zircon crystals. RST zircon crystals are complex aggregates of numerous crystals and crystallites that range in size from <10 μm to >100 μm (Figure 20, a-d; Figure 21, a-h). These aggregates resemble the botryoidal growth habit exhibited by other minerals, for example hematite, although crystallites that comprise RST botryoidal zircon grains are faceted rather than spherical (Figure 20b).

Individual crystallites have generally low aspect ratios and oscillatory zoning that is often overprinted by sector zoning and maybe truncated by adjoining crystallites (Figure 21a). Within the crystal composites, crystallites are randomly arranged and are not crystallographically coherent. Some of these composite crystals exhibit weakly dendritic growth and form short chains of small crystallites that extend from a larger central crystal (Figure 21b). Many are formed by one comparatively large crystal that is fringed by several smaller crystallites (Figure 21c). Others are composed of two or more moderate to large crystallites that are bridged by smaller crystallites (Figure 21c and h). The smallest population (<5% of all RST zircon crystals) are equant crystals, no more than 150 μm in size with sector and oscillatory zoning, but without complex growth textures and adjoining crystallites (Figure 21e, and also some of the grains selected for TIMS analysis shown in Figure 24).

Many of the individual crystallites comprising the botryoidal grains have resorbed cores that are surrounded by a thin, CL bright zone (Figure 21f). In some cases, a bright crystal rim that may or may not be continuous, encompasses all of the crystallites in a zircon aggregate. While this bright rim can be seen in zircon aggregates from all RST samples, it appears thicker on those extracted from whole pumices (Figure 21b and h), compared to those extracted from tuffs (Figure 21f and g).

LA-ICPMS Trace Element Analysis

Results for LA-ICPMS analysis of RST zircon crystals are listed in Table 18. Zircon crystals from the basal fallout comprise the broadest compositional range of RST zircon crystals sampled for this study. Welded and unwelded tuff zircon analyses are excluded from composition diagrams in Figure 24 due to their mixed nature in order better illustrate the relationships among basal fallout and the four pumices. Zircon compositions from the four pumice samples overlap the basal fallout zircon compositions with some grouping and offset. For example, banded pumice zircon is enriched in Hf and Y relative to group B pumice zircon, but also includes a small subset of depleted compositions. Basal fallout and banded pumice zircons have the lowest Eu/Eu* values, while all RST zircons have Eu/Eu* less than 0.3, which corresponds to values determined for the dominant set of RST glasses analyzed for this study (Figure 18), but are lower than values for groups D and E whole pumices and glasses.

Zircon crystal core to rim evolution shows an overall trend from a hotter magma with enriched ITE concentrations to a cooler magma with lower ITE concentrations. Zircon crystals mainly record overlapping Ti-in-zircon crystallization temperatures ranging from 675 °C to 775 °C for multiple crystallization stages. However, earlier stages

of crystallization represented by crystal cores and near-core interior zones are skewed toward higher ITE concentrations and hotter crystallization temperatures. Later stages of crystallization represented by crystal rims and near-rim interior zones are skewed toward cooler crystallization temperatures and lower ITE concentrations.

CA-IDTIMS Geochronology

Forty-six single zircon crystals from all of the RST pumice and tuff samples and two PCT tuff samples were analyzed by CA-ID-TIMS. Weighted mean average ages for individual samples are shown in Table 19. Of those, 16 analyses were immediately discarded due to either lack of radiogenic Pb, contamination by common Pb, or a combination of the two. These rejected analyses included all of the dates from the group B pumice. Outliers from the remaining 30 analyses were identified and rejected using a 95 % confidence interval with paired Thompson's Tau and Chauvenet's rejection criteria.

PCT tuff zircons range in their CA-IDTIMS $^{206}Pb/^{238}U$ dates from 8.587 ± 0.019 Ma to 8.610± 0.019 Ma, with a weighted mean date of 8.600 ± 0.010 (MSWD=1.51; n=3; prob. fit=0.2199). Other analyses that failed both rejection criteria were younger and older outliers that ranged from 8.487 ± 0.020 to 8.645 ± 0.019 Ma (Table 20).

RST basal fallout tuff zircon crystals yielded $^{206}Pb/^{238}U$ dates from 7.229 ± 0.010 Ma to 7.288 ± 0.021 Ma, with a weighted mean date of 7.266 ± 0.007 Ma (MSWD= 1.28; n=7; prob. fit=0.2610). Other analyses have younger dates ranging from 7.123 ± 0.088 Ma to 7.264 ± 0.012. Zircon crystals from the welded and unwelded tuff yielded a weighted mean date of 7.269 ± 0.008 Ma (MSWD= 3.15; n=3; prob. fit=0.0429), spanning from 7.283 ± 0.014 Ma to 7.341 ± 0.010 Ma, the oldest of which was rejected. Zircon crystals from the two group C pumices and the banded pumice yielded dates

ranging from 7.132 ± 0.013 Ma to 7.286 ± 0.011 Ma; rejecting the youngest of these dates yields a weighted mean date of 7.274 ± 0.006 Ma (MSWD=3.22; n=4; prob fit=0.0217). Dates from the basal fallout tuff, welded and unwelded tuffs, and three pumices are statistically unresolvable. When combined, the three data sets yield a robust median date of 7.266 ± 0.010 Ma (n=14; prob. fit=0.031) (Figures 23 and 24; no CL images of sample WNFM061223 were obtained).

Discussion

Compositional Variability

The pumice and tuff samples differ from each other in their physical natures and placement in the eruptive sequence, and thus represent two different samplings of the pre-eruptive magmatic system. Basal fallout tuff comprises the first liquid erupted from the RST magma system, displays the least compositional range and a high degree of evolution. This includes significant crystallization of feldspar, evidenced by a deeply negative Eu/Eu*, and crystallization of REE-rich accessory phases like zircon and chevkinite, evidenced by depleted REE concentrations (Figures 15-17). Basal fallout units of large volume ashflows are commonly interpreted to represent an eruptive event that precedes the main eruption and thus comprise a highly fractionated magma cap in the pre-eruptive chamber (Hildreth 1979; Smith 1979; Hildreth 1981).

The unwelded and welded tuffs and pumices were erupted later in the eruptive sequence than the basal fallout tuff, at greater degrees of magma withdrawal. The unwelded tuff represents a point at which the eruption began to sample mixed magma compositions. Mixing was heightened later in the sequence when the rate of eruption was at its maximum, at which point the welded tuff was deposited (Sparks and Wright 1979).

This may have also the point in the eruption when withdrawal from the chamber was at a maximum and thus sampling a greater volume in the pre-eruptive chamber with a wider range of magma compositions.

Correlated variations in Ba, high field strength elements (HFSE), and REE are found in group C pumice #1, the precursory fallout tuff and compositional subsets of the group B pumice (Figure 25). Linear patterns found within different compositional groups share similar slopes in some cases (Figure 25, e, f, and g). In other cases, linear trends in basal fallout and group B pumice subsets have markedly steeper slopes (Figure 26, a, b, and c). These patterns suggest closed system magma evolution via small degrees of crystal fractionation. More rapid consumption of Ba relative to LREE and HSFE in group C pumice #1 indicates relatively more sanidine crystallization in this group compared to group B and basal fallout because of Ba compatibility in sanidine. More rapid consumption of LREE and HFSE in basal fallout and group B indicates relatively more crystallization of accessory phases that preferentially incorporate these elements, like zircon and chevkinite (Macdonald and Belkin 2002; Hoskin and Schaltegger 2003). Zircon fractionation signature is illustrated by lower Zr concentration in basal fallout and group B pumice analyses compared to group C pumice. Eu/Eu* values for basal fallout have lower values and show little spread compared to compositional subsets of group B pumice, suggesting that the magma or magmas comprising this pumice experienced a lower degree of plagioclase fractionation. Finally, U concentrations in these three groups displays magma compositions that differ fundamentally, a high U magma comprising basal fallout tuff and a subset of the group B pumice and a lower U magma comprising the group C #1 pumice and a group B pumice subset.

Fractional Crystallization Models

Fractional crystallization models show that crystallization of a less evolved composition in group C pumice #1 can produce compositions approaching more fractionated group B pumice and basal fallout samples with respect to some elements. One model assumes the modal mineralogy previously reported for the RST (Streck and Grunder 1997), while the other assumes lower zircon in the mode and an equal amount of zircon and chevkinite. These models are somewhat effective at predicting a genetic relationship among the three samples, with respect to some elements like Ba vs La. In other elements, the plausibility of the fractional crystallization model breaks down, regardless of the mode. For example, using the low zircon model (0.1% zircon), 60% crystallization of the magma comprising group C pumice #1 is required before Ba concentrations reach basal fallout and group B pumice subset concentrations (Figure 25b). The same is true for U, Y, and Zr (Figures 25h and 25i), which require at least 50% crystallization. These high degrees of crystallization are beyond the accepted level of crystallinity that would allow for coeruption of all three compositions (Smith 1979; Bachmann and Bergantz 2004).

The models perhaps more effectively illustrate crystal fractionation trends within the compositional groups and subsets rather than between. This is illustrated by variable but correlated trends in some parameters that form linear arrays within compositional groups. The high zircon model (0.5% zircon) reproduces the range of group C pumice #1 compositions with less than 10 % crystallization, although it does not effectively model whole RST system evolution from least to most evolved (Figures 25e, 25f, 25h, and 25i).

Mixing Model

Mixing between a group D glass composition (Ba rich) and a group A glass composition (Ba poor) shows that 10-40% group D mixed with 10-60 % group A, can produce the range of glasses we found in RST pumice and tuff samples (Figure 26). Multimodal and widely variable compositional ranges seen in shards from group B pumice, group C pumice #2, unwelded basal ignimbrite tuff horizon and the welded ignimbrite tuff horizon cannot be explained by closed system magma evolution alone. Separate but linear clusters from group B pumice, group C pumice #2 and the unwelded basal ignimbrite imply magma mixing but not complete homogenization. The welded ignimbrite exhibits whole system variation, including compositions near the less evolved groups D and E. This sample has considerably more scatter than the others and diverges from the overall trend, toward richer Ba and moderate REE compositions, indicative of magma mixing. In this case, one of the constituent magmas contributing to the welded ignimbrite tuff horizon was perhaps not sampled in this study.

Cumulate Melts, High Ba Magmas and Banded Pumice

Banded pumices that juxtapose markedly contrasting magma compositions are regarded as normal in calc-alkaline arc magmatic systems and preserve syneruptive mingling and instantaneous quenching of contrasting mafic and felsic magma compositions (Smith 1979; Eichelberger et al. 2000). The HLP setting of the RST is a bimodal volcanic province not widely interpreted to be an arc magmatic system and the banded pumice examined in this study comprises two HSR compositions that contrast mainly in ITE and REE. This style of compositional juxtaposition cannot indicate mingling of felsic magma with mafic magma sourced from an underlying reservoir.

Given the narrow range in ME compositions paired with widely variable ITE and REE compositions, the invading magma is more likely derived from a remelted and mobilized feldspar rich and accessory phase bearing cumulate mush in the root zone of the RST magma chamber. Recharge of this cumulate melt occurred at the time of eruption without sufficient time for hybridization, thus preserving pumice scale compositional contrasts.

High Ba compositions in other RST pumice and tuff samples indicate that the cumulate residue fed the magma system prior to eruption. Considering the amount of Ba enrichment, the earlier cumulate melt recharge was perhaps more sanidine-rich. Furthermore, the degree of hybridization exhibited by mixed samples indicates that time lag in between the early recharge and eruption was sufficient for more complete mixing than seen in banded pumices, but insufficient for homogenization.

RST Feldspars

Feldspars from the banded tuff do suggest a late pre-eruptive or syn-eruptive recharge event involving a plagioclase bearing melt that must have been hotter than the RST magma it invaded. Corroded plagioclase grains are evidence of disequilibrium immediately prior to eruption, likely resulting from a reheating event. Mixed plagioclase and representative RST unwelded tuff glass compositions from the sample were modeled to examine the banded pumice compositional spectrum as a derivative of rejuvenation from a remelted cumulate (Figure 27). Modeled results broadly agree with banded pumice REE patterns, although modeled compositions have greater positive Eu anomalies and are generally more enriched than actual compositions. This enrichment could probably be accounted for by the presence of REE rich accessory phases like zircon and chevkinite in the cumulate mush. A 50 % plagioclase/HSR mix marks the transition

from a negative to positive Eu anomaly, suggesting the possibility that the few banded pumice analyses with positive Eu anomalies are glasses comprising a >50% plagioclase component.

RST Zircon Record

Botryoidal zircon in all of the RST pumices and tuff horizons sampled for this study are complex amalgamations of crystals that nucleated in close proximity and grew together as they crystallized. Granular growth textures in zircon grains associated with impact melt assume polycrystalline structures under increasing amounts of shock (Bohor 1993), although these are not primary magmatic textures as are those of RST zircons. Composite magmatic zircons are documented in association with A-type granite (Charoy and Raimbault 1994), and resorbed composite crystals, and 'caulifower zircon' have been recognized in association with metamorphosed mafic and felsic rocks (Pin and Lancelot 1982; Peucat et al. 1990; Corfu et al. 2003). In volcanic rocks of any composition or tectonic environment, the composite botryoidal morphology of RST zircon crystals is previously undocumented.

Unusual botryoidal morphology may be a function of crystallization velocity, resulting from rapid growth and conditions that favored zircon nucleation over crystallization. Rapid nucleation and growth can result from abrupt undercooling in a magma due to depressurization and degassing (Hort 1998). Degassing can occur following replenishment of the system by a more primitive volatile rich magma, which cools as it interacts with the cold evolved magma. This propagates mixing, increases gas pressure, and perhaps ultimately triggers an eruption (Eichelberger et al. 2000). Evidence for multiple episodes of mafic replenishment of the RST magma system is documented

by Streck and Grunder (1999) and illustrated by a small population of intermediate pumices that erupted with the HSR pumices, and crystal rich mafic inclusions mainly found in the intermediate pumices. The evolutionary progression of the RST magma recorded by complex RST zircon crystals is from a hot, ITE enriched magma to a generally cooler magma with lower ITE concentrations, suggesting that each recharge event was followed by a period of rapid cooling and crystallization.

The botryoidal texture of RST zircon grains is likely related to rapid thermochemical changes in the system due to magma influx. Sadly, it is the resulting intricate crystallization textures that give rise to the limitation of the available spatial resolution using standard in situ analysis methods. The complexities of the thermal and chemical history of the RST magma is thus unresolvable in zircon microstratigraphic record. However, the broadly intergrated zircon record illustrates genesis from a hot ITE enriched magma and progression through cooling and ITE depletion. A few bright crystal rims that were thick enough to analyze by LA-ICPMS (n=5) record low ITE concentrations and moderate Ti-in-zircon crystallization temperatures. These thick rims were only found in the RST pumice samples, and perhaps illustrate the final pre-eruptive zircon saturated RST magma composition. The paucity of these rims in tuff samples could be an artifact of sampling technique, or could suggest a fundamental disparity in the storage of and communication among the magma or magmas that comprise the RST compositional groups.

The basal fallout and unwelded tuff samples yielded more zircon than any other pumice or tuff samples. Their depleted Zr and REE glass compositions are consistent with more zircon fractionation, but not consistent with the ITE rich composition of RST

zircon crystal cores. The unwelded tuff along with subsets of both the group B pumice and the banded pumice are peralkaline in composition, which is known to have higher zircon solubility and growth rates (Watson 1979). It is probable that a mixing event between a peraluminous magma and the initial zircon crystallizing host magma, which was peralkaline, enriched in ITE, and fertile with respect to zircon, caused a pulse of zircon nucleation and rapid crystallization resulting in the botryoidal texture of the dominant RST zircon population.

Model for RST Magma System

Compositional trends found in glass provide an opportunity to infer the spatial gradient in the magma chemistry of a zoned magma chamber at the time of or immediately prior to eruption. In the case of the RST, incomplete hybridization of multiple magmas is evidenced by juxtaposed compositions in RST glasses. The fine scale of the in situ analytical methods employed in this study highlight the potential for intricate and transient pre-eruptive processes that may not be discovered otherwise. Prior studies employed analytical methods that homogenized the compositional variability that occurs on a glass shard scale in the RST. While major element compositions could suggest genetic relationships among the RST pumice groups, ITE compositions show that, in some cases, a genetic link formed by crystal fractionation is unlikely. Furthermore, mixing arrays within and among compositional groups indicate that magma mixing and mingling, continuing up to the time of eruption, is evidence that communication among perhaps disparate but neighboring magmas was crucial to the evolution and final state of the RST magma body.

Thus, the in situ glass data presented here requires a revised model of the RST magma system, illustrated in Figure 29. In the revised model, adjoining magma bodies with two end member compositions, peralkaline and peraluminous, mix with enough time prior to eruption to partially hybridize. The initial phase of eruption that deposited the basal fallout unit was dominantly composed of peralkaline magma. Syneruptive mingling between the endmember compositions was maximized after this initial eruption, with the greatest degree of mingling occurring at the height of depositional rate, resulting in the wide compositional range possessed by the densely welded ignimbrite. At some point during or immediately prior to eruption, a cumulate mush underlying the system partially melted and mingled with peralkaline magma as preserved in the banded pumice. Finally, as the eruption continued, various degrees of mingling between peralkaline and peraluminous magmas were preserved in the compositions of whole pumices.

Zircon crystals erupted with the magma offer an approach to reconcile spatial relationships among compositional groups with the temporal gradient of magma differentiation. Common zircon crystal morphology among RST compositional groups means that, despite discrete compositions and lack of a liquid line of descent among them, they were saturated with respect to zircon under similar conditions. This could mean either that zircon began to crystallize in an initial liquid, followed by further evolution of individual melt aliquots, or that zircon crystallized in compartmentalized melts that all promoted the unique botryoidal morphology. Due to the peralkalinity of the host magma, and the high zircon nucleation and growth rates in peralkaline melts (Watson 1979), we prefer the former scenario. Fundamental differences between generation of these types of magma prohibits a genetic link via fractional crystallization

for the peralkaline and peraluminous HSR end member compositions in the RST (Scaillet et al. 2016).

Whatever the mechanics of the eventual merging of the RST HSR magma batches, evidence provided by integrated whole rock, and in situ glass shard, feldspar, and zircon analysis supports the model of an ephemeral system with recurrent influx and disequilibrium. The RST demonstrates that compositionally variable products of an eruptive sequence are not required to be genetically related via a single evolutionary progression.

Conclusion

The evolutionary model for the compositional clusters and gradients in the RST invokes a step-wise progression of crystallization in discrete magma compositions driven by heat loss and cooling near the roof (Streck and Grunder 1997). The finer scale of the in situ glass analysis used in this study reveals broader variations that expand these compositional clusters and define trends between them. The variations between pumice compositions, and in some cases within a single pumice, are too large to be explained by fractional crystallization alone. Mixing arrays between groups suggest that disparate magmas communicated and partially hybridized prior to eruption. Steep Ba and REE enrichments in some glasses suggest that part of the RST magma network was fed by partial melts of remobilized feldspar-rich cumulate residues.

RST zircon crystals display complex disequilibrium crystallization textures and intracrystal thermochemical zoning profiles, offering further evidence for open system recharge and magma mixing. U-Pb zircon geochronology demonstrates zircon growth over $\leq 10^4$ year timescales, precluding protracted closed system differentiation as a

mechanism for development of a compositionally zoned pre-eruptive RST magma body. Rather, the compositional gaps and gradients, as well as complex zircon crystal morphology, are a byproduct of mixing and hybridization of peralkaline and peraluminous magmas.

CHAPTER FOUR: DISCUSSION

Comparison of the Two Systems

The application of zircon petrochronology aims to resolve the timescales and processes by which crustal magmas are generated, subsequently evolve and are eventually erupted. Using whole rock and glass chemistry to supplement the zircon record in compositionally zoned systems clarifies the comparative contributions of crystallization, mixing, and homogenization in the development of compositional variability. The nature of this variability is determined by the timing, and, ultimately, the degree of influence each process imparts on the system up to and continuing through the time of eruption. This study examines two systems that exhibit two contrasting styles of compositional variability.

The PGI and RST are both crystal poor and voluminous; however, they dramatically differ in the character of the zoning they display, from outcrop to crystal scale. The PGI is an example of gradational compositional variability, while the RST exhibits clustered compositions that characterize abrupt changes and span a wider range. Although variability in both systems is attributed to open system behavior, their rejuvenation rates and homogenization timescales differ. This we can conclude without calling upon other factors that can explain heterogeneities, like magma chamber geometry, physical mechanics of influx, and eruptive and depositional processes, although these likely also play a role (Hildreth 1981; Herbert et al. 1988; Huber et al. 2012).

Greater compositional diversity in the RST compared to the PGI is a direct result of more complexity in the pre-eruptive system and less opportunity for homogenization of constituent magmas prior to eruption. The comparative complexities of the two systems are further exemplified by contrasting zircon chemical compositions and crystal morphologies. PGI zircon crystals record a single episode of magma recharge bracketed by two periods of equilibrium crystallization. RST zircon crystals record multiple periods of crystallization that followed disequilibrium conditions resulting from magma influx and mixing. The unusual composite zircon crystals in all of the RST compositional groups sampled for this study suggest that convergence and mixing of compositionally unique magmas began early and recurred throughout the crystallization history of the system. Clustered and widely variable glass shard and feldspar compositions imply that mixing occurred up to the point of eruption.

Implications Regarding Existing Models

The traditional model for a reservoir feeding a compositionally variable deposit is a long-lived magma body that undergoes protracted, closed system fractional crystallization to develop a thermochemical profile, which is preserved as the magma body is inverted upon eruption (Fisher 1966; Hildreth 1979; Smith 1979). However, the contrasting examples of compositional variability provided by the PGI and RST demonstrate the need for a more current open-system model. Continuing improvements in microanalytical techniques have created the ability to chemically map intracrystal isotopic diversity, providing evidence for recycling of crustal material and multigenerational growth from multiple pulses of magma (Claiborne et al. 2010; Drew et al. 2013; Stelten et al. 2013; Bindeman and Simakin 2014; Rivera et al. 2014; Matthews

et al. 2015). Recent work proposes that amalgamation of adjacent magma bodies may create large volumes of eruptible magma in the shallow crust, which could retain compositional heterogeneity upon eruption (Bindeman and Simakin 2014; Ellis et al. 2014). Furthermore, convergence of neighboring magma batches and frequent or rapid influx would result in thermally and mechanically unstable, irregularly shaped chambers ultimately favoring eruption over homogenization. This eliminates the need to relate the products of large-scale rhyolite eruptions to long-lived closed magmatic systems hosted in discrete shallow chambers.

Finally, having established open system behavior in the PGI and RST magma bodies, it is important to note the composition of invading magmas. The RST varies in ITE compositions, in some cases by orders of magnitude, despite hosting a modestly variable SiO_2 range of <3 wt %. Equilibrium zircon compositions modeled using volcanic glass composition in the PGI suggest that the ITE composition of the PGI magma at the time of eruption was more enriched than the magma in which zircon crystal rims formed, indicating that the system continued to evolve through factional crystallization after rims crystallized. Regardless of the contrasting styles of compositional variability derived from fundamentally different influx rates, both systems offer evidence that recharge is not necessarily restricted to mafic or calc-alkaline magmas, and that mixing and mingling are integral processes producing compositional variability in rapidly generated, voluminous rhyolite magmas.

REFERENCES

Allègre CJ, Minster JF (1978) Quantitative models of trace element behavior in magmatic processes. Earth Planet Sci Lett 38:1–25. doi: 10.1016/0012-821X(78)90123-1

Annen C (2009) From plutons to magma chambers: Thermal constraints on the accumulation of eruptible silicic magma in the upper crust. Earth Planet Sci Lett 284:409–416. doi: 10.1016/j.epsl.2009.05.006

Bachmann O, Bergantz GW (2004) On the Origin of Crystal-poor Rhyolites: Extracted from Batholithic Crystal Mushes. J Petrol 45:1565–1582. doi: 10.1093/petrology/egh019

Bachmann O, Bergantz GWGW (2008) Rhyolites and their source mushes across tectonic settings. J Petrol 49:2277–2285. doi: 10.1093/petrology/egn068

Bachmann O, Bergantz GWW (2003) Rejuvenation of the Fish Canyon magma body: A window into the evolution of large-volume silicic magma systems. Geology 31:789–792. doi: 10.1130/G19764.1

Bachmann O, Deering CD, Lipman PW, Plummer C (2014) Building zoned ignimbrites by recycling silicic cumulates: insight from the 1,000 km3 Carpenter Ridge Tuff, CO. Contrib to Mineral Petrol 167:1025. doi: 10.1007/s00410-014-1025-3

Bacon CR, Druitt TH (1988) Compositional evolution of the zoned calcalkaline magma chamber of Mount Mazama, Crater Lake, Oregon. Contrib to Mineral Petrol 98:224–256. doi: 10.1007/BF00402114

Bindeman I (2003) Crystal sizes in evolving silicic magma chambers. Geology 31:367. doi: 10.1130/0091-7613(2003)031<0367:CSIESM>2.0.CO;2

Bindeman IN, Simakin AG (2014) Rhyolites — Hard to produce , but easy to recycle and sequester : Integrating microgeochemical observations and numerical models. Geosphere 10:1–27. doi: 10.1130/GES00969.1

Bohor B, Betterton W, TE K (1993) Impact-shocked zircons; discovery of shock-induced textures reflecting increasing degrees of shock metamorphism. Earth Planet Sci Lett 119:419–424. doi: 10.1016/0012-821X(93)90149-4

Bowen NL (1928) The Evolution of Igneous Rocks. Princeton University Press, Princeton, NJ

Charoy B, Raimbault L (1994) Zr- Th- and REE-rich biotite differentiates in the A-type granite pluton of Suzhou (eastern China); the key role of fluorine. J Petrol 35:919–962.

Cherniak DJ, Watson EB (2003) Diffusion in Zircon. Rev Mineral Geochemistry 53:113–143.

Claiborne LLL, Miller CFF, Flanagan DMM, et al (2010) Zircon reveals protracted magma storage and recycling beneath Mount St. Helens. Geology 38:1011–1014. doi: 10.1130/G31285.1

Colombini LL, Miller CF, Gualda GAR, et al (2011) Sphene and zircon in the Highland Range volcanic sequence (Miocene, southern Nevada, USA): Elemental partitioning, phase relations, and influence on evolution of silicic magma. Mineral Petrol 102:29–50. doi: 10.1007/s00710-011-0177-3

Condon D, Schoene B, Bowring S A, Parrish R, McLean, N, Noble S, & Crowley Q (2007) EARTHTIME; isotopic tracers and optimized solutions for high-precision U-Pb ID-TIMS geochronology. EOS, Transactions, American Geophysical Union, 88(52), Abstract V41E-06.

Corfu F, Hanchar JM, Hoskin PWO (2003) Atlas of Zircon Textures. Rev Mineral Geochemistry 53:469–500.

Crowley JL, Schoene B, Bowring S a. (2007) U-Pb dating of zircon in the Bishop Tuff at the millennial scale. Geology 35:1123. doi: 10.1130/G24017A.1

Draper D (1991) Late Cenozoic bimodal magmatism in the northern Basin and Range Province of southeastern Oregon. J Volcanol Geotherm Res 47:299–328.

Drew DL, Bindeman IN, Watts KE, et al (2013) Crustal-scale recycling in caldera complexes and rift zones along the Yellowstone hotspot track: O and Hf isotopic evidence in diverse zircons from voluminous rhyolites of the Picabo volcanic field, Idaho. Earth Planet Sci Lett 381:63–77. doi: 10.1016/j.epsl.2013.08.007

Dufek J, Bergantz GW (2005) Lower crustal magma genesis and preservation: A stochastic framework for the evaluation of basalt-crust interaction. J Petrol 46:2167–2195. doi: 10.1093/petrology/egi049

Eagar KC, Fouch MJ, James DE, Carlson RW (2011) Crustal structure beneath the High Lava Plains of eastern Oregon and surrounding regions from receiver function analysis. J Geophys Res 116:B02313. doi: 10.1029/2010JB007795

Eichelberger JC, Chertkoff DG, Dreher ST, Nye CJ (2000) Magmas in collision: Rethinking chemical zonation in silicic magmas. Geology 28:603–606. doi: 10.1130/0091-7613(2000)28<603:MICRCZ>2.0.CO

Ellis BS, Bachmann O, Wolff J a. (2014) Cumulate fragments in silicic ignimbrites: The case of the Snake River Plain. Geology 42:431–434. doi: 10.1130/G35399.1

Ferry JM, Watson EB (2007) New thermodynamic models and revised calibrations for the Ti-in-zircon and Zr-in-rutile thermometers. Contrib to Mineral Petrol 154:429–437. doi: 10.1007/s00410-007-0201-0

Fiebelkorn RB, Walker GW, Macleod NS, et al (1982) INDEX TO K-AR AGE DETERMINATIONS FOR THE STATE OF OREGON. United States Geol Surv Open-File Rep 82-596:1–35.

Fisher RV (1966) Geology of a Miocene Ignimbrite Layer, John Day Formation, Eastern Oregon.

Fisher RV (1963) Zeolite-Rich Beds of the John Day Formation, Grant and Wheeler Counties, Oregon. Ore Bin 25:1–16.

Ford MT, Grunder AL, Duncan R a. (2013) Bimodal volcanism of the High Lava Plains and Northwestern Basin and Range of Oregon: Distribution and tectonic implications of age-progressive rhyolites. Geochemistry, Geophys Geosystems 14:2836–2857. doi: 10.1002/ggge.20175

Glazner AF, Bartley JM, Coleman DSS, et al (2004) Are plutons assembled over millions of years by amalgamation from small magma chambers ? GSA Today 5173:4. doi: 10.1130/1052-5173(2004)014<0004

Glazner AF, Coleman DS, Bartley JM (2008) The tenuous connection between high-silica rhyolites and granodiorite plutons. Geology 36:183. doi: 10.1130/G24496A.1

Gualda GAR, Ghiorso MS, Lemons R V., Carley TL (2012) Rhyolite-MELTS: A modified calibration of MELTS optimized for silica-rich, fluid-bearing magmatic systems. J Petrol 53:875–890. doi: 10.1093/petrology/egr080

Halliday AN, Davidson JP, Hildreth W, Holden P (1991) Modeling the petrogenesis of high Rb/Sr silicic magmas. Chem Geol 92:107–114.

Hart WK, Aronson JL, Mertzman S a. (1984) Areal distribution and age of low-K, high-alumina olivine tholeiite magmatism in the northwestern Great Basin. Bull Geol Soc Am 95:186–195. doi: 10.1130/0016-7606(1984)95<186:ADAAOL>2.0.CO;2

Herbert EH, Sparks RSJ, Huppert HE, Sparks RSJ (1988) The Generation of Granitic Magmas by Intrusion of Basalt into Continental Crust. J Petrol 29:599–624. doi: 10.1093/petrology/29.3.599

Hildreth W (2004) Volcanological perspectives on Long Valley , Mammoth Mountain , and Mono Craters : several contiguous but discrete systems. 136:169–198. doi: 10.1016/j.jvolgeores.2004.05.019

Hildreth W (1981) Gradients in Silicic Magma Chambers: Implications for Lithospheric Magmatism. J Geophys Res 86:10153–10192.

Hildreth W (1979) The Bishop Tuff: evidence for the origin of compositional zonation in silicic magma chambers. Geol Soc Am Spec … 180:44–75.

Hildreth W, Wilson CJN (2007) Compositional Zoning of the Bishop Tuff. J Petrol 48:951–999. doi: 10.1093/petrology/egm007

Hooper PR, Binger GB, Lees KR (2002) Ages of the Steens and Columbia River flood basalts and their relationship to extension-related calc-alkalic volcanism in eastern Oregon. Bull Geol Soc Am 114:43–50. doi: 10.1130/0016-7606(2002)114<0043:AOTSAC>2.0.CO;2

Hort M (1998) Abrupt Change in Magma Liquidus Temperature because of Volatile Loss or Magma Mixing: Effects on Nucleation, Crystal Growth and Thermal History of the Magma. J Petrol 39:1063–1076. doi: 10.1093/petroj/39.5.1063

Hoskin PWO, Schaltegger U (2003) The Composition of Zircon and Igneous and Metamorphic Petrogenesis. Rev Mineral Geochemistry 53:27–62. doi: 10.2113/0530027

Housh TB, Bowring SA (1991) Lead isotopic heterogeneities within alkali feldspars; implications for the determination of initial lead isotopic compositions. Geochim Cosmochim Acta 55:2309–2316.

Huber C, Bachmann O, Dufek J (2012) Crystal-poor versus crystal-rich ignimbrites: A competition between stirring and reactivation. Geology 40:115–118. doi: 10.1130/G32425.1

Jaffey a. H, Flynn KF, Glendenin LE, et al (1971) Precision measurement of half-lives and specific activities of U235 and U238. Phys Rev C 4:1889–1906. doi: 10.1103/PhysRevC.4.1889

Johnson DM, Hooper PR, Conrey RM (1999) XRF analysis of rocks and minerals for major and trace elements on a single low dilution Li-tetraborate fused bead. Adv X-ray Anal 41:843–867.

Jordan BT, Grunder AL, Duncan R a., Deino AL (2004) Geochronology of age-progressive volcanism of the Oregon High Lava Plains: Implications for the plume interpretation of Yellowstone. J Geophys Res B Solid Earth 109:1–19. doi: 10.1029/2003JB002776

Krogh T (1973) A low-contamination method for hydrothermal decomposition of zircon and extraction of U and Pb for isotopic age determinations. Geochim Cosmochim Acta 37:485–494. doi: 10.1016/0016-7037(73)90213-5

Lawrence R (1976) Strike-slip faulting terminates the Basin and Range province in Oregon. Geol Soc Am Bull 846–850. doi: 10.1130/0016-7606(1976)87<846:SFTTBA>2.0.CO;2

Leeman WP, Oldow JS, Hart WK (1992) Lithosphere-scale thrusting in the western US Cordillera as constrained by Sr and Nd isotopic transitions in Neogene volcanic rocks. Geology 20:63–66. doi: 10.1130/0091-7613(1992)020<0063:LSTITW>2.3.CO;2

Linnen RL, Keppler H (2002) Melt composition control of Zr/Hf fractionation in magmatic processes. Geochim Cosmochim Acta 66:3293–3301. doi: 10.1016/S0016-7037(02)00924-9

Lipman PW, Bachmann O (2015) Ignimbrites to batholiths: Integrating perspectives from geological, geophysical, and geochronological data. Geosphere 11:705–743. doi: 10.1130/GES01091.1

Lipman PWPW (2007) Incremental assembly and prolonged consolidation of Cordilleran magma chambers: Evidence from the Southern Rocky Mountain volcanic field. Geosphere 3:42. doi: 10.1130/GES00061.1

Luo Y, Ayers JC (2009) Experimental measurements of zircon/melt trace-element partition coefficients. Geochim Cosmochim Acta 73:3656–3679. doi: 10.1016/j.gca.2009.03.027

Macdonald R, Belkin HE (2002) Compositional variation in minerals of the chevkinite group. 66:1075–1098. doi: 10.1180/0026461026660078

Macleod N, Walker G, McKee E (1976) Geothermal significance of eastward increase in age of upper Cenozoic domes in southeast Oregon. In: Second United Nations Symposium on the development and use of geothermal resources. pp 465–474

Matthews N, Vazquez J, Calvert A (2015) Age of the Lava Creek supereruption andmagma chamber assembly at Yellowstone based on 40Ar/39Ar and U-Pb

dating of sanidine and zircon crystals Naomi. Geochemistry Geophys Geosystems 16:2508–2528. doi: doi:10.1002/2015GC005881

Mattinson JM (2005) Zircon U-Pb chemical abrasion ("CA-TIMS") method: Combined annealing and multi-step partial dissolution analysis for improved precision and accuracy of zircon ages. Chem Geol 220:47–66. doi: 10.1016/j.chemgeo.2005.03.011

McClaughry JD, Ferns ML, Streck MJ, et al (2009) Paleogene claderas of central snd eastern Oregon: Eruptive sources of widespread tuffs in the John Day and Clarno Formations. Geoligical Soc Am Feild Guid 15:407–434.

McCurry M, Hayden KP, Morse LH, et al (2008) Genesis of post-hotspot, A-type rhyolite of the Eastern Snake River Plain volcanic field by extreme fractional crystallization. Bull Volcanol 70:361–383.

Nardi LVS, Formoso MLL, Müller IF, et al (2013) Zircon/rock partition coefficients of REEs, Y, Th, U, Nb, and Ta in granitic rocks: Uses for provenance and mineral exploration purposes. Chem Geol 335:1–7. doi: 10.1016/j.chemgeo.2012.10.043

Nekvasil H, Simon A, Lindsley DHH (2000) Crystal Fractionation and the Evolution of Intra-plate hy-normative Igneous Suites: Insights from their Feldspars. J Petrol 41:1743–1757. doi: 10.1093/petrology/41.12.1743

Olin PH, Wolff J a. (2010) Rare earth and high field strength element partitioning between iron-rich clinopyroxenes and felsic liquids. Contrib to Mineral Petrol 160:761–775. doi: 10.1007/s00410-010-0506-2

Peucat JJ, Bernard-Griffiths J, Ibarguchi JG, et al (1990) Geochemical and geochronological cross section of the deep Variscan crust: The Cabo Ortegal high-pressure nappe (northwester Spain). Tectonophysics 177:263–292.

Pierce K, Morgan L (1992) The track of the Yellowstone hotspot: Volcanism, faulting, and uplift. Mem - Geol Soc Am 179:1–53.

Pin C, Lancelot J (1982) U-Pb dating of an early paleozoic bimodal magmatism in the french Massif Central and of its further metamorphic evolution. Contrib to Mineral Petrol 79:1–12. doi: 10.1007/BF00376956

Rivera TA, Schmitz MD, Crowley JL, Storey M (2014) Rapid magma evolution constrained by zircon petrochronology and 40Ar/39Ar sanidine ages for the Huckleberry Ridge Tuff, Yellowstone, USA. Geology 42:643–646. doi: 10.1130/G35808.1

Rivera TA, Storey M, Schmitz MD, Crowley JL (2013) Age intercalibration of 40 Ar / 39 Ar sanidine and chemically distinct U / Pb zircon populations from the Alder Creek Rhyolite Quaternary geochronology standard. Chem Geol 345:87–98.

Rubatto D, Hermann J (2007) Experimental zircon/melt and zircon/garnet trace element partitioning and implications for the geochronology of crustal rocks. Chem Geol 241:38–61. doi: 10.1016/j.chemgeo.2007.01.027

Rustad JR (2015) Interaction of rhyolite melts with monazite, xenotime, and zircon surfaces. Contrib to Mineral Petrol 169:50. doi: 10.1007/s00410-015-1142-7

Scaillet B, Holtz F, Pichavant M (2016) Experimental Constraints on the Formation of Silicic Magmas. Elements 12:109–114. doi: 10.2113/gselements.12.2.109

Schmitz MD, Schoene B (2007) Derivation of isotope ratios, errors, and error correlations for U-Pb geochronology using 205 Pb- 235 U-(233 U)-spiked isotope dilution thermal ionization mass spectrometric data. Geochemistry, Geophys Geosystems 8:n/a–n/a. doi: 10.1029/2006GC001492

Shane P, Nairn IA, Martin SB, Smith VC (2008) Compositional heterogeneity in tephra deposits resulting from the eruption of multiple magma bodies: Implications for tephrochronology. Quat Int 178:44. doi: 10.1016/j.quaint.2006.11.014

Shane P, Nairn IA, Smith VC (2004) Magma mingling in the ~50 Ka Rotoiti eruption from the Okataina Volcanic Centre. Geol. Soc. New Zeal. Misc. Publ. 117A:94.

Smith RL (1979) Ash-flow magmatism. Geol Soc Am Spec Pap 180:5–28.

Smith RL (1960) Ash Flows. Geol Soc Am Bull 1:795. doi: 10.1130/0016-7606(1960)71[795:AF]2.0.CO;2

Sparks RSJ, Wright JV (1979) Welded air-fall tuffs. Geol Soc Am Spec Pap 180:155–166.

Stelten ME, Cooper KM, Vazquez J a., et al (2013) Magma mixing and the generation of isotopically juvenile silicic magma at Yellowstone caldera inferred from coupling 238U–230Th ages with trace elements and Hf and O isotopes in zircon and Pb isotopes in sanidine. Contrib to Mineral Petrol 166:587–613. doi: 10.1007/s00410-013-0893-2

Streck M (2002) Partial melting to produce high-silica rhyolites of a young bimodal suite: compositional constraints among rhyolites, basalts, and metamorphic xenoliths from the Harney Basin, Oregon. Int J Earth Sci 91:583–593. doi: 10.1007/s00531-001-0246-7

Streck MJ (2014) Evaluation of crystal mush extraction models to explain crystal-poor rhyolites. J Volcanol Geotherm Res 284:79–94. doi: 10.1016/j.jvolgeores.2014.07.005

Streck MJ, Grunder AL (1997) Compositional gradients and gaps in high-silica rhyolites of the Rattlesnake Tuff, Oregon. J Petrol 38:133–163. doi: 10.1093/petrology/38.1.133

Streck MJ, Grunder AL (1995) Crystallization and welding variations in a widespread ignimbrite sheet; the Rattlesnake Tuff, eastern Oregon, USA. Bull Volcanol 57:151–169. doi: http://dx.doi.org/10.1007/s004450050086

Streck MJ, Johnson JA, Grunder AL (1999) Field Guide to the Rattlesnake Tuff and High Lava Plains near Burns, Oregon. Oregon Geol 61:64–76.

Streck MJ, Grunder AL (1999) Enrichment of basalt and mixing of dacite in the rootzone of a large rhyolite chamber: inclusions and pumices from the Rattlesnake Tuff, Oregon. Contrib to Mineral Petrol 136:193–212. doi: 10.1007/s004100050532

Streck MJ, Grunder AL (2008) Phenocryst-Poor Rhyolites of Bimodal, Tholeiitic Provinces: The Rattlesnake Tuff and Implications for Mush Extraction Models. Bull Volcanol 70:385–401.

Sun SS, McDonough WF (1989) Chemical and isotopic systematics of oceanic basalts: implications for mantle composition and processes. Geol Soc London, Spec Publ 42:313–345. doi: 10.1144/GSL.SP.1989.042.01.19

Swisher CC, Ach JA, Hart WK (1990) Laser fusion 40Ar/39Ar dating of the type Steens Mountain Basalt, southeastern Oregon and the age of the Steens geomagnetic polarity transition [abs]. Eos (Transactions, Am Geophys Union) 71:p. 1296.

Tappa MJ, Coleman DS, Mills RD, Samperton KM (2011) The plutonic record of a silicic ignimbrite from the Latir volcanic field, New Mexico. Geochemistry Geophys Geosystems 12:n/a–n/a. doi: 10.1029/2011GC003700

Tuttle OF, Bowen NL (1958) Origin of granite in the light of experimental studies in the system NaAlSi3O8–KAlSi3O8–SiO2–H2O. Geol Soc Am Mem 74:1–146.

Walker GW, Macleod NS, McKee EH (1974) Progressive age of late cenozoic silicic volcanism in southeastern oregon and its implications for geothermal exploration. United States Geol Surv Prof Pap 1–46.

Walker GW (1979) Revisions to the Cenozoic Stratigraphy of Harney Basin, Southeastern Oregon.

Wark D a., Hildreth W, Spear FS, et al (2007) Pre-eruption recharge of the Bishop magma system. Geology 35:235–238. doi: 10.1130/G23316A.1

Watson EB (1979) Zircon saturation in felsic liquids: Experimental results and applications to trace element geochemistry. Contrib to Mineral Petrol 70:407–419. doi: 10.1007/BF00371047

Whitaker MLL, Nekvasil H, Lindsley DHH, McCurry M (2008) Can crystallization of olivine tholeiite give rise to potassic rhyolites?--an experimental approach. Bull Volcanol 70:417–434.

Williams H, Soediono B, Williams H (1942) The geology of Crater Lake National Park, Oregon, with a reconnaissance of the Cascade Range southward to Mount Shasta. Carnegie Institution of Washington, Washington, D.C.

Wolff JA, Ellis BS, Ramos FC, et al (2015) Remelting of cumulates as a process for producing chemical zoning in silicic tuffs: A comparison of cool, wet and hot, dry rhyolitic magma systems. Lithos 236-237:275–286. doi: 10.1016/j.lithos.2015.09.002

Wright HMN, Folkes CB, Cas RAF, Cashman K V. (2011) Heterogeneous pumice populations in the 2.08-Ma Cerro Galán Ignimbrite: implications for magma recharge and ascent preceding a large-volume silicic eruption. Bull Volcanol 73:1513–1533. doi: 10.1007/s00445-011-0525-5

APPENDIX A

Figures

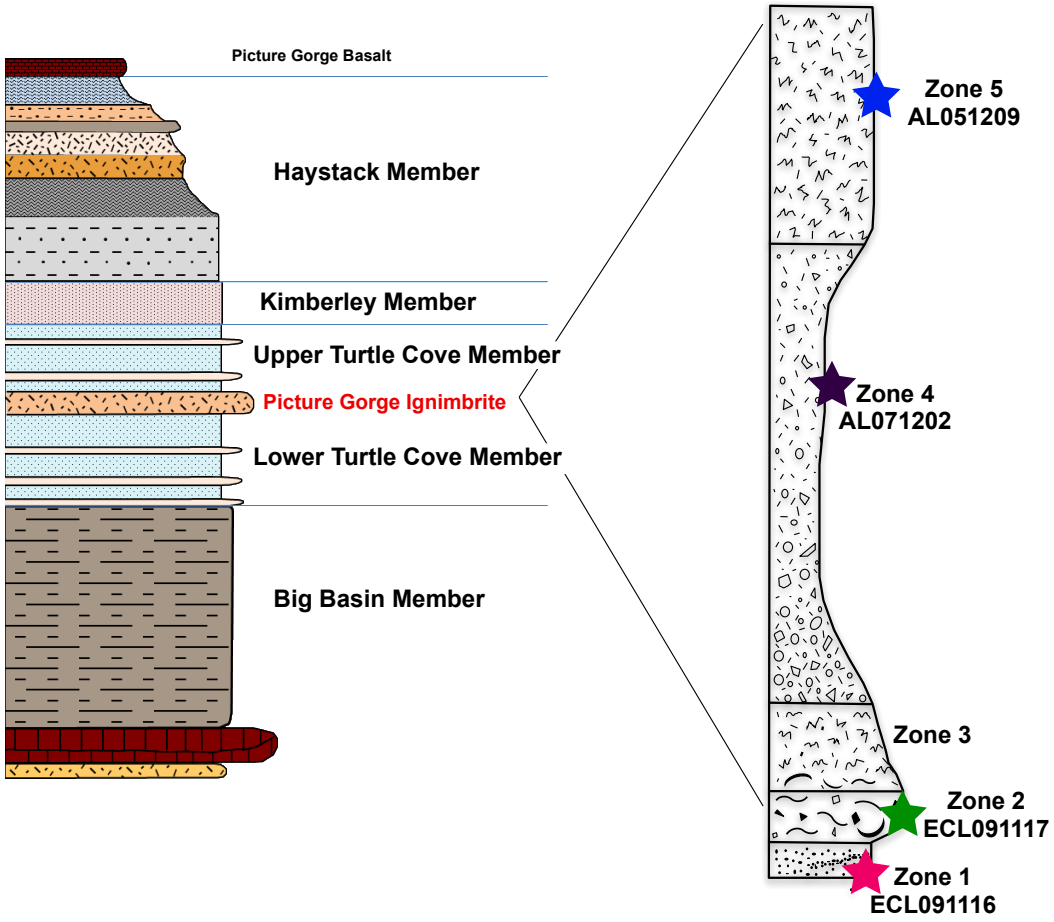

Figure 1 **Generalized stratigraphic column of the John Day Formation. The PGI comprises a conspicuous marker bed within the Turtle Cove Member.**

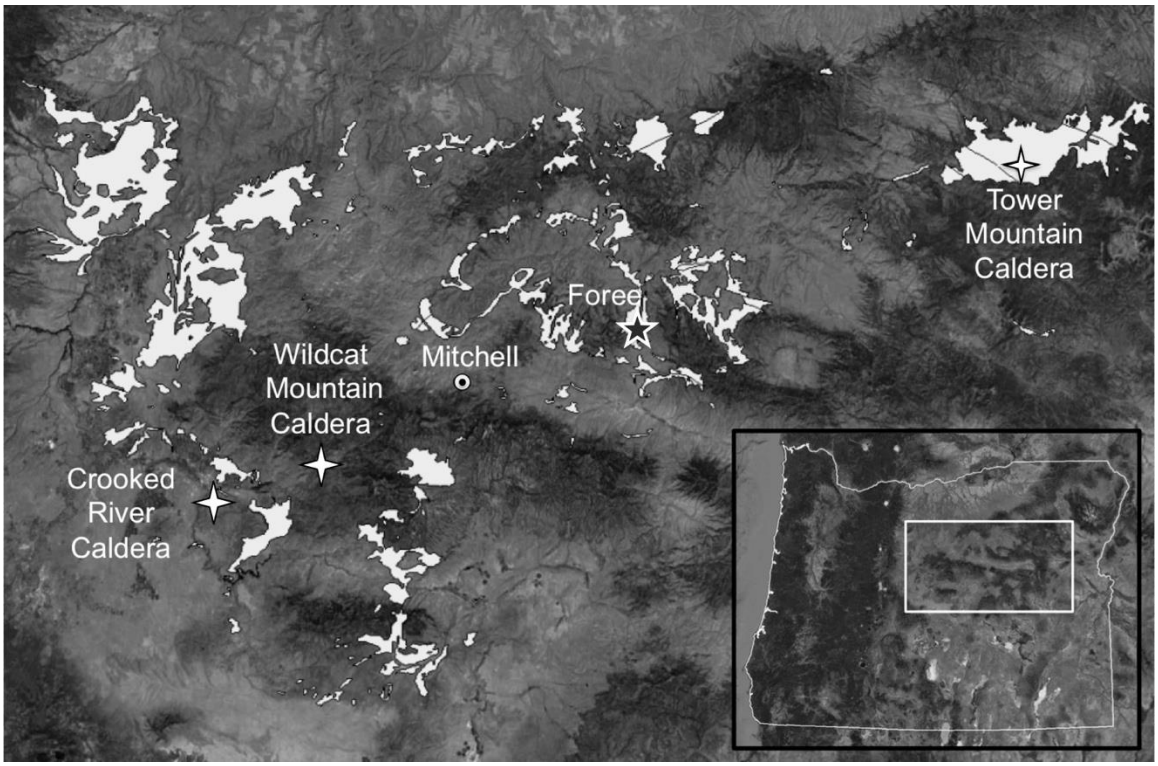

Figure 2 Inset is satellite image of regional setting of PGI. Outcrop pattern of John Day Formation (JDF) shown in light grey. Paleogene caldera structures (Crooked River, Wildcat Mountain, and Tower Mountain), inferred sources of JDF volcanism, are indicated by white stars. Early PGI research suggested a source somewhere southwest of the town of Mitchell, OR (Fisher 1966). More recent research work links PGI with the Crooked River Caldera (McClaughry et al. 2009). Sampling was completed at the Foree trail area, shown by black star.

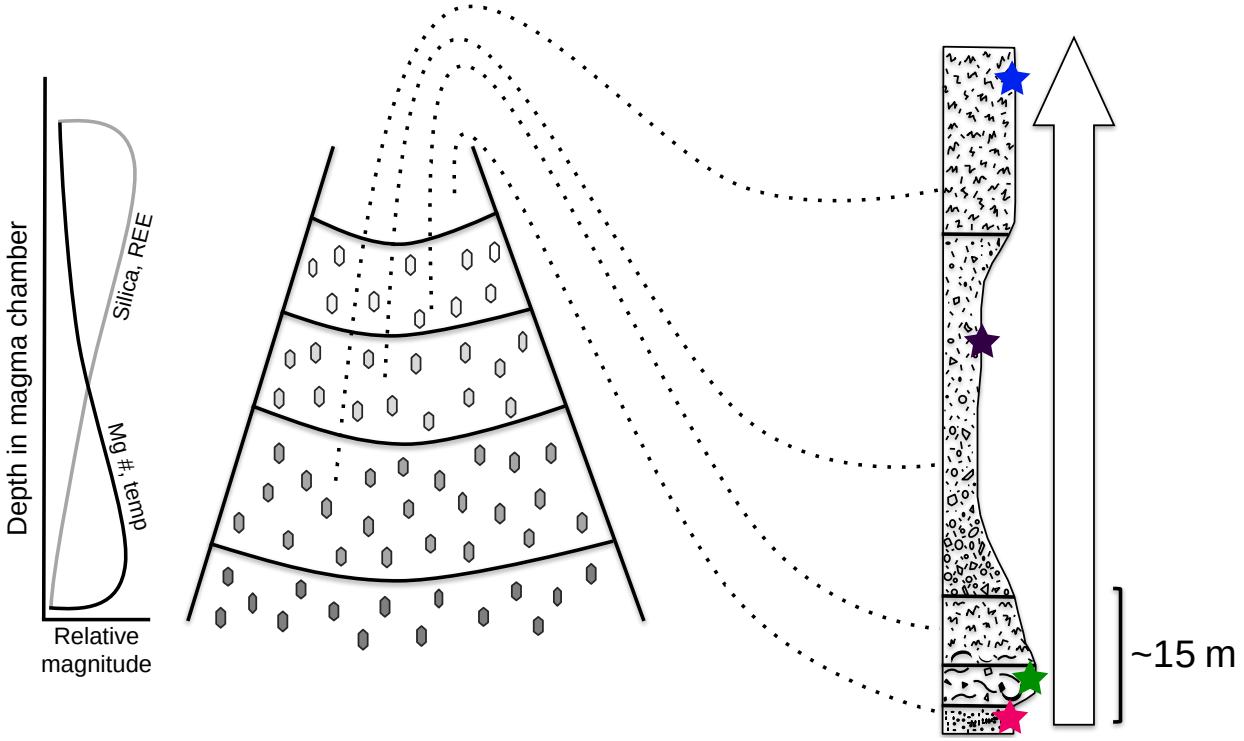

Figure 3 Model PGI magma chamber and inverted stratigraphic order of the ignimbrite after Fisher (1966). Increased stratigraphic height corresponds to increased crystallization temperature and decrease in melt evolution in the pre-eruptive magma chamber.

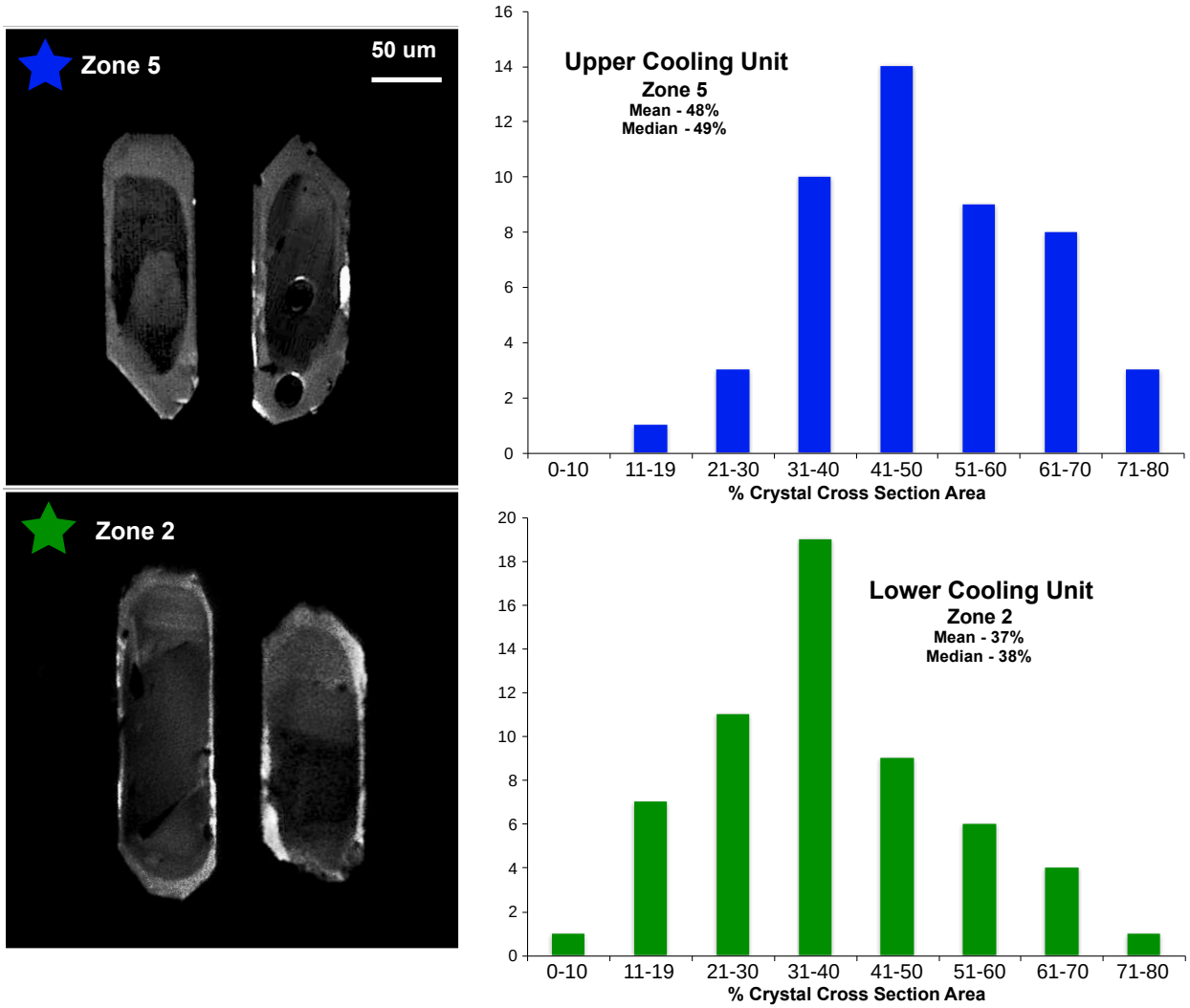

Figure 4 Cathodoluminescent (CL) images of zircon crystals display dark and often sector-zoned crystal cores with bright rim overgrowths. Zircon crystals from the upper cooling unit zone 5 have thicker rim over growths than zircon crystals from the lower cooling unit zone 2. Image analysis determined areas of cross-sectional surfaces of polished crystals for rims and cores. Zircon crystals from the upper zone of the ignimbrite have a greater rim area than those from the lower zone.

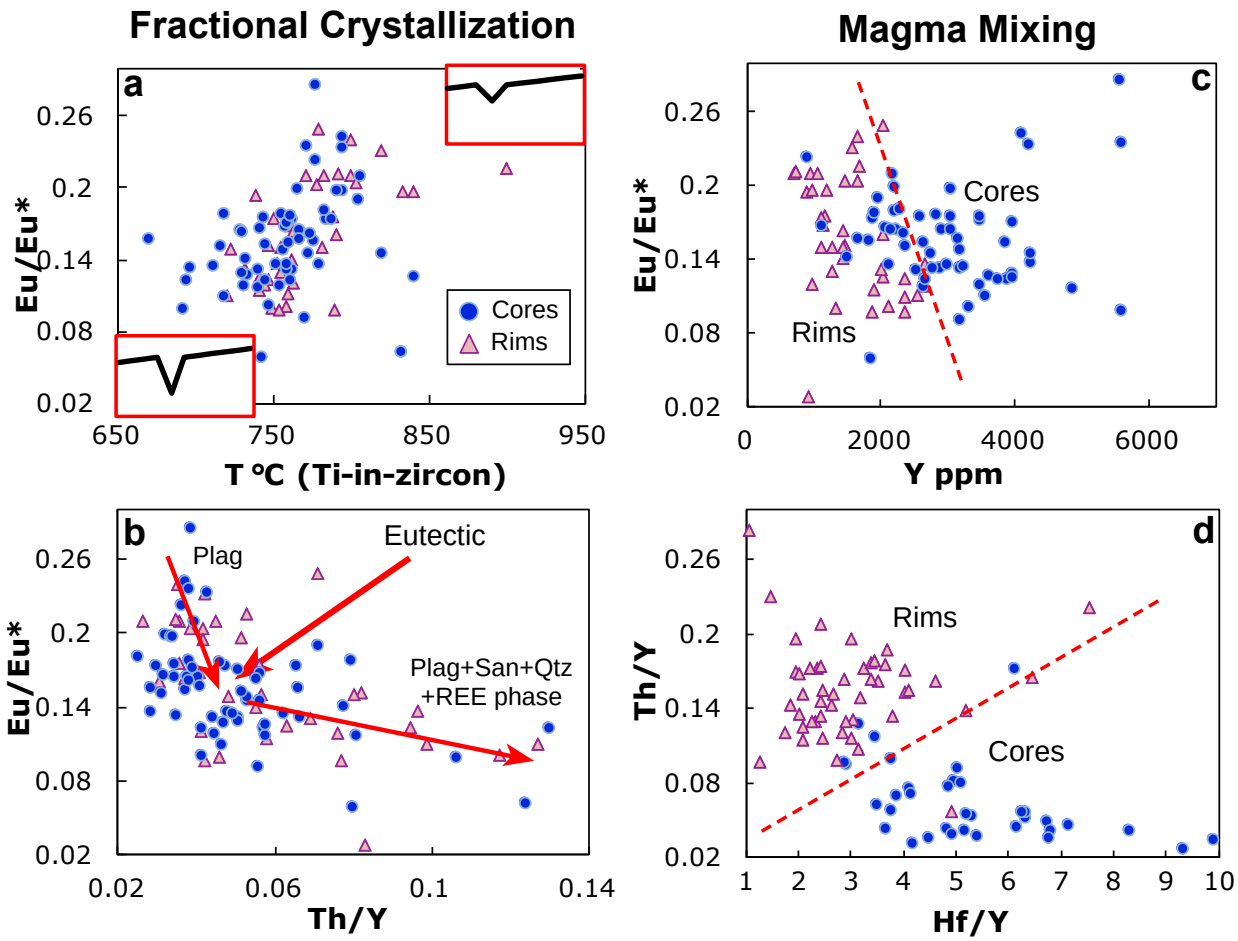

Figure 5 a and b illustrate fractional crystallization for zircon crystal rims and cores. Overlapping crystallization temperatures and europium anomalies for both stages of growth suggest that the system was reheated during core crystallization, followed by down temperature saturation and rim crystallization. Both rim and core crystallization stages followed the same evolutionary path; c and d demonstrate that rims and cores have different chemistry, and show mixing two compositionally distinct magmas present at different times in the pre-eruptive PGI system.

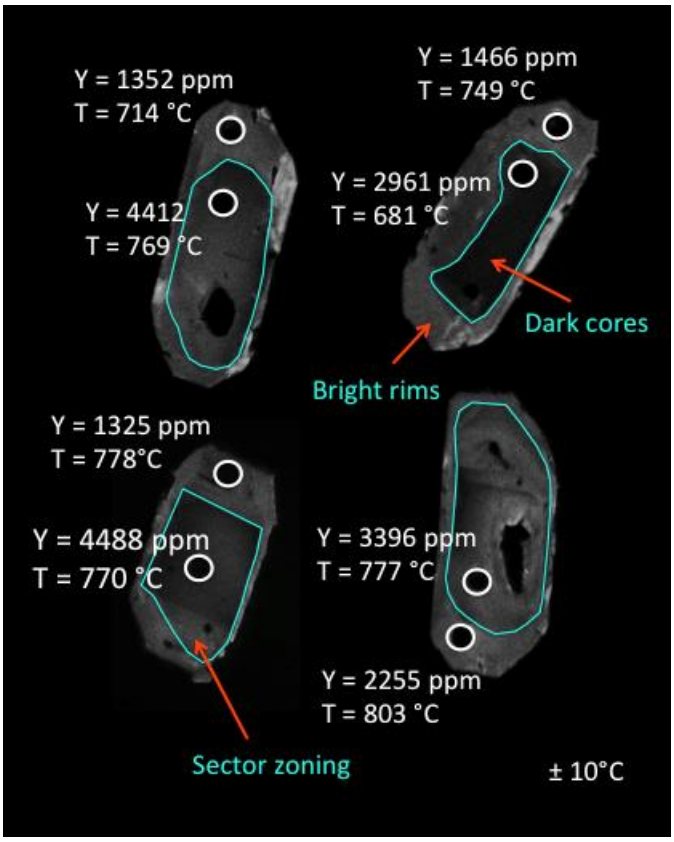

Figure 6 Chemical differences between rims and cores include enrichment of cores in heavy rare earth elements like yttrium as shown above.

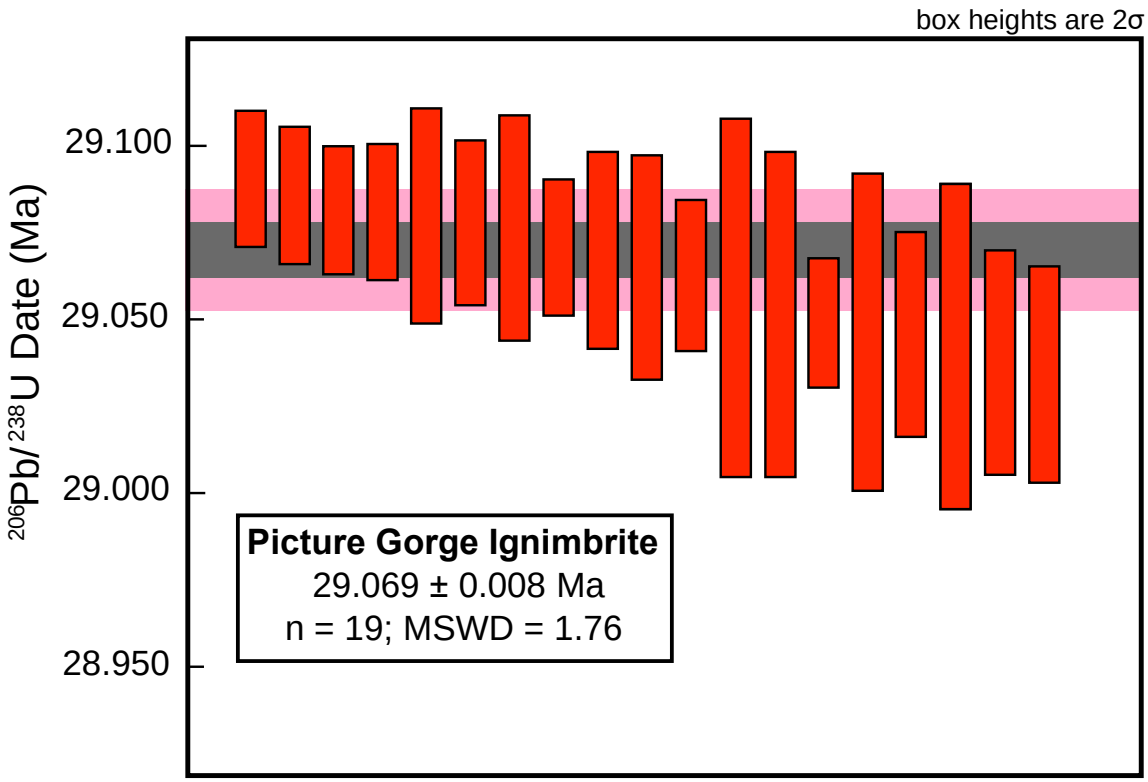

Figure 7 Ranked 206Pb/238U age plot of single PGI zircon crystals. Red bars are single analyses with 2σ errors. Grey bar shows the weighted date of 19 zircon crystals with standard error of ± 8 kyr. Pink bar indicates ~35 kyr standard deviation of weighted mean age, a more conservative estimate of the timescales of magma chamber dynamics.

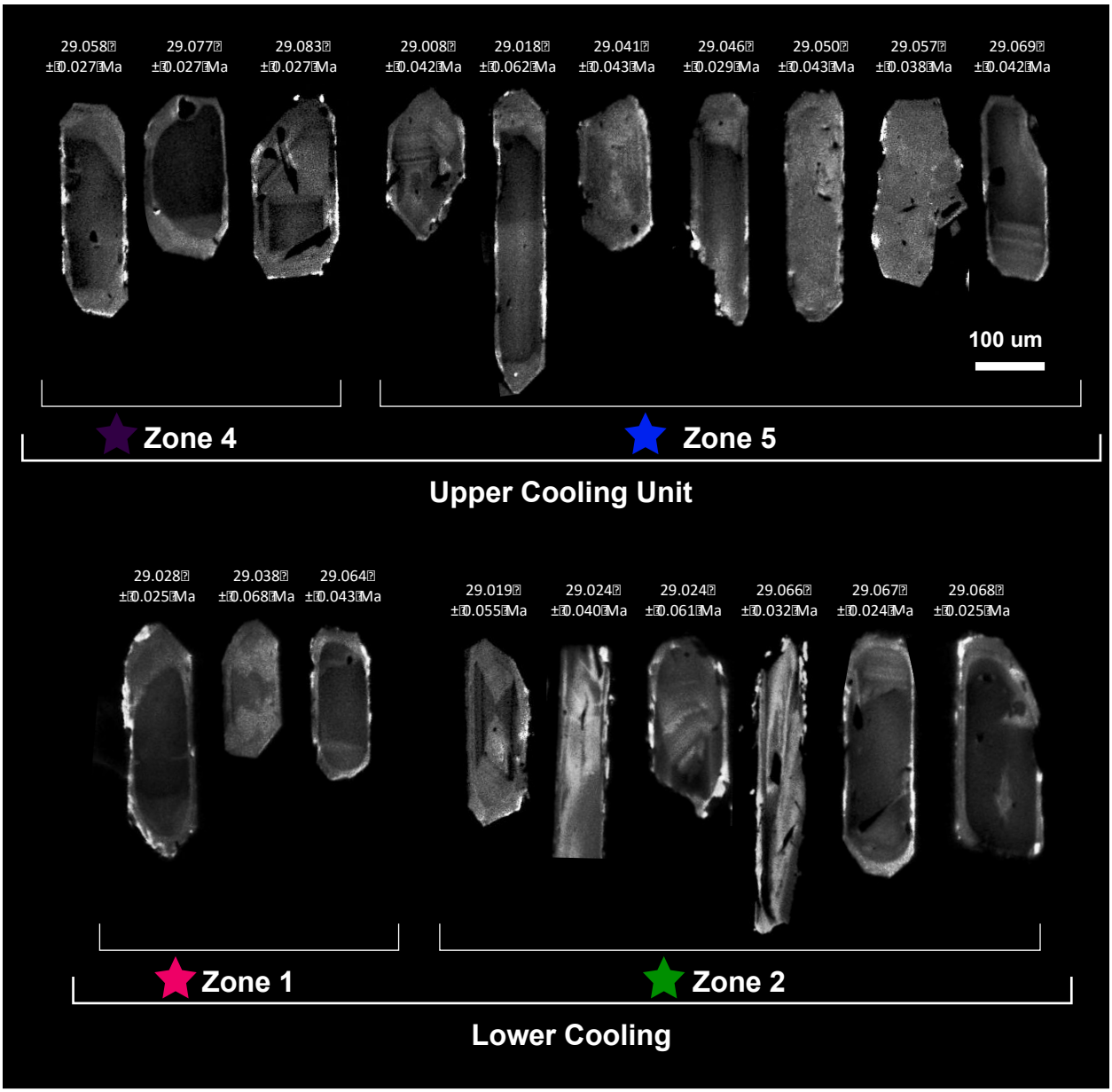

Figure 8 CL images with U-Pb ages for 13 PGI zircon crystals.

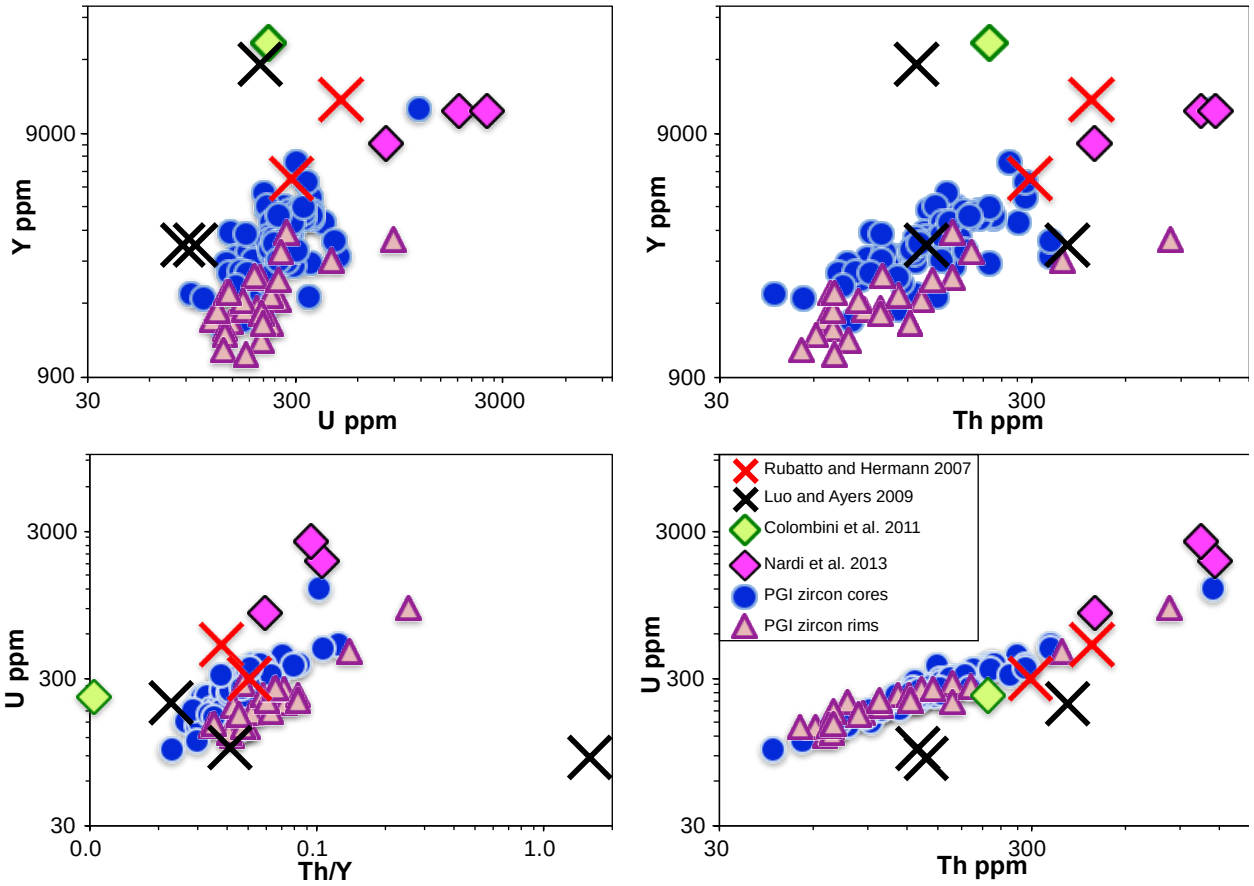

Figure 9 PGI zircon crystal rim and core compositions and modeled equilibrium zircon compositions using PGI glass chemistry and published zircon partition coefficients.

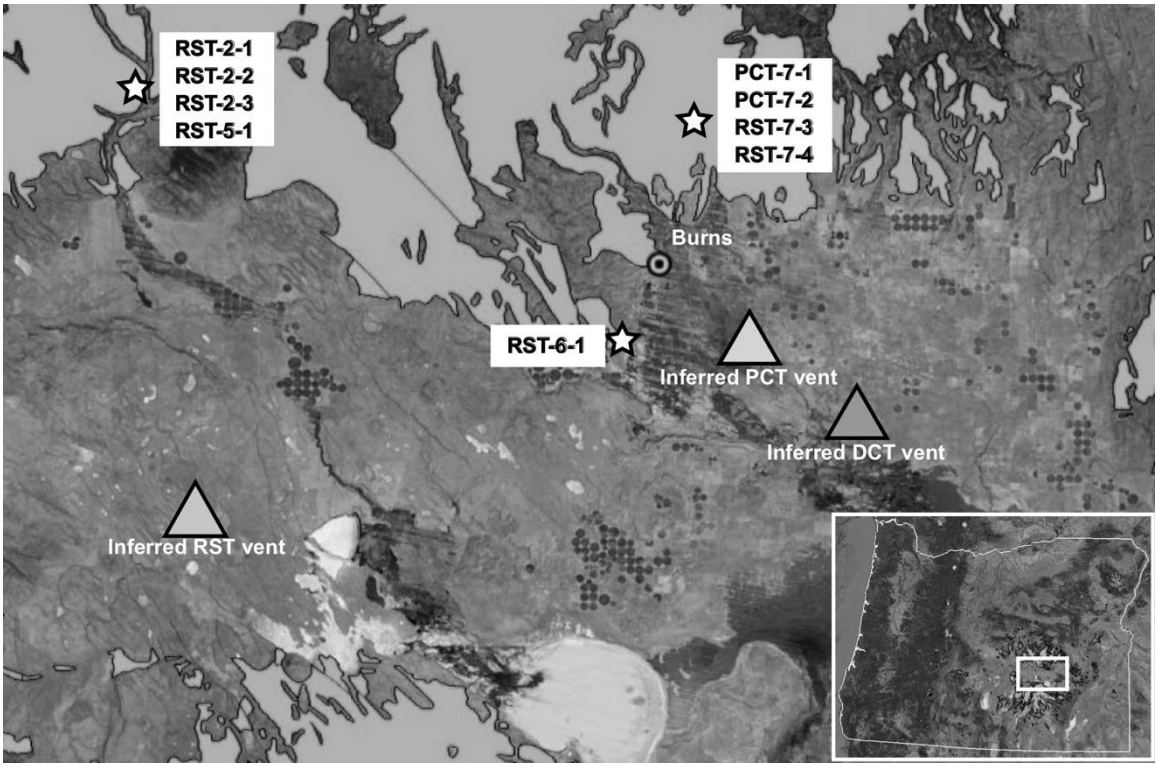

Figure 10 Inset shows regional setting of the Rattlesnake Tuff (RST) in central Oregon; white box outlines the sampling area. Outcrop pattern of Late Miocene silicic volcanic rocks, which includes RST, in solid grey. Triangles mark inferred locations of vents for three large Late Miocene rhyolitic eruptions in the HLP: RST, Prater Creek Tuff (PCT) and Devine Canyon Tuff (DCT) (Streck et al. 1999; Ford et al. 2013).

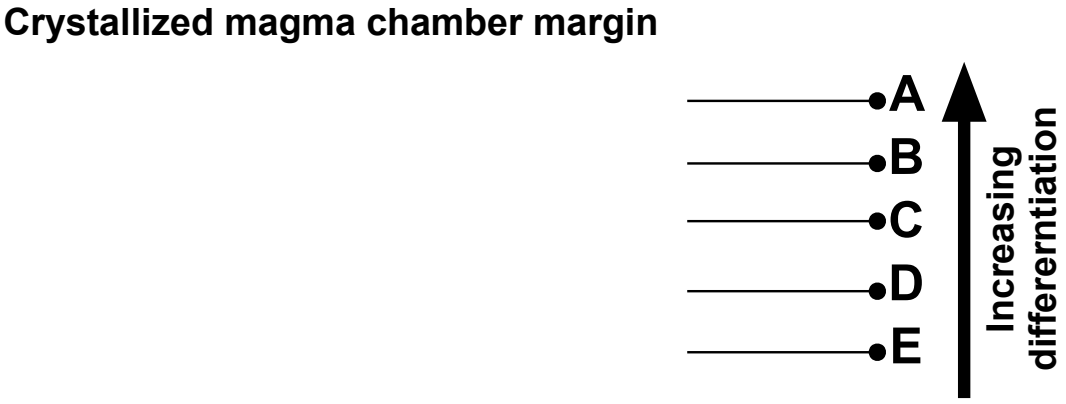

Figure 11 RST magma chamber and magma differentiation model, modified from Streck and Grunder (1997). In the differentiation model, boundary layer fractionation beginning with a parent high silica rhyolite, E, generates a more evolved high silica rhyolite, D. From D, another differentiation interval generates C, and so on, ending with the generation of magma A from differentiation of B.

Figure 12 a) Unwelded pumice rich section of RST at the Silver Creek Ranch sampling location, with rock hammer for scale. Apparently homogenous pumices range in color from white to dark grey and black, and can be >30 cm. b) RST type section north of Burns, OR. c) Banded pumices are assorted mixtures of white, grey, and black. Dark grey and black pumices are low silica rhyolites and dacites and were not examined in this study.

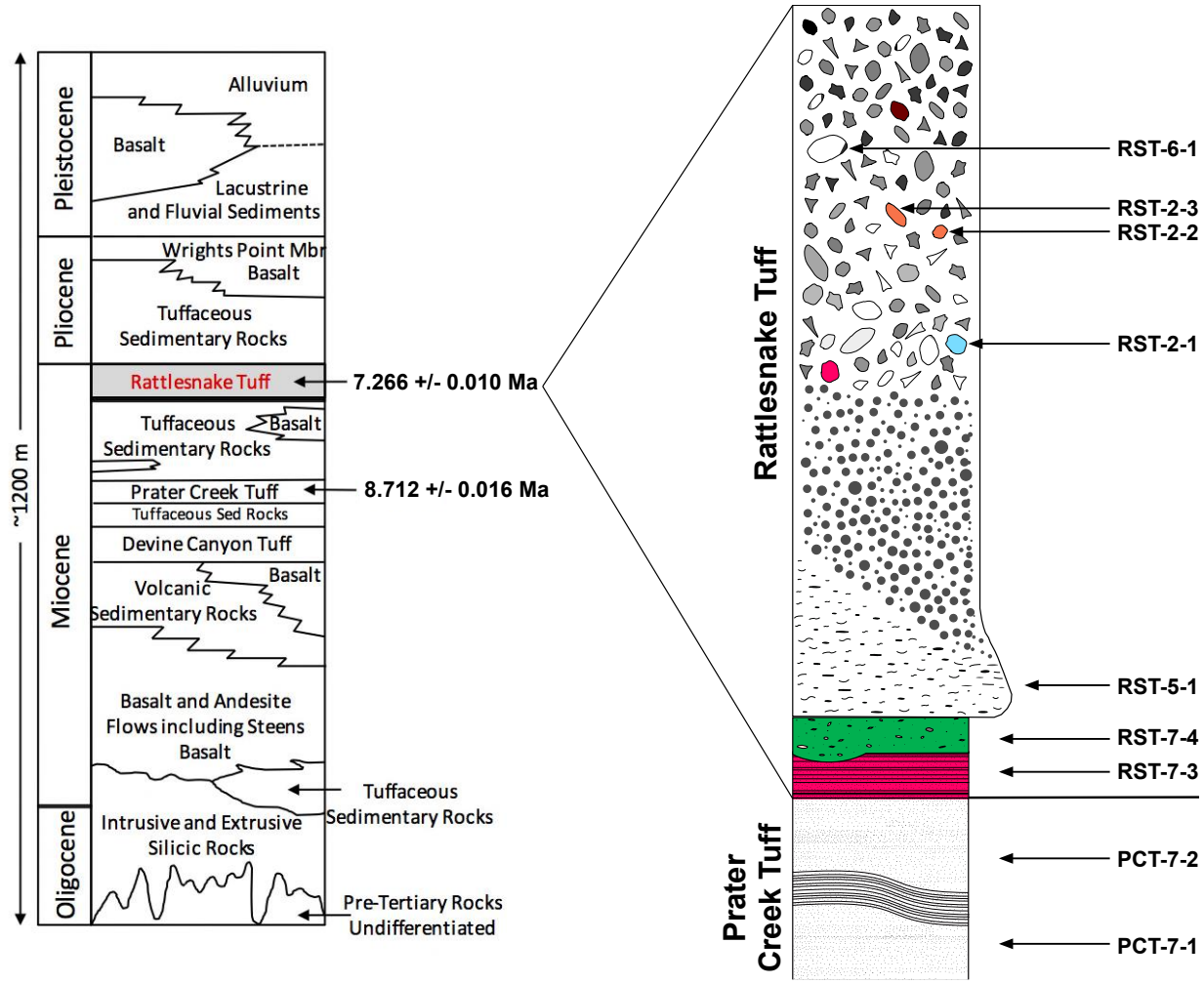

Figure 13 Regional stratigraphic column, modified from Walker 1979, including new U-Pb zircon dates for RST and PCT determined in this study, and generalized stratigraphic column of RST and underlying Prater Creek Tuff and tuffaceous sediments. Sample names point to approximate position within stratigraphy from which samples were collected. RST is somewhat uniform in thickness, typically between 5 and 30 m (Streck and Grunder 1995). It was a maximum of 22 m where sampled for this study.

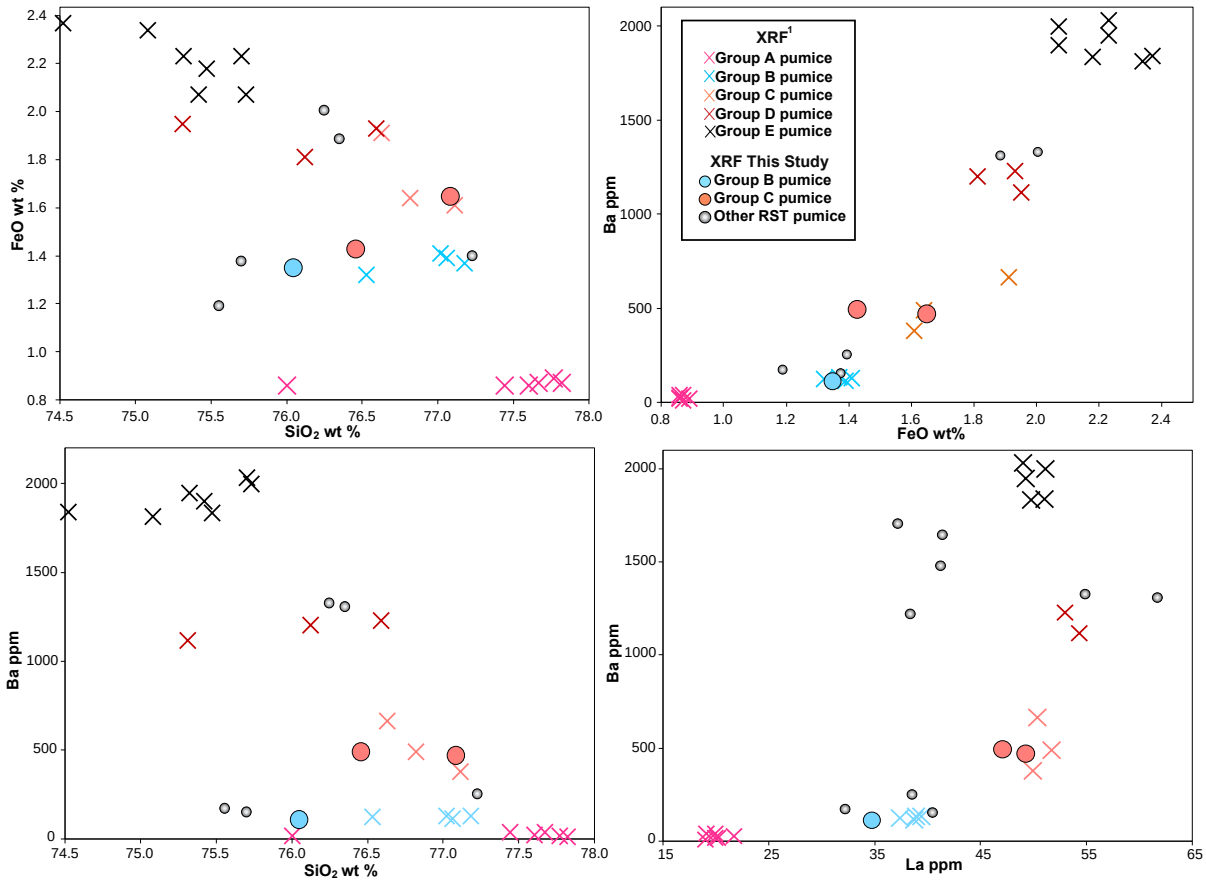

Figure 14 XRF analyses of whole pumice blocks collected for this study and data from [1]Streck and Grunder 1997.

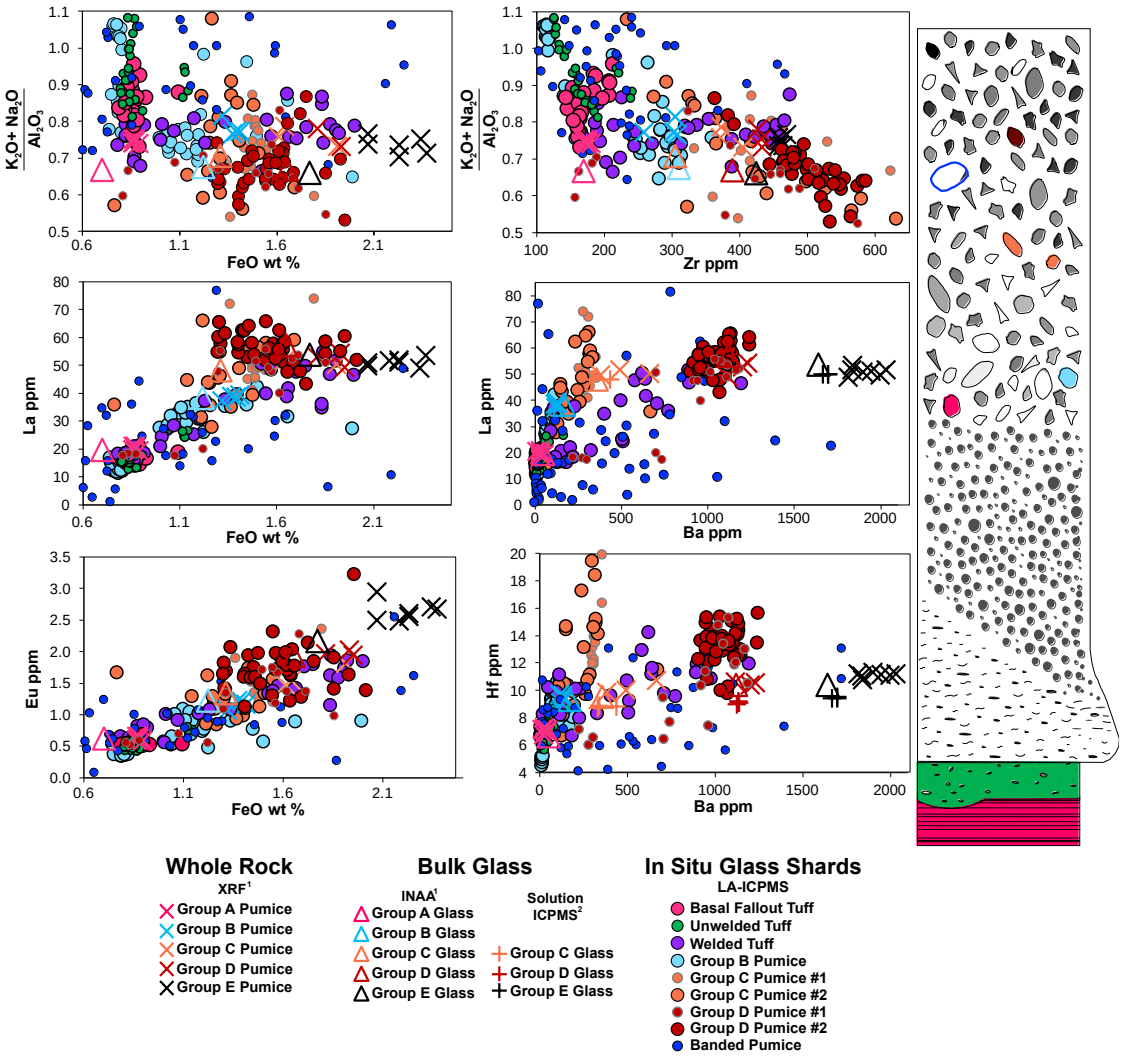

Figure 15 Compositional diagrams RST illustrating the offset between whole rock analysis of clustered pumice compositions and in situ glass shard analysis ([1]Streck and Grunder 1997; [2]Olin and Wolff 2010). These data also reveal internal heterogeneity of groups B and C pumices. Stratigraphic column included show relationship between data and approximate position in generalized RST stratigraphy.

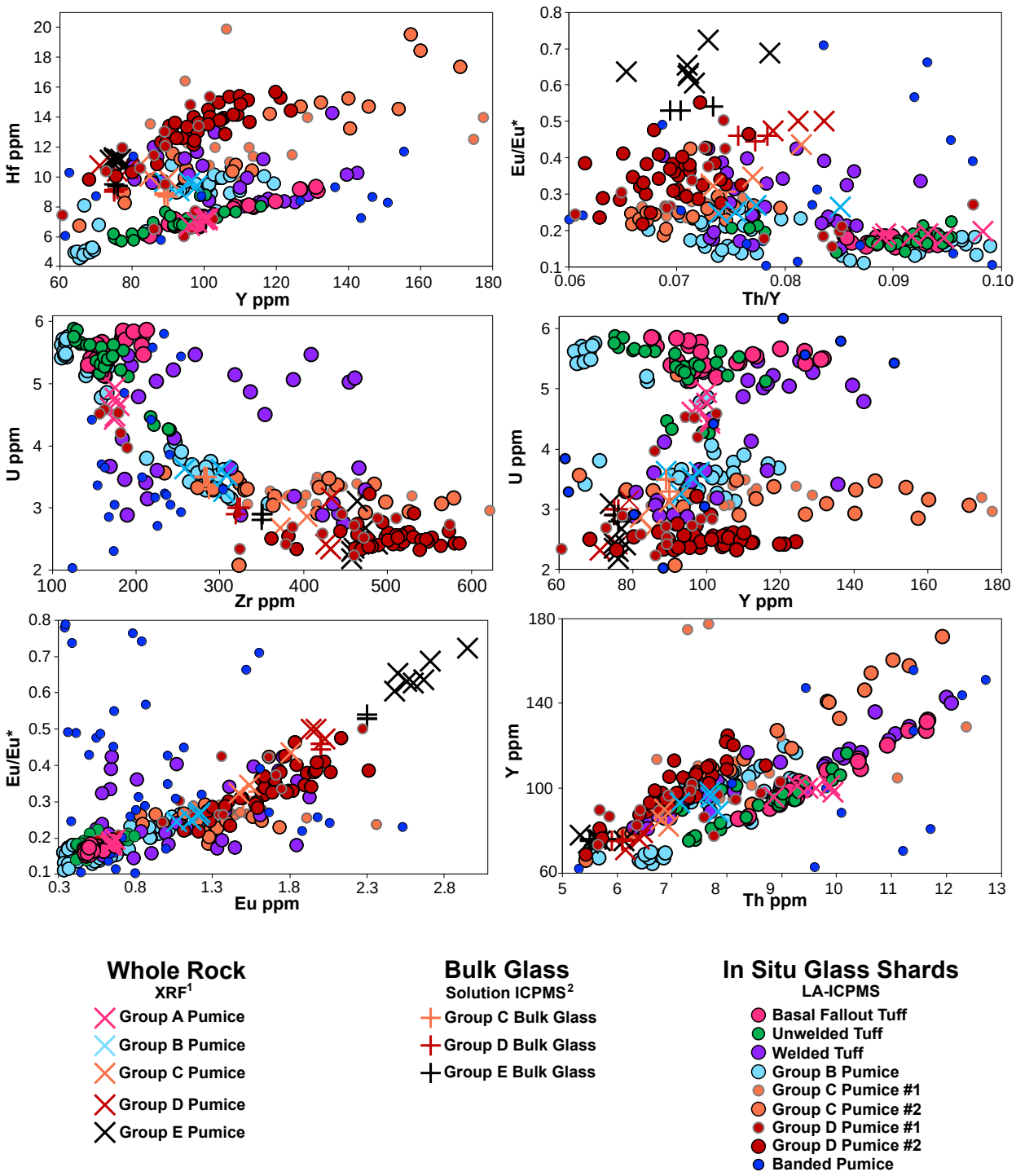

Figure 16 Trace element (TE) variation diagrams of RST glass (this study; [2]Olin and Wolff 2010) and whole pumice ([1]Streck and Grunder 1997).

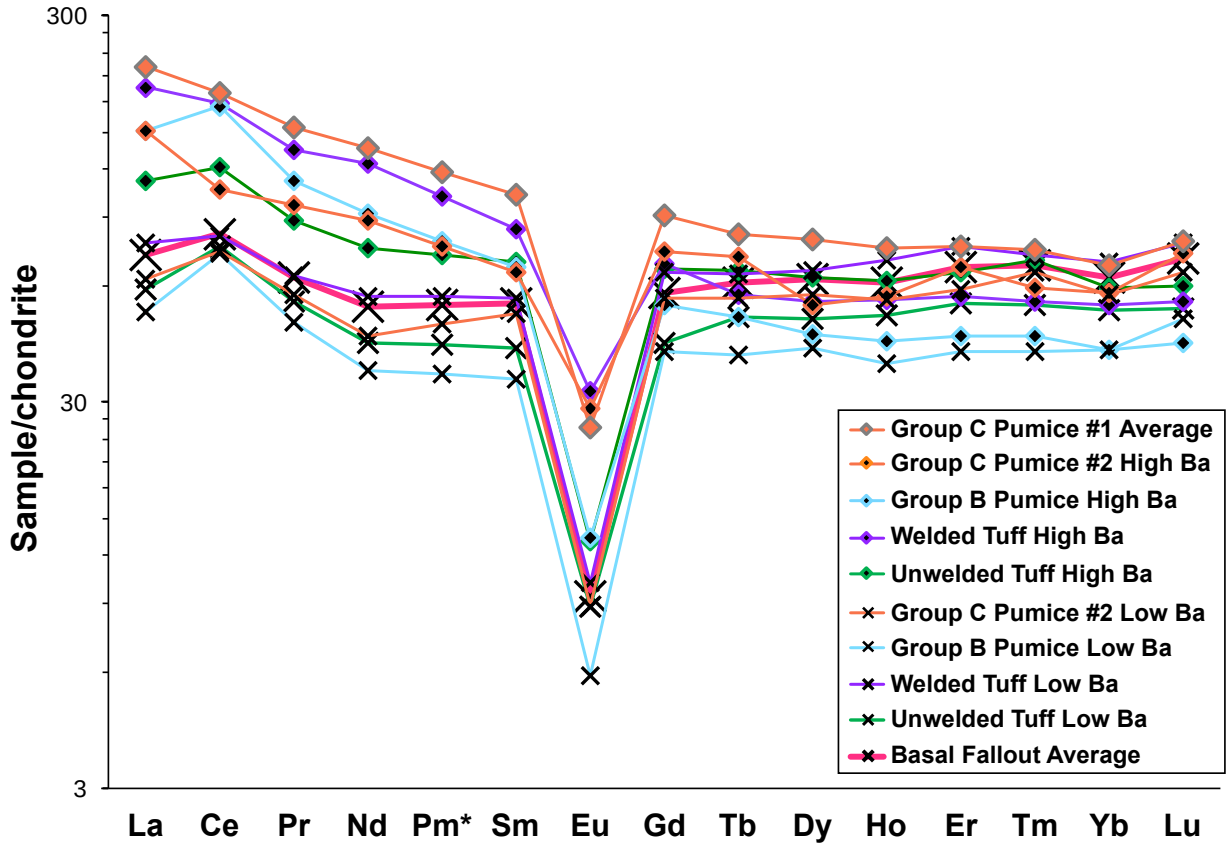

Figure 17 Chondrite normalized (Sun and McDunough 1989) REE compositions of glass shards from RST pumice and tuff. High and low Ba end member analyses of welded and unwelded tuff samples as well as Group B and C#1 pumices were plotted separately to illustrate the mixed nature of those samples. Basal fallout and group C pumice #1 displayed little variation in Ba concentrations (11 and 9 % RSD, respectively) and so were each plotted as a single averaged composition. There is a clear separation of LREE behavior between high Ba welded tuff and pumice samples, and low Ba welded tuff and the two other tuff samples.

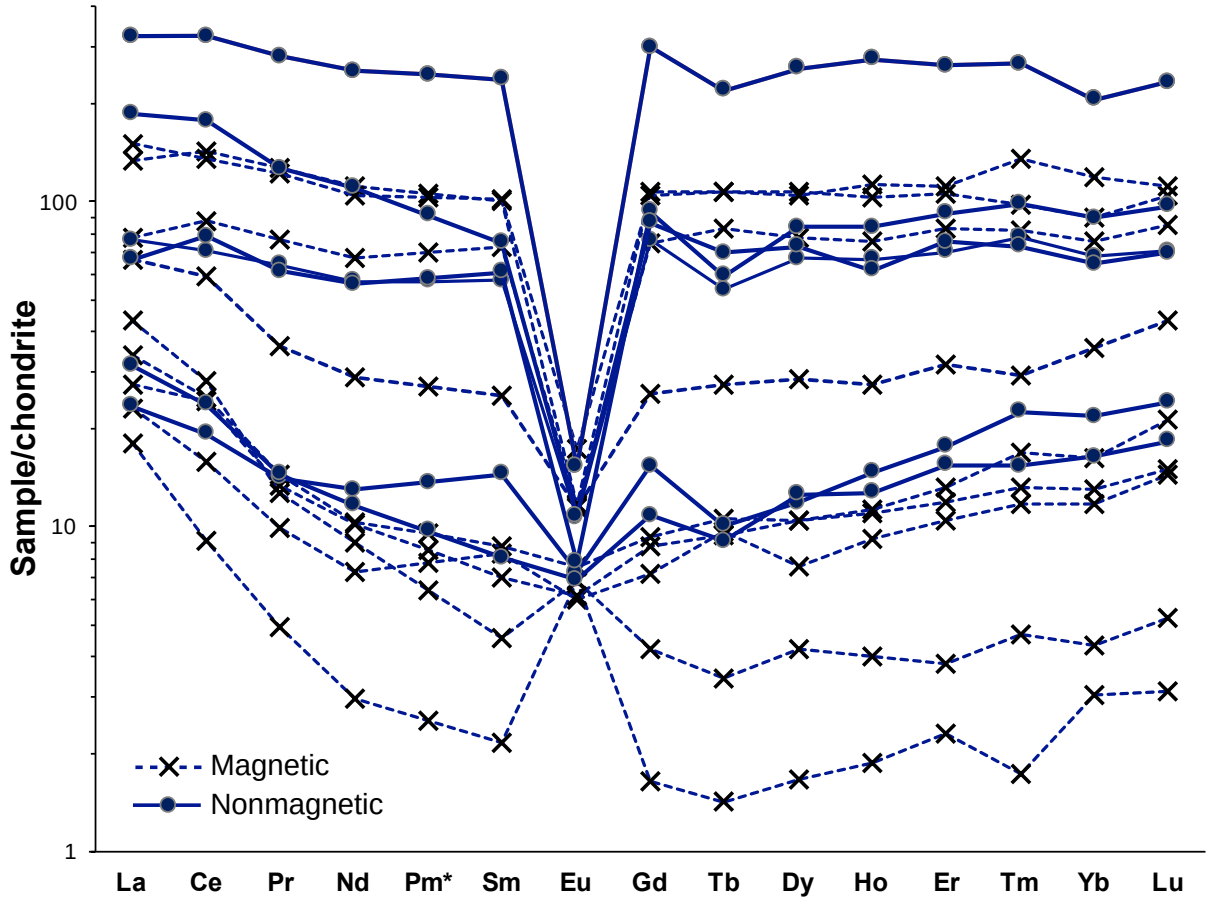

Figure 18 REE compositions of glass shards from a single banded pumice span a wide range from REE depletion and positive Eu anomaly to enriched REE compositions and intensely negative Eu anomaly.

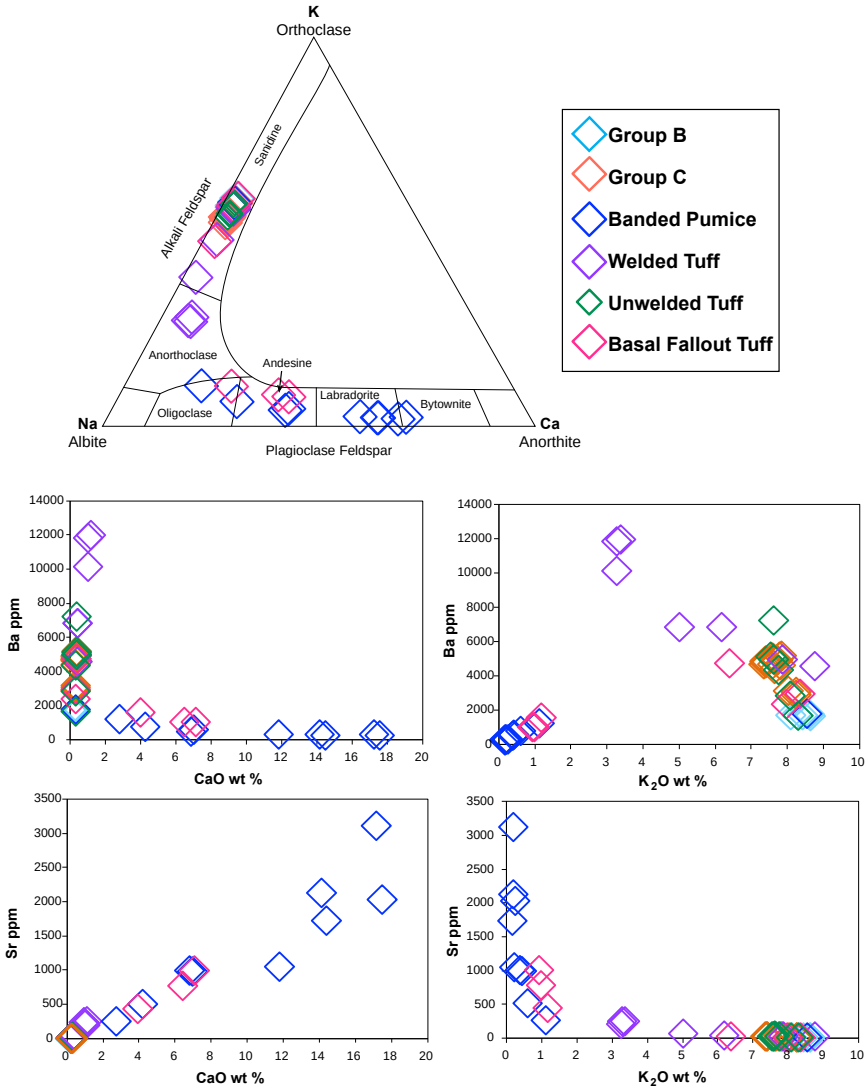

Figure 19 Compositional variation diagrams of feldspars extracted from RST pumice and tuff samples. RST feldspars are both alkali and plagioclase. Groups B and pumices have tightly grouped compositions, while banded pumice and tuff samples display more compositional spread. Plagioclase is only found in banded pumice and basal fallout, and both samples also contain at least a minor alkali feldspar component.

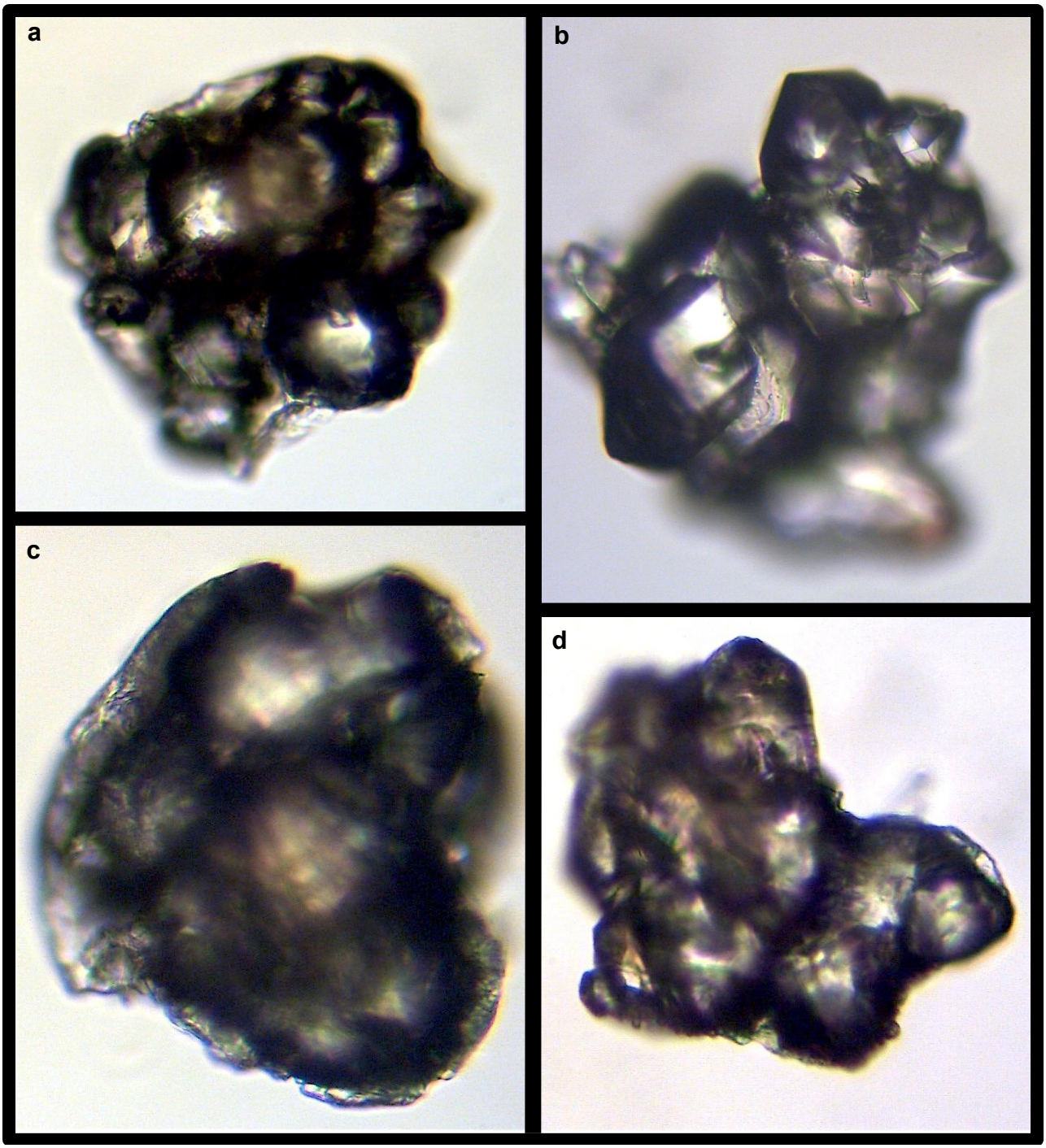

Figure 20 a-d Micropictographs of RST zircon grains taken in reflected light at ~200x magnification. The dominant population of RST zircon grains are unusual crystal aggregates that resemble grape clusters. Facets on individual crystallites comprising the crystal clusters are shown in b and d. Some of the composite crystals were enclosed in a glass rind following standard rock crushing and mineral separation methods shown in c.

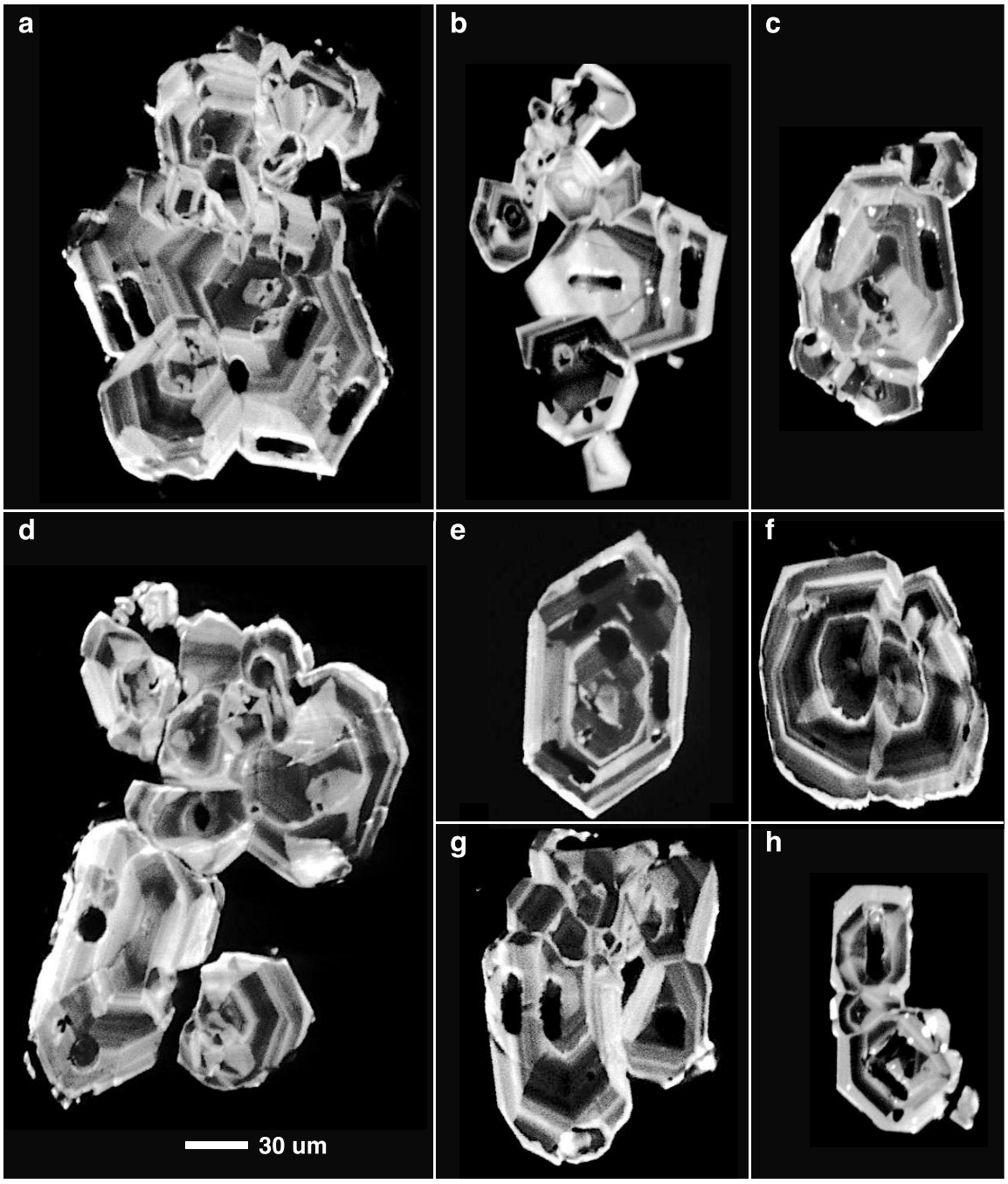

Figure 21 a-h Cathodoluminescence images of complex textures and zoning of botryoidal zircon grains from RST pumice and tuff samples. Images captured at either 200x (a, d, e, f, and g) or 350x (b, c, and h) magnification.

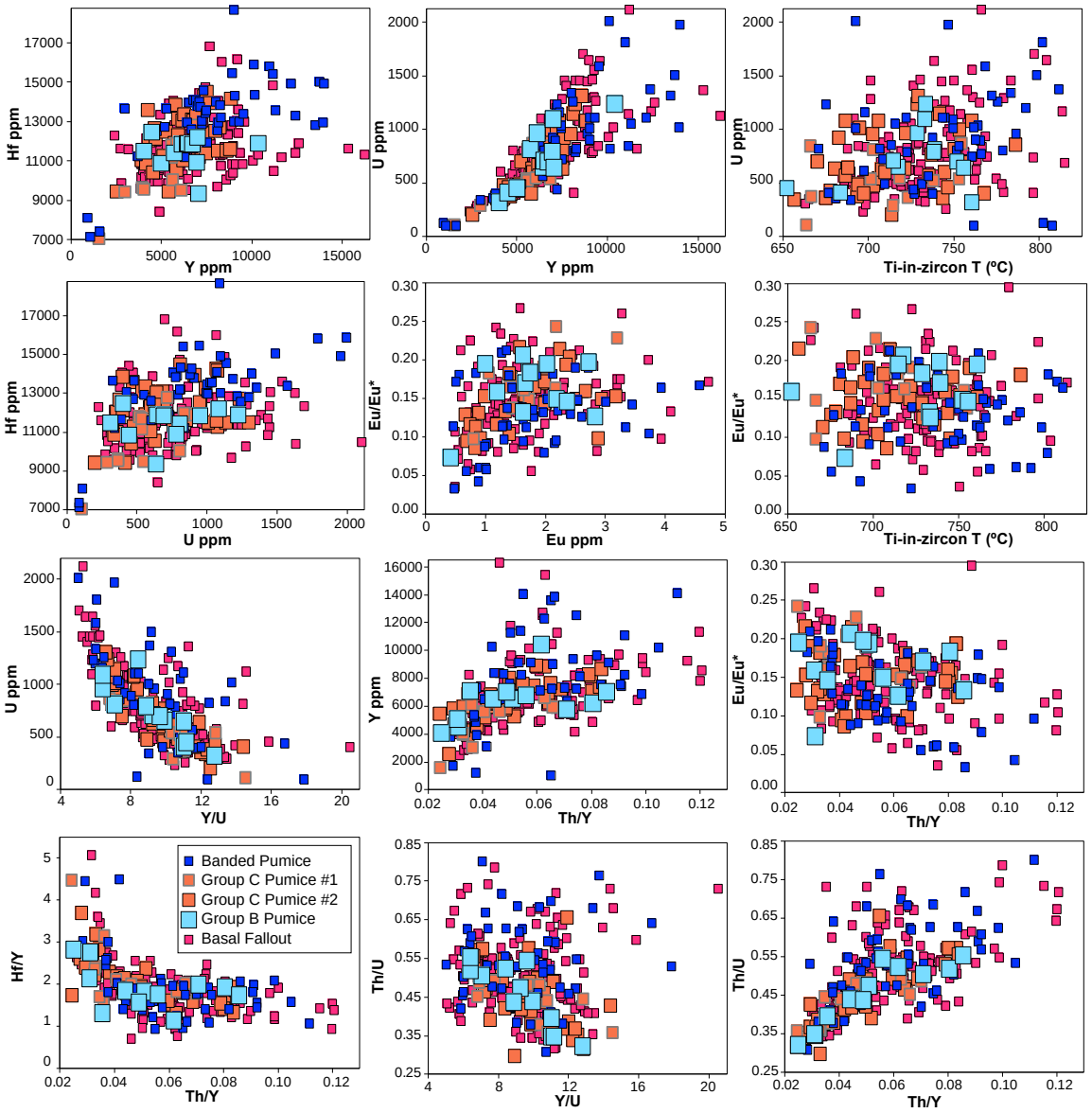

Figure 22 Compositional variation diagrams for in situ spot and line analysis of RST zircon grains

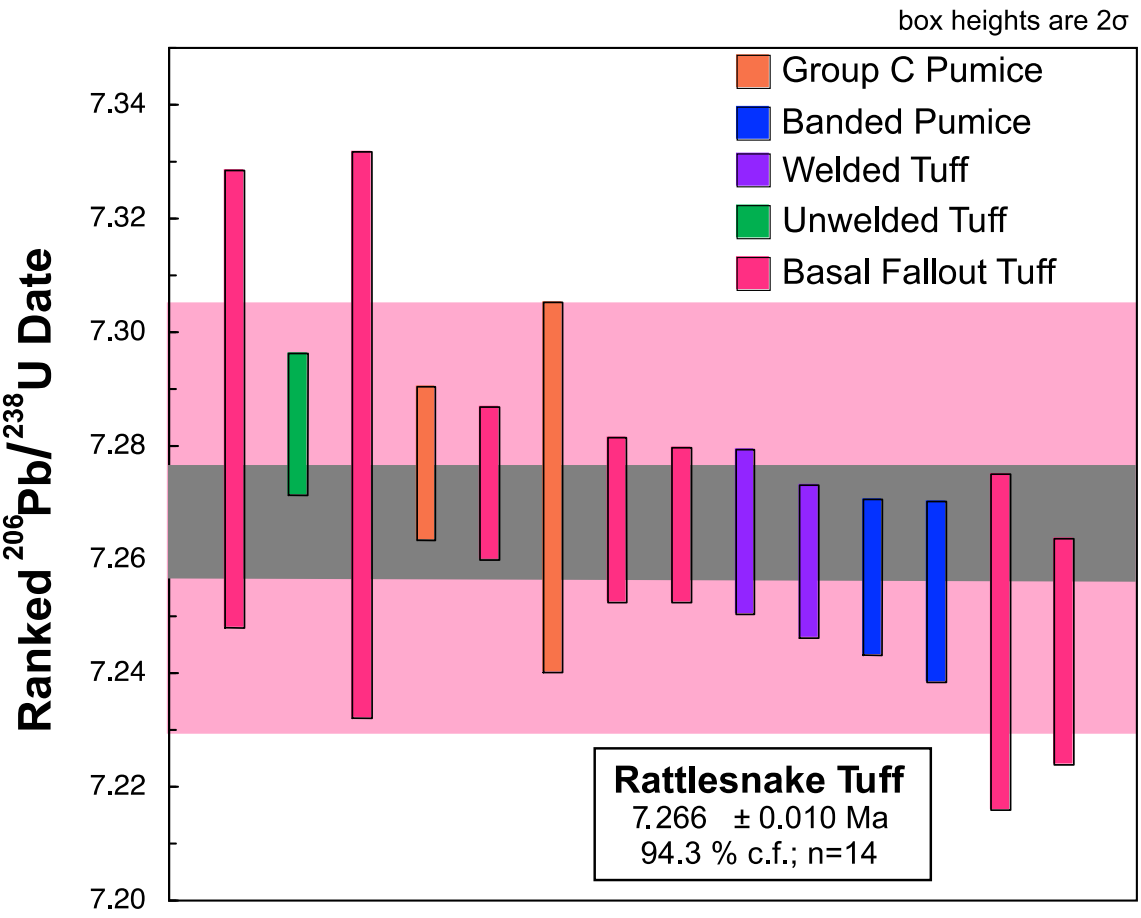

Figure 23 Ranked 206U/238U dates from single RST zircon grains determined using chemical abrasion isotope dilution thermal ionization mass spectrometry (CA-ID-TIMS). Colored bars are individual analyses and include 2σ errors. Grey bar shows the robust median date of 16 zircon crystals with standard error of ± 10 kyr. Pink bar indicates ~40 kyr standard deviation of median age, a more conservative estimate of the timescales of magma chamber dynamics.

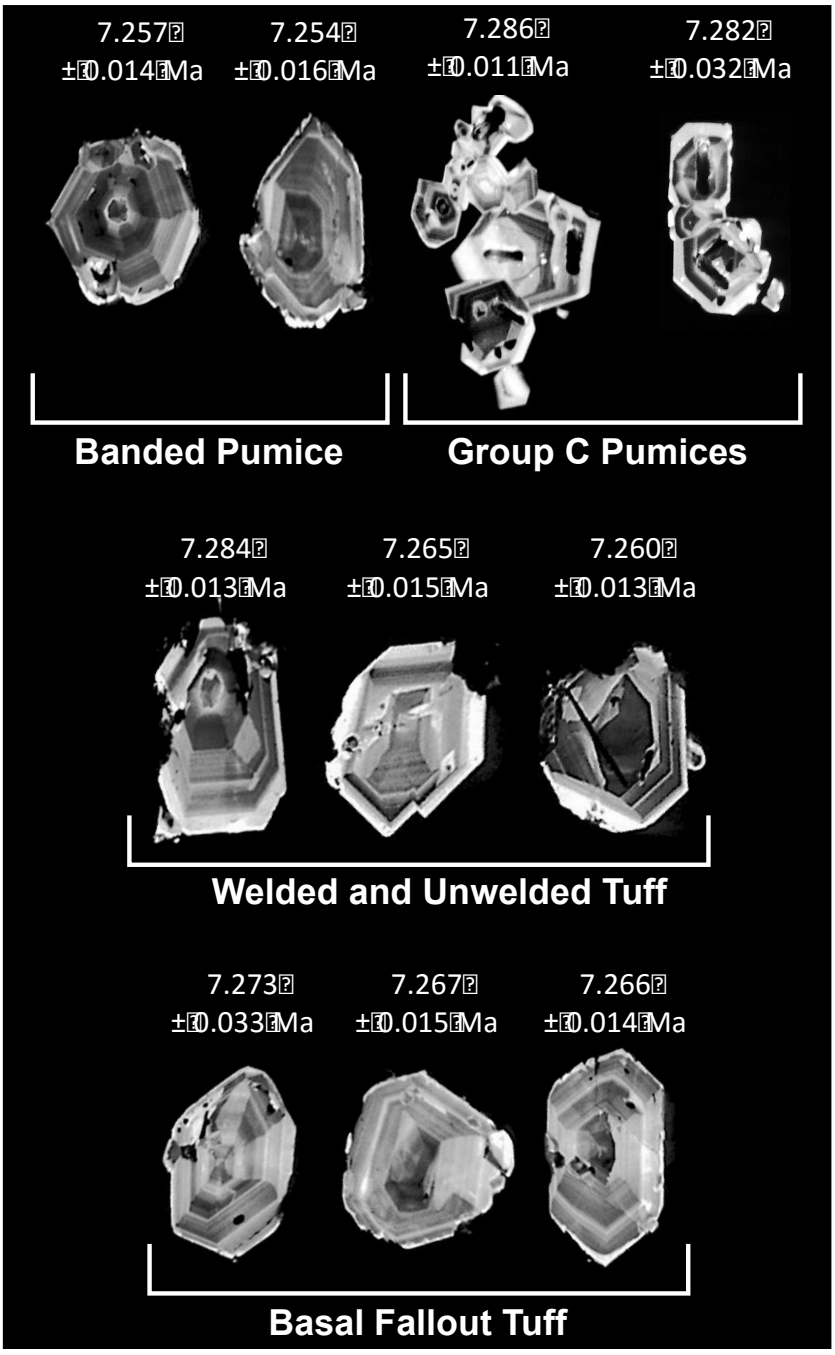

Figure 24 **CL images and dates of 10 RST zircons dated by CA-ID-TIMs for this study.**

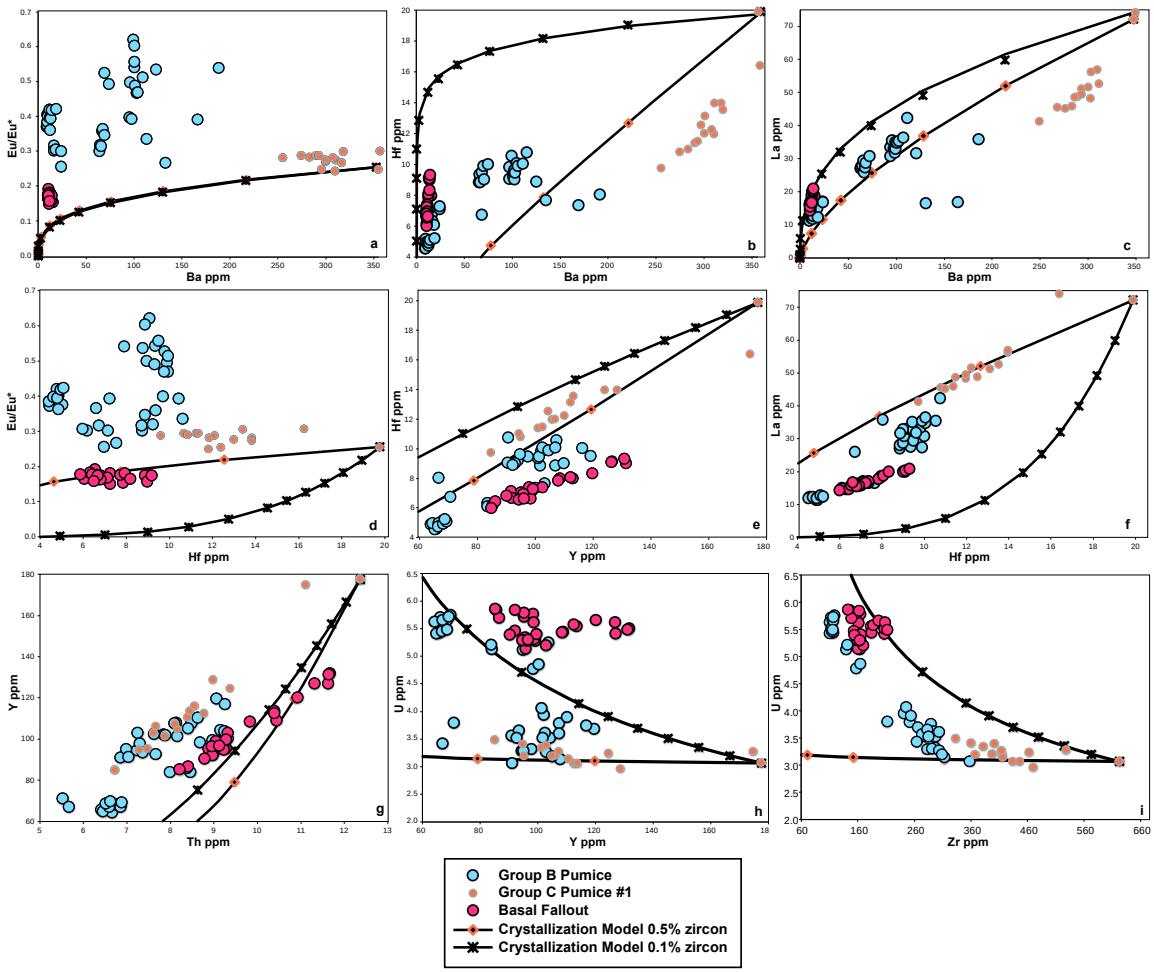

Figure 25 a-i Crystallization models fit data patterns within compositions for some parameters, as in e and f. In other cases, crystallization can explain an evolution from the least to most evolved compositions.

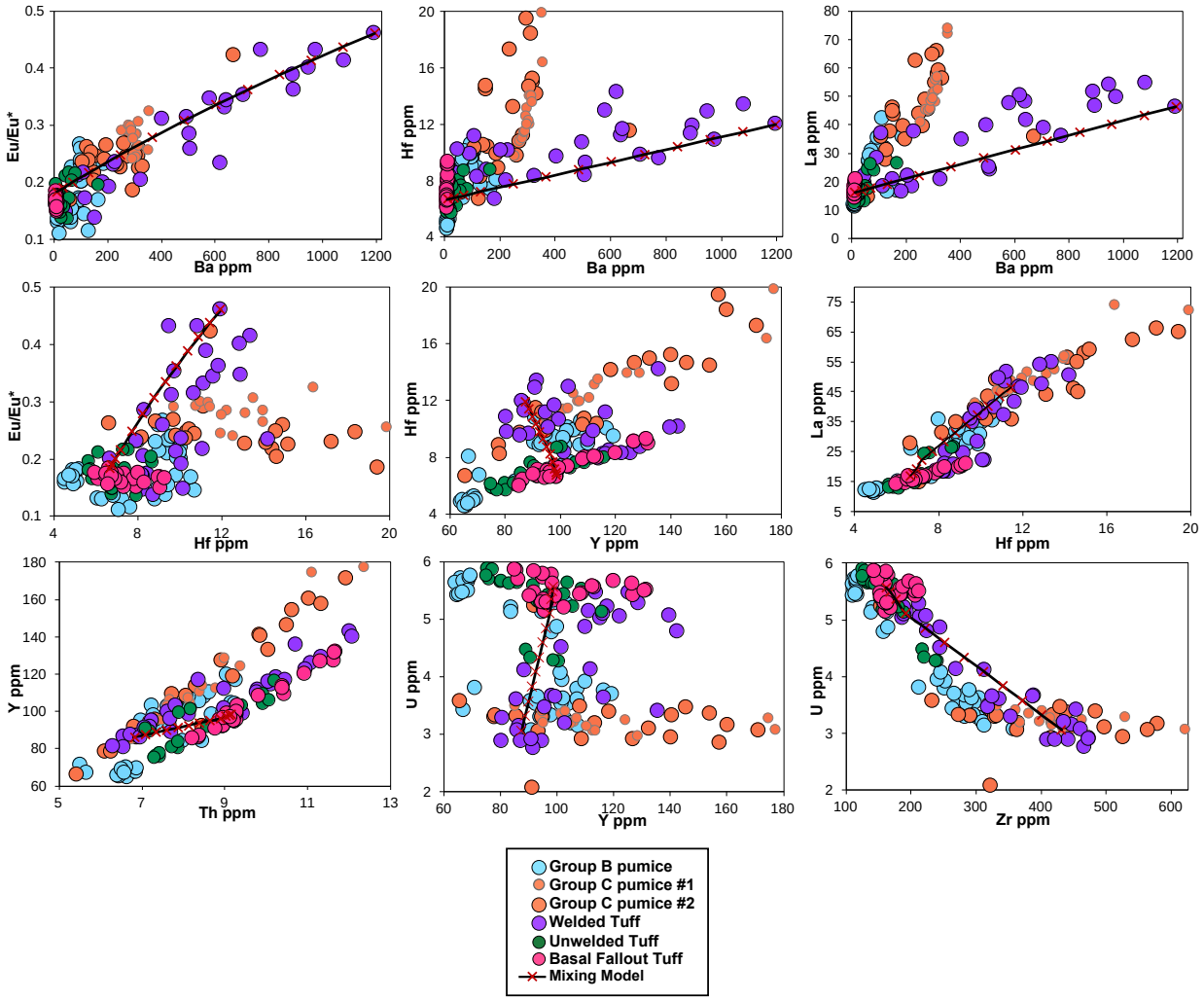

Figure 26 a-i Mixing models show that compositional trends between glass from pumice and tuff samples can be explained by mixing of a high Ba/low U magma with a low Ba/high U magma.

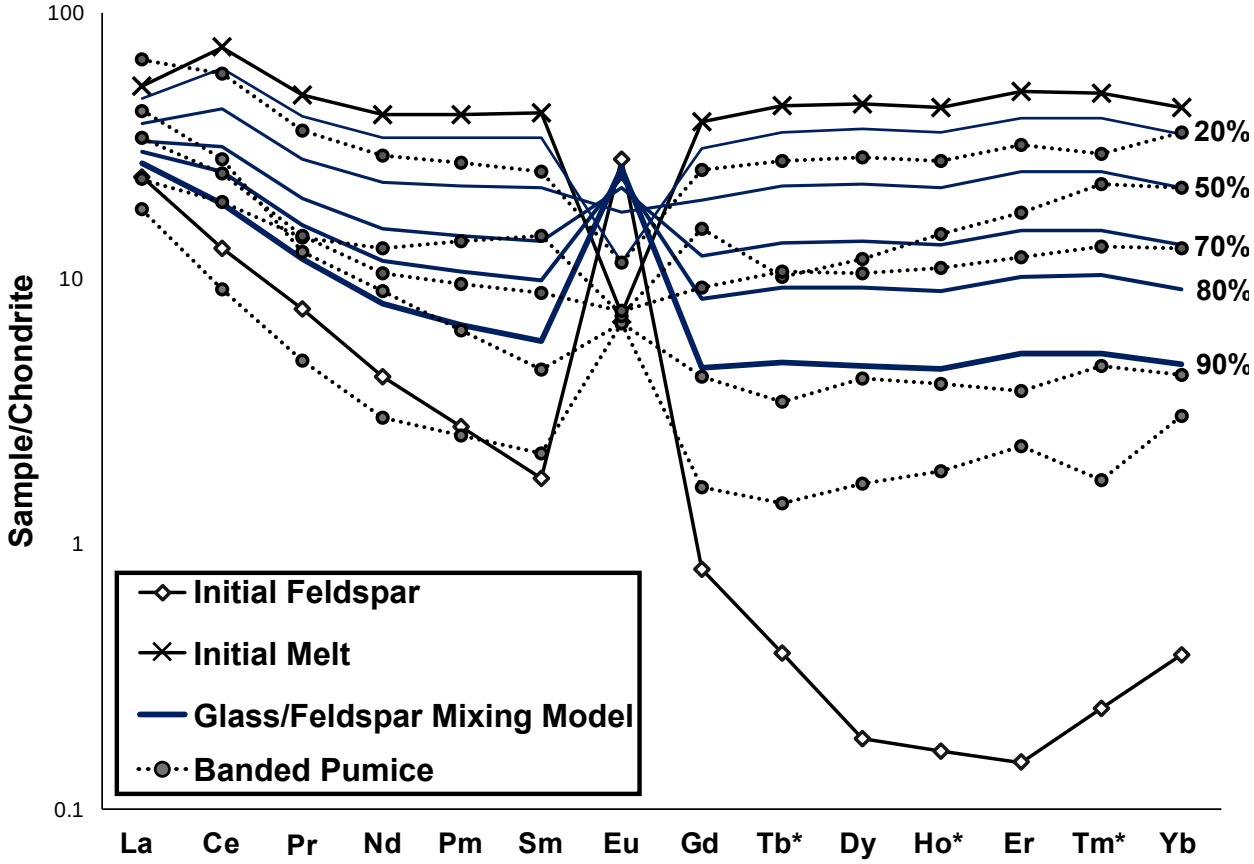

Figure 27 RST glass and feldspar melt mixing model with REE data from banded pumice feldspar grain and unwelded tuff glass.

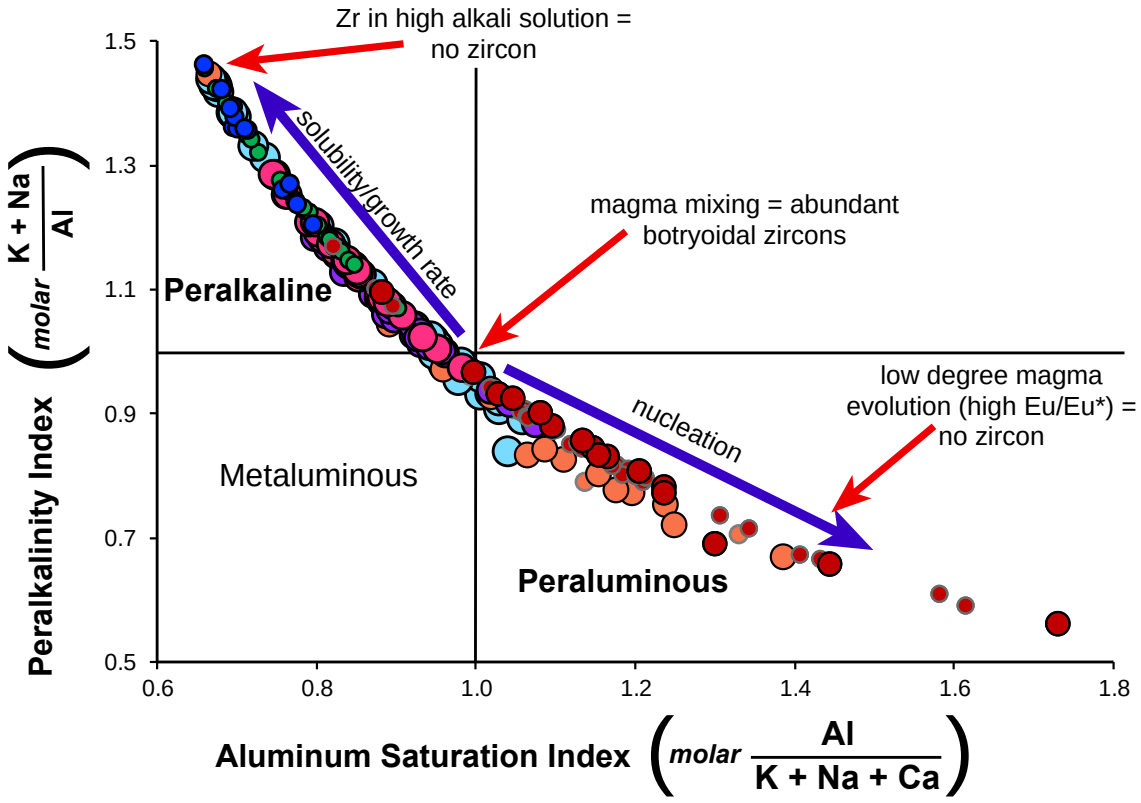

Figure 28 Peralkalinity and Aluminum Saturation indices for RST glasses. Increasing peralkalinity promotes zircon solubility and increases crystal growth rate once saturation is reached (Watson 1979), while greater concentrations of aluminum inhibits crystal growth, but promotes nucleation (Rustad 2015). Magma mixing can promote both rapid nucleation and growth (Hort 1998). Complex botryoidal RST zircon crystals may have resulted from mixing of peralkaline and peraluminous liquids in the RST magma system.

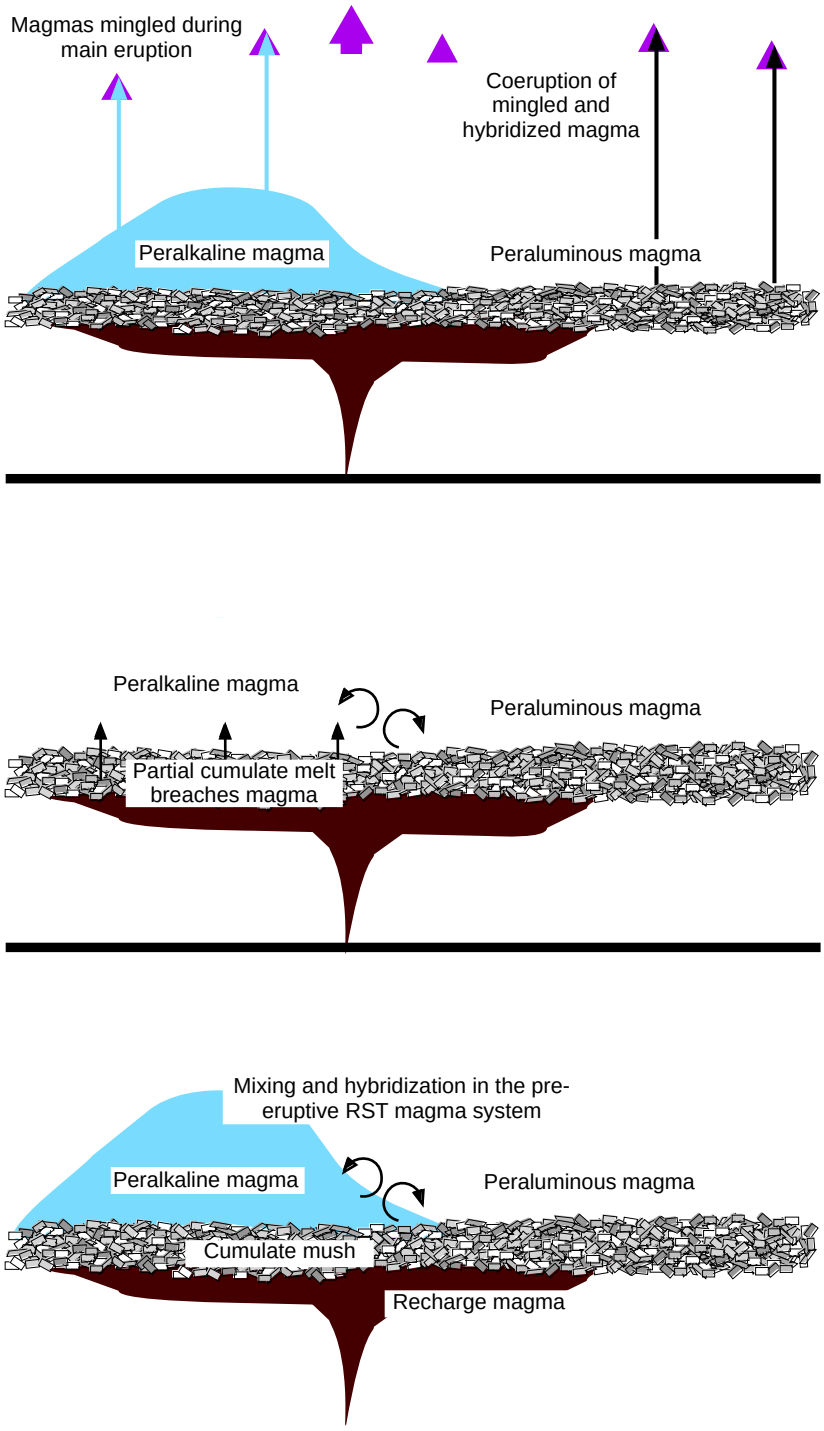

Figure 29 **Time steps of mixing, hybridizing, eruption, and mingling of magmas in the RST system.**

APPENDIX B

Tables

Table 1 Pb isotopic compositions for Picture Gorge Ignimbrite (PGI) sanidine.

Analysis	Isotope ratios									
	$^{208}Pb/^{206}Pb$	±1s (abs)	$^{207}Pb/^{206}Pb$	±1s (abs)	$^{208}Pb/^{204}Pb$	±1s (abs)	$^{207}Pb/^{204}Pb$	±1s (abs)	$^{206}Pb/^{204}Pb$	±1s (abs)
AL051209 L4	2.032167	0.000146	0.818689	0.000060	38.7470	0.0156	15.61329	0.00614	19.07170	0.00763
AL051209 L5	2.032690	0.000064	0.819397	0.000028	38.7668	0.0071	15.62792	0.00284	19.07204	0.00360
AL051209 L6	2.034946	0.000025	0.821095	0.000008	38.6910	0.0018	15.61170	0.00068	19.01272	0.00083
AL051209 L7	2.033729	0.000052	0.819723	0.000015	38.8055	0.0062	15.64158	0.00242	19.07949	0.00292
AL071202 L4	2.061260	0.000061	0.837210	0.000026	38.3590	0.0072	15.58106	0.00292	18.61080	0.00354
AL071202 L6	2.093453	0.000022	0.857766	0.000007	37.8619	0.0022	15.51322	0.00090	18.08596	0.00103
AL071202 L7	2.123106	0.000016	0.876175	0.000009	37.4990	0.0025	15.47538	0.00103	17.66253	0.00116
ECL091116 L4	2.037273	0.000027	0.818186	0.000009	38.8810	0.0017	15.61464	0.00065	19.08445	0.00076
ECL091116 L5	2.036084	0.000024	0.816720	0.000011	38.9203	0.0029	15.61158	0.00118	19.11536	0.00142
ECL091117 L4	2.029002	0.000016	0.816546	0.000005	38.8100	0.0012	15.61871	0.00046	19.12734	0.00054
ECL091117 L5	2.028881	0.000087	0.816724	0.000026	38.7905	0.0043	15.61516	0.00161	19.11942	0.00197
ECL091117 L6	2.029100	0.000021	0.816785	0.000004	38.7852	0.0008	15.61306	0.00024	19.11516	0.00022
ECL091117 L7	2.028228	0.000009	0.816786	0.000003	38.7370	0.0006	15.59984	0.00022	19.09919	0.00025

Table 2 PGI whole rock major element compositions determined using X-ray fluorescence

Unnormalized Major Elements (Wt %)	Zone 1		Zone 2		Zone 4	Zone 5
	ECL091116-1	ECL091116-2	ECL091117-1	ECL091117-2	AL071202	AL051209
SiO_2	71.00	71.99	65.85	66.24	62.57	12.95
TiO_2	0.21	0.19	0.24	0.26	1.00	0.06
Al_2O_3	11.69	11.83	11.71	11.64	14.24	2.52
FeO*	3.37	2.28	1.91	1.41	3.70	0.55
MnO	0.07	0.06	0.04	0.03	0.09	1.30
MgO	0.17	0.11	0.41	0.34	0.81	0.08
CaO	0.90	0.82	1.81	2.01	3.86	43.96
Na_2O	4.19	4.40	3.44	3.39	3.80	0.62
K_2O	3.20	3.15	1.44	1.45	1.80	0.41
P_2O_5	0.01	0.01	0.03	0.03	0.14	0.08
Sum	94.81	94.83	86.87	86.80	92.02	62.53
LOI %	4.30	3.74	13.09	12.92	7.47	37.08
Normalized Major Elements (Wt %):						
SiO_2	74.89	75.92	75.80	76.31	68.00	20.71
TiO_2	0.22	0.20	0.27	0.30	1.09	0.09
Al_2O_3	12.33	12.47	13.48	13.40	15.48	4.04
FeO*	3.56	2.40	2.19	1.63	4.02	0.88
MnO	0.07	0.06	0.05	0.04	0.10	2.08
MgO	0.18	0.11	0.47	0.39	0.88	0.13
CaO	0.95	0.86	2.08	2.31	4.20	70.30
Na_2O	4.42	4.64	3.96	3.91	4.13	1.00
K_2O	3.37	3.32	1.66	1.67	1.96	0.65
P_2O_5	0.02	0.01	0.03	0.03	0.16	0.12
Total	100.00	100.00	100.00	100.00	100.00	100.00

Table 3 PGI whole rock trace element compositions determined using X-ray fluorescence

Unnormalized Trace Elements (ppm)	Zone 1		Zone 2		Zone 4	Zone 5
	ECL091116-1	ECL091116-2	ECL091117-1	ECL091117-2	AL071202	AL051209
Ni	3.069	2.871	8.415	1.485	2.475	4.474614
Cr	3.168	3.564	13.365	3.465	1.98	53.8795
Sc	3.366	3.168	2.673	1.683	2.871	12.411
V	31.482	30.393	5.049	3.267	7.92	30.4365
Ba	724.581	749.826	816.255	857.637	160.182	776.2785
Rb	35.145	34.254	114.939	113.355	6.534	51.9095
Sr	148.995	164.934	37.818	40.293	48.015	254.4255
Zr	453.519	578.952	503.811	855.36	128.997	1664.1575
Y	75.24	68.904	105.336	105.831	155.133	92.2945
Nb	58.014	51.777	64.845	63.063	2.178	59.0015
Ga	21.186	18.612	25.542	26.631	4.554	22.655
Cu	3.861	5.742	16.929	4.257	7.722	10.3425
Zn	129.393	101.772	149.094	144.639	16.929	81.558
Pb	10.098	9.108	13.464	13.365	0.495	13.2975
La	71.775	58.311	73.26	73.062	8.712	55.554
Ce	145.431	124.245	149.094	147.312	24.354	114.457
Th	13.068	11.286	13.761	14.652	1.089	9.3575
Nd	71.874	61.974	75.339	71.478	12.771	57.6225
U	2.772	2.673	4.653	6.237	0.891	4.0385
Total	2006.037	2082.366	2193.642	2547.072	593.802	3368.151114

Table 4 PGI whole rock and glass trace element compositions determined using solution- and laser ablation-inductively coupled mass spectrometry (LA-ICPMS)

Whole Rock Solution ICPMS ppm Sample	La	Ce	Pr	Nd	Sm	Eu	Gd	Tb	Dy	Ho	Er	Tm	Yb	Lu
ECL091116-1	72	151	18.54	72	15.94	2.10	14.89	2.55	15.57	3.13	8.70	1.30	8.38	1.31
ECL091116-2	62	132	16.23	64	13.96	2.15	13.35	2.25	13.80	2.80	7.80	1.18	7.60	1.17
ECL091117-1	75	155	19.07	76	17.23	2.43	16.96	3.07	19.34	4.00	11.12	1.64	10.13	1.61
ECL091117-2	74	154	18.92	76	17.55	2.52	17.13	3.04	19.44	4.05	11.38	1.70	10.66	1.69
AL071202	11	21	3.04	14	5.02	0.46	8.57	2.27	19.24	5.18	15.96	2.16	10.78	1.70
AL051209	60	124	15.17	61	13.83	3.87	13.80	2.51	16.13	3.58	10.85	1.66	10.70	1.79
Glass LA-ICPMS ppm														
Spot # - PGI														
ECL091117 1	54	123	15.81	67	15.26	5.70	16.99	2.81	17.7	3.56	11.5	1.71	10.67	1.64
ECL091117 2	73	161	18.49	77	16.87	1.93	20.07	3.33	20.5	4.50	13.7	2.07	11.29	1.90
ECL091117 3	78	163	19.90	83	17.73	1.86	21.13	3.69	22.4	4.79	15.1	2.20	12.81	1.93
ECL091117 4	50	121	13.35	55	12.48	1.60	13.11	2.38	15.3	3.03	9.9	1.38	9.28	1.40
ECL091117 5	30	90	11.34	46	11.09	1.46	14.07	2.81	18.9	3.87	12.8	1.86	13.03	1.84
ECL091117 6	35	93	10.61	43	10.06	1.47	11.25	1.98	13.3	2.81	8.7	1.39	8.64	1.22
ECL091117 7	21	111	15.62	64	23.46	2.43	31.04	7.58	58.4	11.65	37.2	5.51	30.81	4.37
ECL091117 8	29	89	10.92	46	12.03	1.20	13.45	2.76	18.7	4.02	13.1	2.11	13.21	2.09
ECL091117 9	41	105	12.49	50	11.22	1.36	12.90	2.11	15.7	3.33	9.6	1.60	9.56	1.46
ECL091117 10	57	149	15.11	61	13.18	1.69	15.54	2.65	15.5	3.17	9.8	1.51	9.08	1.34
ECL091117 11	58	150	15.22	63	13.66	1.49	14.27	2.54	16.4	3.26	10.1	1.54	9.13	1.40
ECL091117 12	56	143	15.35	61	12.89	1.68	14.45	2.55	15.5	3.25	9.8	1.40	9.15	1.27
ECL091117 13	62	158	16.29	66	13.70	1.72	15.37	2.61	17.1	3.40	10.8	1.65	9.94	1.43
ECL091117 14	119	296	34.05	138	31.02	5.34	32.22	5.34	32.3	6.43	18.7	2.89	18.10	2.65
ECL091117 15	69	158	17.60	73	15.88	2.06	17.54	3.22	20.4	3.91	13.0	1.93	11.04	1.66
ECL091117 16	186	397	47.12	201	41.78	5.39	42.38	6.90	41.0	8.13	24.2	3.63	22.59	3.29
ECL091117 17	67	154	17.52	70	15.99	2.21	17.47	2.94	19.4	3.97	12.8	1.78	11.20	1.68
ECL091117 18	69	155	17.80	71	16.39	1.46	18.21	3.01	19.7	4.12	13.1	1.85	10.63	1.80
ECL091117 19	70	161	17.76	74	16.56	2.10	18.71	3.25	20.3	4.32	12.7	1.86	11.62	1.78
ECL091117 20	73	157	18.27	76	17.02	1.39	19.10	3.39	20.4	4.13	13.2	1.98	11.71	1.75

Table 4 PGI whole rock and glass trace element compositions determined using solution- and laser ablation-inductively coupled mass spectrometry (LA-ICPMS) (continued)

Whole Rock Solution ICPMS ppm Sample	Ba	Th	Nb	Y	Hf	Ta	U	Pb	Rb	Cs	Sr	Sc	Zr
ECL091116-1	739	12.76	56.9	74	13.36	3.59	2.91	10.65	33.4	7.18	150	3.28	461
ECL091116-2	775	11.19	51.0	67	15.62	3.33	2.66	8.75	33.2	7.37	167	2.92	594
ECL091117-1	844	14.30	62.1	102	14.48	3.90	4.48	13.53	110.7	4.60	38	2.73	509
ECL091117-2	874	14.42	61.7	103	21.67	3.89	4.64	13.23	108.4	4.64	41	2.17	880
AL071202	168	1.10	3.8	164	3.14	0.41	1.20	0.98	7.1	0.25	51	1.33	139
AL051209	787	9.79	56.4	94	35.75	3.11	3.30	12.95	51.0	2.12	258	12.00	1776
Glass LA-ICPMS ppm Spot # - PGI													
ECL091117 1	930	9.03	67	97	23.1	2.98	4.71	n.d.	82	3.55	176	28.57	1189
ECL091117 2	827	15.14	82	123	16.0	4.81	5.03	n.d.	133	4.91	30	8.13	556
ECL091117 3	876	16.50	83	130	17.8	5.08	4.95	n.d.	140	5.26	30	8.77	602
ECL091117 4	403	11.92	67	81	13.1	3.55	4.42	n.d.	87	4.64	14	8.25	437
ECL091117 5	198	16.09	92	84	13.8	3.90	6.72	n.d.	45	4.57	11	8.09	471
ECL091117 6	281	10.93	58	68	11.6	3.28	4.01	n.d.	65	5.16	13	8.04	403
ECL091117 7	564	22.36	204	184	13.6	5.62	29.07	n.d.	23	2.90	72	33.07	591
ECL091117 8	143	16.82	91	85	12.4	3.43	6.75	n.d.	36	4.35	10	8.28	441
ECL091117 9	324	12.76	66	80	12.9	3.78	4.29	n.d.	68	4.89	13	7.87	447
ECL091117 10	740	12.43	80	92	12.0	3.76	5.39	n.d.	92	5.40	27	8.61	421
ECL091117 11	717	11.93	79	91	11.9	4.13	5.46	n.d.	147	5.54	18	8.12	432
ECL091117 12	707	12.00	76	90	12.8	4.05	5.25	n.d.	147	5.37	19	9.09	427
ECL091117 13	720	12.49	80	97	13.0	4.22	5.58	n.d.	156	5.68	17	8.22	460
ECL091117 14	705	9.48	85	147	25.2	3.70	6.28	n.d.	44	1.15	177	21.45	1388
ECL091117 15	807	14.22	81	114	15.5	4.69	5.29	n.d.	142	5.28	22	8.83	528
ECL091117 16	686	11.91	79	191	29.0	4.02	5.23	n.d.	47	0.99	213	22.84	1559
ECL091117 17	776	13.94	79	111	15.4	4.54	4.77	n.d.	137	4.91	21	8.34	518
ECL091117 18	791	14.56	81	116	15.6	4.66	4.91	n.d.	139	5.09	23	9.07	538
ECL091117 19	826	14.80	83	118	14.8	4.56	5.34	n.d.	124	5.09	36	8.93	534
ECL091117 20	815	14.83	83	121	15.6	4.82	4.95	n.d.	123	4.94	58	8.64	558

Table 5 Standard materials trace element compositions determined using solution- and laser ablation-inductively coupled mass spectrometry (LA-ICPMS)

	La	Ce	Pr	Nd	Sm	Eu	Gd	Tb	Dy	Ho	Er	Tm	Yb	Lu
BCR Average	25	53	6.73	29	6.61	1.96	6.66	1.06	6.4	1.29	3.7	0.53	3.41	0.50
σ	0.74	1.84	0.17	1.10	0.26	0.11	0.32	0.03	0.20	0.05	0.12	0.01	0.20	0.02
BIR Average	0.63	2.11	0.41	2.39	1.07	0.54	1.82	0.33	2.40	0.50	1.58	0.25	1.56	0.24
σ	0.05	0.17	0.03	0.10	0.06	0.03	0.11	0.03	0.15	0.03	0.13	0.04	0.09	0.02
NIST 610 Average	549	520	554	558	586	534	659	687	659	683	716	720	661	665
σ	6.00	8.39	8.53	5.58	7.78	1.94	10.71	7.01	12.70	8.51	8.70	3.83	4.22	7.23
Standard Concentration	457	448	430	431	451	461	444	443	427	449	426	420	445	435
Accuracy	20%	16%	29%	30%	30%	16%	48%	55%	54%	52%	68%	71%	49%	53%
NIST 612 Average	38.1	43.2	42.1	39.5	41.4	36.8	44.3	45.9	42.4	45.3	47.6	47.8	44.8	43.9
σ	0.59	0.46	1.01	1.16	1.33	0.67	0.59	0.82	0.93	1.29	1.42	0.93	1.44	1.23
Standard Concentration	35.8	38.7	37.2	35.9	38.1	35	36.7	36	36	38	38	38	39.2	36.9
Accuracy	7%	12%	13%	10%	9%	5%	21%	27%	18%	19%	25%	26%	14%	19%

	Ba	Th	Nb	Y	Hf	Ta	U	Pb	Rb	Cs	Sr	Sc	Zr
BCR Average	674	5.90	13	35	4.9	0.73	1.69	-	47	1.10	337	34.64	184
σ	13.20	0.20	0.46	1.22	0.20	0.02	0.04	-	1.30	0.02	7.85	0.66	4.23
BIR Average	8.14	0.04	0.49	14.26	0.51	0.03	0.03	-	0.35	0.02	113	41.20	13.44
σ	1.50	0.01	0.02	0.60	0.05	0.01	0.01	-	0.19	0.02	1.91	0.77	0.31
NIST 610 Average	511	606	499	718	633	527	493	-	454	396	622	559	634
σ	7.11	9.51	8.78	10.63	5.81	6.28	6.05	-	4.26	4.99	9.10	9.05	10.50
Standard Concentration	435	457.2	419	450	432	452	462	-	425.7	361	515.5	441	440
Accuracy	18%	33%	19%	60%	47%	17%	7%	-	7%	10%	21%	27%	44%
NIST 612 Average	41.1	41.4	38.3	47.2	42.8	36.5	45.1	-	38.8	50.3	83.9	45.9	43.8
σ	0.65	0.92	0.73	1.08	0.83	0.63	1.20	-	0.56	1.32	2.78	1.43	0.74
Standard Concentration	40	37.79	40	38	35	40	37	-	31.4	42	78.4	41	38
Accuracy	3%	10%	4%	24%	22%	9%	22%	-	24%	20%	7%	12%	15%

Table 6 Lower cooling unit zone 1 PGI zircon trace element compositions determined using LA-ICPMS

	Ti-in-zircon	Concentrations (ppm)																						
Spot #	T(°C)	Eu/Eu*	P	Ti	Y	Nb	La	Ce	Pr	Nd	Sm	Eu	Gd	Tb	Dy	Ho	Er	Tm	Yb	Lu	Hf	Ta	Th	U
ECL091116 L 21	767	0.12	239	6.87	3342	12.1	0.518	16.66	0.425	7.91	14.96	1.556	99.6	32.51	377	130	516	115	1061	123	9138	4.75	138	228
ECL091116 L 23	694	0.17	1045	3.08	3228	9.7	114.289	203.41	30.835	208.22	71.36	5.274	122.5	38.17	388	127	484	107	984	111	7802	4.06	132	223
ECL091116 L 26	770	0.17	1416	7.05	4062	16.3	142.772	312.47	45.606	265.04	86.74	6.520	165.2	45.99	489	170	626	134	1290	142	7845	5.80	213	331
ECL091116 L 28	755	0.16	1105	6.03	2773	20.6	73.689	179.68	24.545	142.43	47.53	3.791	104.4	28.95	309	109	430	97	934	99	8206	7.12	124	251
ECL091116 L 29	794	0.17	364	8.93	4251	25.2	9.477	42.34	3.628	27.03	24.74	3.174	125.1	41.50	479	164	647	145	1361	150	7977	7.14	225	368
ECL091116 L 32	739	0.19	250	5.11	2357	5.4	1.858	13.28	1.246	10.62	13.98	1.899	69.3	23.29	270	91	357	81	769	88	7604	3.17	73	146
ECL091116 M 106	755	0.20	286	6.03	2657	8.4	0.980	13.14	0.936	10.20	13.58	2.084	76.9	25.08	288	100	401	90	870	92	7149	3.38	100	191
ECL091116 M 109	763	0.08	342	6.58	1884	6.1	0.156	7.87	0.132	3.23	8.99	0.561	57.2	17.24	214	78	296	66	651	75	9358	2.91	151	358
ECL091116 M 138	842	0.13	2386	14.04	4068	25.6	197.277	470.24	55.222	354.73	92.88	5.375	165.8	41.03	475	160	593	125	1177	143	7511	7.26	230	369
ECL091116 M 114	766	0.14	1232	6.81	2851	12.7	117.778	282.65	44.355	233.11	75.15	4.676	134.4	34.87	348	111	440	107	956	89	6761	4.95	132	235
ECL091116 M 115	777	0.17	300	7.58	1685	20.5	3.415	23.40	1.197	9.07	10.79	1.258	44.7	16.28	211	71	260	65	667	69	6998	6.68	113	216
ECL091116 M 117	731	0.17	305	4.66	3025	27.8	n.d.	28.02	0.411	6.02	14.13	1.970	84.1	27.48	346	120	479	96	943	104	7494	7.93	155	290
ECL091116 M 121	767	0.18	461	6.88	3990	17.7	33.571	75.82	11.589	62.29	32.61	3.849	126.2	39.79	413	140	604	133	1245	130	8107	6.28	205	335
ECL091116 M 123	737	0.16	208	5.01	3518	12.4	0.373	16.12	0.473	9.31	16.64	2.173	105.0	32.51	396	142	553	117	1098	130	8694	5.39	161	264
ECL091116 M 132	751	0.15	418	5.80	2775	36.9	16.378	66.29	5.503	32.55	22.74	2.049	80.9	28.26	344	107	396	89	926	104	6904	12.64	349	493
ECL091116 M 134	745	0.17	364	5.46	4192	12.7	6.505	33.83	2.488	22.52	23.46	3.149	139.3	42.91	441	161	736	154	1340	143	8762	5.74	198	335
ECL091116 S 213	717	0.15	841	4.01	3914	13.3	115.469	255.06	40.834	240.21	77.90	5.504	165.8	47.10	492	159	610	139	1218	137	8182	5.16	189	288
ECL091116 S 214	758	0.19	1061	6.22	2152	20.4	85.291	193.57	28.476	175.25	64.02	4.784	97.3	26.59	277	87	335	77	775	77	7773	6.75	116	228
ECL091116 S 210	786	0.13	351	8.27	3309	33.7		31.17	0.264	5.98	11.31	1.257	82.2	30.34	336	120	490	112	943	120	11282	11.92	179	289
Average	759	0.16	683	6.55	3160	17.8	54.106	119.21	15.693	96.09	38.08	3.205	107.7	32.63	363	124	487	108	1011	112	8081	6.27	168	286
σ	31	0.03	569	2.30	798	8.9	63.271	133.57	19.203	113.96	29.73	1.746	36.3	9.06	88	31	129	26	218	26	1059	2.57	62	81

Table 7 Lower cooling unit PGI zone 2 zircon trace element compositions determined using LA-ICPMS

	Ti-in-zircon		Concentrations (ppm)																				
Spot #	T(°C)	Eu/Eu*	P	Ti	Y	Nb	La	Ce	Pr	Nd	Sm	Eu	Gd	Tb	Dy	Ho	Er	Tm	Yb	Lu	Hf	Ta	Th	U
ECL091117 L 46	748	0.22	330	5.61	2627	3.9	2.319	11.27	1.194	10.66	13.92	2.412	77.6	25.51	305	103	399	94	957	101	6132	1.36	128	279
ECL091117 L 43	767	0.19	338	6.89	3312	11.9	5.211	24.21	2.369	15.80	20.98	2.910	103.9	33.51	389	130	506	113	1113	119	7299	4.50	128	242
ECL091117 L 36	783	0.42	187	8.04	1950	5.6	0.122	6.27	0.276	5.88	15.58	4.478	68.8	22.79	252	80	288	71	705	83	6735	1.72	45	96
ECL091117 L 38	753	0.20	591	5.91	2277	19.1	31.014	84.37	10.871	70.31	24.57	2.787	71.9	21.01	263	86	342	78	769	79	7463	5.91	112	224
ECL091117 L 52	775	0.24	306	7.40	2399	6.9	1.202	11.07	0.688	8.12	13.82	2.372	65.8	22.40	270	93	358	84	791	89	7126	3.19	82	166
ECL091117 L 50	773	0.14	391	7.30	2842	12.3	8.785	34.21	2.990	23.27	21.27	2.002	88.7	30.79	340	113	435	102	1041	98	7291	4.35	127	255
ECL091117 M 147	768	0.22	305	6.92	2367	7.8	2.158	12.25	0.963	11.20	12.79	2.128	69.8	22.93	271	95	370	84	832	89	6983	3.39	92	178
ECL091117 M 163	727	0.16	406	4.50	3212	10.8	21.767	61.22	7.555	51.09	27.71	2.767	104.7	32.66	373	128	491	114	1092	111	7680	4.16	145	257
ECL091117 M 159	741	0.17	401	5.23	3402	14.2	6.393	24.12	1.693	15.68	20.29	2.624	110.5	36.34	401	134	530	123	1153	120	7082	4.71	156	275
ECL091117 M 154	749	0.18	450	5.71	2114	6.7	14.841	36.53	5.209	37.45	19.39	2.148	65.1	21.27	250	83	310	74	757	78	6804	3.16	75	159
ECL091117 M 161	773	0.15	349	7.27	3840	15.1	12.158	43.67	4.367	31.81	26.06	2.679	115.0	36.93	430	148	575	128	1230	127	7473	5.11	166	294
ECL091117 S 219	762	0.16	506	6.50	2975	11.7	19.678	55.40	6.357	43.26	22.94	2.341	86.4	29.13	333	117	454	103	994	108	8374	4.29	125	231
ECL091117 S 220	731	0.18	211	4.69	3123	10.2	0.063	14.17	0.508	8.81	16.39	2.362	93.1	30.14	360	120	471	107	1011	113	8111	3.78	133	242
ECL091117 S 222	734	0.14	291	4.82	2654	15.7	5.069	25.90	1.725	15.21	15.52	1.645	78.9	24.82	287	104	407	90	819	99	8168	6.26	155	253
ECL091117 S 224	741	0.16	328	5.21	4420	17.3	1.314	23.75	0.676	12.24	21.11	2.705	124.6	42.78	517	174	695	153	1353	161	8757	5.50	223	335
ECL091117 S 244	758	0.18	201	6.22	1867	4.7	0.061	5.68	0.084	4.77	11.02	1.374	49.1	16.79	193	69	265	62	579	75	8357	2.72	56	110
ECL091117 S 246	758	0.15	363	6.26	2915	26.5	0.749	25.54	0.574	7.86	15.40	1.746	81.6	29.55	344	121	458	109	979	114	7857	8.66	186	310
ECL091117 S 249	783	0.15	492	8.08	3217	37.3	14.134	62.45	4.864	33.21	21.34	2.238	98.3	31.27	369	127	485	112	1073	115	7897	11.36	350	470
ECL091117 S 245	786	0.38	379	8.33	6714	18.7	1.446	19.58	1.077	22.99	48.81	13.310	231.8	73.66	825	277	1029	211	1875	221	6561	3.71	259	308
ECL091117 S 231	715	0.12	999	3.93	5598	17.1	66.100	152.45	21.918	136.96	52.73	3.626	176.0	52.62	610	219	848	162	1358	221	10481	5.33	290	343
ECL091117 S 228	749	0.15	710	5.67	4050	14.1	43.427	104.50	14.430	87.26	36.39	3.237	120.9	40.37	457	161	621	125	1063	175	10179	4.37	192	254
Average	758	0.19	406	6.21	3232	13.7	12.286	39.93	4.304	31.14	22.76	3.042	99.2	32.25	373	128	492	110	1026	119	7753	4.64	154	252
σ	20	0.08	185	1.25	1191	7.8	16.826	36.76	5.525	32.72	11.01	2.450	41.1	12.71	142	49	185	34	283	42	1082	2.21	76	84

Table 8 Upper cooling unit PGI zone 4 zircon trace element compositions determined using LA-ICPMS

	Ti-in-zircon	Concentrations (ppm)																						
Spot #	T(°C)	Eu/Eu*	P	Ti	Y	Nb	La	Ce	Pr	Nd	Sm	Eu	Gd	Tb	Dy	Ho	Er	Tm	Yb	Lu	Hf	Ta	Th	U
AL071202 L 60	752	0.17	232	5.86	2909	7.9	0.284	10.90	0.296	8.05	16.00	1.985	83.4	27.75	326	112	442	97	914	108	8859	3.62	102	182
AL071202 L 61	782	0.21	175	7.99	2594	5.0	0.112	7.62	0.338	6.88	15.20	2.235	71.4	25.70	292	101	396	88	814	98	8516	2.53	78	141
AL071202 L 57	727	0.19	308	4.46	3120	9.2	10.429	31.01	3.832	27.62	17.82	2.613	95.1	28.53	355	122	476	102	951	113	8856	3.76	132	206
AL071202 M 170	736	0.16	346	4.94	3541	14.9	5.106	29.38	2.413	18.18	18.56	2.364	108.3	35.23	404	142	536	125	1169	126	7624	5.22	166	297
AL071202 M 173	757	0.20	393	6.18	2207	7.2	8.331	25.97	2.876	22.63	20.27	2.376	68.1	22.89	260	90	345	79	786	84	7595	3.33	85	170
AL071202 M 174	780	0.22	263	7.84	1938	19.9	0.036	16.42	0.250	4.10	6.51	1.271	47.6	15.82	194	68	283	64	615	74	7888	6.67	129	209
AL071202 M 182	771	0.15	393	7.16	2522	18.4	6.495	34.15	2.699	19.14	18.22	1.922	82.6	26.60	302	101	381	91	860	87	6133	6.35	171	298
AL071202 M 186	695	0.15	304	3.12	3959	16.9	2.793	28.34	1.450	15.13	24.98	2.630	119.5	41.90	485	158	596	142	1366	135	6777	5.57	230	369
AL071202 M 188	772	0.20	644	7.23	3488	13.7	22.288	55.02	7.121	47.57	31.89	3.942	119.7	37.42	438	149	533	122	1177	121	6748	4.33	137	252
AL071202 M 184	803	0.28	389	9.76	4222	13.9	2.311	15.04	1.314	16.74	29.85	6.057	147.3	47.28	537	180	665	149	1510	153	6323	4.35	184	285
AL071202 S 259	744	0.14	1056	5.37	4279	14.9	78.758	186.51	25.445	161.57	53.84	4.033	153.4	44.46	490	172	668	142	1272	155	8984	5.82	205	313
AL071202 S 265 1	775	0.15	268	7.40	3840	9.2	11.156	35.19	3.956	28.46	18.71	2.130	103.4	33.95	393	136	595	126	944	135	10753	3.94	157	234
AL071202 S 269	750	0.14	444	5.74	4856	25.8	8.356	47.90	3.175	27.85	25.10	2.573	132.7	43.57	526	189	751	155	1285	196	10310	8.44	290	359
Average	757	0.18	401	6.39	3344	13.6	12.035	40.27	4.243	31.07	22.84	2.779	102.5	33.16	385	132	513	114	1051	122	8105	4.92	159	255
σ	28	0.04	229	1.75	883	5.9	20.957	46.02	6.645	40.84	11.41	1.240	31.8	9.53	108	37	140	29	264	34	1448	1.62	60	72

Table 9 Upper cooling unit PGI zone 5 zircon trace element compositions determined using LA-ICPMS

	Ti-in-zircon	Concentrations (ppm)																						
Spot #	T(°C)	Eu/Eu*	P	Ti	Y	Nb	La	Ce	Pr	Nd	Sm	Eu	Gd	Tb	Dy	Ho	Er	Tm	Yb	Lu	Hf	Ta	Th	U
AL051209 L 1	768	0.19	255	6.91	2769	12.3	1.822	14.79	0.848	8.14	12.24	1.802	72.5	25.39	290	106	423	90	817	109.6752523	10078	4.82	114	180
AL051209 L 7	736	0.09	558	4.93	11074	9.8	0.192	45.43	1.396	29.76	68.30	4.687	341.0	114.00	1277	439	1753	380	3489	416	7644	2.38	1152	1203
AL051209 L 8	798	0.36	247	9.33	3459	10.5	0.293	8.81	0.471	14.77	25.63	6.873	133.0	41.34	442	145	537	117	1110	132	7229	2.87	93	148
AL051209 L 4	795	0.23	264	9.02	1422	8.0	0.136	8.70	0.263	3.84	5.55	1.076	36.0	12.74	147	54	227	53	499	64	8480	3.50	68	135
AL051209 L 11	676	0.15	476	2.48	2922	20.6	13.757	50.99	4.798	31.97	19.08	2.045	86.7	26.17	316	113	447	99	938	111	8667	6.71	137	236
AL051209 L 14	810	0.22	270	10.41	4302	19.3	0.339	14.23	0.668	12.60	23.22	4.114	141.7	45.33	507	171	656	142	1290	157	7695	5.15	141	225
AL051209 L 16	779	0.18	362	7.75	4454	14.2	7.036	28.51	2.924	24.67	23.77	3.393	136.7	43.17	494	171	673	148	1275	164	9209	4.72	173	270
AL051209 M 69	718	0.16	265	4.04	2833	13.9	0.758	17.91	0.506	9.04	18.08	2.095	86.6	30.50	352	123	457	104	1004	98	6853	4.87	133	246
AL051209 M 73	757	0.19	301	6.15	2789	10.9	0.459	14.01	0.437	8.45	16.21	2.413	89.0	29.89	337	109	431	100	978	101	7152	4.45	110	215
AL051209 M 74	785	0.19	271	8.19	2710	19.8	0.315	18.88	0.311	5.62	12.91	1.887	74.7	25.75	326	106	416	98	981	99	7624	7.03	126	257
AL051209 M 70	807	0.26	326	10.14	2727	7.9	5.655	18.95	2.275	18.48	20.83	3.962	101.0	29.92	317	104	400	90	914	94	6230	3.08	90	159
AL051209 M 72	804	0.24	830	9.83	2603	6.7	12.835	31.23	3.759	22.19	19.36	3.037	75.5	25.39	295	100	385	92	943	101	6211	2.60	221	364
AL051209 M 97	743	0.16	308	5.34	3372	12.6	12.027	38.83	4.069	28.22	22.91	2.560	98.7	32.97	383	129	481	108	1071	113	7394	4.37	147	269
AL051209 M 89	803	0.15	509	9.81	3801	31.4	13.162	57.87	6.316	35.97	30.97	3.122	122.9	45.25	508	168	604	135	1340	135	6681	9.11	273	419
AL051209 M 78	777	0.19	221	7.61	1521	13.9	n.d.	13.67	0.120	2.39	7.18	1.027	36.3	12.07	156	59	236	54	537	64	8390	5.27	80	172
AL051209 M 82	801	0.36	243	9.60	5062	10.4	0.284	10.87	0.599	12.99	31.89	8.535	162.5	51.24	571	195	738	155	1384	177	7886	2.88	162	215
AL051209 M 84	811	0.20	314	10.59	4481	16.2	2.162	15.81	1.130	16.66	27.32	4.092	143.2	43.74	481	165	650	134	1227	159	8609	4.76	149	223
Average	774	0.21	354	7.77	3665	14.0	4.452	24.09	1.817	16.81	22.67	3.336	114.0	37.35	423	144	560	123	1165	135	7766	4.62	198	290
σ	37.79	0.07	157	2.45	2151	6.10	5.450	15.43	1.884	10.40	13.91	1.978	68.8	22.71	250	85	340	72	649	79	1046	1.77	251	246

Table 10 Trace element standard materials compositions determined using LA-ICPMS

	Concentrations (ppm)																				
	P	Ti	Y	Nb	La	Ce	Pr	Nd	Sm	Eu	Gd	Tb	Dy	Ho	Er	Tm	Yb	Lu	Hf	Ta	Th	U
NIST 610 Average	346	437	450	421	459	448	433	431	452	463	444	443	428	451	427	422	447	435	429	454	457	461
σ	17.5	3.2	8.0	4.5	7.1	5.5	7.4	6.9	4.7	5.4	13.9	9.8	5.9	5.8	11.4	4.2	8.7	10.2	7.9	7.6	5.6	4.9
Standard Concentration	343	434	450	419	457	448	430	431	451	461	444	443	427	449	426	420	445	435	432	452	457.2	462
Accuracy	1.0%	0.6%	0.1%	0.5%	0.4%	0.1%	0.7%	0.0%	0.2%	0.4%	0.0%	0.1%	0.2%	0.4%	0.3%	0.6%	0.5%	0.1%	0.6%	0.4%	0.0%	0.1%
NIST 612 Average	34.7	36.0	33.4	33.2	34.9	38.1	35.6	33.4	35.0	34.9	34.1	33.7	31.4	33.7	31.3	31.6	35.1	33.1	32.6	34.6	35.0	37.6
σ	10.0	1.1	1.5	1.4	0.9	2.7	1.7	2.6	0.9	1.6	2.6	1.9	1.4	1.2	2.1	1.9	2.1	1.1	1.5	2.0	0.9	1.0
Standard Concentration	51	44	38	40	35.8	38.7	37.2	35.9	38.1	35	36.7	36	36	38	38	38	39.2	36.9	35	40	37.79	37
Accuracy	32%	18%	12%	17%	2%	2%	4%	7%	8%	0%	7%	6%	13%	11%	18%	17%	11%	10%	7%	13%	7%	2%

Table 11 PGI single zircon U-Pb CA-IDTIMS isotopic compositions and dates

	Compositional Parameters						Radiogenic Isotope Ratios						Isotopic Dates	
Sample	$\frac{Th}{U}$	$^{206}Pb^*$ x10^{-13} mol	mol % $^{206}Pb^*$	$\frac{Pb^*}{Pb_c}$	Pb_c (pg)	$\frac{^{206}Pb}{^{204}Pb}$	$\frac{^{208}Pb}{^{206}Pb}$	$\frac{^{207}Pb}{^{206}Pb}$	% err	$\frac{^{206}Pb}{^{238}U}$	% err	corr. coef.	$\frac{^{206}Pb}{^{238}U}$	±
(a)	(b)	(c)	(c)	(c)	(c)	(d)	(e)	(e)	(f)	(e)	(f)		(g)	(f)
ECL091116	*Lower Cooling Unit*													
z3	0.471	0.1021	94.71%	5.34	0.47	341	0.151	0.046529	1.404	0.004519	0.150	0.724	**29.064**	**0.043**
z4	0.426	0.0456	91.17%	3.04	0.37	204	0.137	0.046428	3.016	0.004515	0.236	0.664	**29.038**	**0.068**
z2	0.497	0.2340	98.00%	14.71	0.40	904	0.160	0.045720	0.576	0.004513	0.088	0.681	**29.028**	**0.025**
ECL091117														
z6	0.597	0.0596	91.40%	3.26	0.47	210	0.192	0.044220	2.975	0.004498	0.233	0.670	28.929	0.067
z3	0.720	0.1025	90.35%	2.99	0.91	189	0.231	0.045989	1.984	0.004566	0.191	0.730	29.367	0.056
z2	0.543	0.3866	97.80%	13.53	0.72	825	0.175	0.046661	0.488	0.004519	0.084	0.699	**29.067**	**0.024**
z1	0.486	0.3337	97.58%	12.07	0.69	749	0.156	0.046426	0.589	0.004519	0.088	0.710	**29.068**	**0.025**
z7	0.556	0.1253	96.93%	9.63	0.33	588	0.179	0.046559	0.935	0.004519	0.111	0.704	**29.066**	**0.032**
z5	0.415	0.0927	91.56%	3.19	0.71	215	0.133	0.045947	1.963	0.004512	0.190	0.740	**29.019**	**0.055**
z8	0.487	0.0617	92.33%	3.60	0.43	235	0.157	0.046143	2.506	0.004513	0.209	0.664	**29.024**	**0.061**
z9	0.513	0.1115	95.45%	6.31	0.44	396	0.165	0.046451	1.248	0.004512	0.136	0.723	**29.024**	**0.040**
AL071202	*Upper Cooling Unit*													
z1	0.404	0.2107	94.65%	5.19	0.98	341	0.130	0.046790	0.844	0.004528	0.109	0.731	29.126	0.032
z4	0.532	0.1785	97.91%	14.22	0.32	865	0.171	0.046746	0.556	0.004522	0.093	0.659	**29.083**	**0.027**
z2	0.498	0.2231	97.72%	12.87	0.43	792	0.160	0.046595	0.614	0.004521	0.093	0.677	**29.077**	**0.027**
z3	0.477	0.2291	97.40%	11.18	0.51	694	0.154	0.046447	0.654	0.004518	0.092	0.724	**29.058**	**0.027**
AL051209														
z2	0.339	0.1584	97.04%	9.41	0.40	609	0.109	0.046600	0.769	0.005856	0.104	0.693	37.639	0.039
z10	0.468	0.4315	99.02%	30.22	0.35	1850	0.151	0.046666	0.308	0.004678	0.075	0.666	30.088	0.023
z5	0.469	0.1904	97.19%	10.28	0.46	641	0.151	0.046598	0.801	0.004589	0.101	0.714	29.517	0.030
z12	0.609	0.1894	92.92%	4.08	1.19	259	0.196	0.046517	1.045	0.004549	0.128	0.709	29.259	0.037
z1	0.403	0.0854	94.36%	4.88	0.42	320	0.130	0.045570	1.481	0.004536	0.151	0.758	29.176	0.044
z9	0.489	0.1063	95.43%	6.25	0.42	395	0.157	0.046288	1.306	0.004520	0.144	0.693	**29.069**	**0.042**
z3	0.432	0.1289	95.65%	6.47	0.49	414	0.139	0.045750	1.184	0.004518	0.131	0.721	**29.057**	**0.038**
z11	0.440	0.0888	95.11%	5.74	0.38	369	0.142	0.046176	1.561	0.004517	0.148	0.693	**29.050**	**0.043**
z4	0.546	0.1298	97.05%	10.00	0.33	612	0.176	0.046478	0.814	0.004516	0.102	0.731	**29.046**	**0.029**
z6	0.529	0.0747	92.45%	3.70	0.51	239	0.170	0.046387	2.289	0.004512	0.214	0.694	**29.018**	**0.062**
z8	0.410	0.0741	94.79%	5.33	0.34	347	0.132	0.046367	1.499	0.004511	0.148	0.730	**29.014**	**0.043**
z7	0.502	0.0841	95.42%	6.25	0.34	394	0.161	0.045555	1.411	0.004510	0.145	0.698	**29.008**	**0.042**

(a) z1, z2 etc. are labels for single zircon grains or fragments annealed and chemically abraded after Mattinson (2005). **Bold** analyses are used in weighted mean age.
(b) Model Th/U ratio iteratively calculated from the radiogenic 208Pb/206Pb ratio and 206Pb/238U age.
(c) Pb* and Pbc represent radiogenic and common Pb, respectively; mol % $^{206}Pb^*$ with respect to radiogenic, blank and initial common Pb.
(d) Measured ratio corrected for spike and fractionation only. Fractionation estimated at 0.18 +/- 0.03 %/a.m.u. for Daly analyses, based on analysis of NBS-981 and NBS-982.

(e) Corrected for fractionation, spike, and common Pb; up to 1 pg of common Pb was assumed to be procedural blank: 206Pb/204Pb = 18.042 ± 0.61%; 207Pb/204Pb = 15.537 ± 0.52%; $208Pb/_{204Pb}$ = 37.686 ± 0.63% (all uncertainties 1-sigma).
Excess over blank was assigned to initial common Pb, using the Stacey and Kramers (1975) two-stage Pb isotope evolution model at the nominal sample age.
(f) Errors are 2-sigma, propagated using the algorithms of Schmitz and Schoene (2007).

Table 12 Rattlesnake Tuff (RST) whole pumice major element compositions determined via X-ray fluorescence

	RST-1-1	RST-1-2	RST-1-3	RST-2-1	RST-2-2	RST-2-3	RST-2-4	RST-2-5	RST-3-1	RST-3-2	RST-3-3	RST-4-4
	Unnormalized ME (Wt %):											
SiO2	73.61	74.17	72.46	71.76	72.39	73.94	70.81	70.58	59.81	63.32	61.25	66.43
TiO2	0.145	0.118	0.147	0.108	0.113	0.143	0.106	0.119	0.628	0.973	0.645	0.574
Al2O3	11.91	11.65	12.07	11.48	10.96	11.45	10.75	10.99	11.45	13.21	11.30	12.37
FeO*	1.82	1.34	1.91	1.27	1.35	1.58	1.12	1.28	4.61	6.32	4.09	4.05
MnO	0.100	0.096	0.109	0.067	0.079	0.086	0.075	0.057	0.182	0.213	0.137	0.121
MgO	0.10	0.13	0.12	1.30	0.35	0.09	0.39	0.26	1.02	1.76	1.12	0.83
CaO	0.27	0.22	0.25	0.54	0.82	0.39	1.19	1.70	3.13	3.32	2.98	1.79
Na2O	3.03	2.54	2.33	2.20	3.20	3.30	3.30	2.52	4.93	3.51	4.04	3.25
K2O	5.39	5.74	5.62	5.63	5.26	4.89	5.86	5.68	4.04	3.12	5.32	4.68
P2O5	0.025	0.029	0.031	0.008	0.153	0.055	0.123	0.043	0.309	0.456	0.352	0.272
Sum	96.41	96.04	95.03	94.36	94.68	95.93	93.71	93.23	90.11	96.20	91.24	94.38
LOI (%)	3.31	3.57	3.97	5.66	4.60	3.08	5.64	5.73	8.92	3.27	7.29	5.02
	Normalized ME (Wt %):											
SiO2	76.35	77.23	76.25	76.04	76.46	77.08	75.56	75.70	66.37	65.82	67.13	70.39
TiO2	0.150	0.123	0.155	0.114	0.120	0.150	0.113	0.128	0.697	1.012	0.707	0.608
Al2O3	12.36	12.13	12.70	12.17	11.58	11.93	11.47	11.79	12.71	13.73	12.39	13.11
FeO*	1.89	1.40	2.01	1.35	1.43	1.65	1.19	1.38	5.12	6.57	4.49	4.29
MnO	0.104	0.100	0.115	0.071	0.083	0.090	0.080	0.061	0.202	0.222	0.150	0.128
MgO	0.11	0.14	0.12	1.37	0.37	0.09	0.41	0.28	1.13	1.83	1.23	0.88
CaO	0.28	0.23	0.26	0.58	0.87	0.40	1.27	1.83	3.47	3.45	3.27	1.90
Na2O	3.14	2.65	2.45	2.33	3.38	3.44	3.52	2.70	5.48	3.65	4.42	3.44
K2O	5.59	5.98	5.91	5.97	5.56	5.10	6.25	6.09	4.48	3.25	5.83	4.96
P2O5	0.026	0.030	0.032	0.009	0.161	0.057	0.131	0.047	0.343	0.474	0.385	0.288
Total	100	100	100	100	100	100	100	100	100	100	100	100

* Total Fe expressed as FeO, major elements are normalized on a volatile free basis

Table 13 RST whole pumice trace element compositions determined via X-ray fluorescence

	RST-1-1	RST-1-2	RST-1-3	RST-2-1	RST-2-2	RST-2-3	RST-2-4	RST-2-5	RST-3-1	RST-3-2	RST-3-3	RST-4-4
	Unnormalized TE (ppm)											
Ni	3	3	4	3	1	3	1	1	6	17	7	8
Cr	4	4	4	2	3	5	3	4	13	26	15	15
Sc	5	4	4	4	4	4	4	4	16	21	14	12
V	1	3	4	16	4	4	8	7	37	72	47	39
Ba	1306	250	1324	109	492	469	168	151	1702	1646	1218	1478
Rb	66	90	68	94	82	78	89	96	54	53	59	65
Sr	17	11	21	22	32	16	51	87	189	141	146	80
Zr	410	291	419	275	310	327	255	271	501	460	340	403
Y	88	102	82	96	87	88	92	93	74	78	72	73
Nb	24.3	29.5	24.9	29.0	25.2	25.8	27.9	27.9	21.8	21.9	21.1	22.7
Ga	20	20	20	19	19	19	18	18	18	20	18	19
Cu	9	5	9	6	4	6	7	7	15	20	11	11
Zn	89	82	85	93	92	108	84	83	125	146	108	118
Pb	14	11	11	17	11	10	11	9	17	36	16	16
La	62	39	55	35	47	49	32	41	37	41	38	41
Ce	127	91	127	90	105	107	81	86	83	92	82	91
Th	7	8	7	9	7	6	8	8	4	5	5	7
Nd	66	49	64	45	53	57	42	46	48	54	46	52
U	2	4	1	3	3	3	3	2	1	3	2	4
sum tr.	2319	1098	2333	965	1381	1386	984	1041	2961	2951	2264	2555

Table 14 Trace and major element compositions of RST glass shards from pumice and tuff samples determined using LA-ICPMS

Spot #	*RST glass analysis (ppm)*																		
Group B Pumice RST-2-1	Na	Mg	Al	K	Ca	V	Mn	Fe	Co	Zn	Rb	Sr	Cs	Ba	Ti	Y	Zr	Nb	La
1	32955	225	65636	40924	1748	0.17	627	6370	n.d.	85.1	109	4.19	4.56	24.3	728.2	98.4	158.5	41.11	16.7
2	24807	2045	68892	50692	3279	1.52	500	8618	0.15	93.3	98	5.30	3.39	102.8	670.6	103.0	304.3	32.88	34.7
3	28165	3302	69530	43552	3311	10.15	609	10387	0.35	91.7	97	13.15	3.24	104.2	679.7	105.1	310.1	32.86	35.3
4	28661	113	65184	42759	2015	n.d	564	9271	0.03	96.9	100	2.26	3.27	95.6	658.5	102.5	293.9	33.48	33.4
5	26516	1745	69058	47022	2625	3.92	529	9333	0.13	86.3	99	6.44	3.41	97.6	667.4	107.9	314.0	31.60	35.5
6	31693	164	64548	41512	1886	0.24	594	8059	0.06	94.8	108	3.46	3.79	64.2	657.7	102.1	242.0	35.34	27.0
7	31254	171	64847	41688	1998	0.12	610	7761	n.d.	96.0	109	3.09	3.46	64.9	667.6	101.4	246.5	36.20	27.4
8	26430	2761	73203	49532	2942	8.99	577	9307	0.16	76.0	108	8.14	3.68	73.7	723.0	116.8	289.9	35.26	30.8
9	29686	1728	72316	47312	2634	6.42	592	8844	0.19	82.4	112	6.78	3.57	67.2	724.4	119.7	266.9	36.08	29.4
10	32138	172	69202	41511	1811	0.12	622	8133	0.01	96.6	107	3.14	3.61	65.9	699.8	107.5	253.0	36.61	27.9
11	33243	182	68853	41458	1860	0.13	632	8092	n.d.	97.8	110	2.90	3.60	69.6	714.5	110.2	254.3	37.29	28.6
12	25097	12726	72600	45461	6696	48.11	725	15479	0.91	85.7	111	34.30	4.11	69.2	772.6	104.2	280.5	35.81	27.3
13	28386	588	62804	44789	2384	0.75	526	8517	0.10	82.4	91	1.44	3.19	99.3	619.7	94.4	283.3	30.80	33.0
14	31423	143	67617	41436	2500		633	9228	0.07	103.3	105	0.57	3.26	109.4	696.9	107.5	304.9	35.30	36.4
15	31706	130	63458	40150	2525	0.13	615	8879	0.02	105.7	102	0.51	3.05	101.1	656.0	101.7	297.9	33.11	35.1
16	31676	209	63317	41595	1957	0.34	618	5756	0.15	90.9	105	5.98	4.56	166.6	727.2	100.4	165.7	37.60	16.8
17	31938	224	66734	44745	1794	0.29	607	6236	0.08	92.2	111	6.21	4.54	132.7	757.8	103.7	166.4	42.00	16.5
18	26073	4372	66782	50199	3220	12.37	543	11656	0.38	98.5	103	14.61	3.56	113.2	708.8	91.2	358.5	29.29	42.2
19	30392	644	62347	45856	2384	0.25	585	9403	0.04	102.4	97	1.95	3.45	95.8	668.9	90.9	274.3	32.34	30.8
20	27226	2614	66934	49433	2912	2.33	564	9335	0.02	85.0	98	7.26	3.43	100.4	677.0	97.9	297.1	33.31	32.8
21	33104	210	57246	43465	1793	0.29	602	6136	0.06	88.3	108	2.01	4.62	18.3	729.8	83.9	142.4	40.79	14.9
22	33893	212	58957	42580	1831	0.28	606	5830	0.05	94.2	110	2.27	4.79	16.5	722.8	84.0	140.3	39.10	14.6
23	30045	5529	60117	46996	6341	16.46	743	12902	0.30	110.5	112	46.89	3.57	123.2	746.7	92.7	285.9	34.00	31.6
24	33559	129	53787	45208	1913	0.07	579	9525	0.04	119.5	116	2.66	3.46	67.6	654.0	71.1	213.1	32.66	25.9
25	36382	218	52155	45312	2218	0.30	601	6242	0.02	101.0	119	1.16	4.90	12.1	706.5	67.6	114.4	39.31	12.0
26	34485	178	52173	45826	2184	0.28	608	6094	n.d.	97.4	118	1.15	5.03	9.3	711.5	66.2	113.6	38.89	12.1
27	35655	193	50756	44611	2018	0.40	583	6080	0.11	100.1	115	1.00	5.12	9.6	707.3	64.4	111.3	37.71	11.4
28	35327	192	50225	43953	2232	0.30	583	6089	n.d.	96.3	117	1.17	5.01	10.4	697.4	64.9	111.4	38.31	11.3
29	35146	209	50494	44547	2116	0.21	570	5902	0.04	94.6	119	0.96	4.77	9.8	667.3	65.7	117.4	38.05	11.9
30	34374	192	51402	44645	2263	0.19	594	6183	0.06	95.5	117	1.12	4.93	9.7	689.4	68.5	116.5	39.40	12.2
31	34269	206	53659	45261	2184	0.35	604	6253	0.00	101.3	117	1.24	4.98	12.6	731.2	67.1	117.5	39.54	12.1

Table 14 Trace and major element compositions of RST glass shards from pumice and tuff samples determined using LA-ICPMS (continued)

Spot #	*RST glass analysis (ppm)*																
Group B Pumice RST-2-1	Ce	Pr	Nd	Sm	Eu	Gd	Tb	Dy	Ho	Er	Tm	Yb	Lu	Hf	Ta	Th	U
1	46.2	5.62	24.8	6.96	0.37	12	2.05	15.88	3.37	10.7	1.61	10.94	1.9	7.3	2.4	8.69	5
2	80.6	10.47	41.6	12.09	0.91	15	2.89	17.92	3.49	10.5	1.63	9.79	1.8	10.1	1.7	7.25	3
3	80.1	10.38	45.5	11.95	0.90	15	2.89	18.16	3.78	10.6	1.68	10.15	1.8	9.9	2.1	8.41	3
4	84.7	10.12	42.4	11.97	0.74	15	2.68	16.68	3.51	10.6	1.57	10.72	1.7	9.8	2.0	7.62	4
5	78.0	10.09	45.8	12.59	0.76	16	2.82	17.83	3.81	10.6	1.75	10.87	1.7	10.6	1.9	8.14	3
6	71.5	8.29	36.9	10.64	0.53	14	2.68	16.67	3.67	10.9	1.70	11.18	1.8	8.9	2.3	7.85	4
7	71.5	8.40	35.3	11.72	0.57	14	2.57	16.80	3.25	11.0	1.55	10.74	1.6	9.4	2.2	8.16	4
8	70.8	9.41	39.8	12.23	0.96	16	2.86	18.85	4.02	12.2	1.80	12.46	1.9	10.0	2.3	9.26	4
9	71.2	8.88	38.8	11.67	0.69	15	2.95	17.89	3.97	12.5	1.90	12.72	1.9	9.5	2.2	9.06	4
10	72.3	8.94	37.6	11.37	0.54	15	2.45	17.50	3.66	10.9	1.60	11.45	1.8	8.8	2.2	8.49	4
11	75.2	9.12	38.3	11.57	0.65	14	2.84	17.75	3.84	11.5	1.79	11.34	1.6	9.0	2.2	8.63	4
12	62.6	8.21	36.7	10.30	0.90	14	2.64	16.73	3.39	11.1	1.72	11.39	1.6	9.9	2.4	9.15	4
13	79.8	10.09	41.5	11.41	1.09	14	2.53	17.58	3.35	10.7	1.58	9.85	1.6	9.2	1.8	7.24	3
14	91.7	10.67	48.6	12.96	1.02	16	2.84	17.72	3.67	10.7	1.74	10.71	1.7	10.1	2.1	8.09	4
15	88.2	10.57	45.9	12.18	0.90	16	2.60	18.51	3.59	11.0	1.57	11.02	1.8	9.4	2.0	7.89	4
16	47.6	5.28	23.9	7.78	0.54	11	2.25	14.89	3.17	10.6	1.56	11.26	1.8	7.3	2.4	9.32	5
17	47.9	6.06	23.7	7.79	0.37	12	2.36	15.57	3.22	11.2	1.67	11.02	1.8	7.7	2.7	9.24	5
18	103.9	12.00	48.4	12.02	0.57	15	2.27	15.52	3.07	9.9	1.64	9.52	1.3	10.8	1.9	7.04	3
19	82.9	9.85	40.3	11.36	0.82	14	2.20	15.81	3.06	9.6	1.48	9.65	1.7	9.1	2.0	6.86	4
20	83.2	9.87	43.8	11.21	0.96	15	2.60	16.59	3.42	10.7	1.61	10.02	1.7	9.5	1.9	7.30	3
21	46.0	5.26	20.5	6.84	0.35	10	1.75	13.11	2.91	9.0	1.48	9.30	1.5	6.1	2.2	8.46	5
22	45.8	5.04	21.7	7.17	0.36	9	1.89	12.68	2.86	8.8	1.37	8.77	1.5	6.3	2.2	7.99	5
23	125.4	9.88	39.0	10.82	0.89	14	2.40	17.96	3.35	10.2	1.65	11.61	1.8	8.9	1.9	7.67	4
24	82.7	8.31	34.0	8.20	0.48	11	1.95	12.42	2.69	7.9	1.21	7.41	1.2	6.7	1.6	5.53	4
25	44.2	4.70	16.6	5.68	0.40	8	1.46	10.30	2.15	7.3	1.17	7.46	1.1	4.9	1.9	6.80	6
26	44.4	4.57	17.0	5.27	0.34	8	1.49	10.51	2.13	6.7	1.03	6.98	1.3	4.6	2.0	6.49	6
27	43.0	4.36	15.9	5.58	0.37	7	1.40	9.43	2.23	6.8	0.99	6.63	1.1	4.9	1.9	6.66	6
28	43.1	4.11	17.2	5.77	0.37	7	1.38	10.01	2.17	7.2	1.06	6.98	1.2	5.0	1.9	6.45	5
29	44.6	4.52	16.8	6.09	0.38	7	1.49	9.85	2.06	7.1	1.26	7.09	1.1	4.5	1.8	6.41	5
30	45.1	4.55	17.1	6.32	0.38	8	1.53	10.16	2.36	7.2	1.07	7.42	1.1	5.2	2.0	6.84	6
31	44.2	4.65	17.0	6.23	0.36	8	1.44	10.72	2.23	7.2	1.21	7.47	1.2	5.0	2.1	6.85	6

Table 14 Trace and major element compositions of RST glass shards from pumice and tuff samples determined using LA-ICPMS (continued)

Spot #	*RST glass analysis (ppm)*																		
Group B Pumice RST-2-1	Na	Mg	Al	K	Ca	V	Mn	Fe	Co	Zn	Rb	Sr	Cs	Ba	Ti	Y	Zr	Nb	La
32	35332	192	52844	45345	2040	0.25	569	6201	0.02	95.0	120	1.15	4.94	19.1	706.0	69.2	117.0	40.36	12.3
33	36018	203	53459	45999	2151	0.24	612	6131	n.d.	95.9	124	1.20	5.01	14.2	722.3	69.7	119.5	39.71	12.6
34	35649	193	51158	45368	2303	0.28	601	6038	0.03	101.5	121	1.11	5.32	13.5	706.9	68.6	116.0	38.31	11.8
35	37054	195	52027	45374	2224	0.14	597	5939	0.02	99.5	122	1.00	5.13	12.9	739.7	66.9	115.1	39.13	12.3
36	32500	87	53660	44482	2072	0.11	589	11255	0.06	123.9	118	3.31	3.18	188.5	707.5	67.1	264.7	30.46	35.8
37	25463	2082	67562	54124	3042	0.73	501	8793	0.02	82.1	109	7.22	3.62	100.7	652.1	93.5	283.6	35.87	32.9
38	25085	3320	66981	49892	3437	2.17	472	8217	n.d.	73.1	104	9.64	3.42	100.6	632.5	95.1	292.3	32.30	31.7
39	31681	232	58953	43231	1920	0.20	590	6082	n.d.	90.9	110	2.34	4.69	16.4	754.6	94.8	164.0	42.08	16.0
40	34369	220	63470	43465	1938	0.35	616	6110	0.00	97.2	117	2.24	4.61	24.0	751.7	99.3	165.0	43.19	16.9
Group B Avg	31471	1211	61374	45033	2517	3.16	592	8017	0.12	95.0	110	5.56	4.10	65.2	700.3	89.7	214.6	36.44	23.7
σ	3587	2296	7358	3032	1040	8.41	49	2213	0.17	10.0	8	8.91	0.74	48.4	36.2	17.1	80.4	3.55	9.8

	Ce	Pr	Nd	Sm	Eu	Gd	Tb	Dy	Ho	Er	Tm	Yb	Lu	Hf	Ta	Th	U
32	44.3	4.62	17.0	5.55	0.40	8	1.52	10.90	2.21	7.3	1.11	7.09	1.1	5.2	2.0	6.88	6
33	44.2	4.57	18.2	5.98	0.42	8	1.54	11.48	2.36	7.5	1.16	7.83	1.1	5.1	1.9	6.62	6
34	44.7	4.46	17.8	5.88	0.37	8	1.41	10.20	2.38	6.9	1.15	7.56	1.1	4.9	2.0	6.52	5
35	45.4	4.36	17.3	5.96	0.39	8	1.47	10.63	2.30	7.4	1.28	6.87	1.1	4.7	1.9	6.59	5
36	107.0	10.60	43.1	10.21	0.77	11	1.87	11.45	2.44	7.3	1.13	6.96	1.1	8.0	1.5	5.67	3
37	86.6	10.29	42.1	10.86	1.04	14	2.57	15.21	3.31	10.5	1.47	9.13	1.6	9.0	1.8	7.36	4
38	78.7	9.55	40.4	11.89	1.00	14	2.54	16.26	3.21	9.7	1.52	8.97	1.5	9.6	1.8	6.99	3
39	50.7	5.83	23.0	7.89	0.44	11	2.24	13.96	3.35	10.2	1.50	9.64	1.6	6.8	2.4	9.05	5
40	49.8	5.99	24.4	7.99	0.35	12	2.14	13.75	3.21	10.2	1.51	10.27	1.6	7.1	2.6	8.98	5
Group B Avg	66.2	7.56	31.4	9.20	0.62	12	2.19	14.55	3.06	9.5	1.46	9.46	1.5	7.7	2.0	7.61	4
σ	21.6	2.55	11.5	2.66	0.25	3	0.53	3.11	0.60	1.7	0.25	1.79	0.3	2.1	0.3	1.04	1

Table 14 Trace and major element compositions of RST glass shards from pumice and tuff samples determined using LA-ICPMS (continued)

Group C Pumice #1	*RST glass analysis (ppm)*																		
RST-2-3	Na	Mg	Al	K	Ca	V	Mn	Fe	Co	Zn	Rb	Sr	Cs	Ba	Ti	Y	Zr	Nb	La
1	27551	303	91078	46189	3181	0.52	641	10547	0.07	62.0	87	5.92	2.80	352.4	816.3	177.5	622.2	34.81	72.2
2	30273	509	84546	45237	5652	0.39	764	13927	0.26	91.2	91	15.75	3.14	354.1	856.7	174.7	528.9	34.91	74.1
3	32890	157	64706	43022	2460	0.14	684	11540	0.10	91.9	88	2.25	3.25	271.7	770.0	95.4	367.8	31.93	45.5
4	33088	177	76717	44608	2695	0.59	739	11400	0.37	91.3	87	2.78	3.04	307.5	826.8	124.4	463.3	33.99	56.1
5	32212	111	72413	42835	2403	0.10	670	11413	0.05	96.2	83	2.12	3.10	297.4	781.7	112.6	434.1	32.42	51.1
7	34616	114	62378	46707	2462	0.21	654	11461	0.01	112.2	98	1.65	3.46	252.9	783.8	85.1	332.7	32.20	41.2
8	31910	306	71368	45106	2480	1.77	705	12005	0.40	95.9	92	4.14	3.33	307.0	861.2	106.3	397.3	33.53	48.3
9	33243	109	64881	45090	2448	0.01	653	11273	0.06	105.8	87	1.84	3.16	280.2	757.8	94.8	360.4	32.13	45.2
10	34636	133	65915	44423	2447	0.25	652	11574	0.03	106.8	90	2.28	2.97	287.5	770.6	101.4	381.5	33.30	45.8
RST-2-3b																			
1	32313	127	75119	42641	2378	0.17	738	11166	0.09	76.2	87	2.13	3.06	314.2	763.0	128.7	469.9	33.94	56.9
3	32471	119	67299	42417	2471	0.03	674	11465	0.02	108.4	88	1.65	3.03	293.3	775.7	104.8	415.3	33.19	48.8
4	30881	136	68007	44551	2713	0.07	704	11818	0.10	106.1	88	3.29	2.94	304.5	764.7	110.6	416.5	34.09	51.5
6	34002	121	65980	43150	2373	0.04	688	11598	0.02	111.7	89	1.53	3.18	290.0	765.0	103.0	402.1	34.01	48.5
7	35209	120	68529	43936	2390	0.05	706	11686	0.02	114.3	90	1.55	3.10	297.2	783.0	107.2	414.3	34.23	49.4
8	30711	129	69019	44537	2297	0.08	711	11123	0.04	81.7	85	1.83	2.86	315.9	741.0	113.6	446.4	33.46	52.6

RST-2-3	Ce	Pr	Nd	Sm	Eu	Gd	Tb	Dy	Ho	Er	Tm	Yb	Lu	Hf	Ta	Th	U
1	125.2	18.59	86.9	21.67	1.91	28	4.38	29.90	6.18	17.7	2.72	17.30	3.0	19.9	2.4	12.36	3
2	141.8	19.63	88.5	21.59	2.36	28	4.16	29.00	6.45	19.1	2.98	17.27	3.1	16.4	2.3	11.11	3
3	105.5	12.87	55.8	13.16	1.29	15	2.54	17.05	3.54	10.3	1.47	9.67	1.6	10.8	2.0	7.47	3
4	117.2	15.36	69.3	16.71	1.62	21	3.31	22.19	4.58	13.6	2.01	12.35	2.1	14.0	2.2	9.38	3
5	110.1	14.45	62.3	15.74	1.45	18	2.91	19.82	4.48	12.4	1.94	12.37	2.1	13.1	2.0	8.77	3
7	104.1	11.85	51.1	12.47	1.18	14	2.24	15.68	2.99	9.6	1.46	8.67	1.5	9.7	1.8	6.73	3
8	108.0	13.82	58.0	15.03	1.21	17	2.76	18.87	3.97	10.8	1.78	10.63	1.7	12.0	2.0	7.66	3
9	110.9	12.78	54.4	13.70	1.35	16	2.51	16.97	3.61	9.9	1.44	9.35	1.6	11.0	1.9	7.29	3
10	111.5	13.40	57.8	13.52	1.35	16	2.58	17.41	3.73	10.7	1.58	9.55	1.8	11.4	2.0	7.87	3
RST-2-3b																	
1	116.0	14.73	68.3	16.54	1.53	20	3.45	21.96	4.47	14.0	2.02	12.19	2.1	14.0	2.3	8.98	3
3	116.0	13.77	61.0	15.95	1.28	17	3.03	17.98	3.71	12.0	1.84	10.23	1.8	12.5	2.1	8.16	3
4	119.5	14.22	60.5	15.16	1.48	18	3.05	19.69	4.00	11.9	1.78	10.51	2.0	12.2	2.1	8.40	3
6	116.0	13.90	58.5	13.73	1.39	17	2.84	17.94	3.87	11.4	1.75	10.54	1.8	11.5	2.1	7.61	3
7	118.2	14.06	59.9	15.15	1.41	17	2.90	17.99	3.83	12.0	1.80	10.62	1.8	12.0	2.1	8.11	3
8	118.0	14.87	62.8	15.51	1.60	18	3.00	19.89	4.17	12.4	1.86	11.36	2.0	13.5	2.2	8.45	3

Table 14 Trace and major element compositions of RST glass shards from pumice and tuff samples determined using LA-ICPMS (continued)

Group C Pumice #2	*RST glass analysis (ppm)*																		
RST-2-2	Na	Mg	Al	K	Ca	V	Mn	Fe	Co	Zn	Rb	Sr	Cs	Ba	Ti	Y	Zr	Nb	La
9	29968	2644	68232	45658	3574	1.25	629	9754	0.03	59.7	92	8.42	3.07	156.3	636.1	113.6	365.6	31.41	43.5
10	25405	392	71887	35817	2762	0.99	382	5949	n.d.	24.1	58	5.69	1.81	670.9	437.8	91.6	322.8	20.33	35.8
11	34574	116	48855	44026	2191	0.05	586	9835	0.03	116.3	95	0.73	3.50	125.1	631.4	65.7	233.9	29.90	27.7
12	32618	142	60268	45752	2699	0.12	620	10613	n.d.	92.2	95	2.35	3.39	141.0	666.3	95.4	324.5	32.29	37.6
13	28440	442	62824	47971	2318	0.15	535	10106	0.09	69.6	89	4.59	3.00	282.8	650.8	93.8	364.3	28.95	45.5
RST-2-2 b																			
1	32730	1809	61991	45983	3177	0.90	682	10872	0.03	94.0	94	4.59	3.07	189.5	714.6	95.0	329.8	32.71	39.4
2	31639	8306	55834	44267	2426	5.17	632	10618	0.09	115.5	90	3.12	2.90	196.1	706.7	78.1	292.2	29.94	34.9
3	28161	1692	79474	48028	4186	0.97	624	12024	0.05	74.2	90	12.48	2.79	318.4	828.8	132.6	498.5	33.48	57.9
4	28763	5135	83330	45020	3825	2.18	595	9492	0.13	51.2	89	6.92	2.63	314.1	759.7	160.4	579.7	32.23	66.1
5	22023	2986	92765	53375	3342	1.25	643	25708	0.09	75.7	93	14.22	2.84	296.7	881.0	157.7	631.3	35.29	64.8
6	26502	4467	82897	48950	4357	3.29	905	10187	0.66	58.1	92	17.36	3.15	150.6	748.1	154.2	440.3	35.68	46.1
7	34410	143	70723	44258	2351	0.07	643	10949	0.05	99.3	74	1.80	1.99	272.2	792.7	109.0	417.1	26.59	48.9
RST-2-2 b																			
8	22764	4831	76805	54567	5955	2.51	495	9689	0.20	63.7	108	29.82	3.18	250.4	725.4	140.7	418.9	35.65	43.9
9	28017	1075	81420	47700	3760	0.64	612	13163	0.11	84.1	93	10.09	2.58	320.1	812.8	140.4	526.7	31.46	59.1
10	30512	385	75921	50660	3038	0.33	658	11726		72.0	98	4.76	3.08	333.6	793.0	118.5	484.6	35.18	56.4
RST-2-2 c																			
1	34167	207	59693	42536	2365	0.23	652	6425	0.02	98.1	96	1.82	4.81	62.0	761.3	92.2	154.2	43.57	14.7
3	27736	1211	78356	49191	4385	1.31	588	8872	0.20	55.9	99	25.61	3.17	150.8	746.0	145.9	430.5	36.77	44.7
5	33856	117	60641	42438	2468	0.04	652	11499	0.08	117.1	93	4.31	3.19	261.3	756.5	85.8	333.1	33.90	39.4
7	28139	1689	55281	43831	2583	1.95	527	9437	0.04	98.8	89	3.15	3.10	130.1	682.9	78.3	273.5	31.16	31.1
8	27405	2976	91384	49558	5214	1.49	587	11066	0.07	55.3	95	14.47	3.22	237.5	780.2	171.4	565.2	36.45	62.4
9	31938	284	64405	43629	3691	0.41	657	9780	0.03	101.4	98	3.68	3.52	107.9	709.8	108.3	320.5	37.38	35.7
10	28096	4864	73609	49055	27521	1.93	597	10183	0.06	70.4	87	37.73	2.76	306.4	732.9	127.0	473.9	32.27	54.7
Group C Avg	30645	1313	70934	45587	3758	0.86	646	11134	0.11	86.4	90	7.25	3.06	264.9	750.6	116.1	411.7	33.10	48.0
σ	3331	1945	10373	3381	4133	1.10	84	2883	0.13	22.5	8	8.54	0.45	102.7	78.7	28.7	102.9	3.52	12.1

Table 14 Trace and major element compositions of RST glass shards from pumice and tuff samples determined using LA-ICPMS (continued)

Group C Pumice #2	*RST glass analysis (ppm)*																
RST-2-2	Ce	Pr	Nd	Sm	Eu	Gd	Tb	Dy	Ho	Er	Tm	Yb	Lu	Hf	Ta	Th	U
9	93.1	11.90	51.1	14.58	1.20	16	2.80	18.08	4.00	12.3	1.61	11.63	1.8	10.4	1.9	8.31	3
10	65.2	9.22	41.1	9.99	1.67	15	2.67	13.56	3.19	11.1	1.51	9.71	1.8	11.5	1.7	6.81	2
11	86.5	8.86	34.7	9.63	0.84	10	1.83	10.92	2.22	7.7	1.08	6.98	1.1	6.7	1.7	5.43	4
12	94.8	11.09	45.2	12.56	1.08	14	2.52	15.66	3.47	10.4	1.55	9.05	1.7	10.5	1.8	7.33	3
13	103.1	12.30	53.2	12.99	1.26	15	2.45	15.23	3.20	10.6	1.49	9.93	1.6	11.1	1.8	7.21	3
RST-2-2 b																	
1	95.8	11.34	47.7	11.75	0.98	14	2.44	15.96	3.33	10.3	1.51	9.42	1.5	9.9	1.9	7.24	3
2	97.7	10.15	42.0	10.39	0.94	12	2.07	13.80	2.90	8.8	1.21	8.50	1.2	8.9	1.7	6.13	3
3	111.6	15.24	66.6	17.41	1.56	22	3.61	23.18	4.61	14.2	2.28	13.29	2.1	14.9	2.0	10.07	3
4	114.5	16.19	75.5	20.26	1.62	24	3.68	26.93	5.86	18.5	2.73	17.14	2.6	18.4	2.3	11.04	3
5	113.0	16.82	75.7	19.79	1.28	24	4.14	26.69	5.63	16.8	2.58	16.05	2.4	19.4	2.5	11.33	3
6	86.0	12.58	54.4	15.80	1.32	22	4.04	24.05	5.09	16.5	2.40	15.26	2.4	14.5	2.4	10.63	3
7	105.3	12.89	56.8	12.26	1.10	14	2.85	18.56	3.86	9.6	1.52	11.31	1.8	10.7	1.6	7.74	3
RST-2-2 b																	
8	81.9	12.27	53.2	14.97	1.29	21	3.75	26.19	5.07	15.6	2.40	14.79	2.3	13.2	2.2	9.84	3
9	112.3	15.36	63.6	16.44	1.33	20	3.62	23.21	4.91	14.6	2.09	13.19	2.3	15.2	2.3	9.87	3
10	118.6	15.01	66.9	16.65	1.34	21	3.56	21.58	4.93	12.5	1.99	13.30	1.9	14.1	2.3	9.19	3
RST-2-2 c																	
1	45.0	5.41	20.8	7.74	0.52	11	2.08	14.40	3.12	9.7	1.65	9.67	1.6	7.1	2.4	8.47	5
3	88.1	12.26	55.9	16.67	1.28	22	4.13	25.37	5.55	15.6	2.55	13.67	2.4	14.7	2.5	10.51	3
5	103.4	11.98	49.7	12.74	1.12	14	2.36	14.96	3.14	9.3	1.41	8.70	1.5	9.7	1.7	6.88	3
7	86.2	9.77	39.9	10.53	0.85	12	2.09	13.40	3.07	8.8	1.25	8.06	1.5	8.2	1.8	6.27	3
8	109.5	16.37	73.3	21.58	1.74	25	4.55	29.57	6.12	17.6	2.72	16.46	3.0	17.3	2.6	11.93	3
9	88.9	11.00	46.8	12.87	1.09	16	2.86	18.00	3.86	11.2	1.66	10.33	1.9	10.3	2.1	8.07	3
10	104.3	14.27	64.3	16.61	1.39	19	3.26	21.73	4.69	13.2	2.10	12.70	2.2	14.6	1.8	8.93	3
Group C Avg	103.9	13.26	57.7	14.86	1.33	18	3.05	19.82	4.20	12.5	1.88	11.67	2.0	12.6	2.1	8.58	3
σ	17.5	2.73	13.5	3.36	0.32	4	0.71	4.91	1.03	3.0	0.48	2.79	0.5	3.1	0.3	1.69	>1

Table 14 Trace and major element compositions of RST glass shards from pumice and tuff samples determined using LA-ICPMS (continued)

Banded Pumice	*RST glass analysis (ppm)*																		
RST-6-1	Na	Mg	Al	K	Ca	V	Mn	Fe	Co	Zn	Rb	Sr	Cs	Ba	Ti	Y	Zr	Nb	La
1	61700	1315	88508	73745	2921	4.04	403	5684	0.51	17.5	125	1.78	8.29	17.0	681.9	49.5	207.4	16.88	15.8
2	52450	192	79285	66614	2702	1.38	73	2614	0.18	6.5	167	1.22	2.59	10.5	417.2	7.2	92.2	4.82	10.2
3	30922	1042	57779	51444	2141	3.76	56	2732	0.05	7.1	127	2.91	2.10	14.7	669.8	16.8	174.1	10.28	5.5
4	40043	984	64813	50503	2261	5.67	37	2646	0.06	5.8	90	2.60	0.60	13.4	496.3	2.9	107.4	3.42	4.3
5	42491	1922	56557	39211	3231	10.23	178	3751	0.72	16.1	85	7.20	1.83	78.2	802.4	126.8	220.3	47.25	18.5
6	48072	488	59109	43449	2452	2.18	72	2450	0.06	8.6	67	1.24	3.01	11.6	623.3	19.9	159.1	30.63	8.0
7	27918	2164	48689	48348	2414	11.12	222	5636	0.17	17.5	106	4.64	1.87	47.2	621.5	151.0	254.1	38.98	31.9
9	36985	173	53434	55417	1990	1.04	41	2002	0.04	6.2	176	1.29	5.59	12.1	744.4	19.2	163.0	11.53	6.5
10	50655	1974	76280	53282	3298	8.22	669	6635	0.32	23.5	83	4.41	1.02	18.5	782.9	207.0	164.9	21.23	35.9
RST-6-1b																			
1	32268	1935	59301	48626	2281	5.11	622	5987	0.08	20.6	149	3.25	1.51	24.3	2308.0	22.1	180.4	237.36	5.6
2	31380	923	65008	66163	1782	6.63	71	2550	0.05	7.5	269	2.04	9.79	39.9	446.5	21.7	175.0	11.60	7.4
3	33326	3296	55663	54460	2397	15.11	388	8699	0.24	26.1	204	4.94	3.19	20.8	722.5	101.9	218.0	32.71	18.1
7	39637	1282	56944	34738	2186	11.44	208	4777	0.39	17.1	107	7.79	7.80	116.1	756.1	136.5	233.6	53.23	15.8
8	48333	2270	71701	59057	2519	13.26	234	10036	0.37	34.0	113	4.55	1.79	22.1	715.5	411.8	148.3	13.42	76.7
9	52706	1581	63554	41325	2265	5.88	303	9111	0.24	41.0	63	16.79	1.86	265.3	892.0	62.7	304.9	36.30	31.4
10	37683	2949	61349	59691	2424	11.56	254	6932	0.16	26.9	168	5.80	2.04	46.8	712.2	99.5	241.4	27.20	44.2
Banded Pumice Avg	41661	1531	63623	52880	2454	7.29	239	5140	0.23	17.6	131	4.53	3.43	47.4	774.5	91.0	190.3	37.30	21.0
σ	9727	907	10509	10579	412	4.39	198	2625	0.19	10.7	55	3.86	2.83	64.8	428.6	105.2	54.7	55.41	19.3

Table 14 Trace and major element compositions of RST glass shards from pumice and tuff samples determined using LA-ICPMS (continued)

Banded Pumice RST-6-1	*RST glass analysis (ppm)* Ce	Pr	Nd	Sm	Eu	Gd	Tb	Dy	Ho	Er	Tm	Yb	Lu	Hf	Ta	Th	U
1	36.2	3.44	13.5	3.87	0.66	5	1.03	7.24	1.56	5.2	0.75	6.02	1.1	10.7	3.1	11.40	3
2	17.2	1.20	4.2	0.70	0.39	1	0.13	1.07	0.23	0.6	0.12	0.74	0.1	5.9	1.5	2.72	1
3	9.7	0.94	3.4	1.27	0.35	1	0.36	1.92	0.52	1.7	0.30	1.99	0.4	7.7	2.6	5.97	2
4	5.5	0.47	1.4	0.33	0.39	0	0.05	0.43	0.11	0.4	0.04	0.52	0.1	6.7	1.6	1.63	0
5	53.6	7.23	31.2	11.11	0.67	15	3.10	19.63	4.28	13.8	2.10	12.91	2.2	8.4	3.0	11.40	6
6	15.3	1.38	4.8	1.34	0.44	2	0.40	2.65	0.62	2.0	0.34	2.21	0.4	7.3	2.4	6.46	4
7	87.6	12.10	52.0	15.46	0.68	22	4.02	27.30	5.86	17.5	2.51	15.12	2.7	8.3	2.4	12.72	5
9	14.9	1.27	4.8	1.07	0.36	2	0.35	2.64	0.64	2.2	0.43	2.76	0.5	6.9	2.5	8.20	4
10	83.0	11.66	48.6	15.55	1.00	22	4.01	26.68	6.41	18.5	3.44	20.18	2.8	8.5	2.3	16.77	2
RST-6-1b																	
1	11.8	1.35	6.1	2.22	0.42	3	0.38	3.01	0.83	2.9	0.58	3.71	0.6	7.5	4.9	4.15	0
2	14.6	1.38	5.4	1.23	0.40	2	0.34	3.19	0.72	2.6	0.39	2.78	0.5	7.1	2.4	7.20	3
3	43.1	6.06	26.6	8.76	0.62	16	2.01	17.05	3.77	11.6	1.98	11.57	1.8	7.4	2.0	8.10	4
7	48.0	5.80	26.0	9.30	0.45	19	2.21	21.26	4.74	15.2	2.51	15.16	2.5	9.3	3.1	13.96	6
8	197.4	26.65	118.0	36.54	0.89	62	8.26	65.42	15.52	43.5	6.77	35.02	5.9	7.5	1.8	29.22	4
9	75.3	8.46	35.8	9.42	1.07	12	1.58	12.55	2.43	7.3	1.26	7.30	1.2	10.2	2.1	9.61	3
10	108.6	12.04	51.5	11.46	0.63	18	2.61	18.50	3.48	12.4	1.86	10.97	1.8	8.7	2.1	9.81	3
Banded Pumice Avg	51.4	6.34	27.1	8.10	0.59	13	1.93	14.41	3.23	9.8	1.59	9.31	1.5	8.0	2.5	9.96	3
σ	50.6	6.88	30.4	9.31	0.23	15	2.17	16.60	3.89	11.0	1.73	9.15	1.5	1.3	0.8	6.55	2

Table 14 Trace and major element compositions of RST glass shards from pumice and tuff samples determined using LA-ICPMS (continued)

Welded Tuff	*RST glass analysis (ppm)*																		
RST-5-1	Na	Mg	Al	K	Ca	V	Mn	Fe	Co	Zn	Rb	Sr	Cs	Ba	Ti	Y	Zr	Nb	La
1	36006	238	68096	44067	2573	0.76	671	7136	0.09	93.9	113	3.99	5.02	224.5	834.4	111.4	194.6	44.00	18.5
2	34026	133	66232	40693	2904	0.60	655	12233	0.16	100.3	95	6.03	3.02	639.0	881.5	94.8	409.7	30.40	48.3
3	34062	279	71062	46229	3361	2.50	700	12928	0.40	102.6	107	13.54	3.96	643.1	1029.4	98.2	388.9	35.71	41.6
4	34032	205	67380	45589	2603	0.45	640	7854	0.07	93.9	105	6.68	4.35	510.6	846.0	110.1	245.6	42.87	24.4
5	35275	162	68857	45959	3043	1.39	699	14592	0.26	115.3	101	7.74	3.31	895.5	1051.0	86.8	448.0	31.85	46.7
6	35543	210	65261	42857	2700	0.47	653	9128	0.17	96.8	103	5.99	3.87	507.1	865.5	101.7	245.2	39.89	25.1
7	32183	240	78357	45503	2727	0.39	666	11853	0.12	61.5	95	9.23	3.33	620.7	837.6	135.8	454.4	34.57	50.5
9	34503	279	65393	48146	3419	2.73	648	14254	0.24	112.3	113	12.21	4.00	404.4	1044.6	88.8	313.7	36.52	34.8
10	35675	143	69352	45763	3529	1.00	705	15555	0.18	117.0	101	9.12	3.34	1194.5	1111.2	86.3	461.3	31.49	46.4
RST-5-1b																			
1	35760	248	72935	44655	2269	0.34	698	6769	0.05	94.0	115	2.31	4.81	47.1	812.5	125.6	203.4	46.01	19.6
2	30926	158	67754	50782	2772	0.54	681	12037	0.11	107.9	108	4.11	3.37	497.9	907.9	99.7	388.3	35.01	39.9
3	35669	146	67466	42193	3063	1.60	736	14819	0.22	117.4	110	5.89	2.78	889.9	956.2	87.3	441.9	30.01	51.5
4	34443	120	62734	39910	2101	0.09	644	10381	0.04	111.3	96	3.50	3.10	230.7	690.6	96.0	318.8	34.86	37.7
5	35675	79	65863	41091	2687	0.05	709	13614	0.06	120.3	96	6.65	2.54	976.5	880.8	80.6	422.5	29.51	49.7
6	37030	233	65139	45421	2329	0.21	685	6732		102.3	107	3.85	4.79	182.8	802.9	98.8	169.6	45.32	16.3
8	38916	445	63490	42766	3287	2.74	800	14263	0.45	115.4	103	5.05	3.33	773.8	1099.0	85.8	336.9	35.23	36.0
9	31563	243	72015	44062	2464	0.25	631	6743	0.07	75.8	94	5.74	4.23	327.0	733.0	122.5	214.1	41.36	20.9
10	34746	156	63316	48029	2854	0.53	669	12857	0.21	114.4	105	4.64	3.51	708.2	902.3	80.9	354.4	32.39	38.8

Table 14 Trace and major element compositions of RST glass shards from pumice and tuff samples determined using LA-ICPMS (continued)

Welded Tuff	*RST glass analysis (ppm)*																
RST-5-1	Ce	Pr	Nd	Sm	Eu	Gd	Tb	Dy	Ho	Er	Tm	Yb	Lu	Hf	Ta	Th	U
1	51.7	6.53	27.3	8.35	0.80	12	2.43	16.34	3.84	11.9	1.72	11.33	1.9	8.0	2.6	9.80	5
2	111.7	13.67	55.0	12.82	1.45	14	2.55	16.31	3.22	10.3	1.39	9.73	1.7	11.2	1.9	7.24	3
3	97.1	11.83	51.6	11.80	1.41	14	2.44	15.73	3.49	10.7	1.55	10.41	1.8	11.6	2.2	8.14	4
4	60.5	7.67	33.3	10.21	1.00	13	2.51	17.04	3.69	12.4	1.88	12.19	1.9	9.2	2.5	9.78	5
5	110.4	12.86	53.1	12.83	1.57	14	2.50	15.51	2.97	9.6	1.46	9.50	1.6	11.9	1.9	6.91	3
6	66.4	7.94	32.7	9.84	1.02	13	2.24	15.73	3.51	10.9	1.69	11.20	1.8	8.3	2.3	9.00	4
7	100.7	13.55	62.0	16.18	1.34	21	3.47	21.92	4.51	14.6	2.29	14.42	2.2	14.2	2.3	10.71	3
9	86.9	10.16	41.0	9.83	1.14	12	2.35	14.13	2.93	9.3	1.35	8.98	1.4	9.6	1.9	7.71	4
10	109.3	12.74	57.9	12.84	1.85	14	2.13	13.89	3.13	9.3	1.39	9.13	1.4	12.0	1.8	6.57	3
RST-5-1b																	
1	52.1	6.68	30.3	9.87	0.59	14	2.87	18.64	4.14	12.9	2.14	12.56	2.1	8.3	2.9	11.08	5
2	94.5	11.44	49.8	12.51	1.37	14	2.59	16.56	3.49	10.1	1.73	10.21	1.7	10.7	2.1	7.63	4
3	122.5	14.35	61.7	13.22	1.74	14	2.58	14.97	3.21	9.5	1.34	9.13	1.5	11.3	1.7	6.74	3
4	97.1	11.32	48.5	12.78	1.07	15	2.79	16.44	3.47	10.5	1.63	9.87	1.5	10.1	2.0	7.68	3
5	118.4	13.77	59.3	13.49	1.80	14	2.19	14.08	3.00	8.8	1.34	8.20	1.3	10.9	1.7	6.56	3
6	49.5	5.77	24.6	7.68	0.64	11	2.29	15.33	3.33	10.6	1.74	10.49	1.7	6.7	2.5	9.45	5
8	93.9	10.60	44.3	10.86	1.62	13	2.20	13.65	2.99	9.0	1.34	8.83	1.5	9.5	1.9	6.97	4
9	48.1	6.55	29.6	9.53	0.81	14	2.86	18.32	4.02	12.8	2.17	12.59	2.0	8.3	2.5	10.96	5
10	103.1	11.60	48.6	11.50	1.39	12	2.30	13.30	2.79	8.6	1.33	8.46	1.3	9.8	1.9	6.31	3

Table 14 Trace and major element compositions of RST glass shards from pumice and tuff samples determined using LA-ICPMS (continued)

Welded Tuff RST-5-1c	*RST glass analysis (ppm)* Na	Mg	Al	K	Ca	V	Mn	Fe	Co	Zn	Rb	Sr	Cs	Ba	Ti	Y	Zr	Nb	La
4	36019	326	74465	47033	2427	0.48	733	7789	0.08	76.8	115	4.53	4.50	152.8	835.3	129.0	212.6	44.42	20.8
8	37176	252	69821	42277	2274	0.25	710	6543	0.02	97.3	111	2.21	4.75	32.2	782.9	114.1	184.3	45.97	18.5
RST-5-1d																			
1	36142	132	68451	40415	2723	0.34	741	13244	0.11	117.9	101	3.76	3.18	581.3	884.9	103.1	435.5	32.50	47.5
2	33325	161	64449	40783	2095	0.13	675	8329	0.01	105.0	104	2.51	3.85	92.5	706.8	112.2	270.7	38.25	28.4
3	35537	75	69838	41418	2899	0.05	727	14307	0.04	118.8	74	7.36	2.54	1080.9	900.8	91.8	466.7	29.60	54.8
4	35066	243	69937	41352	2230	0.21	676	6077	n.d.	94.8	111	1.23	4.87	46.4	748.3	118.1	190.1	43.53	18.3
5	35570	223	66176	42330	2165	0.19	669	6390	0.05	96.6	107	1.45	4.77	19.3	790.0	115.6	187.0	44.33	18.4
6	34227	127	68910	41798	2126	0.09	653	9567	n.d.	106.8	96	1.33	3.35	109.9	697.5	116.7	325.0	35.48	37.0
7	34990	238	67388	41196	2161	0.18	668	6403	0.01	94.0	105	3.89	4.93	117.2	766.4	116.6	190.4	43.84	18.4
8	33102	268	76468	45687	2193	0.26	738	6729	n.d.	55.7	102	2.89	4.84	47.0	774.5	142.7	225.9	43.83	22.1
9	33915	280	74719	41515	2382	0.32	711	6977	0.05	71.0	101	3.93	4.79	206.2	791.7	139.8	224.2	43.58	22.2
10	33479	124	70817	47782	3048	0.65	758	14942	0.07	122.8	102	6.73	3.00	949.3	967.3	91.1	473.9	29.30	54.0
Welded Tuff Avg	34819	205	68738	43910	2647	0.66	692	10368	0.13	100.3	103	5.27	3.87	456.9	864.4	106.1	313.3	37.72	33.6
σ	1658	79	3889	2807	426	0.77	39	3372	0.11	17.5	8	2.98	0.80	357.5	116.4	17.7	107.0	5.87	13.2

Table 14 Trace and major element compositions of RST glass shards from pumice and tuff samples determined using LA-ICPMS (continued)

Welded Tuff RST-5-1c	*RST glass analysis (ppm)* Ce	Pr	Nd	Sm	Eu	Gd	Tb	Dy	Ho	Er	Tm	Yb	Lu	Hf	Ta	Th	U
4	51.6	6.18	29.0	10.56	0.55	13	2.65	18.45	3.98	13.8	2.23	12.96	2.2	8.8	2.5	11.33	5
8	52.5	6.27	26.6	8.84	0.59	12	2.40	16.45	3.68	12.0	1.94	11.52	1.9	7.9	2.7	10.13	5
RST-5-1d																	
1	109.9	13.45	59.5	15.17	1.76	16	2.90	18.48	3.66	11.0	1.73	10.33	1.7	12.9	2.0	7.83	3
2	72.7	9.09	38.8	11.70	0.91	15	2.70	18.56	3.88	11.8	1.86	11.29	1.7	9.9	2.2	8.99	4
3	124.9	15.03	63.7	14.94	1.93	15	2.49	15.55	3.40	10.5	1.50	9.80	1.6	13.4	1.8	7.19	3
4	50.1	6.28	28.1	9.23	0.65	13	2.60	17.31	4.01	13.3	1.95	12.00	2.0	8.5	2.8	10.24	5
5	49.4	6.06	26.4	8.55	0.59	13	2.40	16.73	3.94	12.6	1.84	11.77	2.0	8.3	2.7	10.06	5
6	89.9	11.30	46.3	13.45	1.07	16	3.11	18.97	3.91	13.0	1.80	11.24	1.8	11.1	2.1	8.37	4
7	50.0	6.38	27.4	8.92	0.63	13	2.61	16.58	4.01	13.0	2.05	12.19	2.0	8.2	2.8	10.46	5
8	50.2	6.78	29.5	11.17	0.66	16	3.03	20.55	5.01	14.5	2.44	14.85	2.5	10.2	3.0	12.01	5
9	50.8	7.10	31.3	11.30	0.84	16	2.95	20.91	4.57	14.6	2.41	14.03	2.3	10.1	2.9	12.09	5
10	124.3	14.42	64.4	14.02	1.86	16	2.61	15.91	3.38	10.4	1.42	9.78	1.6	12.9	1.9	7.08	3
Welded Tuff Avg	81.7	9.91	42.7	11.47	1.16	14	2.59	16.74	3.64	11.4	1.75	10.97	1.8	10.1	2.3	8.83	4
σ	28.3	3.20	13.7	2.20	0.46	2	0.31	2.15	0.53	1.8	0.34	1.76	0.3	1.9	0.4	1.78	1

Table 14 Trace and major element compositions of RST glass shards from pumice and tuff samples determined using LA-ICPMS (continued)

Unwelded Tuff	*RST glass analysis (ppm)*																		
RST-7-4	Na	Mg	Al	K	Ca	V	Mn	Fe	Co	Zn	Rb	Sr	Cs	Ba	Ti	Y	Zr	Nb	La
2	37592	227	56231	47019	2454	0.29	674	6595	0.02	110.6	118	0.52	5.01	46.5	753.5	80.2	133.7	40.64	13.2
4	38397	215	57353	46588	2407	0.19	683	6521	0.04	112.0	117	0.23	5.07	9.7	751.1	80.6	133.7	41.88	13.9
5	37826	224	55466	48017	2337	0.23	674	6692	0.02	112.3	117	0.48	5.08	18.7	757.0	76.1	128.0	40.69	13.3
7	39494	220	55319	49419	2390	0.17	686	6736	0.03	115.2	121	0.44	5.37	24.0	764.4	75.4	126.6	42.32	13.0
8	38056	219	58363	46918	2373	0.19	684	6560	0.06	107.4	118	0.46	5.16	27.5	763.7	86.1	141.4	42.47	14.5
9	39309	224	56533	49738	2358	0.28	700	6840	0.04	119.1	122	0.42	5.20	27.6	760.4	77.4	129.8	42.76	13.1
10	38738	217	54190	48652	2270	0.24	668	6496	0.01	115.1	120	0.30	5.30	12.2	737.8	75.2	125.9	41.78	12.5
RST-7-4b																			
1	32845	254	68306	52029	2252	0.68	671	7069	0.04	100.3	119	2.56	4.74	43.2	803.8	109.0	184.9	45.07	17.6
2	32572	241	69439	52031	1998	0.93	671	6667	0.05	84.1	114	2.95	4.54	50.9	785.8	116.1	190.4	42.82	18.4
3	37041	245	60992	45798	2121	0.43	672	6482	0.03	95.7	117	0.70	5.13	17.8	779.2	95.7	162.4	42.72	16.4
4	35764	213	61962	45476	2035	0.28	661	6264	0.03	96.3	113	1.15	4.78	28.0	762.9	94.0	159.6	43.65	15.8
5	34050	169	64197	50683	2311	0.24	685	8896	0.05	107.1	114	1.82	4.09	167.0	718.3	100.8	241.1	38.58	26.6
6	37221	224	59951	45803	2142	0.21	662	6295	0.04	98.5	114	0.56	5.08	15.3	756.5	91.7	159.1	42.62	15.3
7	37107	223	59708	45942	2215	0.17	685	6516	0.04	98.0	115	0.39	5.02	15.2	782.9	91.8	153.2	43.64	15.2
8	36685	158	58380	45491	2124	0.11	661	8731	0.06	111.5	114	0.80	4.06	59.7	704.2	89.4	218.3	37.85	24.3
9	32264	164	59757	51328	2003	0.41	697	8768	0.06	106.6	114	1.66	4.05	82.9	709.1	90.8	221.7	37.87	24.1
10	37300	236	56839	47041	2066	0.28	677	6551	0.03	105.1	119	0.52	5.17	16.2	796.8	83.5	145.4	43.12	14.8

Table 14 Trace and major element compositions of RST glass shards from pumice and tuff samples determined using LA-ICPMS (continued)

Unwelded Tuff	*RST glass analysis (ppm)*																
RST-7-4	Ce	Pr	Nd	Sm	Eu	Gd	Tb	Dy	Ho	Er	Tm	Yb	Lu	Hf	Ta	Th	U
2	44.8	5.04	19.1	7.14	0.56	8	1.71	12.27	2.73	9.3	1.34	8.02	1.5	6.2	2.4	7.89	6
4	46.4	5.17	19.9	6.33	0.51	9	1.86	12.55	2.86	8.9	1.36	8.81	1.3	5.7	2.3	7.72	6
5	45.4	4.82	18.3	6.54	0.47	9	1.77	11.92	2.59	8.4	1.39	7.75	1.3	5.8	2.3	7.35	6
7	45.1	4.81	19.0	6.15	0.42	8	1.82	12.13	2.61	8.6	1.27	7.85	1.2	5.9	2.3	7.43	6
8	45.9	5.13	21.2	7.12	0.50	9	1.76	13.35	3.00	9.5	1.53	8.90	1.6	6.9	2.4	8.36	6
9	46.2	4.89	19.3	6.20	0.45	9	1.74	12.21	2.76	8.6	1.40	8.31	1.4	5.7	2.2	7.44	6
10	45.3	4.65	19.3	6.43	0.43	8	1.66	11.52	2.49	8.3	1.28	7.43	1.4	6.1	2.3	7.32	6
RST-7-4b																	
1	49.9	6.11	26.4	8.88	0.57	12	2.35	16.49	3.61	11.7	1.89	11.33	1.9	7.6	2.6	9.92	6
2	49.7	6.18	26.5	9.53	0.49	13	2.37	17.42	3.84	11.6	2.03	11.99	1.9	8.0	2.7	10.20	5
3	48.2	5.51	24.0	7.95	0.52	11	2.24	14.74	3.32	10.5	1.71	9.59	1.7	7.2	2.6	9.05	5
4	48.4	5.41	22.7	7.80	0.42	11	2.07	14.70	3.10	9.8	1.73	10.22	1.6	6.8	2.5	8.85	5
5	74.2	8.37	35.0	10.60	0.76	14	2.45	16.06	3.48	10.7	1.78	10.06	1.5	8.7	2.1	8.19	4
6	47.3	5.63	23.5	7.54	0.47	11	2.16	14.11	3.27	9.8	1.76	9.49	1.7	6.6	2.5	8.95	6
7	48.3	5.45	21.5	7.50	0.49	10	2.06	14.00	3.01	10.1	1.73	10.00	1.6	6.7	2.6	8.58	5
8	72.4	7.75	32.2	9.66	0.76	13	2.17	14.49	3.14	9.3	1.41	8.83	1.4	7.6	2.1	7.20	4
9	70.2	7.76	32.6	9.54	0.74	13	2.13	14.90	3.28	9.7	1.53	9.13	1.5	7.3	2.0	7.10	4
10	48.5	5.11	21.3	6.78	0.46	10	1.86	12.37	2.72	9.1	1.46	8.84	1.5	6.2	2.4	7.89	6

Table 14 Trace and major element compositions of RST glass shards from pumice and tuff samples determined using LA-ICPMS (continued)

Basal Fallout	*RST glass analysis (ppm)*																		
RST-7-3	Na	Mg	Al	K	Ca	V	Mn	Fe	Co	Zn	Rb	Sr	Cs	Ba	Ti	Y	Zr	Nb	La
1	36394	222	63462	44728	2511	0.22	698	6809	0.02	102.8	143	0.12	5.10	10.5	815.9	95.4	161.0	45.76	16.4
2	37167	226	64462	46623	2590	0.13	710	6698	n.d.	102.3	145	0.21	5.43	11.6	839.8	98.4	165.1	45.91	16.5
3	30550	225	62353	54834	2588	0.30	695	6540	0.03	101.0	144	0.33	5.37	11.0	808.3	98.7	162.1	45.47	16.2
4	36319	227	62548	46113	2520	0.25	690	6671	0.00	104.6	145	0.16	5.36	11.2	807.3	95.3	158.7	45.69	16.1
5	36675	221	60260	46910	2594	0.25	693	6663	0.06	105.9	144	0.21	5.54	10.7	816.0	85.7	146.1	45.15	14.7
6	37725	289	60893	46197	2643	0.58	703	6963	0.10	102.3	145	0.37	5.27	11.6	817.1	86.6	149.6	45.12	14.6
7	33101	296	65678	51979	2530	1.53	770	7209	0.16	86.6	147	4.05	5.71	13.0	848.0	92.1	162.9	47.49	16.7
8	34796	228	62084	49419	2575	0.42	711	6640	0.01	97.8	141	0.61	5.44	10.7	815.4	92.2	153.4	45.20	15.8
9	36451	219	58983	47707	2440	0.23	685	6734		102.9	145	0.18	5.30	10.9	796.7	85.3	143.2	44.37	14.2
RST-7-3b																			
1	34618	236	66598	45870	2503	0.16	710	6641	0.01	94.7	143	0.22	5.06	13.0	822.7	113.5	184.3	44.89	18.2
2	29994	259	72082	53801	2488	0.27	720	6649	0.04	93.8	145	0.41	4.99	13.4	823.3	127.0	207.8	47.37	20.0
3	35729	274	71565	45227	2507	0.26	754	6662	0.07	96.8	142	0.34	5.27	14.0	821.3	131.8	207.7	47.41	19.8
4	26866	344	64605	59023	2475	2.38	726	8497	0.31	93.1	145	2.18	4.97	15.4	874.2	108.9	185.2	46.86	18.6
5	31339	261	67160	51998	2415	0.61	724	6735	0.06	97.0	144	0.87	4.86	12.5	823.1	108.4	184.6	46.99	17.7
6	34952	258	68103	48117	2372	0.26	721	6748	0.03	95.7	145	0.22	5.18	12.8	824.6	112.6	187.9	47.03	18.8
7	35623	252	69937	46573	2261	0.24	727	6719	0.02	97.3	144	0.37	5.01	13.7	814.0	120.2	197.7	46.96	19.9
8	37729	302	70565	46660	2556	0.44	736	6875	0.06	94.2	145	0.33	5.23	13.9	844.5	126.8	209.0	46.99	20.3
9	34228	318	75487	48183	2500	0.57	754	6938	0.08	85.1	147	1.87	5.15	14.5	856.8	131.2	212.9	48.54	20.8

Table 14 Trace and major element compositions of RST glass shards from pumice and tuff samples determined using LA-ICPMS (continued)

Basal Fallout	*RST glass analysis (ppm)*																
RST-7-3	Ce	Pr	Nd	Sm	Eu	Gd	Tb	Dy	Ho	Er	Tm	Yb	Lu	Hf	Ta	Th	U
1	48.5	5.70	24.2	7.28	0.51	11	2.16	15.58	3.32	10.6	1.65	10.32	1.7	6.9	2.5	9.28	6
2	49.8	5.64	23.1	7.79	0.54	11	2.16	14.87	3.45	11.0	1.79	10.60	1.8	7.4	2.6	9.26	6
3	49.0	5.73	23.3	8.05	0.58	11	2.16	15.79	3.21	10.2	1.62	9.97	1.8	6.7	2.4	9.16	6
4	48.5	5.71	23.0	7.37	0.48	11	2.08	14.44	3.11	10.5	1.59	9.40	1.7	6.9	2.5	8.89	6
5	48.0	5.19	21.3	7.86	0.48	10	1.87	13.84	3.05	9.5	1.48	9.61	1.6	6.2	2.3	8.38	6
6	48.5	5.35	21.5	7.40	0.50	10	1.99	13.95	2.94	9.2	1.46	9.38	1.6	6.4	2.4	8.40	6
7	51.3	5.82	24.3	8.47	0.52	11	2.07	14.75	3.11	10.1	1.57	9.57	1.8	7.1	2.5	8.97	6
8	47.8	5.56	24.2	7.77	0.50	11	2.01	14.87	3.20	10.0	1.55	9.90	1.7	6.7	2.6	8.97	5
9	47.9	5.01	20.9	6.69	0.48	10	1.92	13.66	2.87	9.7	1.41	9.28	1.6	6.0	2.3	8.22	6
RST-7-3b																	
1	51.8	6.35	26.7	8.93	0.56	13	2.50	16.78	3.73	12.0	1.90	12.04	1.8	8.0	2.7	10.39	6
2	54.2	6.92	29.4	9.30	0.66	14	2.84	19.56	4.26	13.9	1.97	12.80	2.1	9.1	2.9	11.63	5
3	54.2	7.05	29.1	9.65	0.66	14	2.75	19.76	4.15	13.6	2.09	13.22	2.3	9.0	2.9	11.67	5
4	54.1	6.66	27.1	9.26	0.54	12	2.35	17.10	3.83	11.3	1.89	11.38	1.9	8.0	2.7	10.45	5
5	52.2	6.37	27.0	8.94	0.60	12	2.50	16.37	3.65	11.6	1.81	11.09	1.8	7.8	2.6	9.83	5
6	53.0	6.38	26.5	9.00	0.64	13	2.53	17.43	3.84	12.1	1.93	12.10	2.0	8.1	2.6	10.39	6
7	54.0	6.82	29.1	9.25	0.58	13	2.53	18.18	3.99	12.3	1.97	12.33	2.1	8.3	2.6	10.93	6
8	55.0	6.89	29.1	9.98	0.60	14	2.83	19.76	4.20	13.1	2.14	13.05	2.2	9.1	2.8	11.32	6
9	53.7	7.24	30.7	9.82	0.67	14	2.89	19.53	4.18	13.8	2.21	13.37	2.1	9.3	2.8	11.65	5

Table 14 Trace and major element compositions of RST glass shards from pumice and tuff samples determined using LA-ICPMS (continued)

Basal Fallout RST-7-3c	*RST glass analysis (ppm)* Na	Mg	Al	K	Ca	V	Mn	Fe	Co	Zn	Rb	Sr	Cs	Ba	Ti	Y	Zr	Nb	La
1	34746	222	63027	43375	2087	0.18	664	6365	0.04	97.1	123	0.21	5.10	11.0	779.4	98.9	164.4	43.87	16.2
2	34913	229	61964	43169	2206	0.19	670	6329	0.00	97.0	138	0.16	4.99	11.1	794.8	95.6	162.2	43.10	15.9
3	33797	217	61412	42642	2067	0.28	654	6244	0.01	95.3	136	0.15	4.87	11.0	759.7	95.8	161.7	42.17	16.1
4	31771	250	64924	47471	2121	0.53	679	6327	0.05	91.9	136	0.71	4.89	11.4	769.5	102.9	170.1	43.09	16.9
5	35831	216	63699	43341	2087	0.20	659	6110	0.01	97.5	135	0.14	5.05	11.2	766.5	99.6	166.9	42.48	16.5
6	35519	226	61350	43786	2240	0.26	675	6502	0.02	96.1	138	0.20	5.15	11.6	760.8	96.4	163.1	43.54	15.6
7	35020	217	61937	43366	2135	0.19	658	6382		98.5	138	0.19	4.92	10.7	773.6	94.8	159.6	42.89	15.7
8	36174	221	60301	43916	2032	0.23	648	6465	0.02	100.6	141	0.16	4.94	10.9	779.3	90.5	154.5	41.86	15.4
9	32893	252	63430	49344	2146	0.44	723	6830	0.01	88.6	140	0.57	5.10	12.3	778.5	96.6	164.1	44.00	16.7
Basal Fallout Average	34478	248	64773	47421	2377	0.43	702	6702	0.05	96.9	142	0.57	5.16	12.1	808.6	103.0	172.1	45.19	17.1
σ	2552	35	4157	4003	200	0.47	33	432	0.07	5.1	5	0.85	0.22	1.4	30.3	13.9	20.3	1.88	1.9

RST-7-3c	Ce	Pr	Nd	Sm	Eu	Gd	Tb	Dy	Ho	Er	Tm	Yb	Lu	Hf	Ta	Th	U
1	47.1	5.84	24.2	7.93	0.53	11	2.24	14.54	3.23	10.8	1.61	10.09	1.7	6.6	2.5	9.05	5
2	47.9	5.53	22.7	7.82	0.51	12	1.96	14.10	3.32	10.2	1.50	10.57	1.6	7.0	2.4	9.16	5
3	47.5	5.77	22.7	7.52	0.53	11	2.11	14.31	3.21	10.0	1.66	9.54	1.6	6.8	2.4	9.18	5
4	47.5	5.80	23.8	8.74	0.51	12	2.24	14.51	3.33	10.9	1.58	10.41	1.7	7.4	2.5	9.32	5
5	48.7	5.92	23.3	8.25	0.52	11	2.26	15.09	3.49	10.9	1.69	10.44	1.7	7.3	2.6	9.28	5
6	48.1	5.61	22.4	8.01	0.52	12	2.12	14.24	3.33	10.7	1.54	9.77	1.6	6.9	2.5	8.96	5
7	48.3	5.56	23.1	7.57	0.53	11	2.14	15.02	3.14	10.1	1.64	9.92	1.6	6.5	2.5	9.23	5
8	46.8	5.36	22.5	7.38	0.49	10	1.99	13.47	3.16	10.0	1.55	9.26	1.6	6.8	2.4	8.79	5
9	48.3	5.77	23.7	8.10	0.50	12	2.22	14.78	3.08	10.1	1.59	10.65	1.5	6.6	2.5	9.13	5
Basal Fallout Avg	50.1	5.98	24.8	8.30	0.55	12	2.27	15.79	3.46	11.0	1.72	10.74	1.8	7.4	2.5	9.63	6
σ	2.7	0.61	2.8	0.87	0.06	1	0.30	2.02	0.42	1.3	0.22	1.32	0.2	0.9	0.2	1.04	0

Table 15 Standard materials major and trace element compositions determined using LA-ICPMS

Standard Materials	Na	Mg	Al	K	Ca	V	Mn	Fe	Co	Zn	Rb	Sr	Cs	Ba	Ti	Y	Zr	Nb	La
BCR Avg	23512	21145	72772	14810	51165	416.89	1521	95606	37.02	128.1	47	339.47	1.09	677.0	13740.2	35.0	184.0	12.60	24.7
σ	272	545	1627	202	1278	5.73	25	1028	0.53	4.7	1	5.10	0.04	12.6	220.8	0.7	3.3	0.30	0.6
%RSD	1%	3%	2%	1%	2%	3%	1%	4%	2%	1%	1%	19%	9%	4%	7%	2%	2%	2%	4%
BIR Average	13325	58734	79214	203	95061	318.01	1406	80598	52.02	66.7	0	109.62	0.03	6.5	5533.7	13.8	13.0	0.50	0.6
σ	198	1033	2202	6	1926	5.72	22	790	0.62	2.8	0	3.93	0.02	0.4	156.6	0.8	0.8	0.06	0.1
%RSD	10%	35%	4%	6%	72%	7%	24%	7%	3%	6%	6%	12%	9%	5%	7%	9%	13%	8%	9%
NIST 610 Avg	120104	536	11486	577	94850	510.29	537	582	471.48	466.6	486	604.26	408.51	504.1	486.8	647.8	577.2	492.91	517.0
σ	2247	29	374	24	3839	10.72	24	35	10.48	22.9	12	27.44	11.59	19.5	18.5	44.9	37.4	22.93	27.9
%RSD	2%	6%	3%	4%	4%	6%	2%	3%	5%	6%	2%	19%	8%	5%	11%	3%	5%	7%	3%
Standard Concentration	99408	465	10796	486	82190	442.00	485	458	405.00	456.0	426	515.50	361.00	435.0	434.0	450.0	440.0	419.00	457.0
Accuracy	17%	13%	6%	16%	13%	13%	10%	21%	14%	2%	12%	15%	12%	14%	11%	31%	24%	15%	12%
NIST 612 Avg	147827	67	10021	150	84584	50.97	45	87	43.21	45.4	43	78.80	55.03	39.0	41.0	41.5	39.0	37.14	35.0
σ	6044	22	482	283	2996	1.74	2	20	1.60	2.4	2	2.81	2.69	1.5	2.4	2.2	2.0	1.44	1.5
%RSD	4%	32%	5%	188%	4%	6%	3%	6%	4%	24%	4%	19%	9%	5%	12%	4%	4%	5%	5%
Standard Concentration	103859	77	11167	66	85049	39.00	38	51	35.00	38.0	31	78.40	42.00	40.0	44.0	38.0	38.0	40.00	35.8
Accuracy	30%	15%	11%	56%	1%	23%	16%	41%	19%	16%	27%	1%	24%	3%	7%	8%	3%	8%	2%
Estimated Overall Uncertainty	20%	15%	10%	20%	10%	20%	15%	25%	20%	5%	20%	5%	20%	5%	10%	10%	5%	10%	5%

Table 15 Standard materials major and trace element compositions determined using LA-ICPMS (continued)

Standard Materials	Ce	Pr	Nd	Sm	Eu	Gd	Tb	Dy	Ho	Er	Tm	Yb	Lu	Hf	Ta	Th	U
BCR Avg	53.3	6.70	28.9	6.55	1.96	7	1.07	6.41	1.28	3.7	0.54	3.39	0.5	4.9	0.7	5.90	2
σ	1.2	0.13	0.7	0.21	0.06	0	0.04	0.22	0.05	0.1	0.03	0.13	0.0	0.1	0.0	0.12	0
%RSD	2%	5%	3%	2%	2%	2%	2%	2%	2%	2%	2%	3%	3%	4%	4%	3%	4%
BIR Average	1.9	0.37	2.3	1.02	0.51	2	0.34	2.37	0.51	1.5	0.22	1.50	0.2	0.5	0.0	0.03	0
σ	0.1	0.03	0.2	0.13	0.04	0	0.03	0.17	0.05	0.1	0.02	0.12	0.0	0.1	0.0	0.01	0
%RSD	8%	7%	11%	9%	11%	8%	12%	12%	24%	21%	29%	7.89	11.9	11.8	24.2	21.45	29
NIST 610 Avg	528.0	530.27	519.5	546.19	522.06	773	591.06	592.46	617.51	625.3	638.63	597.90	608.5	575.5	506.1	552.27	536
σ	18.7	24.66	28.5	33.17	27.41	741	125.39	43.47	42.44	43.7	50.27	36.52	45.7	40.2	28.6	33.61	11
%RSD	4%	6%	7%	4%	7%	6%	5%	5%	4%	5%	5%	6%	5%	96%	21%	7%	7%
Standard Concentration	448.0	430.00	431.0	451.00	461.00	444	443.00	427.00	449.00	426.0	420.00	445.00	435.0	432.0	452.0	457.20	462
Accuracy	15%	19%	17%	17%	12%	43%	25%	28%	27%	32%	34%	26%	29%	25%	11%	17%	14%
NIST 612 Avg	42.4	38.42	35.4	36.56	34.38	50	38.30	37.08	39.58	40.1	40.68	38.73	38.7	38.1	34.0	36.39	50
σ	1.4	1.42	1.7	1.77	1.21	47	7.86	2.13	2.10	2.0	2.48	1.86	2.2	1.9	1.4	1.60	2
%RSD	4%	4%	59%	6%	5%	5%	4%	4%	3%	4%	5%	5%	4%	95%	21%	6%	5%
Standard Concentration	38.7	37.20	35.9	38.10	35.00	37	36.00	36.00	38.00	38.0	38.00	39.20	36.9	35.0	40.0	37.79	37
Accuracy	9%	3%	1%	4%	2%	26%	6%	3%	4%	5%	7%	1%	5%	8%	18%	4%	25%
Estimated Overall Uncertainty	10%	5%	5%	5%	5%	25%	10%	5%	5%	5%	10%	5%	5%	10%	20%	5%	25%

Table 16 Pb isotopic compositions for RST sanidine.

Analysis	Isotope ratios									
	$^{208}Pb/^{206}Pb$	±1s (abs)	$^{207}Pb/^{206}Pb$	±1s (abs)	$^{208}Pb/^{204}Pb$	±1s (abs)	$^{207}Pb/^{204}Pb$	±1s (abs)	$^{206}Pb/^{204}Pb$	±1s (abs)
RST-2-1 L4	2.046484	0.000029	0.8295286	0.0000118	38.5231	0.0015	15.61511	0.00060	18.82441	0.00075
RST-2-1 L5	2.046024	0.000008	0.8294614	0.0000028	38.4918	0.0005	15.60470	0.00020	18.81321	0.00023
RST-3-2 L4	2.052274	0.000015	0.8341506	0.0000076	38.3091	0.0025	15.57083	0.00102	18.66684	0.00122
RST-3-2 L5	2.052744	0.000030	0.8338130	0.0000098	38.3891	0.0035	15.59340	0.00142	18.70104	0.00168
RST-3-3 L4	2.047235	0.000015	0.8301276	0.0000074	38.4973	0.0026	15.61047	0.00108	18.80471	0.00130
RST-3-3 L5	2.047416	0.000020	0.8303949	0.0000085	38.4662	0.0026	15.60094	0.00107	18.78745	0.00129
RST-4-2 L4	2.045965	0.000022	0.8297546	0.0000085	38.4644	0.0027	15.59914	0.00110	18.79962	0.00132
RST-4-2 L5	2.046100	0.000011	0.8297600	0.0000045	38.4569	0.0014	15.59553	0.00054	18.79527	0.00065
RST-4-3 L4	2.045966	0.000007	0.8295698	0.0000031	38.4645	0.0007	15.59608	0.00027	18.80024	0.00032
RST-4-3 L5	2.047357	0.000013	0.8299353	0.0000057	38.5213	0.0019	15.61538	0.00075	18.81521	0.00091

Table 17 Major and trace element compositions of RST feldspars determined using LA-ICPMS

Concentration (ppm)

Spot #	Na	Al	K	Ca	Ti	Rb	Sr	Ba	La	Ce	Pr	Nd	Sm	Eu	Gd	Dy	Er	Yb	Th	U
Group B pumice																				
RST-2-1 1	46815	73674	71736	1831	53.6	36	6.46	1683	0.71	0.82	0.031	0.068	0.017	2.94	n.d.	n.d.	n.d.	n.d.	n.d.	n.d.
RST-2-1 2	46347	79178	71594	1868	48.1	35	6.59	1767	0.76	0.80	0.041	0.126	0.013	2.93	n.d.	0.02	0.0163	0.0042	n.d.	n.d.
RST-2-1 4	48503	75472	67359	1816	62.5	34	7.69	1721	1.31	1.31	0.253	0.824	0.184	3.14	0.255	0.27	0.0486	0.0397	0.0285	0.020
RST-2-1 5	47545	77858	70043	1828	57.8	35	7.02	1691	0.85	0.89	0.043	0.100	0.003	3.17	0.037	n.d.	n.d.	0.0184	0.0017	0.003
RST-2-1 7	48764	78861	68715	1623	64.6	33	7.19	1765	0.81	0.84	0.042	0.102	0.011	3.32	n.d.	0.04	n.d.	n.d.	0.0029	0.002
Group C pumice #1																				
RST-2-3 16	50374	79099	63646	1980	57.1	27	17.61	4402	0.96	1.10	0.055	0.111	n.d.	4.17	0.027	0.06	n.d.	n.d.	0.0029	n.d.
RST-2-3 17	52012	79363	61616	2289	56.6	26	18.49	4924	1.05	1.21	0.053	0.166	n.d.	4.25	n.d.	n.d.	n.d.	n.d.	n.d.	0.003
RST-2-3 18	51576	78668	63236	2342	54.3	27	19.19	5004	1.02	1.15	0.058	0.125	0.018	4.29	0.084	0.06	n.d.	0.0006	n.d.	0.002
RST-2-3 19	51937	79532	64188	1820	56.3	27	18.32	4900	1.07	1.10	0.063	0.122	0.012	4.16	n.d.	0.05	0.0097	n.d.	0.0015	0.004
RST-2-3 20	49126	80235	61300	1969	59.8	26	18.41	4832	1.01	1.06	0.051	0.145	n.d.	4.26	n.d.	0.04	n.d.	n.d.	0.0015	0.000
RST-2-3 21	49482	82570	63480	2296	56.8	25	20.10	4931	1.14	1.16	0.053	0.135	0.003	4.46	n.d.	0.11	n.d.	n.d.	n.d.	n.d.
RST-2-3 22	49105	81739	61074	1891	51.5	25	18.50	4697	1.04	1.08	0.054	0.141	n.d.	4.16	0.087	n.d.	n.d.	n.d.	n.d.	0.003
RST-2-3 23	50700	82745	63112	2185	55.9	26	18.87	5102	1.08	1.16	0.063	0.133	n.d.	4.38	0.032	0.04	n.d.	n.d.	n.d.	0.006
RST-2-3 24	48807	75124	62989	2151	53.7	27	17.59	4662	0.95	1.12	0.063	0.155	0.003	3.90	0.057	n.d.	n.d.	0.0141	0.0013	0.004
Group C pumice #2																				
RST-2-2 10	50917	80916	65192	2199	55.7	27	19.73	5175	1.09	1.20	0.068	0.133	0.026	4.46	n.d.	0.03	n.d.	n.d.	0.0015	0.009
RST-2-2 11	51683	80053	64958	2161	58.9	26	18.88	4624	1.07	1.16	0.060	0.132	n.d.	4.27	n.d.	n.d.	0.0061	n.d.	n.d.	0.002
RST-2-2 12	49227	78163	61569	2020	55.5	26	18.29	4740	1.00	1.05	0.055	0.157	n.d.	4.01	n.d.	n.d.	0.0036	n.d.	n.d.	0.000
RST-2-2 13	50835	84750	64605	2342	53.0	26	20.51	5117	1.08	1.18	0.055	0.130	0.028	4.73	n.d.	n.d.	n.d.	0.0109	0.0047	0.006
RST-2-2 14	46480	79603	68468	2117	52.7	32	10.54	2908	0.89	0.99	0.051	0.085	0.027	3.51	n.d.	0.02	n.d.	0.0099	n.d.	0.003
RST-2-2 15	47218	80181	68539	1879	49.8	31	10.87	3064	0.86	0.99	0.044	0.121	0.009	3.52	0.008	n.d.	n.d.	n.d.	0.0015	0.003
RST-2-2 9	47810	76583	66672	1992	53.7	31	11.03	3146	0.91	0.97	0.049	0.129	n.d.	3.64	n.d.	0.05	n.d.	0.0103	0.0014	n.d.

Table 17 Major and trace element compositions of RST feldspars determined using LA-ICPMS (continued)

Concentration (ppm)

Spot #	Na	Al	K	Ca	Ti	Rb	Sr	Ba	La	Ce	Pr	Nd	Sm	Eu	Gd	Dy	Er	Yb	Th	U
Banded pumice																				
RST-6-1 36	74120	104404	9331	19578	82.5	2	259.69	1218	5.48	7.00	0.549	1.525	0.149	2.74	0.149	n.d.	n.d.	0.0150	n.d.	n.d.
RST-6-1 37	62942	139677	3602	49800	133.4	1	984.83	581	5.75	7.96	0.725	1.993	0.271	1.63	0.165	0.05	0.0248	0.0648	0.0114	0.006
RST-6-1 38	63895	137634	3276	48700	145.3	0	993.93	499	5.42	7.51	0.661	2.003	0.194	1.57	0.209	0.03	0.0150	n.d.	n.d.	0.002
RST-6-1 39	52902	177964	1788	84270	390.9	1	1046.40	320	3.46	5.20	0.518	2.062	0.227	2.11	0.193	0.32	0.0153	0.0010	0.0023	n.d.
RST-6-1 40	48561	84344	70982	1800	50.6	35	7.85	1769	0.89	0.87	0.050	0.114	n.d.	3.26	n.d.	n.d.	n.d.	n.d.	0.0048	0.001
RST-6-1 41	52631	207703	1690	101003	302.9	0	2126.72	301	5.06	7.75	0.833	3.091	0.363	1.29	0.244	0.12	0.0549	0.0038	0.0028	n.d.
RST-6-1 42	51791	237283	1589	122809	379.2	0	3119.46	280	4.97	7.27	0.815	3.016	0.340	1.19	0.133	0.17	n.d.	0.0270	n.d.	n.d.
RST-6-1 43	47801	240098	2085	125029	551.0	4	2028.33	267	6.02	9.87	1.121	4.848	0.639	1.21	0.513	0.57	0.2195	0.1947	0.6054	0.207
RST-6-1 44	54529	210551	1462	103113	381.5	0	1726.55	252	2.89	4.47	0.483	1.995	0.197	1.65	0.214	0.12	0.0283	0.0387	0.0087	0.011
RST-6-1 46	67300	117570	5126	30172	71.6	2	505.63	774	5.36	7.40	0.663	2.004	0.230	3.65	0.082	0.09	0.0278	0.0210	0.0757	0.017
Welded tuff																				
RST-5-1 26	52250	78580	51409	2618	72.0	19	39.00	6837	2.23	3.87	0.369	1.388	0.211	5.25	0.268	0.08	0.1082	0.1804	0.1376	0.070
RST-5-1 27	68862	93406	27319	7087	71.9	6	239.13	11840	3.09	3.47	0.232	0.560	0.050	10.99	n.d.	n.d.	n.d.	0.0107	n.d.	n.d.
RST-5-1 28	70951	94285	28062	8063	73.9	6	246.81	11966	3.26	3.63	0.224	0.659	0.072	11.78	0.130	n.d.	0.0042	n.d.	n.d.	n.d.
RST-5-1 29	64472	90248	27167	7172	65.5	6	194.29	10120	3.24	3.72	0.239	0.693	0.039	10.90	0.005	n.d.	n.d.	n.d.	n.d.	0.007
RST-5-1 33	47411	97610	65407	2446	66.4	30	20.34	4942	1.34	1.49	0.091	0.274	0.014	4.69	0.052	0.07	0.0206	0.0088	0.0570	0.170
RST-5-1 34	51897	114848	72723	2570	58.5	34	20.70	4593	1.61	1.28	0.099	0.321	n.d.	5.57	n.d.	n.d.	n.d.	n.d.	0.0026	n.d.
RST-5-1 35	64483	79210	41752	2933	58.0	12	53.56	6846	1.11	1.29	0.073	0.164	n.d.	5.01	0.015	n.d.	n.d.	n.d.	n.d.	0.000
Unwelded tuff																				
RST-7-4 50	50471	87769	62705	2223	57.1	26	20.44	5131	1.15	1.12	0.059	0.126	0.019	4.77	n.d.	n.d.	n.d.	n.d.	n.d.	0.002
RST-7-4 51	48463	85948	63240	2220	54.1	25	20.03	4983	1.17	1.21	0.065	0.178	n.d.	4.46	0.015	0.10	n.d.	n.d.	0.0014	n.d.
RST-7-4 52	49253	85188	63363	2412	60.8	26	35.48	7224	1.26	1.40	0.080	0.138	0.004	5.36	0.058	n.d.	n.d.	n.d.	n.d.	n.d.
RST-7-4 53	47160	83040	67158	2168	54.6	31	10.40	2826	0.89	0.98	0.048	0.138	n.d.	3.36	n.d.	0.02	0.0022	n.d.	0.0111	n.d.
RST-7-4 54	50251	79087	64409	2079	57.9	25	17.83	4363	1.05	1.22	0.069	0.229	0.010	3.99	0.003	0.05	0.0157	0.0105	0.0310	0.007
RST-7-4 55	47503	78479	68882	1943	66.7	34	6.48	1661	1.09	1.82	0.120	0.523	0.125	2.95	0.051	0.19	0.1225	0.1497	0.1693	0.090
Basal fallout																				
RST-7-3 56	65254	135576	8203	45843	136.5	2	775.93	1037	7.26	9.85	0.860	2.864	0.285	4.63	0.180	0.10	0.0291	0.0095	n.d.	0.002
RST-7-3 57	64947	145592	7823	50561	161.3	2	1003.72	1013	6.63	8.71	0.789	2.732	0.381	5.07	0.280	0.13	0.0472	0.0544	0.1550	0.034
RST-7-3 59	70462	108559	9810	28275	135.8	2	435.03	1573	8.71	11.75	0.873	2.424	0.254	2.12	0.173	0.02	0.0187	0.0133	0.0142	0.002
RST-7-3 61	48737	83006	69377	2093	53.2	30	10.74	2939	0.96	1.04	0.059	0.128	n.d.	3.50	0.055	n.d.	n.d.	0.0008	0.0014	0.003
RST-7-3 62	42928	96437	66321	1908	175.9	45	10.31	2357	11.10	20.61	2.734	12.679	3.377	3.61	3.986	5.12	3.2490	3.0176	2.2131	0.665
RST-7-3 63	55278	84370	53096	2334	57.6	22	20.04	4735	1.09	1.11	0.066	0.131	0.018	4.39	n.d.	0.05	0.0031	n.d.	0.0013	n.d.

Table 18 RST zircon trace element compositions, crystallization temperatures and apparent U-Pb ages determined using LA-ICPMS

	Apparent age				*Concentration (ppm)*																	
Spot #	206Pb*/ 238U*	±2s (Ma)	Ti-in-zircon T(°C)	Eu/Eu*	P	Ti	Y	Nb	La	Ce	Pr	Nd	Sm	Eu	Gd	Tb	Dy	Ho	Er	Tm	Yb	Lu
Group B pumice																						
RST-2-1 L 70	8.23	1.12	739	0.17	1158	5.59	5749	75	n.d.	109.49	0.056	2.64	9.89	1.67	91.0	39.35	545	217	878	206	2081	308
RST-2-1 L 71	7.60	0.97	652	0.16	1920	2.00	5045	29	3.318	47.05	1.123	7.02	7.86	1.20	68.6	27.98	436	179	750	176	1904	287
RST-2-1 L 72	7.07	0.60	733	0.13	1343	5.23	7029	112	n.d.	147.27	0.143	2.15	14.24	1.64	100.7	46.17	641	257	1081	249	2459	369
RST-2-1 L 73	7.14	0.61	734	0.13	2567	5.26	10407	107	4.981	165.97	3.343	22.30	27.22	2.84	174.8	70.01	983	391	1578	353	3381	510
RST-2-1 L 74	7.16	1.08	729	0.18	1136	5.00	6158	95	n.d.	129.09	n.d.	2.52	8.75	1.75	97.7	42.02	573	228	923	216	2019	326
RST-2-1 L 75	6.89	0.72	718	0.21	1185	4.41	6469	75	n.d.	116.63	0.066	1.85	6.85	1.63	85.2	42.77	592	236	982	224	2271	364
RST-2-1 L 76	6.83	1.04	756	0.15	1193	6.66	7085	73	n.d.	112.63	0.107	2.68	16.70	2.36	147.1	53.79	726	266	1083	234	2281	315
RST-2-1 L 77	7.33	0.72	752	0.15	1273	6.42	6740	51	5.519	139.10	1.881	8.52	17.76	2.19	114.1	47.89	655	249	1050	239	2359	356
RST-2-1 L 78	6.50	1.12	761	0.19	1459	7.02	4066	22	0.211	40.04	0.187	1.85	4.63	0.99	52.7	25.24	358	150	636	149	1506	230
RST-2-1 L 79	6.87	0.77	739	0.20	1316	5.55	6989	74	n.d.	127.86	0.119	1.67	15.00	2.73	119.7	52.54	692	266	1078	231	2288	351
RST-2-1 L 81	7.41	1.29	715	0.19	1344	4.26	6506	75	0.410	115.52	0.139	2.25	10.36	2.03	98.7	40.43	594	238	1001	225	2196	360
RST-2-1 L 82	5.37	1.01	684	0.07	1378	2.97	4513	25	n.d.	44.55	n.d.	1.42	5.91	0.43	54.4	28.25	396	157	693	155	1587	255
Average	7.03	0.92	726	0.16	1439	5.03	6396	67	2.888	107.93	0.716	4.74	12.10	1.79	100.4	43.04	599	236	978	221	2194	336
σ	0.68	0.23	31	0.04	412	1.47	1616	30	2.490	41.80	1.103	5.97	6.42	0.70	35.7	12.61	167	63	245	53	477	71
Group C pumice #1																						
RST-2-3 L 20	8.07	2.79	664	0.24	829	2.32	1574	9	20.855	70.90	8.487	47.89	16.37	2.19	46.7	15.92	184	63	243	53	498	77
RST-2-3 L 21	6.62	0.54	703	0.16	1255	3.73	5623	75	n.d.	115.14	0.172	3.07	7.85	1.40	87.2	39.04	543	215	905	206	2086	312
RST-2-3 L 22	7.00	1.92	715	0.18	778	4.25	2996	29	n.d.	51.92	n.d.	1.51	6.37	1.05	49.2	20.84	286	109	463	105	1092	164
RST-2-3 L 23	6.41	1.28	701	0.23	1600	3.66	5584	32	10.361	103.88	5.498	36.18	20.07	3.20	91.9	43.70	537	208	877	206	1975	293
RST-2-3 L 24	11.64	2.96	738	0.54	1722	5.54	5602	32	3.865	67.78	1.979	23.07	19.84	7.87	99.2	39.70	517	193	834	189	1848	289
RST-2-3 L 25	9.77	2.62	723	0.19	1020	4.69	3959	32	0.923	56.95	0.449	7.94	13.29	2.01	78.1	30.54	410	158	615	141	1362	205
RST-2-3 L 26	6.24	0.68	719	0.16	1816	4.45	6095	48	0.279	74.74	0.310	3.53	14.36	2.17	115.4	45.39	629	247	951	207	1942	298
RST-2-3 L 27	6.37	0.88	666	0.15	1438	2.40	6571	79	1.866	125.18	0.775	5.21	13.06	1.73	98.1	41.77	619	245	1035	236	2361	373
RST-2-3 L 28	6.48	1.20	667	0.10	1318	2.40	4035	25	0.503	45.97	0.268	3.34	9.08	0.80	69.7	26.60	366	151	639	146	1461	221
RST-2-3 L 29	8.36	1.40	755	0.14	1415	6.60	5890	71	0.141	107.31	0.090	3.57	11.80	1.45	88.3	40.92	543	212	903	207	2057	315
RST-2-3 L 30	7.23	1.37	713	0.19	8985	4.19	6933	55	475.703	1267.97	167.503	976.68	314.37	20.58	352.5	77.06	770	266	1046	221	2186	347
RST-2-3 L 31	5.42	1.30	753	0.16	2048	6.48	6857	43	0.686	79.07	0.379	2.42	10.62	1.64	92.3	40.57	602	249	1060	231	2404	394
Average	7.47	1.58	710	0.20	2019	4.22	5143	44	51.518	180.57	16.901	92.87	38.09	3.84	105.7	38.50	500	193	797	179	1773	274
σ	1.76	0.82	32	0.11	2227	1.46	1658	22	149.188	343.41	50.023	278.74	87.11	5.59	80.2	15.41	163	62	256	56	566	92

Table 18 RST zircon trace element compositions, crystallization temperatures and apparent U-Pb ages determined using LA-ICPMS (continued)

	Concentration (ppm)				*Trace Element Ratios*			
Spot #	Hf	Ta	Th	U	Th/U	Th/Y	Hf/Y	Y/U
Group B pumice								
RST-2-1 L 70	11376	13.82	408	809	0.50	0.07	1.98	7.11
RST-2-1 L 71	10816	7.26	157	451	0.35	0.03	2.14	11.19
RST-2-1 L 72	12165	18.13	603	1090	0.55	0.09	1.73	6.45
RST-2-1 L 73	11856	18.12	643	1231	0.52	0.06	1.14	8.46
RST-2-1 L 74	11811	16.31	496	957	0.52	0.08	1.92	6.43
RST-2-1 L 75	11857	11.11	285	649	0.44	0.04	1.83	9.96
RST-2-1 L 76	9313	10.34	253	642	0.39	0.04	1.31	11.04
RST-2-1 L 77	11802	11.10	378	697	0.54	0.06	1.75	9.67
RST-2-1 L 78	11450	5.64	102	317	0.32	0.03	2.82	12.81
RST-2-1 L 79	10859	11.38	342	785	0.44	0.05	1.55	8.90
RST-2-1 L 81	11850	13.06	332	702	0.47	0.05	1.82	9.27
RST-2-1 L 82	12407	4.91	141	408	0.35	0.03	2.75	11.07
Average	11463	11.77	345	728	0.45	0.05	1.90	9.36
σ	825	4.42	174	271	0.08	0.02	0.50	2.01
Group C pumice #1								
RST-2-3 L 20	7020	1.89	39	108	0.36	0.02	4.46	14.53
RST-2-3 L 21	10017	12.95	394	810	0.49	0.07	1.78	6.94
RST-2-3 L 22	9420	5.95	109	288	0.38	0.04	3.14	10.42
RST-2-3 L 23	11152	6.29	258	539	0.48	0.05	2.00	10.37
RST-2-3 L 24	11764	6.46	228	518	0.44	0.04	2.10	10.81
RST-2-3 L 25	9624	7.16	131	365	0.36	0.03	2.43	10.84
RST-2-3 L 26	9481	7.23	219	547	0.40	0.04	1.56	11.14
RST-2-3 L 27	11944	14.27	413	841	0.49	0.06	1.82	7.82
RST-2-3 L 28	9529	5.33	133	366	0.36	0.03	2.36	11.01
RST-2-3 L 29	11859	13.46	389	863	0.45	0.07	2.01	6.83
RST-2-3 L 30	12768	10.72	345	718	0.48	0.05	1.84	9.65
RST-2-3 L 31	11675	7.79	237	534	0.44	0.03	1.70	12.84
Average	10521	8.29	241	541	0.43	0.04	2.27	10.27
σ	1616	3.76	124	236	0.05	0.01	0.81	2.26

Table 18 RST zircon trace element compositions, crystallization temperatures and apparent U-Pb ages determined using LA-ICPMS (continued)

	Apparent age				*Concentration (ppm)*																
Spot #	206Pb*/238U*	±2s (Ma)	Ti-in-zircon T(°C)	Eu/Eu*	P	Ti	Y	Nb	La	Ce	Pr	Nd	Sm	Eu	Gd	Tb	Dy	Ho	Er	Tm	Yb	Lu
Group C pumice #2																						
RST-2-2 L 32	6.92	0.86	729	0.12	4285	5.02	8625	95	99.055	382.85	46.397	266.78	131.44	7.67	270.0	75.83	923	323	1328	296	2952	431
RST-2-2 L 33	6.97	1.36	675	0.13	1364	2.68	3911	22	0.176	46.28	0.161	0.70	4.59	0.67	54.9	23.57	352	148	637	148	1510	229
RST-2-2 L 34	7.33	0.92	695	0.17	1805	3.39	7213	75	n.d.	126.25	n.d.	1.25	11.33	1.99	111.6	47.57	675	266	1124	259	2629	385
RST-2-2 L 35	7.51	1.31	742	0.16	1968	5.76	8128	92	0.980	136.74	0.390	6.00	19.15	2.68	138.2	56.39	793	310	1275	276	2828	417
RST-2-2 L 36	8.63	1.72	768	0.46	1671	7.55	4697	22	0.964	43.47	0.892	5.00	7.31	3.35	66.9	27.73	409	172	721	169	1768	280
RST-2-2 L 37	5.89	0.73	722	0.17	1499	4.62	6932	84	n.d.	126.32	n.d.	2.26	10.72	1.83	106.7	44.14	631	253	1086	239	2482	371
RST-2-2 L 38	8.74	1.27	671	0.11	1615	2.53	5255	43	0.302	71.48	0.193	3.01	7.03	0.84	74.4	34.99	479	201	862	196	1982	314
RST-2-2 L 39	7.17	0.90	687	0.14	1699	3.08	7034	83	n.d.	132.76	0.032	1.91	15.34	2.01	118.3	53.50	743	280	1157	255	2512	384
RST-2-2 L 40	7.40	0.83	737	0.59	1949	5.46	7468	55	7.390	102.54	5.044	31.08	30.34	12.22	130.4	54.52	720	272	1115	241	2318	380
RST-2-2 L 42	7.71	0.84	722	0.15	1214	4.60	7550	28	0.790	107.28	0.223	3.31	21.07	2.51	125.1	51.92	722	283	1157	242	2381	393
RST-2-2 L 43	5.19	0.71	745	0.10	1230	5.95	5931	55	n.d.	93.71	0.088	1.28	9.88	0.92	83.5	39.68	558	224	925	201	1998	330
RST-2-2 L 44	6.97	1.31	747	0.18	869	6.06	4553	43	0.612	73.48	0.147	4.01	7.18	1.43	84.2	32.15	451	176	710	151	1453	241
RST-2-2 L 45	7.18	0.68	831	0.99	1369	13.89	6207	71	9.682	109.06	7.202	41.14	43.70	24.46	130.9	48.70	624	215	897	200	2038	303
RST-2-2 L 46	6.74	1.16	657	0.22	1599	2.12	4177	21	n.d.	39.84	n.d.	1.21	7.97	1.58	62.9	23.18	362	144	649	151	1612	237
RST-2-2 L 47	6.77	0.96	680	0.17	1698	2.85	5860	52	n.d.	99.10	n.d.	2.17	12.44	1.95	100.1	40.30	552	221	894	206	2090	304
RST-2-2 L 48	6.67	0.59	787	0.18	1314	9.10	6226	74	0.569	126.57	0.251	2.94	9.33	1.73	92.1	40.31	559	223	954	221	2247	315
RST-2-2 L 49	5.68	0.98	710	0.21	1664	4.05	6206	36	n.d.	81.64	n.d.	0.90	11.19	2.24	91.7	41.31	578	233	985	221	2213	323
RST-2-2 L 50	5.63	0.91	678	0.13	1936	2.77	5415	28	n.d.	44.69	n.d.	2.12	11.57	1.33	81.3	38.05	528	203	843	185	1788	259
RST-2-2 L 51	6.88	0.91	694	0.09	1653	3.35	5147	27	n.d.	57.47	n.d.	n.d.	7.01	0.69	71.8	28.73	452	183	791	178	1777	283

Table 18 RST zircon trace element compositions, crystallization temperatures and apparent U-Pb ages determined using LA-ICPMS (continued)

	Concentration (ppm)				*Trace Element Ratios*			
Spot #	Hf	Ta	Th	U	Th/U	Th/Y	Hf/Y	Y/U
Group C pumice #2								
RST-2-2 L 32	11479	16.06	723	1304	0.55	0.08	1.33	6.62
RST-2-2 L 33	10995	5.36	135	359	0.38	0.03	2.81	10.90
RST-2-2 L 34	11491	14.34	498	1009	0.49	0.07	1.59	7.15
RST-2-2 L 35	11492	16.84	652	1139	0.57	0.08	1.41	7.13
RST-2-2 L 36	12117	5.86	148	403	0.37	0.03	2.58	11.66
RST-2-2 L 37	12418	15.62	445	960	0.46	0.06	1.79	7.22
RST-2-2 L 38	12469	10.15	272	695	0.39	0.05	2.37	7.56
RST-2-2 L 39	11269	15.98	566	1076	0.53	0.08	1.60	6.54
RST-2-2 L 40	11367	9.20	439	765	0.57	0.06	1.52	9.77
RST-2-2 L 42	12365	6.52	414	633	0.65	0.05	1.64	11.92
RST-2-2 L 43	12273	9.51	252	600	0.42	0.04	2.07	9.89
RST-2-2 L 44	10396	7.23	174	460	0.38	0.04	2.28	9.90
RST-2-2 L 45	11825	14.29	278	665	0.42	0.04	1.91	9.33
RST-2-2 L 46	10834	4.81	115	340	0.34	0.03	2.59	12.28
RST-2-2 L 47	10517	9.85	285	631	0.45	0.05	1.79	9.29
RST-2-2 L 48	11601	14.58	402	851	0.47	0.06	1.86	7.32
RST-2-2 L 49	11028	8.45	277	601	0.46	0.04	1.78	10.33
RST-2-2 L 50	9405	6.11	133	421	0.31	0.02	1.74	12.86
RST-2-2 L 51	11240	6.44	210	482	0.44	0.04	2.18	10.68

Table 18 RST zircon trace element compositions, crystallization temperatures and apparent U-Pb ages determined using LA-ICPMS (continued)

	Apparent age				*Concentration (ppm)*																	
Spot #	206Pb*/ 238U*	±2s (Ma)	Ti-in-zircon T(°C)	Eu/Eu*	P	Ti	Y	Nb	La	Ce	Pr	Nd	Sm	Eu	Gd	Tb	Dy	Ho	Er	Tm	Yb	Lu
Group C pumice #2																						
RST-2-2 L 52	6.69	0.54	703	0.10	2132	3.72	7983	61	3.348	103.45	1.402	11.23	15.41	1.40	110.3	49.52	733	292	1249	283	2815	434
RST-2-2 L 53	6.95	0.78	729	0.14	1916	4.98	8249	94	0.385	121.57	0.491	3.43	15.08	2.00	119.4	52.59	766	302	1240	271	2709	419
RST-2-2 L 54	6.88	0.99	708	0.09	2003	3.95	6174	30	0.182	52.24	0.188	2.28	9.95	0.82	87.0	37.75	537	218	952	208	2147	350
RST-2-2 L 55	6.32	0.88	706	0.15	2397	3.85	8804	91	8.781	159.33	4.063	28.35	24.87	2.95	148.4	61.08	819	323	1338	299	2793	460
RST-2-2 L 56	6.42	1.09	706	0.18	1957	3.87	5921	31	n.d.	52.11	n.d.	0.78	7.38	1.40	74.9	32.24	506	211	928	212	2125	358
RST-2-2 L 57	6.70	0.89	754	0.15	1358	6.50	6953	91	0.189	139.29	0.151	4.66	10.29	1.64	102.4	43.90	619	248	1035	230	2317	383
RST-2-2 L 58	5.56	1.06	694	0.12	1432	3.34	4660	30	0.044	45.62	0.141	2.81	6.56	0.74	57.6	25.45	392	162	726	172	1742	280
RST-2-2 L 59	6.82	0.56	761	0.15	2056	7.03	8853	114	36.939	222.58	11.593	62.34	29.10	3.19	141.3	56.39	794	322	1373	302	2918	508
RST-2-2 L 60	7.80	1.39	688	0.20	1498	3.13	6822	62	1.492	103.62	0.394	3.90	13.90	2.41	94.1	40.61	586	241	1013	219	2164	375
RST-2-2 L 61	6.28	0.86	751	0.15	1443	6.32	7525	78	0.168	126.08	n.d.	1.78	10.33	1.67	107.3	47.23	676	280	1181	257	2540	456
RST-2-2 L 62	6.35	0.98	757	0.19	1301	6.72	6701	73	0.564	115.15	0.343	3.48	11.67	1.99	88.2	41.02	562	235	997	217	2030	379
RST-2-2 L 63	6.87	0.72	642	0.19	1528	1.74	7373	89	n.d.	137.99	n.d.	1.44	14.19	2.36	98.4	47.57	661	267	1135	251	2364	405
RST-2-2 L 64	8.84	1.54	703	0.13	2944	3.73	4260	15	118.780	334.67	47.684	287.46	89.06	5.02	145.1	34.42	419	153	661	142	1420	266
RST-2-2 L 65	10.42	1.43	744	0.13	998	5.86	4300	32	0.100	54.71	n.d.	3.03	6.61	0.90	65.9	27.09	380	153	662	143	1405	244
RST-2-2 L 66	7.23	1.31	687	0.16	1735	3.08	6258	29	0.597	66.28	0.277	4.11	11.57	1.73	90.0	41.31	568	234	973	209	2110	368
RST-2-2 L 67	7.25	1.00	683	0.10	3039	2.93	7650	95	31.911	238.15	17.193	92.45	57.30	2.89	141.9	48.03	660	271	1117	241	2374	413
RST-2-2 L 68	6.12	0.84	736	0.12	954	5.38	5766	57	n.d.	92.12	n.d.	2.51	11.41	1.19	85.0	34.74	500	203	860	179	1733	305
RST-2-2 L 69	10.63	1.82	697	0.19	12341	3.49	5805	28	567.853	1515.03	218.330	1251.60	374.97	24.64	421.8	80.24	669	220	825	175	1674	280
Average	7.08	1.02	717	0.19	2039	4.71	6394	57	35.674	153.55	14.531	59.57	29.68	3.54	112.8	43.34	593	234	983	217	2161	348
σ	1.16	0.31	38	0.16	1851	2.28	1383	28	114.961	241.82	44.415	214.40	63.39	5.51	64.6	12.93	141	52	210	46	442	71

Table 18 RST zircon trace element compositions, crystallization temperatures and apparent U-Pb ages determined using LA-ICPMS (continued)

	Concentration (ppm)				*Trace Element Ratios*			
Spot #	Hf	Ta	Th	U	Th/U	Th/Y	Hf/Y	Y/U
Group C pumice #2								
RST-2-2 L 52	12496	10.69	398	949	0.42	0.05	1.57	8.41
RST-2-2 L 53	12687	18.03	652	1232	0.53	0.08	1.54	6.69
RST-2-2 L 54	13044	5.93	259	625	0.41	0.04	2.11	9.88
RST-2-2 L 55	11574	15.14	554	1074	0.52	0.06	1.31	8.20
RST-2-2 L 56	13117	8.41	196	540	0.36	0.03	2.22	10.96
RST-2-2 L 57	13231	15.74	564	993	0.57	0.08	1.90	7.00
RST-2-2 L 58	12642	6.45	138	376	0.37	0.03	2.71	12.39
RST-2-2 L 59	14141	19.70	529	1075	0.49	0.06	1.60	8.23
RST-2-2 L 60	13016	12.39	294	642	0.46	0.04	1.91	10.62
RST-2-2 L 61	14460	12.70	375	812	0.46	0.05	1.92	9.26
RST-2-2 L 62	13070	13.24	335	685	0.49	0.05	1.95	9.78
RST-2-2 L 63	14242	17.34	613	1073	0.57	0.08	1.93	6.87
RST-2-2 L 64	13542	5.80	141	475	0.30	0.03	3.18	8.97
RST-2-2 L 65	12035	7.38	138	358	0.39	0.03	2.80	12.03
RST-2-2 L 66	13339	7.13	275	561	0.49	0.04	2.13	11.15
RST-2-2 L 67	13909	16.47	499	915	0.55	0.07	1.82	8.36
RST-2-2 L 68	11902	9.52	279	562	0.50	0.05	2.06	10.26
RST-2-2 L 69	13817	6.01	171	403	0.43	0.03	2.38	14.42
Average	12239	10.95	347	723	0.46	0.05	2.00	9.51
σ	1178	4.44	176	277	0.08	0.02	0.45	2.03

Table 18 RST zircon trace element compositions, crystallization temperatures and apparent U-Pb ages determined using LA-ICPMS (continued)

	Apparent age				*Concentration (ppm)*																	
Spot #	206Pb*/238U*	±2s (Ma)	Ti-in-zircon T(°C)	Eu/Eu*	P	Ti	Y	Nb	La	Ce	Pr	Nd	Sm	Eu	Gd	Tb	Dy	Ho	Er	Tm	Yb	Lu
Banded pumice																						
RST-6-1 L 194	5.97	0.94	710	0.21	1752	4.03	5321	25	0.088	43.78	0.028	1.76	5.26	1.36	73.9	31.35	433	182	902	202	2142	288
RST-6-1 L 195	6.77	1.37	690	0.11	687	3.20	3043	41	n.d.	55.71	n.d.	0.50	3.88	0.48	43.0	18.83	253	108	516	132	1362	171
RST-6-1 L 196	7.57	1.44	727	0.20	1584	4.91	4552	28	n.d.	40.45	n.d.	1.39	4.62	1.02	55.2	26.73	376	162	755	182	1934	251
RST-6-1 L 197	7.21	0.71	671	0.09	2744	2.55	8332	42	n.d.	56.89	n.d.	1.18	10.48	1.00	119.1	51.82	776	303	1408	322	3201	429
RST-6-1 L 198	5.50	0.56	766	0.12	1491	7.43	7156	84	3.013	133.84	0.856	6.66	18.27	1.82	108.7	46.87	637	252	1174	285	2790	375
RST-6-1 L 201	6.42	0.69	750	0.10	3600	6.28	9071	96	41.492	254.06	20.478	133.19	64.18	3.75	192.3	68.32	872	318	1471	325	3294	412
RST-6-1 L 202	7.76	1.25	677	0.13	1733	2.74	4774	26	20.796	110.12	11.497	60.20	34.58	2.43	96.8	33.57	417	168	769	181	1871	236
RST-6-1 L 203	6.08	0.62	714	0.18	1409	4.21	6301	74	n.d.	119.95	0.218	3.00	12.21	2.14	106.6	44.23	580	219	1005	237	2420	306
RST-6-1 L 204	10.57	3.51	682	0.18	1450	2.89	3723	23	0.346	32.16	0.158	1.77	4.12	0.85	49.0	22.69	314	124	618	145	1658	190
RST-6-1 L 205	6.61	1.09	698	0.19	1276	3.52	6800	29	0.192	90.15	0.065	3.82	16.09	2.52	103.9	45.69	651	240	1129	268	2618	332
RST-6-1 L 206	8.96	2.05	761	0.11	1299	7.05	6443	92	0.357	117.61	0.299	3.89	13.01	1.37	104.2	42.50	589	242	1086	278	2903	345
RST-6-1 L 209	5.89	0.97	735	0.11	947	5.37	6456	76	n.d.	101.57	0.160	3.00	11.23	1.30	109.9	43.06	604	229	1075	242	2420	329
RST-6-1 L 210	6.61	0.66	750	0.14	1179	6.29	6799	122	n.d.	133.70	0.120	1.49	10.11	1.37	94.0	41.77	583	239	1106	250	2629	358
RST-6-1 L 211	6.14	0.63	698	0.18	1479	3.53	7382	114	n.d.	126.11	n.d.	1.18	5.54	1.40	104.3	48.32	652	256	1239	284	2801	375
RST-6-1 L 212	7.00	0.81	723	0.14	2039	4.68	8274	65	n.d.	95.75	0.098	2.39	11.34	1.63	115.7	49.35	718	284	1322	310	3240	425
RST-6-1 L 213	6.87	0.78	732	0.16	1673	5.15	5208	33	1.151	52.41	0.226	3.82	10.43	1.46	71.9	34.38	468	188	883	208	2151	285
RST-6-1 L 214	7.61	1.62	738	0.18	1664	5.53	3882	35	9.407	86.14	3.792	30.11	14.97	1.87	68.2	27.20	382	150	673	164	1863	202
RST-6-1 L 312	7.49	0.79	722	0.03	2192	4.65	9056	49	0.179	64.90	0.215	3.22	16.68	0.49	133.4	59.88	820	315	1429	357	3420	481
RST-6-1 L 313	6.04	0.70	744	0.09	2403	5.87	12190	98	n.d.	128.60	0.101	5.32	26.64	2.16	196.3	80.32	1162	445	1953	452	4409	570
RST-6-1 L 314	6.84	0.56	803	0.08	2414	10.63	11023	98	4.747	136.96	2.728	25.89	29.71	1.99	204.1	82.31	1133	403	1793	448	4491	563
RST-6-1 L 315	7.10	0.61	763	0.11	2298	7.19	9087	88	n.d.	100.33	0.166	3.46	16.54	1.70	131.7	59.56	858	327	1416	371	3664	444
RST-6-1 L 316	7.99	0.48	799	0.11	2818	10.29	13785	183	9.061	193.88	4.439	31.30	35.67	3.36	236.5	100.37	1452	547	2364	560	5610	683
RST-6-1 L 317	7.08	0.52	747	0.09	2580	6.09	14024	209	0.090	207.73	0.135	5.27	21.92	2.19	227.8	97.90	1383	521	2230	543	5154	625

Table 18 RST zircon trace element compositions, crystallization temperatures and apparent U-Pb ages determined using LA-ICPMS (continued)

	Concentration (ppm)				*Trace Element Ratios*			
Spot #	Hf	Ta	Th	U	Th/U	Th/Y	Hf/Y	Y/U
Banded pumice								
RST-6-1 L 194	13585	8.44	197	482	0.41	0.04	2.55	11.03
RST-6-1 L 195	13597	11.50	128	335	0.38	0.04	4.47	9.09
RST-6-1 L 196	12428	7.17	147	389	0.38	0.03	2.73	11.71
RST-6-1 L 197	13168	10.23	371	809	0.46	0.04	1.58	10.29
RST-6-1 L 198	13935	19.03	470	887	0.53	0.07	1.95	8.07
RST-6-1 L 201	12962	19.15	525	997	0.53	0.06	1.43	9.10
RST-6-1 L 202	12449	6.67	180	395	0.46	0.04	2.61	12.07
RST-6-1 L 203	11152	15.60	449	848	0.53	0.07	1.77	7.43
RST-6-1 L 204	11174	5.01	106	346	0.31	0.03	3.00	10.75
RST-6-1 L 205	11571	8.47	355	603	0.59	0.05	1.70	11.27
RST-6-1 L 206	11833	17.04	311	736	0.42	0.05	1.84	8.75
RST-6-1 L 209	12896	15.03	265	560	0.47	0.04	2.00	11.54
RST-6-1 L 210	14027	22.73	672	1080	0.62	0.10	2.06	6.30
RST-6-1 L 211	14518	24.63	674	1147	0.59	0.09	1.97	6.44
RST-6-1 L 212	13762	13.87	399	780	0.51	0.05	1.66	10.60
RST-6-1 L 213	12674	7.72	193	481	0.40	0.04	2.43	10.83
RST-6-1 L 214	11608	8.01	148	393	0.38	0.04	2.99	9.88
RST-6-1 L 312	18620	14.62	784	1097	0.71	0.09	2.06	8.25
RST-6-1 L 313	14872	20.55	768	1103	0.70	0.06	1.22	11.05
RST-6-1 L 314	15766	25.56	1020	1799	0.57	0.09	1.43	6.13
RST-6-1 L 315	14240	19.27	487	897	0.54	0.05	1.57	10.13
RST-6-1 L 316	14979	34.82	921	1493	0.62	0.07	1.09	9.23
RST-6-1 L 317	14880	35.19	1568	1962	0.80	0.11	1.06	7.15

Table 18 RST zircon trace element compositions, crystallization temperatures and apparent U-Pb ages determined using LA-ICPMS (continued)

	Apparent age				*Concentration (ppm)*																	
Spot #	206Pb*/ 238U*	±2s (Ma)	Ti-in-zircon T(°C)	Eu/Eu*	P	Ti	Y	Nb	La	Ce	Pr	Nd	Sm	Eu	Gd	Tb	Dy	Ho	Er	Tm	Yb	Lu
Banded pumice																						
RST-6-1 L 318	6.41	0.66	716	0.09	3332	4.34	11328	57	n.d.	81.04	0.099	3.12	17.78	1.64	164.4	73.06	982	410	1740	432	4352	511
RST-6-1 L 319	6.21	0.56	676	0.05	2360	2.70	7259	45	n.d.	57.43	0.050	2.00	13.87	0.69	107.7	47.49	698	278	1200	314	3245	383
RST-6-1 L 320	6.75	0.56	812	0.16	2816	11.61	12439	135	0.485	174.60	0.318	6.86	26.39	3.94	207.5	83.24	1161	459	1899	457	4645	535
RST-6-1 L 321	7.69	1.03	765	0.15	1608	7.31	7510	121	n.d.	134.86	0.047	2.06	16.05	2.04	110.9	48.81	674	274	1206	314	3324	376
RST-6-1 L 322	6.27	0.81	707	0.13	3221	3.91	10193	49	0.134	71.08	0.154	2.72	17.05	2.21	151.4	65.50	911	371	1641	421	4294	487
RST-6-1 L 323	6.93	0.53	784	0.06	2255	8.89	8038	75	1.177	96.69	0.655	5.57	20.35	1.01	130.6	56.83	825	314	1391	356	3749	432
RST-6-1 L 324	6.00	0.87	709	0.11	2342	3.98	7552	38	n.d.	55.68	0.097	2.73	11.19	1.29	110.4	48.53	673	260	1153	287	3020	356
RST-6-1 L 325	7.28	0.71	793	0.06	2354	9.67	7190	43	1.369	59.82	0.973	7.62	20.13	0.92	110.7	51.96	735	276	1173	312	3380	381
RST-6-1 L 327	6.68	0.80	776	0.15	2048	8.21	8163	117	0.548	117.90	0.353	7.15	20.49	2.56	138.5	58.55	831	317	1328	330	3555	386
RST-6-1 L 328	7.02	0.45	769	0.06	2854	7.62	9571	60	0.444	90.90	0.145	6.90	19.78	1.03	151.2	66.42	925	345	1552	394	4131	468
RST-6-1 L 329	7.34	0.96	752	0.10	2131	6.42	6542	33	0.980	56.67	0.384	5.10	18.27	1.32	97.4	42.76	630	253	1059	272	2936	323
RST-6-1 L 330	6.98	0.67	693	0.04	2266	3.31	10155	111	n.d.	138.48	0.147	4.27	23.40	0.90	189.1	73.87	1089	408	1751	451	4734	518
RST-6-1 L 331	6.71	1.06	693	0.13	1676	3.33	7495	91	n.d.	108.86	n.d.	2.13	14.01	1.80	120.0	49.76	689	268	1204	295	2953	341
RST-6-1 L 332	6.44	0.69	745	0.14	1994	5.96	9329	136	n.d.	139.58	0.079	3.15	16.41	2.23	137.0	59.64	875	328	1410	352	3786	402
RST-6-1 L 333	6.59	0.82	738	0.13	1666	5.51	7038	78	0.605	100.26	0.371	3.44	14.37	1.68	112.8	50.05	668	263	1127	289	2991	351
RST-6-1 L 335	7.27	1.02	698	0.09	2420	3.51	6708	34	0.084	50.52	n.d.	2.01	12.81	1.02	94.7	44.04	598	235	1058	279	2888	335
RST-6-1 L 336	11.63	1.44	767	0.14	2173	7.47	6951	66	25.597	136.00	8.340	58.04	30.25	3.02	135.8	54.55	741	271	1188	298	3124	362
RST-6-1 L 337	6.68	0.69	773	0.14	2551	7.96	13549	114	0.691	148.73	0.513	6.82	25.75	3.46	217.9	90.83	1162	459	1980	484	4880	540
RST-6-1 L 338	6.61	0.97	762	0.17	3034	7.11	13999	107	2.363	176.55	0.878	8.65	29.54	4.59	240.8	99.37	1354	522	2081	490	5041	586
RST-6-1 L 339	6.48	1.28	727	0.19	2430	4.89	7267	29	0.297	56.40	0.153	2.37	16.02	2.72	121.6	49.93	695	268	1148	295	2983	352
RST-6-1 L 340	6.98	0.82	753	0.13	2680	6.50	11215	62	6.170	103.39	2.616	17.55	23.87	2.62	171.9	76.93	1007	407	1735	424	4098	527
RST-6-1 L 341	7.01	0.79	787	0.13	2375	9.11	8945	75	0.235	95.44	0.049	3.93	15.23	1.98	140.6	60.12	901	339	1488	373	3782	463
Average	7.02	0.92	738	0.12	2118	5.85	8247	76	4.718	105.19	1.595	11.07	18.23	1.87	131.3	55.76	776	301	1330	326	3332	402
σ	1.10	0.51	37	0.04	642	2.30	2767	43	9.505	47.80	3.888	22.75	10.46	0.93	49.7	20.05	280	105	422	103	1000	115

Table 18 RST zircon trace element compositions, crystallization temperatures and apparent U-Pb ages determined using LA-ICPMS (continued)

	Concentration (ppm)				*Trace Element Ratios*			
Spot #	Hf	Ta	Th	U	Th/U	Th/Y	Hf/Y	Y/U
Banded pumice								
RST-6-1 L 318	13492	15.99	616	1041	0.59	0.05	1.19	10.88
RST-6-1 L 319	12788	12.72	511	1221	0.42	0.07	1.76	5.94
RST-6-1 L 320	13246	23.59	931	1364	0.68	0.07	1.06	9.12
RST-6-1 L 321	13502	26.30	684	1027	0.67	0.09	1.80	7.31
RST-6-1 L 322	14283	12.64	444	815	0.54	0.04	1.40	12.50
RST-6-1 L 323	13971	19.65	611	1328	0.46	0.08	1.74	6.05
RST-6-1 L 324	11902	10.07	379	713	0.53	0.05	1.58	10.59
RST-6-1 L 325	13685	15.90	538	1190	0.45	0.07	1.90	6.04
RST-6-1 L 327	12507	26.25	756	1248	0.61	0.09	1.53	6.54
RST-6-1 L 328	13335	15.12	789	1577	0.50	0.08	1.39	6.07
RST-6-1 L 329	13890	10.12	374	795	0.47	0.06	2.12	8.23
RST-6-1 L 330	15828	30.10	1066	2002	0.53	0.10	1.56	5.07
RST-6-1 L 331	13398	22.98	628	1004	0.63	0.08	1.79	7.47
RST-6-1 L 332	12951	28.87	687	1100	0.62	0.07	1.39	8.48
RST-6-1 L 333	13717	21.80	433	912	0.47	0.06	1.95	7.72
RST-6-1 L 335	12561	8.22	315	609	0.52	0.05	1.87	11.02
RST-6-1 L 336	14023	17.72	401	764	0.52	0.06	2.02	9.10
RST-6-1 L 337	12745	22.57	886	1304	0.68	0.07	0.94	10.39
RST-6-1 L 338	12902	20.94	772	1014	0.76	0.06	0.92	13.81
RST-6-1 L 339	13003	7.32	277	433	0.64	0.04	1.79	16.79
RST-6-1 L 340	15366	14.38	566	835	0.68	0.05	1.37	13.43
RST-6-1 L 341	15392	19.07	592	950	0.62	0.07	1.72	9.42
Average	13537	17.17	542	953	0.54	0.06	1.82	9.31
σ	1385	7.62	295	409	0.11	0.02	0.64	2.46

Table 18 RST zircon trace element compositions, crystallization temperatures and apparent U-Pb ages determined using LA-ICPMS (continued)

	Apparent age				*Concentration (ppm)*																	
Spot #	206Pb*/238U*	±2s (Ma)	Ti-in-zircon T(°C)	Eu/Eu*	P	Ti	Y	Nb	La	Ce	Pr	Nd	Sm	Eu	Gd	Tb	Dy	Ho	Er	Tm	Yb	Lu
Welded tuff																						
RST-5-1 L 215	6.58	0.75	705	0.08	2065	3.79	5582	32	n.d.	40.26	n.d.	0.56	4.26	0.46	74.9	34.65	498	194	924	214	2145	289
RST-5-1 L 216	8.60	1.33	726	0.14	13207	4.85	8748	29	304.939	947.06	112.014	885.47	346.49	20.21	555.4	106.35	972	320	1278	276	2854	360
RST-5-1 L 217	7.21	0.86	710	0.12	1577	4.04	6537	83	n.d.	104.05	0.052	2.25	8.06	1.10	97.4	45.25	606	241	1100	260	2638	345
RST-5-1 L 218	6.14	1.09	650	0.15	1867	1.94	4845	30	n.d.	38.94	0.093	1.40	4.31	0.77	58.6	28.45	446	175	778	191	2079	256
RST-5-1 L 219	6.25	0.74	681	0.14	2127	2.87	6097	40	n.d.	61.22	n.d.	1.01	10.23	1.36	82.2	38.54	529	212	929	218	2471	320
RST-5-1 L 221	4.80	1.07	681	0.14	1061	2.88	2869	20	n.d.	29.77	n.d.	0.38	3.90	0.51	31.9	16.11	246	94	466	115	1206	165
RST-5-1 L 222	9.00	1.86	761	0.15	2883	7.06	3219	27	61.519	220.52	32.947	198.15	66.20	4.37	127.5	29.21	318	116	496	123	1328	171
RST-5-1 L 342	6.22	0.73	756	0.13	1644	6.66	7056	90	10.013	132.37	5.564	36.11	25.59	2.44	129.5	49.57	680	256	1106	265	2499	333
RST-5-1 L 343	7.26	0.92	744	0.12	2004	5.89	7211	42	0.681	73.32	0.256	4.37	13.05	1.55	114.7	49.12	691	263	1119	286	2878	367
RST-5-1 L 344	5.98	0.68	784	0.16	1545	8.83	7732	90	n.d.	131.12	0.058	2.91	16.98	2.37	114.2	52.91	765	292	1232	302	3047	373
RST-5-1 L 345	7.05	0.79	747	0.10	1998	6.06	9779	109	n.d.	131.73	0.053	2.80	20.30	1.90	171.0	71.96	1041	393	1719	409	4008	479
RST-5-1 L 346	10.71	2.97	930	0.30	1621	31.53	7804	95	21.610	125.16	5.892	25.32	24.53	5.58	129.2	53.46	736	283	1270	313	3160	376
RST-5-1 L 348	6.87	1.37	752	0.15	4519	6.41	6255	44	91.791	269.93	41.127	262.00	101.00	7.15	208.7	55.94	613	230	944	231	2560	306
RST-5-1 L 349	6.43	0.75	691	0.10	2177	3.22	8369	56	n.d.	87.54	n.d.	3.11	18.09	1.53	127.5	53.64	805	300	1321	319	3321	413
RST-5-1 L 350	9.29	1.33	714	0.20	1947	4.23	5572	32	0.049	35.63	0.215	0.99	5.54	1.24	67.1	33.07	483	207	900	241	2528	314
RST-5-1 L 351	6.71	0.94	693	0.20	1262	3.31	6317	91	0.214	101.55	0.098	2.44	10.57	1.99	85.6	41.29	592	230	1022	267	2772	332
RST-5-1 L 352	6.26	0.63	724	0.13	1984	4.74	6793	32	n.d.	61.08	0.078	2.15	12.31	1.51	102.5	42.70	618	238	1055	271	2736	325
RST-5-1 L 353	7.15	1.02	669	0.18	1338	2.49	4071	42	n.d.	45.82	n.d.	n.d.	7.44	1.21	56.8	24.92	359	144	655	173	1898	220
Average	7.14	1.10	729	0.15	2601	6.16	6381	55	61.352	146.50	15.265	84.20	38.83	3.18	129.7	45.95	611	233	1017	249	2563	319
σ	1.42	0.56	62	0.05	2753	6.60	1843	29	103.960	209.88	32.094	219.86	80.63	4.61	114.4	20.16	210	74	306	71	675	79

Table 18 RST zircon trace element compositions, crystallization temperatures and apparent U-Pb ages determined using LA-ICPMS (continued)

	Concentration (ppm)				*Trace Element Ratios*			
Spot #	Hf	Ta	Th	U	Th/U	Th/Y	Hf/Y	Y/U
Welded tuff								
RST-5-1 L 215	11417	8.09	166	409	0.40	0.03	2.05	13.65
RST-5-1 L 216	12781	7.33	342	593	0.58	0.04	1.46	14.75
RST-5-1 L 217	12639	19.17	465	877	0.53	0.07	1.93	7.45
RST-5-1 L 218	11192	8.86	177	446	0.40	0.04	2.31	10.85
RST-5-1 L 219	11414	10.11	241	550	0.44	0.04	1.87	11.08
RST-5-1 L 221	12909	7.85	75	237	0.32	0.03	4.50	12.12
RST-5-1 L 222	11131	6.59	95	256	0.37	0.03	3.46	12.56
RST-5-1 L 342	14727	20.88	665	878	0.76	0.09	2.09	8.04
RST-5-1 L 343	14321	11.46	291	513	0.57	0.04	1.99	14.05
RST-5-1 L 344	13107	21.87	568	797	0.71	0.07	1.70	9.70
RST-5-1 L 345	14162	26.40	595	1005	0.59	0.06	1.45	9.73
RST-5-1 L 346	12302	18.81	583	911	0.64	0.07	1.58	8.57
RST-5-1 L 348	12998	11.24	244	513	0.48	0.04	2.08	12.20
RST-5-1 L 349	14375	15.85	487	871	0.56	0.06	1.72	9.61
RST-5-1 L 350	14493	9.02	152	385	0.39	0.03	2.60	14.47
RST-5-1 L 351	13675	21.77	368	679	0.54	0.06	2.16	9.30
RST-5-1 L 352	13558	9.65	355	653	0.54	0.05	2.00	10.41
RST-5-1 L 353	13447	12.51	131	323	0.41	0.03	3.30	12.59
Average	13036	13.75	333	605	0.51	0.05	2.24	11.17
σ	1178	6.18	189	241	0.12	0.02	0.79	2.24

Table 18 RST zircon trace element compositions, crystallization temperatures and apparent U-Pb ages determined using LA-ICPMS (continued)

	Apparent age				*Trace element concentration (ppm)*																	
Spot #	206Pb*/238U*	±2s (Ma)	Ti-in-zircon T(°C)	Eu/Eu*	P	Ti	Y	Nb	La	Ce	Pr	Nd	Sm	Eu	Gd	Tb	Dy	Ho	Er	Tm	Yb	Lu
Unwelded tuff																						
RST-7-4 XL 1	6.37	0.68	690	0.17	1486	3.20	5862	87	0.123	115.91	0.099	2.52	12.51	1.82	90.0	40.74	556	220	960	244	2608	296
RST-7-4 XL 2	6.71	0.67	721	0.55	1881	4.57	7962	99	4.345	222.67	4.110	29.64	32.69	13.01	160.3	60.01	737	271	1140	275	2984	332
RST-7-4 XL 3	6.39	0.81	699	0.13	2096	3.54	5079	28	n.d.	42.74	0.026	1.19	6.61	0.87	62.2	32.32	452	182	829	203	2253	272
RST-7-4 XL 4	6.30	1.08	664	0.15	1675	2.33	3967	24	n.d.	29.99	n.d.	1.08	5.11	0.78	49.4	24.27	346	144	656	172	1896	221
RST-7-4 XL 5	6.35	0.68	718	0.11	2841	4.43	6750	40	n.d.	45.35	0.082	1.59	10.33	1.05	90.3	43.35	613	245	1076	276	2988	329
RST-7-4 XL 6	6.03	0.66	673	0.12	1404	2.60	5491	91	n.d.	121.64	0.056	1.02	11.04	1.18	84.3	34.78	532	203	870	221	2400	261
RST-7-4 XL 7	6.24	0.63	767	0.10	2049	7.45	8829	167	n.d.	159.91	0.154	2.49	16.87	1.79	162.9	63.80	901	338	1452	338	3638	407
RST-7-4 XL 8	6.84	0.60	691	0.07	1704	3.24	6784	95	n.d.	99.40	0.159	1.79	13.03	0.88	101.9	46.77	662	248	1081	282	3137	354
RST-7-4 XL 9	7.03	0.79	766	0.13	1723	7.44	7178	95	0.413	117.61	0.210	4.42	12.11	1.56	112.9	48.55	698	269	1175	293	3040	357
RST-7-4 XL 10	6.66	0.64	680	0.09	1260	2.84	5248	75	n.d.	105.67	n.d.	2.21	11.27	0.89	84.9	32.68	477	195	832	204	2287	259
RST-7-4 XL 11	7.21	0.94	698	0.12	1056	3.50	4641	62	n.d.	79.90	0.101	1.95	8.66	1.12	88.8	36.10	467	171	719	172	1862	204
RST-7-4 XL 12	6.91	0.79	683	0.15	1313	2.93	5468	23	14.344	126.87	7.982	49.09	26.18	2.54	107.8	42.91	557	201	844	200	2194	243
RST-7-4 XL 13	7.12	1.12	714	0.14	1783	4.21	4377	30	0.040	38.07	0.146	0.99	6.36	0.89	59.5	27.43	410	160	729	188	2057	246
RST-7-4 XL 14	6.37	1.22	736	0.10	1669	5.37	4110	25	0.451	37.44	0.220	1.85	7.65	0.64	50.6	26.30	372	148	674	176	1909	232
RST-7-4 XL 15	5.37	1.00	689	0.23	640	3.17	3249	30	n.d.	51.60	0.053	1.19	5.48	1.37	60.5	26.27	343	121	522	121	1362	150
RST-7-4 XL 225	6.25	0.64	813	0.05	2933	11.71	9029	42	9.474	101.37	4.566	35.53	36.41	1.35	164.7	67.21	899	332	1455	372	4195	446
RST-7-4 XL 226	5.61	0.55	777	0.13	2502	8.24	8329	63	4.551	105.95	1.843	14.16	20.10	2.44	160.5	59.91	841	316	1343	355	3818	399
RST-7-4 XL 227	7.17	0.78	764	0.12	1513	7.24	5130	35	0.583	61.79	0.445	5.47	12.05	1.20	84.7	34.96	499	186	801	207	2255	255
Average	6.50	0.79	719	0.15	1752	4.89	5971	62	3.814	92.44	1.266	8.79	14.14	1.97	98.7	41.57	576	219	953	239	2605	292
σ	0.51	0.20	42.20	0.11	583	2.54	1740	39	5.061	50.03	2.30	14.24	9.13	2.81	39.32	13.63	180	65	276	70	758	78

Table 18 RST zircon trace element compositions, crystallization temperatures and apparent U-Pb ages determined using LA-ICPMS (continued)

	Concentration (ppm)				*Trace Element Ratios*			
Spot #	Hf	Ta	Th	U	Th/U	Th/Y	Hf/Y	Y/U
Unwelded tuff								
RST-7-4 XL 1	10594	18.43	432	866	0.50	0.07	1.81	6.77
RST-7-4 XL 2	10613	20.64	566	1003	0.56	0.07	1.33	7.94
RST-7-4 XL 3	11290	7.84	193	550	0.35	0.04	2.22	9.24
RST-7-4 XL 4	11470	7.61	117	414	0.28	0.03	2.89	9.58
RST-7-4 XL 5	10764	10.65	278	762	0.36	0.04	1.59	8.86
RST-7-4 XL 6	10854	20.47	693	1149	0.60	0.13	1.98	4.78
RST-7-4 XL 7	10989	33.56	1345	2022	0.67	0.15	1.24	4.37
RST-7-4 XL 8	11234	22.52	496	1347	0.37	0.07	1.66	5.04
RST-7-4 XL 9	10554	18.76	507	1049	0.48	0.07	1.47	6.84
RST-7-4 XL 10	9981	16.42	349	747	0.47	0.07	1.90	7.02
RST-7-4 XL 11	9045	13.95	250	589	0.42	0.05	1.95	7.88
RST-7-4 XL 12	10569	6.47	284	474	0.60	0.05	1.93	11.53
RST-7-4 XL 13	11366	8.22	152	474	0.32	0.03	2.60	9.23
RST-7-4 XL 14	10059	6.06	111	338	0.33	0.03	2.45	12.16
RST-7-4 XL 15	8343	7.23	105	295	0.36	0.03	2.57	11.03
RST-7-4 XL 225	13220	12.89	775	1470	0.53	0.09	1.46	6.14
RST-7-4 XL 226	11583	16.71	535	1023	0.52	0.06	1.39	8.14
RST-7-4 XL 227	11894	9.91	306	595	0.51	0.06	2.32	8.62
Average	10801	14.35	416	843	0.46	0.06	1.93	8.07
σ	1069	7.28	307	452	0.11	0.03	0.49	2.24

Table 18 RST zircon trace element compositions, crystallization temperatures and apparent U-Pb ages determined using LA-ICPMS (continued)

	Apparent age				*Concentration (ppm)*																	
Spot #	206Pb*/ 238U*	±2s (Ma)	Ti-in-zircon T(°C)	Eu/Eu*	P	Ti	Y	Nb	La	Ce	Pr	Nd	Sm	Eu	Gd	Tb	Dy	Ho	Er	Tm	Yb	Lu
Basal fallout																						
RST-7-3 XL 16	7.81	0.98	726	0.11	1882	4.84	4407	28	n.d.	41.62	0.028	1.25	8.11	0.78	57.9	26.15	393	164	721	186	2017	228
RST-7-3 XL 17	7.67	1.14	735	0.15	1414	5.35	5918	82	n.d.	111.78	n.d.	3.18	11.24	1.50	85.6	41.24	560	208	918	237	2573	279
RST-7-3 XL 18	6.94	0.83	681	0.19	1696	2.88	3919	22	n.d.	31.70	n.d.	0.81	4.25	0.88	47.1	23.24	356	141	676	167	1917	216
RST-7-3 XL 19	5.92	0.73	666	0.24	1574	2.37	3881	25	n.d.	31.04	0.146	0.54	4.11	1.19	55.2	25.11	340	138	627	162	1781	205
RST-7-3 XL 20	6.75	0.76	734	0.09	1192	5.31	4818	86	n.d.	101.84	0.049	2.23	8.69	0.78	72.0	32.78	452	169	772	187	2125	237
RST-7-3 XL 21	6.62	0.58	743	0.16	1988	5.84	8952	152	n.d.	142.91	0.075	3.07	13.53	2.29	134.7	67.85	904	332	1402	354	3805	409
RST-7-3 XL 22	6.33	0.63	721	0.12	1006	4.58	4188	57	n.d.	75.46	0.026	3.22	8.01	0.83	58.5	29.74	414	157	664	166	1829	213
RST-7-3 XL 23	8.39	1.71	726	0.14	1251	4.81	5713	73	0.250	104.20	0.170	2.93	10.73	1.48	93.1	40.42	524	204	913	225	2445	280
RST-7-3 XL 24	6.14	0.96	688	0.19	1835	3.12	4860	25	n.d.	44.00	n.d.	1.90	5.88	1.29	71.2	29.28	447	178	780	196	2263	257
RST-7-3 XL 25	7.23	0.95	713	0.15	2659	4.18	5417	75	31.747	173.10	15.841	95.94	37.03	3.28	117.9	43.12	538	205	873	220	2368	274
RST-7-3 XL 26	6.99	0.72	685	0.13	1714	3.02	6116	24	16.351	140.84	10.937	58.93	34.74	2.82	125.5	48.19	588	223	941	222	2336	278
RST-7-3 XL 27	7.61	0.81	721	0.10	3856	4.58	10381	41	38.040	214.44	17.102	97.40	62.72	3.94	245.3	85.78	1082	386	1612	380	3918	461
RST-7-3 XL 28	6.06	0.56	734	0.09	1993	5.29	8446	92	n.d.	137.90	0.082	2.47	17.80	1.52	140.7	64.02	838	319	1370	329	3511	401
RST-7-3 XL 29	6.84	0.74	713	0.11	2527	4.18	7279	34	0.182	48.33	0.082	1.60	11.89	1.28	100.8	45.97	671	265	1151	284	3030	376
RST-7-3 XL 30	7.33	1.06	574	0.16	1912	0.66	4461	28	n.d.	38.33	n.d.	1.51	5.92	1.00	58.4	28.48	405	160	705	179	2005	233
RST-7-3 XL 31	6.12	0.42	692	0.14	1419	3.27	6379	91	n.d.	109.62	0.101	2.49	11.31	1.46	87.5	42.05	580	225	986	247	2644	306
RST-7-3 XL 32	7.28	0.88	698	0.14	3230	3.52	8320	45	1.617	68.91	1.452	8.52	14.31	1.89	112.5	55.75	800	308	1349	320	3454	403
RST-7-3 XL 33	7.24	1.12	722	0.17	1105	4.64	5265	68	n.d.	93.74	0.026	3.50	10.80	1.67	88.4	34.69	508	188	833	208	2262	279
RST-7-3 XL 34	6.52	0.83	697	0.16	2039	3.46	6229	35	n.d.	52.75	n.d.	0.69	7.07	1.22	78.6	38.77	546	215	992	237	2548	330
RST-7-3 XL 35	7.21	0.78	743	0.14	1376	5.84	5718	81	0.044	106.09	0.079	2.73	9.09	1.23	77.9	39.94	538	211	924	234	2454	304
RST-7-3 XL 36	6.11	0.87	756	0.19	1525	6.66	6109	71	0.380	95.33	0.281	2.95	7.87	1.73	93.9	39.59	557	217	981	239	2496	307
RST-7-3 XL 37	6.20	0.71	690	0.26	1430	3.20	6666	27	n.d.	73.97	0.028	3.14	14.09	3.29	106.5	44.84	642	247	1055	250	2551	326
RST-7-3 XL 38	6.41	0.65	724	0.14	1238	4.75	5312	88	n.d.	95.51	n.d.	1.55	8.13	1.17	77.1	33.10	490	193	835	212	2301	283
RST-7-3 XL 39	6.80	0.64	767	0.16	1459	7.48	7519	90	0.321	123.48	0.409	5.02	16.93	2.18	106.1	50.33	723	271	1218	288	3053	375
RST-7-3 XL 40	6.13	0.57	723	0.14	1593	4.66	6835	61	n.d.	105.00	0.052	2.25	16.48	1.98	109.7	48.10	668	253	1118	270	2778	340
RST-7-3 XL 41	7.16	1.10	746	0.15	782	6.00	2776	25	0.292	41.29	0.158	1.62	4.36	0.61	35.0	18.10	243	105	469	110	1239	144
RST-7-3 L 77	6.48	1.01	742	0.36	2341	5.73	7364	30	4.282	52.94	2.826	20.43	26.45	7.21	140.7	52.36	689	263	1121	266	2581	351
RST-7-3 L 78	6.56	0.81	707	0.19	1405	3.92	5937	80	n.d.	105.97	n.d.	2.47	7.32	1.54	83.8	38.31	573	221	979	226	2418	307
RST-7-3 L 79	5.37	0.89	720	0.08	1951	4.50	5739	27	0.044	36.82	n.d.	0.69	6.15	0.56	70.2	32.57	463	192	890	215	2251	306
RST-7-3 L 80	5.88	0.86	686	0.09	1956	3.06	5664	28	n.d.	43.18	n.d.	1.46	6.40	0.64	70.4	32.31	490	197	910	222	2306	307

Table 18 RST zircon trace element compositions, crystallization temperatures and apparent U-Pb ages determined using LA-ICPMS (continued)

	Concentration (ppm)				*Trace Element Ratios*			
Spot #	Hf	Ta	Th	U	Th/U	Th/Y	Hf/Y	Y/U
Basal fallout								
RST-7-3 XL 16	10014	8.47	162	473	0.34	0.04	2.27	9.32
RST-7-3 XL 17	10475	18.15	414	825	0.50	0.07	1.77	7.17
RST-7-3 XL 18	10142	7.02	110	349	0.31	0.03	2.59	11.23
RST-7-3 XL 19	9562	5.39	109	342	0.32	0.03	2.46	11.33
RST-7-3 XL 20	9909	17.14	389	791	0.49	0.08	2.06	6.09
RST-7-3 XL 21	10791	28.68	745	1438	0.52	0.08	1.21	6.23
RST-7-3 XL 22	9551	12.53	177	456	0.39	0.04	2.28	9.17
RST-7-3 XL 23	9770	14.49	263	617	0.43	0.05	1.71	9.26
RST-7-3 XL 24	10249	5.90	185	479	0.39	0.04	2.11	10.15
RST-7-3 XL 25	10632	15.49	280	629	0.45	0.05	1.96	8.61
RST-7-3 XL 26	10902	6.21	351	536	0.65	0.06	1.78	11.40
RST-7-3 XL 27	11285	11.07	684	1013	0.68	0.07	1.09	10.25
RST-7-3 XL 28	11249	21.05	516	1067	0.48	0.06	1.33	7.91
RST-7-3 XL 29	11629	9.15	268	660	0.41	0.04	1.60	11.03
RST-7-3 XL 30	10001	7.39	153	431	0.35	0.03	2.24	10.34
RST-7-3 XL 31	11312	21.22	620	1090	0.57	0.10	1.77	5.85
RST-7-3 XL 32	10698	8.87	387	828	0.47	0.05	1.29	10.05
RST-7-3 XL 33	11111	14.47	271	569	0.48	0.05	2.11	9.25
RST-7-3 XL 34	11807	9.28	227	512	0.44	0.04	1.90	12.16
RST-7-3 XL 35	11790	18.43	384	737	0.52	0.07	2.06	7.76
RST-7-3 XL 36	11716	17.22	335	709	0.47	0.05	1.92	8.61
RST-7-3 XL 37	12136	7.86	367	596	0.61	0.05	1.82	11.18
RST-7-3 XL 38	11741	19.92	393	765	0.51	0.07	2.21	6.94
RST-7-3 XL 39	12136	18.26	389	825	0.47	0.05	1.61	9.11
RST-7-3 XL 40	11426	13.85	321	640	0.50	0.05	1.67	10.67
RST-7-3 XL 41	11561	8.39	93	249	0.37	0.03	4.16	11.16
RST-7-3 L 77	12892	7.89	291	569	0.51	0.04	1.75	12.93
RST-7-3 L 78	12399	17.07	378	692	0.55	0.06	2.09	8.58
RST-7-3 L 79	12755	7.52	194	462	0.42	0.03	2.22	12.41
RST-7-3 L 80	11464	8.18	215	482	0.45	0.04	2.02	11.76

Table 18 RST zircon trace element compositions, crystallization temperatures and apparent U-Pb ages determined using LA-ICPMS (continued)

	Apparent age				*Concentration (ppm)*																	
Spot #	206Pb*/238U*	±2s (Ma)	Ti-in-zircon T(°C)	Eu/Eu*	P	Ti	Y	Nb	La	Ce	Pr	Nd	Sm	Eu	Gd	Tb	Dy	Ho	Er	Tm	Yb	Lu
Basal fallout																						
RST-7-3 L 81	6.44	1.16	716	0.15	896	4.33	4241	47	3.524	75.05	1.730	11.17	11.88	1.27	58.3	26.66	382	148	675	165	1703	224
RST-7-3 L 82	6.90	1.04	699	0.11	1543	3.56	3921	22	n.d.	32.35	0.055	0.85	4.22	0.50	49.9	24.30	344	139	637	155	1698	224
RST-7-3 L 83	7.41	0.84	618	0.12	2528	1.26	6662	39	n.d.	56.13	n.d.	1.44	10.66	1.17	83.3	42.29	559	237	1085	261	2874	357
RST-7-3 L 84	6.80	0.86	755	0.37	1646	6.62	6996	96	2.163	122.07	0.752	8.59	16.52	5.45	122.6	49.60	630	259	1157	272	2872	347
RST-7-3 L 85	7.05	0.76	725	0.16	1251	4.79	5393	81	0.046	98.66	0.145	1.58	14.81	1.93	94.7	40.87	538	207	916	217	2284	263
RST-7-3 L 86	6.94	0.87	769	0.15	1477	7.62	6515	100	n.d.	129.50	n.d.	1.33	9.25	1.49	105.4	46.93	642	252	1109	269	2875	331
RST-7-3 L 87	6.02	0.85	797	0.15	5121	10.09	6971	73	93.054	391.07	53.550	318.71	139.19	9.00	243.5	67.03	754	264	1067	259	2710	322
RST-7-3 L 88	6.36	0.81	715	0.18	2377	4.30	6548	38	n.d.	60.33	n.d.	1.37	9.33	1.69	88.6	41.80	590	232	1073	264	2777	329
RST-7-3 L 89	6.92	1.39	664	0.23	1655	2.31	4008	20	0.387	33.62	0.058	0.98	7.38	1.48	54.6	27.25	370	149	644	159	1728	207
RST-7-3 L 90	7.10	1.18	761	0.17	2359	7.04	7952	77	18.521	160.23	10.297	69.24	25.05	3.21	136.7	53.05	753	286	1252	293	2868	398
RST-7-3 L 91	5.97	0.69	741	0.16	1389	5.68	7493	77	0.471	115.96	0.350	5.41	12.25	1.92	110.7	48.86	672	262	1196	281	2783	403
RST-7-3 L 93	6.55	0.76	731	0.12	1885	5.09	9199	125	n.d.	153.55	0.175	3.88	18.28	2.01	152.8	65.38	910	342	1478	354	3461	434
RST-7-3 L 94	5.73	0.73	704	0.22	1612	3.78	4676	22	n.d.	40.01	n.d.	n.d.	6.55	1.43	62.6	26.65	401	171	742	185	1916	253
RST-7-3 L 95	6.38	0.83	724	0.07	2009	4.71	5596	30	0.095	47.12	0.060	2.72	7.28	0.56	80.9	35.77	530	202	903	216	2363	305
RST-7-3 L 96	7.19	0.65	700	0.12	1645	3.61	6346	29	n.d.	65.27	n.d.	2.15	7.74	1.08	92.2	41.39	578	228	1000	244	2540	319
RST-7-3 L 97	6.85	1.15	730	0.11	2071	5.05	5072	27	0.143	46.85	0.182	1.56	9.29	0.84	61.2	30.69	442	184	825	209	2196	277
RST-7-3 L 98	6.38	0.94	650	0.16	1189	1.94	5719	23	n.d.	75.11	0.029	2.67	16.94	2.06	97.6	43.36	543	206	922	215	2270	268
RST-7-3 L 99	7.39	0.90	736	0.17	1170	5.41	4131	49	0.237	77.85	0.181	2.23	7.74	1.21	61.3	30.90	389	153	704	164	1819	211
RST-7-3 L 100	7.70	1.04	719	0.14	1641	4.49	5972	30	n.d.	67.57	0.029	1.06	9.82	1.40	93.7	40.52	567	220	979	232	2471	306
RST-7-3 L 101	6.62	0.81	685	0.16	1358	3.02	6239	68	0.503	115.26	0.175	3.16	9.60	1.71	105.6	43.33	585	223	1002	248	2578	314
RST-7-3 L 102	5.96	0.72	758	0.08	3525	6.83	15368	61	10.848	167.86	5.519	47.24	49.62	2.87	237.2	97.59	1325	475	2044	465	4785	563
RST-7-3 L 103	6.70	0.71	688	0.13	1325	3.13	5931	86	n.d.	116.27	n.d.	2.06	9.73	1.20	84.7	37.00	538	218	977	237	2518	297
RST-7-3 L 105	6.26	0.64	757	0.16	1454	6.74	5768	80	n.d.	107.57	0.087	1.49	8.86	1.44	84.0	39.49	542	209	923	226	2418	282
RST-7-3 L 107	6.93	0.92	717	0.12	1722	4.36	5177	41	0.094	52.20	0.256	3.30	8.75	1.04	75.0	31.25	464	182	848	212	2344	273
RST-7-3 L 108	5.64	0.89	733	0.23	1836	5.20	4404	26	n.d.	42.88	n.d.	0.98	5.10	1.27	54.9	26.86	385	161	727	188	1962	240
RST-7-3 L 109	7.21	1.03	712	0.12	1955	4.15	4881	31	n.d.	37.75	0.297	1.73	7.06	0.79	61.9	31.00	440	177	821	198	2259	255
RST-7-3 L 110	6.59	0.67	739	0.08	2481	5.58	7137	50	0.352	76.01	0.118	4.34	19.59	1.22	111.7	49.68	657	259	1087	282	3078	357
RST-7-3 L 111	7.02	0.93	716	0.19	1300	4.34	4954	73	n.d.	94.16	n.d.	1.95	9.90	1.84	92.1	41.00	542	197	799	197	2048	220
RST-7-3 L 112	6.07	0.46	743	0.16	2042	5.85	8121	113	0.285	137.62	0.127	3.91	21.96	2.66	123.8	60.22	818	304	1311	313	3347	372
RST-7-3 L 113	7.06	0.88	732	0.09	1321	5.17	4789	24	0.285	68.97	0.173	2.15	7.31	0.74	77.4	33.85	466	179	749	188	2100	235

Table 18 RST zircon trace element compositions, crystallization temperatures and apparent U-Pb ages determined using LA-ICPMS (continued)

	Concentration (ppm)				*Trace Element Ratios*			
Spot #	Hf	Ta	Th	U	Th/U	Th/Y	Hf/Y	Y/U
Basal fallout								
RST-7-3 L 81	12112	11.26	143	341	0.42	0.03	2.86	12.43
RST-7-3 L 82	10797	5.50	118	290	0.41	0.03	2.75	13.53
RST-7-3 L 83	11321	10.07	263	576	0.46	0.04	1.70	11.56
RST-7-3 L 84	11614	21.65	491	853	0.58	0.07	1.66	8.20
RST-7-3 L 85	9817	15.32	369	721	0.51	0.07	1.82	7.48
RST-7-3 L 86	10037	20.33	563	931	0.61	0.09	1.54	7.00
RST-7-3 L 87	10395	13.79	366	728	0.50	0.05	1.49	9.57
RST-7-3 L 88	11519	9.17	254	564	0.45	0.04	1.76	11.62
RST-7-3 L 89	10485	5.67	105	299	0.35	0.03	2.62	13.40
RST-7-3 L 90	13139	14.58	392	735	0.53	0.05	1.65	10.82
RST-7-3 L 91	14682	19.09	486	809	0.60	0.06	1.96	9.26
RST-7-3 L 93	13002	28.82	1064	1455	0.73	0.12	1.41	6.32
RST-7-3 L 94	11541	6.36	148	361	0.41	0.03	2.47	12.94
RST-7-3 L 95	12642	7.63	303	739	0.41	0.05	2.26	7.57
RST-7-3 L 96	11344	7.92	273	501	0.54	0.04	1.79	12.68
RST-7-3 L 97	10940	8.25	209	496	0.42	0.04	2.16	10.22
RST-7-3 L 98	11183	6.61	257	409	0.63	0.04	1.96	13.97
RST-7-3 L 99	10125	12.98	307	595	0.52	0.07	2.45	6.94
RST-7-3 L 100	11394	8.04	272	503	0.54	0.05	1.91	11.88
RST-7-3 L 101	11297	15.82	320	636	0.50	0.05	1.81	9.81
RST-7-3 L 102	11583	14.08	972	1356	0.72	0.06	0.75	11.33
RST-7-3 L 103	11230	17.73	429	808	0.53	0.07	1.89	7.34
RST-7-3 L 105	10276	16.63	425	782	0.54	0.07	1.78	7.37
RST-7-3 L 107	10589	8.87	196	484	0.41	0.04	2.05	10.69
RST-7-3 L 108	11161	6.97	146	404	0.36	0.03	2.53	10.90
RST-7-3 L 109	10487	8.47	204	501	0.41	0.04	2.15	9.73
RST-7-3 L 110	11351	12.71	496	1224	0.40	0.07	1.59	5.83
RST-7-3 L 111	8364	15.16	306	653	0.47	0.06	1.69	7.59
RST-7-3 L 112	9633	20.73	602	1178	0.51	0.07	1.19	6.89
RST-7-3 L 113	10652	8.76	292	581	0.50	0.06	2.22	8.25

Table 18 RST zircon trace element compositions, crystallization temperatures and apparent U-Pb ages determined using LA-ICPMS (continued)

	Apparent age			*Concentration (ppm)*																	
Spot #	206Pb*/238U*	±2s (Ma)	Ti-in-zircon T(°C)	Eu/Eu*	P	Ti	Y	Nb	La	Ce	Pr	Nd	Sm	Eu	Gd	Tb	Dy	Ho	Er	Tm	Yb	Lu
Basal fallout																						
RST-7-3 L 114	6.52	1.08	738	0.18	2121	5.51	5448	30	n.d.	50.70	0.059	1.70	11.85	1.80	79.7	35.13	485	193	884	222	2457	279
RST-7-3 L 115	6.79	0.78	731	0.21	1482	5.13	6423	80	n.d.	120.24	0.062	2.55	9.70	2.26	108.3	45.05	623	232	1039	256	2757	307
RST-7-3 L 116	5.64	1.39	734	0.22	873	5.26	3951	24	0.943	63.39	0.630	5.18	8.61	1.80	71.0	27.15	381	142	603	149	1663	179
RST-7-3 L 118	7.80	0.63	695	0.17	2974	3.38	9551	48	n.d.	88.54	n.d.	4.06	17.70	2.86	151.7	72.44	926	354	1528	364	3620	425
RST-7-3 L 119	5.68	0.97	710	0.12	2412	4.06	6207	41	0.141	57.10	0.200	2.90	8.56	1.04	88.0	40.90	574	224	1054	251	2837	307
RST-7-3 L 120	6.35	0.74	780	0.29	2189	8.50	8856	123	1.957	148.48	1.155	12.75	24.61	6.01	158.3	70.00	884	337	1411	331	3536	391
RST-7-3 L 121	7.36	0.87	720	0.13	1427	4.52	5377	76	0.192	101.57	0.061	2.36	10.65	1.28	84.7	35.93	494	194	824	217	2303	259
RST-7-3 L 122	6.16	0.50	749	0.20	2195	6.19	8627	66	0.389	125.27	0.292	5.75	21.00	3.74	157.5	68.82	891	332	1390	344	3617	381
RST-7-3 L 123	6.48	0.66	805	0.09	2198	10.83	9012	142	0.098	159.97	0.443	4.57	21.22	1.75	150.2	70.66	906	341	1490	368	3979	425
RST-7-3 L 124	7.07	0.78	766	0.08	2662	7.43	11251	194	0.146	190.77	0.236	5.07	26.73	1.90	196.6	82.59	1179	425	1824	444	4646	498
RST-7-3 L 125	9.21	1.21	780	0.77	2035	8.49	4352	36	12.158	92.54	6.957	35.20	28.79	13.13	94.3	32.97	430	159	672	164	1902	210
RST-7-3 L 126	6.30	1.05	713	0.21	1291	4.17	6097	80	n.d.	122.68	0.063	3.28	10.06	2.08	92.6	41.65	580	219	994	256	2847	309
RST-7-3 L 127	7.02	1.02	695	0.11	2104	3.40	5773	33	n.d.	45.60	0.059	0.81	6.53	0.69	61.0	32.70	503	199	923	231	2512	317
RST-7-3 L 128	6.26	0.59	745	0.15	2111	5.96	9381	116	n.d.	159.83	0.144	3.54	21.36	3.02	168.9	70.07	968	345	1489	347	3542	418
RST-7-3 L 129	8.03	0.54	770	0.21	1961	7.70	6429	62	0.928	79.78	0.403	6.21	13.63	2.47	98.3	43.83	614	240	1032	253	2621	331
RST-7-3 L 130	6.56	1.26	731	0.22	1432	5.11	3227	24	n.d.	33.11	0.115	0.59	2.75	0.76	38.5	20.35	287	114	525	133	1490	181
RST-7-3 L 131	5.78	1.10	707	0.14	1820	3.91	4260	26	n.d.	40.73	n.d.	2.48	6.44	0.86	57.3	28.09	383	153	713	180	1987	234
RST-7-3 L 132	6.22	0.88	737	0.13	995	5.45	4258	61	n.d.	79.71	0.091	0.98	4.66	0.74	64.3	28.44	389	159	668	175	1940	211
RST-7-3 L 133	6.65	1.13	730	0.12	2334	5.04	6558	32	1.808	60.08	1.210	12.52	12.10	1.34	101.9	41.50	632	241	1037	272	3017	336
RST-7-3 XL 228	5.77	0.77	729	0.16	1495	4.98	5938	98	0.123	106.47	0.117	1.63	16.21	1.99	89.0	39.94	602	224	951	253	2737	272
RST-7-3 XL 229	6.87	1.25	710	0.16	2373	4.04	5908	33	n.d.	47.41	0.027	1.19	10.31	1.60	93.0	38.14	569	226	929	245	2737	272
RST-7-3 XL 230	7.18	1.20	779	0.33	1833	8.43	5037	45	2.985	55.81	1.575	11.19	18.22	4.13	79.7	35.08	467	180	786	207	2260	243
RST-7-3 XL 231	7.00	1.29	691	0.13	2216	3.23	5303	34	n.d.	50.08	n.d.	0.78	9.25	1.14	75.6	33.55	500	194	853	221	2409	259
RST-7-3 XL 232	5.97	0.49	762	0.08	2555	7.14	8801	43	0.337	81.98	0.242	5.36	21.50	1.48	133.4	61.83	852	316	1432	356	3909	428
RST-7-3 XL 233	6.03	0.72	761	0.05	3153	7.06	9306	71	20.633	150.94	12.912	80.71	50.28	1.78	196.4	69.63	944	363	1585	381	3988	478
RST-7-3 L 238	6.67	0.74	707	0.16	1656	3.90	9235	103	n.d.	127.36	0.137	2.54	15.09	2.31	125.4	60.37	836	339	1493	364	3683	479
RST-7-3 L 239	12.34	1.74	723	0.27	1764	4.68	4992	28	0.275	38.74	0.248	1.15	5.61	1.59	60.0	27.66	408	171	759	202	2076	263
RST-7-3 L 240	6.86	0.80	754	0.14	2223	6.56	11202	120	0.155	161.85	0.413	3.30	20.15	2.85	189.8	82.38	1132	446	1851	479	4498	556
RST-7-3 L 241	6.73	0.85	764	0.10	1847	7.22	5471	29	0.363	47.68	0.082	3.11	8.77	0.90	86.9	36.80	532	203	912	241	2470	304
RST-7-3 L 242	6.38	0.99	696	0.17	2039	3.43	5723	31	0.337	43.53	0.110	2.11	5.22	1.12	73.7	33.78	511	216	977	249	2614	318

Table 18 RST zircon trace element compositions, crystallization temperatures and apparent U-Pb ages determined using LA-ICPMS (continued)

	Concentration (ppm)				*Trace Element Ratios*			
Spot #	Hf	Ta	Th	U	Th/U	Th/Y	Hf/Y	Y/U
Basal fallout								
RST-7-3 L 114	10378	7.95	200	530	0.38	0.04	1.90	10.28
RST-7-3 L 115	9492	14.25	302	663	0.45	0.05	1.48	9.69
RST-7-3 L 116	10771	6.82	148	315	0.47	0.04	2.73	12.53
RST-7-3 L 118	10772	10.22	486	833	0.58	0.05	1.13	11.47
RST-7-3 L 119	10261	9.35	352	813	0.43	0.06	1.65	7.64
RST-7-3 L 120	10203	22.98	788	1286	0.61	0.09	1.15	6.89
RST-7-3 L 121	9760	15.93	391	786	0.50	0.07	1.82	6.84
RST-7-3 L 122	10004	13.02	515	926	0.56	0.06	1.16	9.32
RST-7-3 L 123	10362	28.67	893	1638	0.55	0.10	1.15	5.50
RST-7-3 L 124	10457	35.26	1350	2109	0.64	0.12	0.93	5.33
RST-7-3 L 125	10452	8.03	141	407	0.35	0.03	2.40	10.70
RST-7-3 L 126	10698	15.04	328	738	0.44	0.05	1.75	8.27
RST-7-3 L 127	11956	8.08	193	454	0.43	0.03	2.07	12.71
RST-7-3 L 128	11364	23.38	928	1254	0.74	0.10	1.21	7.48
RST-7-3 L 129	11632	12.81	340	738	0.46	0.05	1.81	8.71
RST-7-3 L 130	11522	7.45	111	324	0.34	0.03	3.57	9.97
RST-7-3 L 131	11361	7.01	169	472	0.36	0.04	2.67	9.03
RST-7-3 L 132	10788	14.44	204	488	0.42	0.05	2.53	8.72
RST-7-3 L 133	11282	8.90	250	604	0.41	0.04	1.72	10.85
RST-7-3 XL 228	10838	21.97	460	855	0.54	0.08	1.83	6.94
RST-7-3 XL 229	11181	9.04	230	591	0.39	0.04	1.89	9.99
RST-7-3 XL 230	10722	11.63	191	481	0.40	0.04	2.13	10.46
RST-7-3 XL 231	11361	6.95	213	509	0.42	0.04	2.14	10.42
RST-7-3 XL 232	12713	12.31	548	1018	0.54	0.06	1.44	8.65
RST-7-3 XL 233	13534	18.15	777	1546	0.50	0.08	1.45	6.02
RST-7-3 L 238	16104	25.71	502	791	0.63	0.05	1.74	11.68
RST-7-3 L 239	13293	8.77	154	380	0.41	0.03	2.66	13.15
RST-7-3 L 240	14804	27.27	757	1131	0.67	0.07	1.32	9.90
RST-7-3 L 241	13842	10.14	292	617	0.47	0.05	2.53	8.87
RST-7-3 L 242	13997	9.28	210	478	0.44	0.04	2.45	11.98

Table 18 RST zircon trace element compositions, crystallization temperatures and apparent U-Pb ages determined using LA-ICPMS (continued)

	Apparent age				*Concentration (ppm)*																	
Spot #	206Pb*/238U*	±2s (Ma)	Ti-in-zircon T(°C)	Eu/Eu*	P	Ti	Y	Nb	La	Ce	Pr	Nd	Sm	Eu	Gd	Tb	Dy	Ho	Er	Tm	Yb	Lu
Basal fallout																						
RST-7-3 L 243	6.86	1.19	723	0.16	1455	4.69	7327	93	n.d.	112.17	0.083	2.75	9.73	1.62	96.0	47.09	668	264	1169	292	3037	369
RST-7-3 L 244	6.59	0.74	736	0.13	2032	5.37	6617	53	n.d.	77.45	0.078	2.07	12.83	1.53	99.5	44.39	581	241	1048	276	3011	335
RST-7-3 L 245	5.98	0.91	725	0.14	1223	4.75	6222	82	n.d.	99.13	n.d.	2.74	13.36	1.60	95.2	38.87	594	225	989	246	2644	318
RST-7-3 L 246	6.19	0.96	765	0.13	2356	7.36	12640	114	0.092	152.48	0.304	5.23	23.74	2.71	176.7	77.37	1016	385	1668	413	4238	464
RST-7-3 L 247	6.53	0.92	841	0.18	3281	15.17	11688	72	14.039	168.74	8.124	67.84	51.14	6.77	252.8	89.46	1132	416	1633	416	4326	444
RST-7-3 L 248	5.42	0.78	639	0.17	2424	1.69	6192	40	0.417	52.74	0.100	2.67	7.85	1.45	89.7	40.80	599	240	1013	265	2808	320
RST-7-3 L 249	6.94	1.10	702	0.10	2140	3.67	8532	129	n.d.	122.84	0.047	2.19	20.40	1.91	155.3	69.18	1018	371	1612	390	4129	452
RST-7-3 L 250	11.17	2.38	763	0.14	1113	7.17	5141	72	0.047	85.23	0.107	3.73	9.87	1.33	86.5	34.75	523	205	898	220	2356	263
RST-7-3 L 252	7.39	0.97	751	0.03	2679	6.32	8298	69	0.344	83.55	0.295	3.76	15.81	0.50	123.1	50.01	760	279	1252	335	3621	382
RST-7-3 L 253	7.23	0.96	748	0.09	2567	6.13	6545	37	0.264	59.80	0.111	5.35	11.19	1.07	115.4	47.06	666	245	1047	290	3236	337
RST-7-3 L 254	7.07	1.14	730	0.06	2056	5.05	6711	36	0.204	62.48	0.136	2.77	15.42	0.76	108.0	47.31	633	238	1100	281	3055	328
RST-7-3 L 255	5.74	0.68	762	0.17	1918	7.08	9281	132	0.043	144.31	0.078	2.94	19.84	3.26	166.1	63.40	920	357	1529	363	3897	417
RST-7-3 L 256	7.04	0.86	753	0.13	2839	6.47	9005	45	0.127	78.95	0.203	4.22	18.59	2.15	144.2	63.27	887	346	1448	359	3813	391
RST-7-3 L 257	6.17	0.88	738	0.15	2410	5.50	7219	59	n.d.	81.71	0.153	1.97	13.64	1.93	106.2	51.49	719	276	1140	296	3343	335
RST-7-3 L 258	6.49	0.94	744	0.13	2184	5.86	5007	30	2.350	49.35	1.087	6.10	9.38	1.25	87.6	33.15	496	182	779	222	2472	246
RST-7-3 L 259	6.68	0.97	702	0.06	2679	3.68	7543	57	n.d.	66.94	n.d.	1.94	11.79	0.71	98.7	45.90	675	262	1200	333	3773	414
RST-7-3 L 260	7.07	0.75	739	0.09	2356	5.59	9616	147	n.d.	148.38	0.089	3.76	18.70	1.65	171.1	69.72	939	362	1591	382	4135	429
RST-7-3 L 261	7.94	0.92	709	0.17	1632	4.00	6279	77	0.618	105.35	0.117	3.24	18.04	2.33	98.5	43.03	603	225	986	268	2828	312
RST-7-3 L 262	6.10	0.79	747	0.21	1327	6.06	6939	89	n.d.	116.65	0.028	2.63	12.82	2.57	108.0	51.51	682	257	1097	291	3133	339
RST-7-3 L 263	6.92	0.81	758	0.19	1506	6.84	8376	103	n.d.	130.00	0.159	3.69	15.98	2.82	127.4	52.54	815	300	1352	323	3014	404
RST-7-3 L 264	6.49	0.89	764	0.10	2280	7.28	7700	42	0.545	62.16	0.368	4.12	15.10	1.41	119.2	49.07	684	287	1302	316	3103	430
RST-7-3 L 265	7.78	1.28	797	0.22	2404	10.08	8189	40	14.883	128.96	6.589	50.00	40.12	6.38	190.1	65.00	837	311	1327	308	2949	381
RST-7-3 L 266	5.88	0.93	733	0.16	2314	5.21	7124	30	0.080	52.46	0.121	5.19	13.63	1.94	102.0	46.15	687	266	1117	278	2742	364
RST-7-3 L 267	6.51	0.94	814	0.17	2557	11.85	12457	121	3.468	188.46	1.084	15.39	32.88	4.74	220.8	86.81	1153	419	1727	409	4221	494
RST-7-3 L 268	8.27	0.99	815	0.73	1939	12.00	7182	86	5.777	125.07	3.892	25.89	30.45	15.65	139.7	53.66	683	263	1066	264	2857	330
RST-7-3 L 269	6.95	0.75	725	0.08	2119	4.80	6858	43	0.208	65.19	0.125	3.82	13.15	0.96	101.0	46.29	644	257	1116	286	3186	353
RST-7-3 L 270	6.08	0.84	748	0.13	2082	6.15	8925	136	n.d.	128.55	0.080	3.20	19.34	2.29	141.0	66.50	905	341	1466	386	3914	440
RST-7-3 L 271	6.53	0.81	732	0.11	1786	5.16	6945	89	0.704	98.65	0.471	5.31	15.99	1.51	112.2	49.88	684	258	1093	289	2985	323
RST-7-3 L 272	7.09	0.88	745	0.17	2884	5.96	9156	60	1.125	94.26	0.900	6.29	20.16	3.22	158.3	61.05	881	344	1453	368	3720	392
RST-7-3 L 273	8.00	1.00	784	0.13	1830	8.87	7673	100	0.491	109.23	0.268	4.58	16.63	1.79	112.5	53.82	732	289	1244	330	3647	393

Table 18 RST zircon trace element compositions, crystallization temperatures and apparent U-Pb ages determined using LA-ICPMS (continued)

	Concentration (ppm)				*Trace Element Ratios*			
Spot #	Hf	Ta	Th	U	Th/U	Th/Y	Hf/Y	Y/U
Basal fallout								
RST-7-3 L 243	13144	23.58	481	820	0.59	0.07	1.79	8.94
RST-7-3 L 244	12339	14.90	288	583	0.49	0.04	1.86	11.36
RST-7-3 L 245	13003	19.10	322	611	0.53	0.05	2.09	10.18
RST-7-3 L 246	11841	22.15	788	1239	0.64	0.06	0.94	10.20
RST-7-3 L 247	11121	13.38	590	810	0.73	0.05	0.95	14.42
RST-7-3 L 248	11544	10.76	302	682	0.44	0.05	1.86	9.08
RST-7-3 L 249	11668	32.54	1031	1443	0.71	0.12	1.37	5.91
RST-7-3 L 250	10638	15.04	227	525	0.43	0.04	2.07	9.79
RST-7-3 L 252	11228	18.45	633	1450	0.44	0.08	1.35	5.72
RST-7-3 L 253	12694	11.50	432	995	0.43	0.07	1.94	6.58
RST-7-3 L 254	12484	11.49	401	867	0.46	0.06	1.86	7.74
RST-7-3 L 255	12379	28.92	735	1289	0.57	0.08	1.33	7.20
RST-7-3 L 256	11722	11.81	461	802	0.58	0.05	1.30	11.23
RST-7-3 L 257	11050	14.74	426	822	0.52	0.06	1.53	8.78
RST-7-3 L 258	11506	9.99	192	497	0.39	0.04	2.30	10.06
RST-7-3 L 259	13491	17.51	493	1276	0.39	0.07	1.79	5.91
RST-7-3 L 260	12953	33.95	868	1632	0.53	0.09	1.35	5.89
RST-7-3 L 261	13303	20.47	461	870	0.53	0.07	2.12	7.22
RST-7-3 L 262	12198	18.26	365	733	0.50	0.05	1.76	9.46
RST-7-3 L 263	15953	25.29	840	1072	0.78	0.10	1.90	7.81
RST-7-3 L 264	16758	12.16	370	701	0.53	0.05	2.18	10.99
RST-7-3 L 265	14011	10.53	290	399	0.73	0.04	1.71	20.53
RST-7-3 L 266	14371	7.52	268	449	0.60	0.04	2.02	15.88
RST-7-3 L 267	11371	22.29	777	1161	0.67	0.06	0.91	10.73
RST-7-3 L 268	12327	18.96	378	676	0.56	0.05	1.72	10.63
RST-7-3 L 269	12759	13.76	487	1045	0.47	0.07	1.86	6.56
RST-7-3 L 270	12779	27.96	572	1165	0.49	0.06	1.43	7.66
RST-7-3 L 271	11158	18.61	536	1004	0.53	0.08	1.61	6.92
RST-7-3 L 272	10794	12.45	460	767	0.60	0.05	1.18	11.94
RST-7-3 L 273	12297	24.94	609	1450	0.42	0.08	1.60	5.29

Table 18 RST zircon trace element compositions, crystallization temperatures and apparent U-Pb ages determined using LA-ICPMS (continued)

	Apparent age			*Concentration (ppm)*																		
Spot #	206Pb*/ 238U*	±2s (Ma)	Ti-in-zircon T(°C)	Eu/Eu*	P	Ti	Y	Nb	La	Ce	Pr	Nd	Sm	Eu	Gd	Tb	Dy	Ho	Er	Tm	Yb	Lu
Basal fallout																						
RST-7-3 L 274	6.83	0.95	798	0.43	2831	10.15	8705	68	3.020	100.15	1.897	13.50	25.72	9.02	159.1	58.55	800	324	1383	354	3877	422
RST-7-3 L 275	7.86	1.01	727	0.13	1847	4.89	7772	128	n.d.	131.12	n.d.	2.74	14.23	1.81	135.1	54.75	774	278	1132	297	3319	350
RST-7-3 L 276	7.09	0.89	741	0.13	3180	5.67	16259	60	6.705	149.71	3.393	26.95	36.78	4.11	248.6	96.68	1269	457	1857	461	4819	497
RST-7-3 L 277	8.12	1.35	747	0.16	1921	6.05	7444	78	0.430	119.44	0.196	5.28	20.18	2.71	132.6	56.52	739	282	1192	311	3303	339
WNFM061233B L 1	6.58	1.02	697	0.10	1522	3.46	3879	24	0.147	35.28	0.074	1.75	6.57	0.65	55.2	25.49	370	154	643	142	1451	219
WNFM061233B L 2	6.98	0.86	760	0.17	1733	6.97	6937	66	0.619	116.28	0.389	4.17	16.87	2.53	116.0	49.01	692	266	1125	247	2510	380
WNFM061233B L 3	8.61	1.82	746	0.13	1298	6.00	3099	19	0.129	26.95	n.d.	0.52	4.90	0.57	39.0	18.58	286	120	507	122	1195	192
WNFM061233B L 5	6.02	1.06	724	0.17	1261	4.73	5755	55	0.598	109.74	0.463	3.92	12.55	2.00	98.0	37.52	530	217	901	200	1974	315
WNFM061233B L 6	5.92	0.94	724	0.16	663	4.71	2952	38	n.d.	63.64	n.d.	0.51	4.42	0.71	40.8	17.44	282	117	512	114	1219	186
WNFM061233B L 7	6.87	1.12	726	0.14	1476	4.82	5276	38	0.127	71.15	0.026	1.92	7.24	1.06	76.9	33.08	474	197	853	191	2010	306
WNFM061233B L 8	6.34	0.78	701	0.19	1177	3.65	4902	24	0.119	68.30	0.050	2.52	9.37	1.80	88.5	35.34	498	193	775	174	1761	264
WNFM061233B L 10	6.76	1.05	713	0.07	2128	4.16	6172	32	n.d.	59.82	n.d.	0.81	8.84	0.67	88.1	38.32	563	230	987	233	2273	366
WNFM061233B L 11	8.07	0.97	702	0.15	1432	3.68	4128	37	0.560	51.06	0.230	1.75	8.71	1.10	56.5	26.43	388	154	676	155	1664	246
WNFM061233B L 12	8.31	1.05	865	0.23	1997	18.68	5862	27	2.401	55.40	0.652	7.37	11.21	2.21	77.6	37.25	550	218	944	220	2238	340
WNFM061233B L 13	8.11	0.94	727	0.09	2790	4.91	9265	74	n.d.	106.46	0.055	3.79	15.61	1.45	147.8	63.73	934	356	1523	336	3424	517
WNFM061233B L 15	6.56	1.01	720	0.09	2411	4.53	6568	44	0.174	58.12	0.139	1.72	10.38	0.87	91.9	40.64	619	251	1061	238	2470	394
WNFM061233B L 16	6.40	0.82	745	0.14	1534	5.96	7032	28	0.680	99.95	0.244	5.82	14.92	1.88	114.1	50.95	653	248	1114	238	2329	367
WNFM061233B L 17	7.57	1.56	705	0.17	1498	3.82	5065	33	n.d.	55.00	n.d.	0.55	6.78	1.14	61.7	29.43	433	183	820	181	1820	307
WNFM061233B L 18	7.12	0.99	730	0.10	1163	5.05	6398	78	0.046	129.14	0.089	3.15	10.91	1.06	87.5	41.99	592	233	995	233	2232	380
WNFM061233B L 19	7.93	1.04	689	0.14	1881	3.15	5412	26	n.d.	47.96	n.d.	1.25	7.20	0.96	65.1	30.83	467	205	911	209	2155	350
Average	6.85	0.93	730	0.16	1922	5.42	6678	61	4.126	92.46	1.656	10.19	15.44	2.13	106.2	45.68	633	244	1060	261	2756	329
σ	0.92	0.27	38	0.09	642	2.36	2211	35	12.141	48.35	5.805	31.31	14.45	2.09	45.2	16.58	214	76	314	76	779	83

Table 18 RST zircon trace element compositions, crystallization temperatures and apparent U-Pb ages determined using LA-ICPMS (continued)

	Concentration (ppm)				*Trace Element Ratios*			
Spot #	Hf	Ta	Th	U	Th/U	Th/Y	Hf/Y	Y/U
Basal fallout								
RST-7-3 L 274	12300	19.33	733	1698	0.43	0.08	1.41	5.13
RST-7-3 L 275	11837	29.98	935	1395	0.67	0.12	1.52	5.57
RST-7-3 L 276	11278	13.74	755	1113	0.68	0.05	0.69	14.61
RST-7-3 L 277	11398	15.79	531	967	0.55	0.07	1.53	7.69
WNFM061233B L 1	9653	3.98	124	358	0.35	0.03	2.49	10.83
WNFM061233B L 2	11467	13.52	436	867	0.50	0.06	1.65	8.01
WNFM061233B L 3	10316	3.96	78	284	0.28	0.03	3.33	10.91
WNFM061233B L 5	11615	10.21	315	630	0.50	0.05	2.02	9.13
WNFM061233B L 6	13155	8.67	121	348	0.35	0.04	4.46	8.48
WNFM061233B L 7	10939	7.04	233	526	0.44	0.04	2.07	10.04
WNFM061233B L 8	10615	5.53	243	488	0.50	0.05	2.17	10.05
WNFM061233B L 10	12435	7.50	279	648	0.43	0.05	2.01	9.52
WNFM061233B L 11	11248	7.15	171	462	0.37	0.04	2.73	8.94
WNFM061233B L 12	11224	6.54	271	650	0.42	0.05	1.91	9.02
WNFM061233B L 13	11599	13.36	547	1162	0.47	0.06	1.25	7.97
WNFM061233B L 15	12373	9.52	303	734	0.41	0.05	1.88	8.95
WNFM061233B L 16	12712	6.89	413	687	0.60	0.06	1.81	10.24
WNFM061233B L 17	12346	8.39	203	506	0.40	0.04	2.44	10.01
WNFM061233B L 18	12794	13.59	339	707	0.48	0.05	2.00	9.05
WNFM061233B L 19	12182	7.67	189	491	0.38	0.03	2.25	11.02
Average	11586	13.94	394	762	0.49	0.06	1.89	9.48
σ	1341	6.87	234	348	0.10	0.02	0.57	2.42

Table 19 RST single zircon U-Pb CA-IDTIMS isotopic compositions and dates

	Compositional Parameters						Radiogenic Isotope Ratios						Isotopic Ages	
Sample (a)	Th/U (b)	$^{206}Pb^*$ x10^{-13} mol (c)	mol % $^{206}Pb^*$ (c)	Pb^*/Pb_c (c)	Pb_c (pg) (c)	$^{206}Pb/^{204}Pb$ (d)	$^{208}Pb/^{206}Pb$ (e)	$^{207}Pb/^{206}Pb$ (e)	% err (f)	$^{206}Pb/^{238}U$ (e)	% err (f)	corr. coef.	$^{206}Pb/^{238}U$ (g)	± (f)
Group C pumice #1														
z4	0.459	0.0210	86.98%	1.99	0.26	139	0.149	0.047014	5.590	0.001130	0.443	0.546	**7.282**	**0.032**
Group C pumice #2														
z6	0.461	0.1934	95.45%	6.28	0.76	400	0.150	0.047329	1.282	0.001131	0.146	0.741	**7.286**	**0.011**
Banded pumice														
z1	0.511	0.1291	94.68%	5.37	0.60	339	0.166	0.047378	1.298	0.001128	0.179	0.653	**7.265**	**0.013**
z2	0.481	0.0698	54.25%	0.36	4.81	41	0.156	0.049706	5.040	0.001107	0.946	0.212	7.132	0.067
z3	0.482	0.2880	92.82%	3.92	1.82	259	0.157	0.047467	0.897	0.001128	0.155	0.554	**7.266**	**0.011**
Welded tuff														
z1	0.479	0.1278	95.35%	6.14	0.52	388	0.156	0.047884	1.131	0.001128	0.203	0.676	**7.265**	**0.015**
z2	0.454	0.1310	95.98%	7.10	0.46	449	0.148	0.047336	1.042	0.001127	0.187	0.690	**7.260**	**0.014**
Unwelded tuff														
z1	0.383	0.7104	97.34%	10.81	1.59	698	0.124	0.047486	0.284	0.001139	0.135	0.716	7.341	0.010
z2	0.434	0.2061	91.25%	3.12	1.62	212	0.141	0.047669	0.946	0.001130	0.188	0.618	**7.283**	**0.014**
Basal fallout														
z1	0.457	0.1945	91.90%	3.40	1.41	228	0.148	0.047739	1.053	0.001129	0.195	0.652	**7.273**	**0.014**
z2	0.461	0.1070	92.22%	3.54	0.75	234	0.150	0.047522	1.600	0.001123	0.230	0.722	7.233	0.017
z4	0.492	0.1165	96.42%	8.08	0.36	504	0.160	0.047553	0.957	0.001128	0.188	0.701	**7.266**	**0.014**
z6	0.492	0.1512	95.46%	6.32	0.60	398	0.160	0.047314	1.123	0.001128	0.200	0.715	**7.267**	**0.015**
z1	0.442	0.0395	93.44%	4.22	0.23	275	0.144	0.046575	5.271	0.001124	0.276	0.477	**7.244**	**0.020**
z2	0.489	0.0478	76.13%	0.96	1.23	77	0.159	0.045150	27.765	0.001130	0.714	0.297	**7.282**	**0.052**
z3	0.463	0.0274	91.75%	3.32	0.20	219	0.150	0.049251	11.543	0.001133	0.308	0.241	7.299	0.022
z4	0.511	0.0352	82.30%	1.40	0.63	102	0.166	0.047050	12.198	0.001131	0.555	0.348	**7.288**	**0.040**
z5	0.401	0.0077	64.47%	0.53	0.35	51	0.130	0.044103	168.913	0.001129	1.474	0.085	**7.273**	**0.107**

(a) z1, z2 etc. are labels for single zircon grains or fragments annealed and chemically abraded after Mattinson (2005). **Bold** analyses are used in weighted mean age.
(b) Model Th/U ratio iteratively calculated from the radiogenic 208Pb/206Pb ratio and 206Pb/238U age.
(c) Pb* and Pbc represent radiogenic and common Pb, respectively; mol % $^{206}Pb^*$ with respect to radiogenic, blank and initial common Pb.
(d) Measured ratio corrected for spike and fractionation only. Fractionation estimated at 0.18 +/- 0.03 %/a.m.u. for Daly analyses, based on analysis of NBS-981 and NBS-982.
(e) Corrected for fractionation, spike, and common Pb; up to 1 pg of common Pb was assumed to be procedural blank: 206Pb/204Pb = 18.042 ± 0.61%; 207Pb/204Pb = 15.537 ± 0.52%; $208Pb/_{204Pb}$ = 37.686 ± 0.63% (all uncertainties 1-sigma). Excess over blank was assigned to initial common Pb, using the Stacey and Kramers (1975) two-stage Pb isotope evolution model at the nominal sample age.

Table 20 Prater Creek Tuff (PCT) single zircon U-Pb CA-IDTIMS isotopic compositions and dates

	Compositional Parameters						Radiogenic Isotope Ratios						Isotopic Ages	
Sample (a)	$\frac{Th}{U}$ (b)	$^{206}Pb^*$ x10^{-13} mol (c)	mol % $^{206}Pb^*$ (c)	$\frac{Pb^*}{Pb_c}$ (c)	Pb_c (pg) (c)	$\frac{^{206}Pb}{^{204}Pb}$ (d)	$\frac{^{208}Pb}{^{206}Pb}$ (e)	$\frac{^{207}Pb}{^{206}Pb}$ (e)	% err (f)	$\frac{^{206}Pb}{^{238}U}$ (e)	% err (f)	corr. coef.	$\frac{^{206}Pb}{^{238}U}$ (g)	± (f)
Prater Creek Tuff														
z1	0.451	0.1013	90.55%	3	0.87	193	0.145	0.046979	1.822	0.001342	0.223	0.719	8.645	0.019
z2	0.475	0.1138	90.00%	3	1.04	183	0.153	0.046721	2.096	0.001333	0.226	0.742	**8.587**	**0.019**
z3	0.527	0.1515	92.38%	4	1.03	240	0.170	0.047664	1.939	0.001337	0.224	0.709	**8.610**	**0.019**
z1	0.877	0.3861	98.36%	20	0.54	1098	0.280	0.047182	0.471	0.001317	0.235	0.638	8.487	0.020
z2	0.460	0.2523	96.06%	7	0.86	462	0.148	0.046662	0.923	0.001335	0.157	0.696	**8.602**	**0.013**
z3	0.478	0.0946	93.98%	5	0.50	300	0.154	0.046272	1.784	0.001322	0.211	0.749	8.515	0.018

(a) z1, z2 etc. are labels for single zircon grains or fragments annealed and chemically abraded after Mattinson (2005). **Bold** analyses are used in weighted mean age.
(b) Model Th/U ratio iteratively calculated from the radiogenic 208Pb/206Pb ratio and 206Pb/238U age.
(c) Pb* and Pbc represent radiogenic and common Pb, respectively; mol % $^{206}Pb^*$ with respect to radiogenic, blank and initial common Pb.
(d) Measured ratio corrected for spike and fractionation only. Fractionation estimated at 0.18 +/- 0.03 %/a.m.u. for Daly analyses, based on analysis of NBS-981 and NBS-982.
(e) Corrected for fractionation, spike, and common Pb; up to 1 pg of common Pb was assumed to be procedural blank: 206Pb/204Pb = 18.042 ± 0.61%; 207Pb/204Pb = 15.537 ± 0.52%; $208Pb/_{204Pb}$ = 37.686 ± 0.63% (all uncertainties 1-sigma). Excess over blank was assigned to initial common Pb, using the Stacey and Kramers (1975) two-stage Pb isotope evolution model at the nominal sample age.